Magnetisation dynamics and tuneable GHz properties of unsaturated magnetic nanostructures

Submitted by **David Osuna Ruiz**, to the University of Exeter

as a thesis for the degree of Doctor of Philosophy in Physics,

In October 2020

I certify that all material in this thesis which is not my own work has been identified and that no material has previously been submitted and approved for the award of a degree by this or any other University.

Signature: ……………… ………………..

I dedicate this doctoral dissertation to my family

Dedico esta tesis doctoral a mi familia

Declaration

I hereby declare that except where specific reference is made to the work of others, the contents of this dissertation are original and have not been submitted in whole or in part for consideration for any other degree or qualification in this, or any other University. This dissertation is the result of my own work and includes nothing which is the outcome of work done in collaboration, except where specifically indicated in the text. This dissertation contains less than 100,000 words including appendices, bibliography, footnotes, tables and equations and has less than 150 figures.

David Osuna Ruiz

2020

Acknowledgements

As of August the 7th of 2020, I write the last but not the least page of my PhD dissertation, 'Acknowledgements'. Four years ago, I decided to move to another country to pursue a high goal I set for myself, professionally and personally speaking, that was to work towards the completion of a PhD in Physics. How greatful I am to myself for having made such a decision, back in January of 2016. It just feels like yesterday, although four full years have passed by already since I arrived in Exeter. During these years, so many things happened, so many people I met, so many anecdotes and experiences I had in the UK, in Spain, and in quite a few other places worldwide. It has been an unexpectedly enriching and life-changing period of my life. After all this time, I am even more convinced that, what makes the difference is the people you meet and the fewer people you feel by your side. I would like to employ the next paragraphs as a dedicatory to all those who, one way or another, have been important and that without their support, everything would have been very different.

Firstly, I would like to thank my supervisors, **Feodor Y. Ogrin** and **Alastair P. Hibbins** for their support throughout these four years. Your, not only, scientific advices have educated me as a scientist, to always question myself what I know and what I say with rigour, something that I realize now to be crucial for the world we live in. Along the same line, I would like to thank my M.Sc.'s former supervisor **Miguel Beruete** from Spain, who introduced me into scientific research, thank you a lot. Thanks to the University of Exeter for the financial support and opportunities for widening my education. I would like to thank all the important people from the Physics Building. **Mark Heath** for all your invaluable help in the cleanroom, **David Colridge** and **Chris Forrest** for all your help in those critical situations when my computer or the internet connection played tricks on me close to deadlines, all the people from the workshop, my tutor **Nick Stone**, my colleagues **Nick Bukin**, **Fedor Mushenok**, **Erick Burgos**, **Jonathon Ventham**, **Kevin Fripp**, thanks a lot. Thanks also to my colleagues **Paul Keatley** from Exeter and **Farkhad Aliev**, **Antonio Lara**, **Isidoro Martínez** and **César González-Ruano** from Madrid for such fruitful work visits and collaborations. Thanks to all the people that made my stage in Exeter a bit warmer and homey. I am thinking of my basque friends from Goierri's food, friends from Peppino restaurant in Exeter and all the good people I met. I am also thinking of my colleagues **Zahid**, **Iago**, **Valentin**, **Santi**, **Natalie** and my former housemates **Joaquin** and **Miquel** for all the crazy moments we lived in our little house during last year.

I find it impossible to thank enough my best friends from Exeter enough with just words, for all the experiences lived together. To my colleagues and Spanish friends **Joaquin** and **Julia**, for all the good moments, chats, walks, trips to Exmouth, Dawlish, Cambridge, Liverpool and beyond. Also, to **Lizzie**, I am so glad to have met you and to have shared for so long not only desk and coffee breaks but also so many memorable moments and great times. Also, I would like to mention my friends from my hometown Pamplona: **Pablo**, **Íñigo**, **Miguel**… I have known you for a long time, more than 15 years now since high school, and we have always kept in touch and friendship. I hope it stays that way forever. Also, to **Lulu**, an inexhaustible source of joy.

Last but not the least, at the end of my academic training and learning, although there is never such a thing, I would like to have my final words to my family. Their invaluable support, every time I felt things were turning awry, and all the uncountable moments of rest and joy in their company, are without doubt what pushed me forward in the most difficult times. They are the people I truly love. I dedicate my PhD dissertation to my brother **Víctor** and my parents **Manuel** and **Silvia**. Dedico mi tesis doctoral a mi hermano **Víctor** y a mis padres **Manuel** y **Silvia**. Os quiero muchísimo. I especially dedicate my work to my grandmothers **María Luisa**, who passed away during my PhD, and **Lourdes**.

Four years is such a long time, that I may well have forgotten some names so, my apologizes for that. Nevertheless, I very well know that I will hardly forget all the good moments I had during these last four years. As of today, it is obviously very difficult, if not impossible, to picture myself in a specific place even in a short time. Regardless of the future and its certain uncertainty, I do believe that this whole experience has made me stronger, more resilient, and a little more ‘crazy’. Hopefully, more prepared for future challenges and aware that, even when things look uncertain, dark and beyond oneself, one can adapt to them, and always come out reinforced. This may be the most important lesson that I take after all.

Abstract

In this Thesis, investigations on spin wave propagation in sufficiently thick, magnetic unsaturated nanostructures of various shapes have been carried out. Analytical, numerical and experimental techniques in the time and the frequency domains have been used throughout this thesis. Unsaturated magnetic states are of high interest, more specifically the magnetic vortex configuration since the remanent state is typically dominated and stabilised by the shape anisotropy of the structure, with no need of strong or any bias fields. Due to the diversity of magnetic inhomogeneities, a high degree of reconfigurability by applying external low bias fields can be obtained. On the other hand, the inhomogeneous magnetic landscape becomes, very often, difficult to model analytically and therefore, propagating spin waves can turn out to be complicate to control in practice.

The aim of this work has been twofold. Firstly, to explore the most prominent magnetisation dynamics found in thick enough magnetic patches, or '2.5-dimensional' nanostructures. The explored propagating modes are exchange-dominated spin waves in the range of GHz, which allows us to obtain very short wavelength spin waves that can propagate along different 'paths' in the unsaturated landscape. The 'thickness and shape-induced' enhancing of these spin waves in structures in a flux closure configuration, suggests their use as highly tuneable spin wave emitters. Secondly, analytical and mathematical models are proposed for controlling the spin wave propagation in multidomain structures of various shapes and in domain walls. Their magnetic configuration is dominated by the shape anisotropy of the patch, which allows us to design particularized shapes to control the spin wave wavenumber (or equivalently, wavelength) while it propagates. Also, the modes are shown to be sensitive to bias fields, which further enhances their tuneability and reconfigurability.

All this previous work is joint in the last part of the Thesis, more focused on potential applications for Magnonics, where spin waves are not necessarily seen as undesirable energy loss mechanisms in magnetic structures but as information carriers or the base of novel computing paradigms. Single, or interconnected unsaturated elements of various shapes are proposed to be the base of interesting highly tuneable spin wave devices.

Contents

List of Figures

“He practicado catorce horas diarias durante 37 años y ahora me llaman genio!”

“For 37 years I’ve practiced fourteen hours a day, and now they call me a genius!”

Pablo de Sarasate (1844-1908), Spanish Violinist and Composer

List of Publications

Scientific Journal publications as of October 2020:

1. D. Osuna Ruiz, E. Burgos, N. Bukin, A. Lara, F. G. Aliev, A. P. Hibbins and F. Y. Ogrin, “Dynamics of Spiral Spin Waves in Magnetic Nano-patches: Influence of Thickness and Shape”, Phys. Rev. B 100, 214437
2. D. Osuna Ruiz, A. P. Hibbins and F. Y. Ogrin, “Hippopede curves for modelling radial spin waves in an azimuthal graded magnonic landscape”, Phys. Rev. B. 102, 104430
3. D. Osuna Ruiz, P. S. Keatley, J. R. Childress, J. A. Katine, R. J. Hicken, A. P. Hibbins and F. Y. Ogrin, “Time-imaging of curling modes in a confined magnetic vortex and a micromagnetic study exploring the role of spiral spin waves emitted by the core”, arXiv:2007.02043v2 (Resubmitted after peer review to Phys. Rev. B)
4. D. Osuna Ruiz, A. P. Hibbins and F. Y. Ogrin, "Graded Index Confined Spin Waves in an Intermediate Domain Wall", arXiv.org:2009.03195 (Resubmitted after peer review to Phys. Rev. B)
5. D. Osuna Ruiz, A. P. Hibbins and F. Y. Ogrin, “A reconfigurable spin wave emitter based on a teardrop shape”, (In preparation)
6. A. S. Bir, S. V. Grishin, O. Moskalenko, A. N. Pavlov, M. O. Zhuravlev and D. Osuna Ruiz, “Experimental Observation of Ultrashort Hyperchaotic Dark Multisoliton Complexes in a Magnonic Active Ring Resonator”, PhysRevLett.125.083903

Oral presentations:

1. D. Osuna Ruiz*, A.P. Hibbins, F.Y. Ogrin, "Refractive Index Manipulation of Confined Spin Waves in Bloch Domain Walls", *Intermag Conference 2020* Montreal, Canada, May 2020. (accepted)

2. D. Osuna Ruiz*, E. Burgos Parra, N. Bukin, A. Lara, F.G. Aliev, A.P. Hibbins, F.Y. Ogrin, "Improving Excitation and Detection of Propagating Spiral Spin Waves in Magnetic Nano-patches: Influence of Thickness and Shape", *Joint MMM-Intermag Conference 2019.* Washington D.C., USA, January 2019.
3. D. Osuna Ruiz*, E. Burgos Parra, N. Bukin, A. Lara, F.G. Aliev, A.P. Hibbins, F.Y. Ogrin, "Propagating spiral spin waves in magnetic nano-patches: Influence of Thickness and Shape", *International Conference on Magnetism (ICM) 2018*. San Francisco, USA, July 2018.
4. D. Osuna Ruiz*, E. Burgos Parra, N. Bukin, A.P. Hibbins, F.Y. Ogrin, "Propagating spiral spin waves in magnetic nano-patches", *IEEE International Conference in Microwave Magnetics (ICMM) 2018*. Organized by the University of Exeter - Exeter, UK, July 2018.
5. D. Osuna Ruiz*, E. Burgos Parra, N. Bukin, A.P. Hibbins, F.Y. Ogrin, "Propagating spiral spin waves in magnetic nano-patches", *International Symposium on Spin Waves 2018*. Organized by the Ioffe Institute, Saint Petersburg, Russia, June 2018.

Poster presentations:

1. D. Osuna Ruiz, A.P. Hibbins, F.Y. Ogrin, "Graded Index Confined Modes in Bloch domain walls", *Magnetism 2020.* Organized by IOP Magnetism group. Sheffield, UK, April 2020. (accepted)
2. D. Osuna Ruiz, A.P. Hibbins, F.Y. Ogrin, "Magnetic actuated tuning of Winter's magnons propagation in Bloch domain walls", *Magnonics 2019.* Organized by IEEE Magnetics and others. Carovigno, Italy, July 2019.
3. D. Osuna Ruiz, E. Burgos Parra, N. Bukin, A.P. Hibbins, F.Y. Ogrin, "Dispersion characteristics and control of propagating spiral spin waves in magnetic nano-patches", *IEEE International Conference in Microwave Magnetics 2018*. Organized by the University of Exeter - Exeter, UK, July 2018.
4. D. Osuna Ruiz, A.P. Hibbins, F.Y. Ogrin, "Propagating spiral spin waves in magnetic nano-patches", *Magnetism 2018.* Organized by IOP Magnetism group. Manchester, UK, April 2018.

5. D. Osuna Ruiz, A.P. Hibbins and F. Y. Ogrin, "Spiral Spin Waves in Magnetic Nano-patches", *Nano-Magnonics Workshop 2018*. Organized by the Technische Universitat Kaiserslautern - Kaiserslautern, Germany, February 2018.
6. D. Osuna Ruiz, A.P. Hibbins and F. Y. Ogrin, "Spiral Spin Waves in Magnetic Nano-structures", *XM3 Microwave Metamaterials Meeting 2018*. Organized by the University of Exeter - Exeter, UK, December 2017

Chapter 1 Introduction

In this first chapter, the purpose of research and a thesis outline are shown. The chapter starts with a summary of previous work on spin waves, focusing on applications and devices. The main advantages and disadvantages of different implementations are described to set the ground for the main purpose of the research.

Once the aim of the Thesis is clear, the Thesis structure is described. A brief description of the content in each chapter is summarised.

1.1 Purpose of the Research

Spin waves, or magnetic perturbations in magnetic materials, have always attracted attention to the magnetics community (V V Kruglyak, et al., 2010; Gurevich, et al., 1996; Stancil & Prabhakar, 2009), initially due to undesired effects such as background signals in magnetic disk readers. However, in recent years, the propagating properties of these waves, or their equivalent quasi-particles ‘magnons’, have interested the community for more beneficial purposes. Primarily, as information carriers and novel information processing, computing and boolean devices, principally based on wave interferometry and/or non-reciprocal phenomena (Jamali, et al., 2013; Chumak, 2019). Based on these principles, a vast collection of magnonic devices have been proposed since then including logical gates (Lee & Kim, 2008; Kostylev, et al., 2005), diodes (Lan, et al., 2015) and transistors (Chumak, et al., 2014). Even more complex operations such as resolving images in the nanoscale, overpassing diffraction limits for EM waves and signal spectrum analysers, all based on spin waves, are nowadays being investigated (Mansfeld, et al., 2012; Papp, et al., 2017). This paves a new road on novel highly compact and beyond-Moore nano-devices for computing. All this can be achieved since, for a given frequency of excitation, the wavelength of the spin wave is much smaller to that of an electromagnetic (EM) wave in free space, especially for exchange spin waves. Wavelength of exchange spin waves can be comparable to that of sound and light. This shows the potential of spin waves as information carriers for higher bit rates than those found in electronic devices and for novel memory storage devices (Mc Donald, 2019).

However, as in any other technology the advantages are always countered with problems that arise. Regarding circuits based on spin waves, the first encountered problem is the emitting of spin waves. One standard way to do it is attaching a micro-size microwave antenna to a specific area, usually one end of the magnetic track to launch the spin wave (Kittel, 1958). In a similar way that sources of electric currents are required in spintronics (Slavin & Tiberkevich, 2008), very precisely attached conducting lines to the magnetic material are required for an efficient local excitation. The oscillating magnetic field provided by the conducting line would excite only one section of the track, allowing propagation into the rest of the circuit. A constantly provided current would be required for spin wave excitation. Also, although this technique is more efficient for magnetostatic spin waves, is not that much for shorter wavelength spin waves, since the size of the required antenna becomes too small in practice for an easy manufacturing.

Once launched, spin waves for transmitting information give rise to a second issue: They decay too quickly, just after a few microns propagating in standard soft magnetic materials such as Permalloy (Yamanoi, et al., 2013). This imposes another limitation to the design of magnetic tracks for spin waves in circuitry based on this phenomenon. To overcome this problem, one first solution would be to excite the spin wave more efficiently at the source, enhancing its initial amplitude by coupling to ferromagnetic resonances. While the decay would still be the same, the amplitude of the wave at a point on the magnetic track would be larger, which would also improve its detection, i.e., reading of information. This solution would not need of other materials or complementary devices would be required, which is the ideal case. Other solutions proposed in the literature consist on focusing and beaming of spin waves or amplification by spin transfer torque effects (Gladii, et al., 2016), which still requires externally attached devices or more complex structures than single films.

Therefore, attached secondary conducting structures are usually required for a proper transmission of the launched spin wave. Very often, to retain magnetic saturation in soft magnetic materials, the magnetic track is attached to conducting materials that provide an inducted field used to saturate the material (Vogt, et al., 2014). Regions with different magnetisation orientation can lead to magnonic gradients that act as spin wave channels (Langner, et al., 2018) or steering based on mode conversion (Vogel, et al., 2018), although still requiring external biasing to retain the desired magnetisation orientation. A simpler scenario, which avoids these external constant inputs, would be working in the non-saturated regime. On the one hand, this induces magnetic inhomogeneities, which potentially work as natural spin wave sources and channels. On the other hand, the magnetic landscape can become more complex and therefore, a clever steering of the emitted wave would be required.

In this Thesis, an important goal is to take advantage of the non-uniform magnetic landscape for better excite and propagate short-wavelength spin waves in it. The use of magnetic inhomogeneities such as vortex cores as sources and domain walls as channels for spin waves is not new. However, in this Thesis we show an intensive exploration of the highest amplitude propagating modes that can be found in vortex state configurations of single film elements and some designs of structures based on the fewest elements possible. All are formed after a natural magnetisation relaxation process and where the equilibrium state is a remanence state with very low coercivity. This means that no external biasing devices are needed to retain magnetisation, apart from the oscillating magnetic field for the spin wave activation and low biasing for tuning properties in certain structures.

1.2 Thesis outline

This Thesis can be divided into two well-differentiated topics that cover some of the most common problems in efficient emitting and control of spin wave propagation in Magnonic systems. Firstly, the problem of a better sourcing of spin waves in non-saturated simple shaped patches is addressed. To this purpose, the understanding of the origins of high amplitude spin waves from magnetic inhomogeneities such as vortex cores in simple shapes is addressed. The detection and observation of these spin waves and other dynamics, such as spiral and curling modes present in non-saturated elements are experimentally shown. Secondly, further analytical, and numerical work on controlling spin wave propagation and conceptual device ideas are shown, which may help in the design of more complex spin wave circuits or devices based on non-saturated shapes.

The chapters in the Thesis are organised as follows. In Chapter 2, the basic and necessary background in Magnetism is introduced. Due to the extension of some general topics, we refer to the bibliography for further reading. The core of this thesis is the study of magnetization dynamics and so, its main concepts are explained in more detail. From there, the chapter evolves into the field of Magnonics, a sub-field in modern Magnetism. Some of the most relevant studies are mentioned, with a special focus on magnonic devices and circuitry. All the referenced material has been accordingly acknowledged.

In Chapter 3, the background principles of numerical and experimental techniques used in his Thesis are described. The chapter starts describing the software package use in simulations, as well as the basic criteria for an adequate modelling of the magnetisation dynamics under study. Next, the main experimental techniques used in this Thesis are described, these are, the ‘Vector Network Analyser - Ferromagnetic Resonance’ (VNA-FMR) and ‘Time Resolved Scanning Kerr Microscopy’ (TR-SKM). The underlying physics and the measurement procedure are explained.

In Chapter 4, we study the dynamics of spiral spin waves in nano-elements with different shapes. Here, we show how thick enough elements in the vortex state can efficiently emit these radially propagating spin waves, along with other complex dynamics, and act as highly tuneable emitters. Depending on the shape, the spiral dynamics and other ultra-short wavelength spin waves can be simultaneously emitted and therefore, enhancing the potential of the nano-element as a spin wave emitter. The high amplitude modes are proved to be more susceptible to be measured through standard techniques. Also, a mathematical model based on geometrical curves is shown, which describes the propagation of radial spin waves in structures with vertices in the vortex state.

In Chapter 5, we study curling modes in 40 nm thick nano-discs and their connection with the short wavelength spiral spin waves in a wide range of frequencies. Experiments were performed by my colleague Dr. Paul Keatley. Different curling waves and radial patterns are directly observed by means of TR-SKM and explained as either superposition or hybridization of eigenmodes of the disc. Following basic rules of hybridization, the observed modes give information of the magnonic landscape of the disc, such as the vorticity and polarity of the vortex and also the chirality of the spiral spin waves emitted from the core region.

In Chapter 6, we explore the confined modes in magnetic nanostructures presenting Bloch domain walls. Confined modes in domain walls allow high directionality making them useful for engineering the propagation of the wave in the magnetic element. A non-uniform magnetized element shows a high complex magnonic landscape. Therefore, numerical models or approximate models for describing magnetization dynamics are preferred for practical purposes. In this study, the effects of non-homogeneous demagnetizing fields on the propagation of confined modes are studied and a model for the local wavenumber of the spin wave is proposed. The model equation is derived from the fundamental Bloch equations of motion. Next, the analytical model is validated by means of numerical simulations. Some mathematical implications from the model are further explored, leading to a physically consistent model for describing the local wavenumber of the confined wave.

In Chapter 7, following on from the study of confined modes, a uni-directional spin wave emitter based on a 'teardrop' shape is proposed. The chapter starts with a brief introduction to similar uni-directional devices discussed in the literature. Next, the magnetic configuration of such a shape is studied and we explore how it can be used as a highly tuneable spin wave emitter under the effects of external biasing fields. Experimental results from VNA-FMR prove its anisotropic behaviour depending on the biasing field orientation.

In Chapter 8, more conceptual spin wave devices based on non-saturated nanostructures are proposed. Numerical results on these novel designs show their high tuneability under external biasing fields. Combining some of the main results from previous chapters, a few conceptual devices such as a spin wave phase-shifter, a magnetic field sensor and a spin wave interferometer are proposed. Their implementation, further study and optimisation are left as future work.

Finally, in Chapter 9, the main conclusions of the Thesis are summarised.

Chapter 2 Background concepts on Magnetism

2.1 Introduction

The aim of this background review is to get insight of the context of the work and to review the basic concepts of magnetism to understand the relevant experimental techniques and results. To that purpose, the descriptions will not aim to be exhaustive therefore the reader is referred to the bibliography.

2.2 The Origins of Magnetism

The phenomenon of magnetism in solid state has been known for a long time since the ancient world, when people noticed that lodestones could attract small pieces of iron. A long time after, in modern times and especially after much ground-breaking research, magnetism is a unified, well-explained phenomenon, incorporated with Electricity and Optics into the field of Electromagnetism. More lately, in the 20th century, magnetism continued to develop being incorporated into the fundamental theory of quantum mechanics. Quoting 1977's Nobel Prize J. H. Van Vleck, "[Quantum mechanics] is the master key to understanding magnetism", which gives a clear idea of the power of this discipline to explain magnetic phenomena and, more importantly, pointing out its atomic origins. Therefore, for a proper macroscopic explanation of magnetism in matter, it is required to look into its most basic building unit: the atom and its magnetic moment.

2.3 The Magnetic Moment

According to Gauss's law for magnetism and the consequent absence of the magnetic monopole, atoms have a dipolar magnetic moment **m**. This be a fictitious positive magnetic pole separated a distance r from a negative magnetic pole. The first understanding of the origin of magnetic moment came from macroscopic observations, assuming a current I in a loop of area S,

$$|\mathbf{m}| = \iint \mathrm{I}\, dS\,. \tag{2.1}$$

From this classical approach, the atomic magnetic moment is created by electrons orbiting the atomic nucleus[1]. Nevertheless, global magnetic moment of an atom is the sum of two main elementary momenta that contribute to the existence of a total magnetic moment. One of them is, indeed, the orbital motion of electrons around the nucleus, analogously to a macroscopic electric current in a loop. But there are also contributions from intrinsic particle properties such as electrons' intrinsic moment or *spin*. Both contributions, orbital **L** and spin **S**, couple in order to give a larger angular momentum to the atom, **J** = **L** + **S**. Nucleus have also intrinsic moment but is less relevant than other contributions since it is usually three orders of magnitude smaller (Stancil & Prabhakar, 2009).

Whereas electron spin is a purely quantum property, angular momentum of orbiting electrons can have a classical analogue like a spinning top. The constant of proportionality between the magnetic moment and the angular momentum is called the gyromagnetic ratio:

$$\mathbf{m} = \gamma\, \mathbf{J}\,. \tag{2.2}$$

---

[1] An electron's 'orbit' is not an orbit in the classical sense. It does not follow a fixed trajectory as this would violate the Heisenberg Uncertainty Principle. Instead, it has a probability distribution function about the nucleus.

The value of γ for orbital angular momentum is:

$$\gamma_L = \frac{\mathrm{m}}{\mathrm{L}} = \frac{\mathrm{q_e}}{2\,\mathrm{m_e}}, \tag{2.3}$$

where $\mathrm{q_e}$ and $\mathrm{m_e}$ are the charge and mass of the electron, respectively. It is known that the orbital precession motion of the electron can be perturbed by applying an external magnetic induction field **B**, as it follows from Lenz's law. Whether the material is diamagnetic or shows permanent magnetic moment, the angular precession frequency is related to the gyromagnetic ratio by (Stancil & Prabhakar, 2009),

$$\omega_P = |\gamma \mathbf{B}|\,, \tag{2.4}$$

where $\gamma = \gamma_L$. The precession frequency is called the *Larmor precession frequency*.

Macroscopic magnetism, since it is originated from many particles, can still be treated to some extent with classical or semi-classical models. If we return to the classical model of a closed current loop and the total atomic magnetic dipole, we can express the torque the dipole will experience in an external magnetic field,

$$\boldsymbol{\tau} = \boldsymbol{m} \times \mathbf{B}\,. \tag{2.5}$$

Also, this is the force moment that a dipole will experience due to a magnetic field **B** created by another dipole if both are placed far enough from each other, so the classical model still holds and quantum interactions are not present. Dipolar, and magnetic interactions in general, will be treated in section 2.4 in this chapter. Because of these atomic interactions and others, there are different types of arrangements of magnetic moments in matter, as it will be described in the next section.

2.4 Magnetism in Matter: Classification of Magnetic Materials

Macroscopic magnetism in matter can be regarded as the average magnetic dipole moment per unit volume V, i.e. $\mathbf{M} = \frac{\sum_V \boldsymbol{m}}{V}$. Since it is originated from many particles, it can still be treated to some extent with classical or semi-classical models. Depending on the electronic configuration, materials can show different magnetic properties and response to an external magnetic field. This allows to classify magnetic materials and sets a wide collection of different 'types' of magnetism in matter. The property that characterizes these different types is called *susceptibility* (χ) and relates the total magnetization in matter, **M** to an applied magnetic field **H**,

$$\mathbf{M} = \mathbf{M_0} + \overleftrightarrow{\chi} \cdot \mathbf{H}\,, \tag{2.6}$$

where $\mathbf{M_0}$ is the spontaneous magnetization in absence of **H**. For isotropic materials, the susceptibility tensor $\overleftrightarrow{\chi}$ becomes a scalar and the total magnetization is parallel to the applied field. Depending of the value of magnetic susceptibility we encounter different types of magnetic materials. These are generally classified in being: diamagnetic, paramagnetic, ferromagnetic, ferrimagnetic and antiferromagnetic.

All atoms in matter, to a certain extent, exhibit diamagnetism. Induced by an external magnetic field, electronic orbital motion will be modified to create an opposing magnetic field, according to a microscopic application of Lenz's law. These materials do not have a spontaneous magnetization ($\mathbf{M_0} = 0$) as they lack atoms or ions with permanent magnetic moments. Once the external excitation is removed, the induced field will disappear. Therefore, for isotropic diamagnetic materials, susceptibility is a negative scalar, remarking the dominance of the induced opposing magnetic field.

In paramagnetic materials, magnetic moments of electrons are randomly oriented in absence of an external magnetic field. This means that the net magnetization is very weak or zero. When an external magnetic field is applied, the moments tend to align with the field, resulting in a non-zero net magnetization. This means that, considering isotropy, they present a positive magnetic susceptibility, slightly greater than one and not that large as in ferromagnetic materials. The origin of paramagnetism comes from unpaired electrons. Electrons fill up their atomic orbitals following Hund's rule and those atoms with incompletely filled orbitals, are paramagnetic. The spin of these unpaired electrons acts as a subatomic magnet, getting aligned with an external magnetic field, and randomized when it is removed because of thermal motion.

In contrast to other type of magnetic materials, ferromagnetic materials retain a certain net magnetism when the external field is removed. In other words, they show spontaneous magnetization which leads to magnetic hysteresis. Ferromagnetic materials (also ferrimagnetic materials) are also called permanent magnets and they are the reason of the magnetic phenomenon in magnets encountered in everyday life. They show stronger forces of attraction, in comparison with other types of magnetism, presenting a large value of magnetic susceptibility. In this type of magnetism, under a certain temperature, thermal motion is not enough to randomize orientation of magnetic moments in atoms and this result in a spontaneous arrangement of them. The origin of ferromagnetism comes from a competition of magnetic interactions (see section 3) where exchange interactions are stronger than dipole interactions and are the responsible of forcing an antiparallel alignment of dipoles. The alignment of magnetic moments remains as it is under a certain temperature threshold called Curie temperature above which, material becomes paramagnetic.

Other types of magnetism that show magnetic ordering are ferrimagnetism and antiferromagnetism. The characteristic feature of ferrimagnetic materials is that they present an arrangement where different atoms alternate in the lattice, showing an alternating orientation of the respective magnetic moments. This implies that moments tend to cancel each other out, but not entirely and some magnetization remains. These materials are usually oxides, which makes them interesting magnets for certain applications where corrosion in metal or induced electric currents in conductors at high frequencies could become a problem.

Similarly to ferromagnetic materials, ferrimagnets lose their magnetic ordering when temperature goes above the Curie temperature. The same applies to antiferromagnets with Neel Temperature. An antiferromagnetic arrangement is like ferrimagnetism with the exception that dipolar moments cancel each out entirely.

The most interesting magnetic properties usually come from materials with an ordered arrangement of atoms such as in ferromagnetic materials. In these materials, magnetic moments remain aligned even in absence of an external magnetic field. In paramagnetic materials, the alignment is due to the applied field and by removing it, moments get misaligned again. In ferromagnetism, without external field, the interaction between atoms and their magnetic moments is the cause of that spontaneous alignment. From this point onwards, we will focus on magnetism in ferromagnetic materials.

2.5 Dipole-Dipole Interactions

The magnetic dipole-dipole interaction or dipolar coupling was first studied in 1948 by means of relaxation time of the atomic nuclei in several substances (Bloembergen, et al., 1948). Let us consider two interacting magnetic moments, $\mathbf{m_1}$ and $\mathbf{m_2}$, whose centers are separated by a distance *r*. The interaction energy between both, also called magnetostatic, dipolar or demagnetizing energy, that is minimised when they are antiparallel, is given by[2],

$$E_\mathrm{d} = \frac{\mu_0}{4\pi r^3}\left[\mathbf{m_1}\cdot\mathbf{m_2} - \frac{3}{r^2}(\mathbf{m_1}\cdot\boldsymbol{r})(\mathbf{m_2}\cdot\boldsymbol{r})\right]. \tag{2.7}$$

Dipole energy is a long-range interaction and that is why computing it is the most time-consuming part of any micromagnetic simulation. Let $\mathrm{m}_1 = \mathrm{m}_2 = \mu_\mathrm{B}$ be the Bohr magneton,

---

[2] The derivation of the dipolar energy between two magnetic moments can be found in most classical electrodynamics textbooks and it is analogous to the derivation from the potential of the electric dipole, which is equivalent to apart from using different units. It is addressed here as follows. The moment of the magnet can be resolved into the components parallel and normal to $\boldsymbol{r}$, $H_\mathrm{r} = 2(m\cos\theta)/r^3$ and $H_\theta = (m\sin\theta)/r^3$, respectively. The field at $\mathbf{m_2}$, parallel to $\mathbf{m_2}$, and due to $\mathbf{m_1}$, is $H_\mathrm{p} = H_\mathrm{r}\cos(\theta_2) - H_\theta\cos(90° - \theta_2)$, where θ_1 and θ_2 are the angles between $\mathbf{m_1}$ (or $\mathbf{m_2}$) and $\boldsymbol{r}$. Combining these equations, the potential energy of $\mathbf{m_2}$ in the field of $\mathbf{m_1}$ is $E_\mathrm{p} = m_1 m_2[\cos(\theta_1 - \theta_2) - 3\cos(\theta_1)\cos(\theta_2)]/r^3$. Since $\mathbf{m_1}\cdot\mathbf{m_2} = m_1 m_2\cos(\theta_1 - \theta_2)$ and $\mathbf{m_{1,2}}\cdot\boldsymbol{r} = m_{1,2}\cdot\cos(\theta_{1,2})$, an expression for the dipolar interaction energy between the magnets can be found. A factor of $\mu_0/4\pi$ is finally introduced to obtain Eq. (2.7).

and $r = 1$ Å as typical values for two atoms, Eq. (2.7) gives us an energy that corresponds to 1 K. This low value in comparison with thermal energy at room temperature means that thermal energy would destroy the magnetic ordering and so, in order to explain ferromagnetism, another type of subatomic interaction needs to be considered.

2.6 The Exchange Interaction

The Weiss field (Weiss, 1907) explains spontaneous magnetic ordering in ferromagnetic materials with the existence of a 'molecular' internal magnetic field, giving information about magnitude of magnetization but not about direction. Some of these materials are Co, Fe, Ni, Gd and alloys, and present very strong magnetization typically in the order of the saturation magnetization (M_s). Weiss introduces this 'molecular field' as an additional field to the external magnetic field in the form of $H_\mathrm{w} = N_\mathrm{w}M$, where N_w is characteristic of the material. From Weiss's work, the Curie-Weiss Law can be found, which describes the dependence of susceptibility with temperature, $\chi \propto (T - T_\mathrm{c})^{-1}$, where $T_\mathrm{c} = \frac{\mu_0 M_\mathrm{s} m_0 N_\mathrm{w}}{3k_\mathrm{B}}$ is the Curie Temperature. Therefore, the material loses its ferromagnetic behaviour at high temperatures, above Curie Temperature and behaves like paramagnetic[3]. A more detailed description of the Weiss field and the phenomenological verification of the Curie-Weiss Law can be found in Ref. (Weiss, 1907).

The phenomenological approach from Weiss found support in Heisenberg's theoretical model, based on exchange interactions, which explains the origin of this internal field in terms of exchange or 'short-range' interactions between magnetic moments. These interactions are

---

[3] Examples of Curie Temperature for some common elements and compounds are (Buschow, 2001): 1043 K (Fe), 1400 K (Co), 627 K (Ni), 292 K (Gd), 948 K (Fe_2O_3), 630 K (MnBi), 560 K (Yttrium Iron Garnet, YIG), ~600 K (Neodymium magnets). Analogous to Curie Temperature for ferromagnets, there is a Neel temperature for antiferromagnets. Some examples are: 116 K (MnO), 160 K (MnS), 198 K (FeO), 9 K (FeI_2), 24 K ($FeCl_2$), 525 K (NiO).

closely related to electrostatic energy of electrons and Pauli's exclusion principle. This principle dictates that two electrons (or fermions) cannot occupy the same energy level with the same quantum numbers. In order to understand these interactions, a fully mathematical quantum mechanical description is needed but this is not in the scope of this chapter.

From Heisenberg's model, the exchange energy can be expressed as:

$$E_{\mathrm{ex}} = -\sum_{\mathrm{i,j}} J_{\mathrm{i,j}}\, S_{\mathrm{i}} \cdot S_{\mathrm{j}}\,, \tag{2.8}$$

where $J_{i,j}$ is the exchange constant between atoms i and j and $S_{i,j}$ is the spin angular momentum of each electron. The value of the exchange constant is experimentally determined, and it determines if the atoms tend to align in the same direction ($J > 0$) or opposite direction ($J < 0$). The first case leads to ferromagnetism in magnetic materials and the second, to antiferromagnetism. This energy is minimized when spins are parallel oriented to each other and decreases greatly when increasing the distance between them.

2.7 Energy in Magnetic Systems

The state of minimum energy is determined by a competition between energies in the magnetic system. In addition to the exchange energy (E_{ex}) and the dipolar energy (E_{d}), previously explained, the most significant contributions to the total energy are:

$$E_{\mathrm{Total}} = E_{\mathrm{d}} + E_{\mathrm{ex}} + E_{\mathrm{Z}} + E_{\mathrm{ani}}\,. \tag{2.9}$$

The Zeeman potential energy (E_{Z}) comes from the magnetization **M** interacting with the external magnetic field $\mathbf{H}_{\mathbf{ext}}$:

$$E_{\mathrm{Z}} = \mu_0 \iiint \mathbf{M} \cdot \mathbf{H}_{\mathbf{ext}} dV\,. \tag{2.10}$$

The Zeeman energy is minimal when all the magnetic moments per volume in a sample, i.e. the macroscopic magnetization $\mathbf{M}$, are aligned with the magnetic field $\mathbf{H_{ext}}$. This implies that magnetic moments will tend to align with an external field, or so-called biasing field.

The anisotropy energy is mainly due to two types of magnetic anisotropies, *magnetocrystalline anisotropy* and *shape anisotropy*. Magnetic anisotropy is the directional dependence of a material's magnetic properties. For anisotropic materials[4], a tensorial description of magnetization is required for full characterization.

2.7.1 Magnetocrystalline anisotropy

This anisotropy is due to the atomic structure of a crystal, which introduces preferential directions for the magnetic moments via the exchange interaction. The energy is generally expressed as an expansion in powers of the direction's cosines (components of a unit vector) of the magnetization ($\mathbf{M} = \mathrm{M_S}(\alpha, \beta, \gamma)$). The energetically favourable direction of spontaneous magnetization is called the *easy axis*. Other axes are directions of greater energy. Magnetocrystalline anisotropy is the energy required to deflect the magnetic moment from the easy axis to the energetically least favourable axis or *hard axis*. For example, a magnetic particle with uniaxial anisotropy has one easy axis, and the anisotropy energy per unit volume can be expressed as (assuming the easy axis in the *z* direction),

$$\frac{E_{\mathrm{ani}}}{V} = K_{\mathrm{u}}(1-\gamma^2)\,, \tag{2.11}$$

---

[4] In principle, all standard magnetic materials (Fe, Co, Ni, alloys…) present a magnetic anisotropy of some sort. A magnet whose crystal grains directions are aligned and have their easy axes lines up are anisotropic and their magnetic force is strong. However, magnets can be designed to not have their crystal grain directions aligned and therefore, show isotropic magnetic behaviour. Isotropic magnets include bond magnets using quick-cooled thin alloys and isotropic ferrites (Tokunaga, et al., 1989).

where K_u is the uniaxial anisotropy constant. It has units of energy density and is dependent on composition and temperature. Depending on the crystal lattice of the material, the anisotropy energy can depend on other directions in different ways. For example, for a cubic crystal presenting cubic anisotropy (the easy axes correspond to the cubic crystal axes), the lowest order terms for the energy per unit volume are:

$$\frac{E_\mathrm{ani}}{V} = K_1(\alpha^2\beta^2 + \beta^2\gamma^2 + \gamma^2\alpha^2) + K_2\,(\alpha^2\beta^2\gamma^2)\,. \tag{2.12}$$

The anisotropy constants K_1 and K_2 determine the preferred axis in the lattice or easy axis. Due to magnetocrystalline anisotropy, depending on the orientation of the sample in a magnetic field, the magnetization reaches saturation in different fields. This connects magnetic anisotropy with hysteresis loop (or magnetization curves), since it is easier to saturate the sample along its easy axis, while it requires stronger fields to do so on its hard axis. This behaviour is useful for material characterization and allows to find the values of the anisotropy constants K_i from the magnetization curves of the sample.

2.7.2 Shape anisotropy

This anisotropy is governed by the dipole interaction and therefore is long range and dependent on the shape of the sample. If the sample is not perfectly spherical, the demagnetizing field is not equal for all directions, creating one or more easy axis. The preferred axis is usually the longest dimension in the sample or in plane of a thin film. By this, the field leakage and the demagnetizing field are minimized. A magnetized body will create magnetic charges or poles at the surface that are the source of that demagnetizing field. In non-saturated ferromagnets, this field gives rise to *magnetic domains*, regions where magnetization **M** is aligned in the same direction, but the macroscopic total magnetization tends to zero in order to reduce the stray field and magnetostatic energy of the system. Due to the vast extension of this topic, further reading on magnetic domains is recommended on (Hubert & Schäfer, 1998).

Magnetic domains are separated by *domain walls*, a transition region that is necessary for energy minimization, since a sudden change of orientation requires high exchange energy.

Depending on a competition between minimizing exchange energy or magnetocrystalline anisotropy, mainly two types of walls can be formed: Neel Wall or Bloch Wall. In Neel walls, magnetization rotates in plane of the domain whereas in Bloch walls, it rotates out of plane. Fig. 2.1 shows schematics of both configurations.

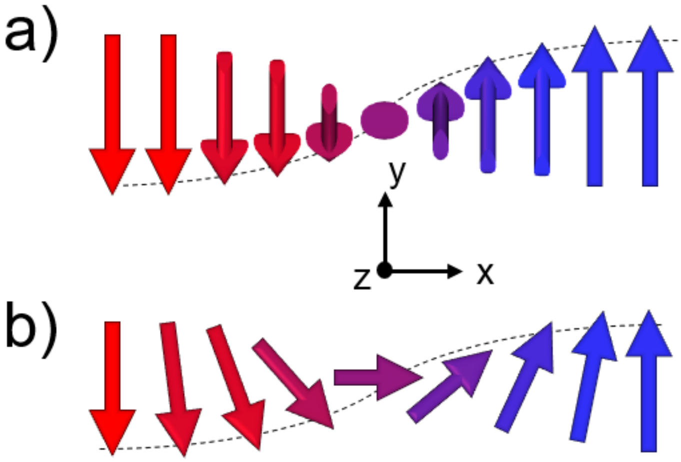

Figure 2.1 Schematics showing a Bloch wall (a) and a Neel wall (b) in a 180° transition in the x-direction. They qualitatively show the magnitude of magnetization in the y-direction (blacked dashed curves). Colour scale shows the domain regions (red and blue arrows) and the domain wall region (graded purple arrows).

In thinner films, it is energetically favourable for Neel walls to form, as the easy axis lies in plane and rotation out of plane is energetically expensive because of magnetic anisotropy. However, magnetocrystalline anisotropy in thick films is not as high as in thin films, allowing the characteristic out of plane rotation of a Bloch wall. Domain walls are not the only type of possible magnetic inhomogeneity in a sample. Some shapes such as circular dots form a flux closure structure with a singularity in the centre to reduce the stray field. This singularity is called a *vortex core* and consists of an out of plane component of magnetization in order to conserve symmetry in the sample. All these inhomogeneities also alter the distribution of the internal magnetic field, which makes them interesting topological, naturally formed objects in Magnetism regarding external reconfigurability and control of magnetization.

An expression of the demagnetizing field ($\mathbf{H_d}$) is not trivial to find as specific shapes can make calculations very complicated. If we consider the magnetostatic approach to solve Maxwell equations,

$$\nabla \times \mathbf{H_d} = 0\,, \tag{2.13}$$

$$\nabla(\mathbf{H_d} + \mathbf{M}) = 0\,, \tag{2.14}$$

we can now solve the system of equations above to find a potential for the demagnetizing field,

$$\mathbf{H_d} = \ -\nabla\varphi(\boldsymbol{r})\,, \tag{2.15}$$

where $\varphi(\boldsymbol{r})$ is the magnetostatic potential,

$$\varphi(\boldsymbol{r}) = \int_V d\boldsymbol{r}'\mathbf{M}(\boldsymbol{r}')\frac{\partial}{\partial r_i}\left(\frac{1}{\boldsymbol{r}-\boldsymbol{r}'}\right). \tag{2.16}$$

One of the simplest and most common shapes for calculating the demagnetizing field is an ellipsoid (Gurevich, et al., 1996). If the sample is uniformly magnetized and dimensions are small in comparison with the length of the electromagnetic wave in the sample, the demagnetizing field can be calculated as:

$$\mathbf{H} = \mathbf{H}_{\text{ext}} + \ \mathbf{H}_{\text{d}} = \mathbf{H}_{\text{ext}} - \overleftrightarrow{N}\mathbf{M}\,, \tag{2.17}$$

where $\overleftrightarrow{N}$ is known as the *demagnetizing tensor*. From Eq.(2.15), Eq.(2.16) and Eq.(2.17) it follows that:

$$\overleftrightarrow{N} = \ N_{ij}(\boldsymbol{r}) = \frac{1}{4\pi}\frac{\partial^2}{\partial r_i \partial r_j}\int_V \frac{d\boldsymbol{r}'}{|\boldsymbol{r}-\boldsymbol{r}'|'}\ . \tag{2.18}$$

The demagnetizing tensor is symmetric and becomes diagonal in the axis of the ellipsoid. The components of the diagonal are N_{xx}, N_{yy} and N_{zz}, and are also called the *demagnetizing factors*. Their sum is (in Gaussian units),

$$N_{\text{xx}} + N_{\text{yy}} + N_{\text{zz}} = 4\pi\,. \tag{2.19}$$

It is worth to note that, in literature, this is sometimes normalized to 1 (SI units) and then the 4π factor appears in Eq. (2.17). As one can see from Eq. (2.18), the demagnetizing field is very sensitive to the shape of the sample. Some work has been done in order to tabulate the demagnetizing factors for more complicated shapes, like rectangular shapes and prisms (Aharoni, 1998).

We have shown that a magnetic moment in a magnetic field experiences a torque that tends to align the dipole with the field, in virtue of minimizing magnetic energy of the system. The dynamics of this process and others related to spin dynamics are widely studied in the field of magnetization dynamics, or in other words, how matter gets magnetized.

2.8 The Equation of Motion: The Landau-Lifshitz Equation

The equation that describes this motion or, more generally, the response of magnetization vector to torques is called the Landau-Lifshitz equation (Landau & Lifshits, 1935). A more complete form of the equation, including the Gilbert damping term (α) of the spin wave is called the Landau-Lifshitz-Gilbert (LLG) equation. This equation reads as:

$$\frac{\partial \mathbf{M}}{\partial t} = -\gamma[\mathbf{M} \times \mathbf{H_{eff}}] + \frac{\alpha}{\mathrm{M_S}}\left[\mathbf{M} \times \frac{\partial \mathbf{M}}{\partial t}\right], \tag{2.20}$$

where γ is the gyromagnetic ratio, α is the Gilbert damping term, dependent on the material composition, $\mathrm{M_S}$ is the saturation magnetization and $\mathbf{H_{eff}}$, the effective or internal field, which is usually dominated by the external field and the demagnetizing field. Two terms can be noticed in the sum at the right hand side of the LLG equation: The first one describes a precessional movement around the effective magnetic field and the second, which includes the time evolution of **M**, a damping that forces the magnetization **M** to align with the external field. The combination of both implies a spiralling-in motion of **M** towards $\mathbf{H_{eff}}$ (see Fig.2.2). Multiplying scalarly both sides of Eq. (2.20) by **M**, we get,

$$\frac{\partial \mathrm{M}^2}{\partial t} = 0\,. \tag{2.21}$$

This means that, in a ferromagnet, the orientation of magnetization **M** can vary but its magnitude remains constant as that of the saturation magnetization.

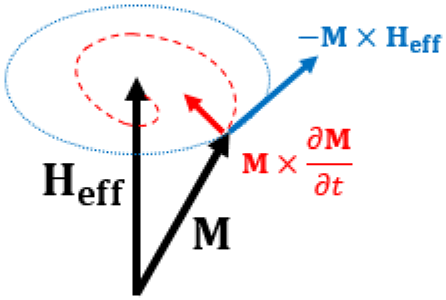

Figure 2.2. Sketch of the dynamical behaviour of magnetization **M** in an effective (or internal) magnetic field $\mathbf{H}_{\mathbf{eff}}$. Vectors show the precessional motion and damping terms (blue and red vectors, respectively) from LLG equation and the resulting motion with (red dashed line) and without (dotted blue line) damping.

The LLG equation is used to predict time domain behaviour of magnetic systems in a magnetic field and it is commonly used in micromagnetic simulators such as OOMMF® or Mumax3® (see Chapter III), usually in the differential form. For sake of completion, Slonczewski added to the equation the effect of *spin transfer torque*, i.e. the torque induced by a spin polarized current through the ferromagnet, giving rise to the Landau-Lifshitz-Gilbert-Slonczewski equation (Slonczewski, 1996).

2.9 Ferromagnetic Resonance

The precessional motion of **M** gives rise to a *Ferromagnetic Resonance*. To understand its origin, we need to consider the magnetization **M** under the influence of an oscillating magnetic field (h_{ac}) perturbing the static equilibrium state (H_0 and M_0):

$$H = H_0 + h_{\mathrm{ac}}\,, \tag{2.22}$$

$$M = M_0 + m_{\mathrm{ac}} . \tag{2.23}$$

For calculations we make the following assumptions,

$$h_{\mathrm{ac}} \ll H_0 , \tag{2.24}$$

$$m_{\mathrm{ac}} \ll M_0 . \tag{2.25}$$

Now we must consider the time dependence of oscillating fields h_{ac} and m_{ac} and a linearization of LLG equation. The derivation of the linearized LLG equation can be easily found in literature (Gurevich, et al., 1996).

$$h_{\mathrm{ac}} = h_0 \, e^{-i\omega t} , \tag{2.26}$$

$$m_{\mathrm{ac}} = m_0 \, e^{-i\omega t} . \tag{2.27}$$

By solving the system of Eq. (2.20), Eq. (2.26) and Eq. (2.27), we obtain a relation between the magnetic susceptibility tensor and frequency which gives rise to a *dynamical susceptibility*: $\chi = \chi(\omega)$. Due to dynamic processes in matter, magnetization cannot follow the fast time variations of the applied field and susceptibility is no longer a constant proportionality ratio between both magnitudes in frequency. The expression for $\chi(\omega)$ was first derived by Polder and it can be found in his work (Polder, 1949). In this chapter, it is only worth to note that it is of the form: $A(\omega)/({\omega_{\mathrm{H}}}^2 - \omega^2)$, where $\omega_{\mathrm{H}} = \gamma H_{\mathrm{eff}}$. This last feature of the susceptibility tensor shows its resonance dependence, which gives rise to the phenomenon of *ferromagnetic resonance* (FMR), i.e. the resonant absorption of electromagnetic energy in a ferromagnetic sample. From the expression for ω_{H}, one can infer that the resonance frequency is also dependent on the shape of the sample, since it depends directly on the internal or effective field H_{eff}. Following this, Kittel proposed an equation relating the ferromagnetic resonance frequency with the strength of the field and the demagnetizing factors of a shape (Kittel, 1948).

Absorption of energy is linked inevitably with losses in the magnetic sample, so we need to take these into account to understand the final resonance spectra. LLG equation incorporates these losses with the Gilbert's damping term, which modifies ω_{H} to be $\omega_{\mathrm{H}} = \gamma H_{\mathrm{eff}}/(1+\alpha^2)$ and gives the new resonant condition,

$$\omega_0 = \frac{\omega_{\mathrm{H}}}{1+\alpha^2}, \tag{2.28}$$

We can simply express frequency with its real and imaginary part which leads also to a complex expression for susceptibility. Real and imaginary parts of the diagonal components of the susceptibility tensor are (Gurevich, et al., 1996):

$$\chi' = \frac{\gamma M_0 \omega_{\mathrm{H}}[\omega_{\mathrm{H}}^2 - (1-\alpha^2)\omega^2]}{D(\omega)}, \tag{2.29}$$

$$\chi'' = \frac{\gamma \alpha M_0 \omega_{\mathrm{H}}[\omega_{\mathrm{H}}^2 + (1+\alpha^2)\omega^2]}{D(\omega)}, \tag{2.30}$$

$$D(\omega) = [\omega_{\mathrm{H}}^2 - (1+\alpha^2)\omega^2]^2 + 4\alpha^2\omega^2\omega_{\mathrm{H}}^2 . \tag{2.31}$$

These expressions show the dependence of susceptibility with the internal field. The imaginary part of susceptibility peaks at the resonant frequency, due to the maximized absorption.

2.10 Waves and Magnetism: Magnetostatic Spin Waves

We have shown in last section that LLG equation predicts the time evolution of macroscopic magnetization **M** when an external field is applied. Microscopically, this perturbation on a magnetic moment can be coupled by exchange interactions to the neighbouring magnetic moments in the sample, implying a propagating perturbation described by the same equation (see Fig.2.3). This collective excitation is called a *spin wave*. Depending on which interaction dominates, dipolar or exchange, spin waves are called dipolar (magnetostatic) spin waves or exchange spin waves.

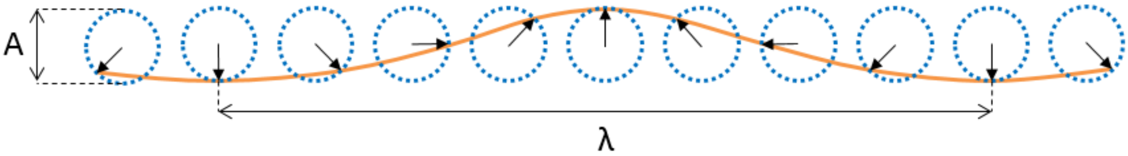

Figure 2.3. Schematic view from above of a row of coupled precessing magnetic moments. The wavelength (λ) and amplitude (A) of the spin wave can be easily identified.

Now we consider the case of having larger spin wavelengths than the one from an ordinary electromagnetic wave at the same frequency. Thus, to derive equations for magnetostatic modes, we must consider the magnetostatic approximation, which turns Maxwell's equations into,

$$\nabla \times \mathbf{H} = 0\,, \tag{2.32}$$

$$\nabla \cdot \mathbf{B} = 0\,. \tag{2.33}$$

Considering now the dynamic susceptibility tensor and the following relation,

$$\mathbf{B} = \mu_0 (1 + \overleftrightarrow{\chi})\mathbf{H}\,. \tag{2.34}$$

A wave equation for the spatial part of the magnetostatic potential φ, can be derived:

$$(1+\chi)\left[\frac{\partial^2 \varphi}{\partial x^2} + \frac{\partial^2 \varphi}{\partial y^2}\right] + \frac{\partial^2 \varphi}{\partial z^2} = 0\,. \tag{2.35}$$

This last equation is known as Walker's equation and describes magnetostatic modes in homogeneous media. Two cases can be noticed: If $\chi = -1$, equation leads to uniform precession of magnetic moments i.e., the FMR main mode. Solutions for $\chi \neq -1$ are magnetostatic propagating spin waves. In this case, assuming that $\varphi \propto e^{-i\mathbf{k}\cdot\mathbf{r}}$, the angle of propagation with respect to $\hat{\mathbf{z}}$ is θ, the wavenumber components are, $k_x^2 + k_y^2 = k^2 \sin^2\theta$ and $k_z^2 = k^2 \cos^2\theta$. Replacing them in Eq. (2.35), yields $\chi \sin^2\theta = -1$. This anisotropic susceptibility $\chi(\theta)$ highlights in turn the anisotropic behaviour of spin wave propagation.

Together with the Polder susceptibility expression (Eq. (2.29)), susceptibility can be expressed in terms of frequency. The resulting expression is independent of the magnitude of k so the obtained dispersion relations can yield different wavelengths for the same excitation frequency.

Exchange interaction becomes relevant in the propagation of spin waves when their wavelength is of the order of the exchange length (λ_{ex}),

$$\lambda_{\mathrm{ex}} = \sqrt{\frac{2A_{\mathrm{ex}}}{\mu_0 {\mathrm{M_S}}^2}}, \tag{2.36}$$

being A_{ex} the exchange stiffness constant. Characterizing spin waves in a magnetic material is key to understand important features as magnetic anisotropy, homogeneity of the internal field and coupling between structures.

Considering a thin film, spin waves amplitude and dispersion properties depend on its propagation direction and the orientation of the magnetization respect to the film plane. A modification of Kittel's formula by Herring leads to the spin wave spectra in a continuum media (Herring & Kittel, 1951). Applying an RF magnetic field (h_{RF}) and adding boundary conditions in the perpendicular direction of the film i.e., its top and bottom surfaces, we can get a discretized spin wave spectrum, since magnetic moments close to the surface are pinned due to anisotropies of the internal field ($\mathrm{H_i}$) (see Fig.2.4).

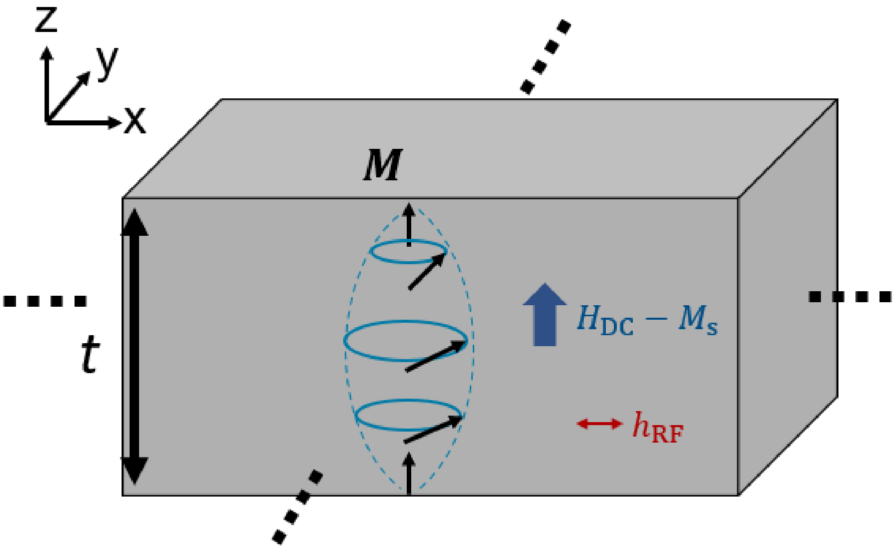

Figure 2.4. Standing spin wave resonance in a normally magnetised thin film of thickness *t*, infinite in the x-y plane saturated in the z-direction. Precession cone angle (blue ellipses) and dimensions of the film are exaggerated for clarity. Dashed blue curve shows a standing wave of the $n = 1$ mode as an example.

Therefore, for a normally magnetised thin film, spin wave resonances through the film thickness can be described by the following discretized $k_z = \pi n/t$ dispersion relation in the exchange regime (more of this later, towards the end of the section),

$$\omega_n = \omega_H + \omega_M \lambda_{ex} \left(\frac{\pi n}{t}\right)^2, \tag{2.37}$$

where $\omega_M = \gamma M_S$ and ω_H is the ferromagnetic resonance.

Kalinikos derived dispersion relations for magnetostatic spin waves (Kalinikos, 1980) assuming in some cases no spin pinning in the surfaces. If the film is magnetized out of plane, the dispersion relation is:

$$\omega^2 = \omega_H \left[\omega_H + \omega_M \left(1 - \frac{1 - e^{-k_z t}}{k_z t}\right)\right], \tag{2.38}$$

where $\omega_H = \gamma\mu_0(H_{\mathrm{DC}} - M_{\mathrm{s}})$ which the internal field ($H_{\mathrm{i}} = H_{\mathrm{DC}} - M_{\mathrm{s}}$) accounts for the demagnetizing field $H_{\mathrm{d}} = -M_{\mathrm{s}}$ originated by the density charges on the sample surfaces. These waves are called Forward Volume Spin Waves (FVSW), since group velocity and phase velocity are parallel and in the same direction. Standing spin waves occur when $k_z = 0$ due to the confinement in that direction.

If magnetization is in-plane, more different types of dipolar spin waves are found. These are:

1) Backward Volume Spin Waves (BVSW)

When the wavevector **k** is parallel to the direction of magnetization **M**, we have Backward Volume Spin Waves. From Ref. (Kalinikos, 1980), their dispersion relation is,

$$\omega^2 = \omega_H \left[\omega_H + \omega_M \left(\frac{1 - e^{-kt}}{kt}\right)\right], \tag{2.39}$$

where $\omega_H = \gamma\mu_0 H_{\mathrm{DC}}$ ($H_{\mathrm{i}} = H_{\mathrm{DC}}$). If the film is infinitely extent in the plane of the sample, H_{i} accounts only for the external applied field, since demagnetizing field is considered negligible (magnetization lies in-plane). The interesting property of these spin waves is their *negative* dispersion relation at low **k**, since phase and group velocity are *antiparallel*.

2) Surface Spin Waves

When the wavevector **k** is perpendicular to the direction of magnetization **M**, we have Surface Spin Waves. Their dispersion relation is,

$$\omega^2 = \omega_H(\omega_H + \omega_M) + \frac{\omega_M^2}{4}[1 - e^{-2kt}], \tag{2.40}$$

with $k = k_x = k_y$ and $\omega_H = \gamma\mu_0 H_{\mathrm{DC}}$. Amplitude of these waves is not distributed through the thickness of the sample, rather, it decays exponentially towards the centre, being maximal at the surfaces. Phase and group velocity are parallel, and these modes are usually called Damon-Eshbach modes due to their founders (Eshbach & Damon, 1960).

Fig. 2.5 shows results from Eq.(2.38) (blue curve), Eq.(2.39) (red curve) and Eq.(2.40) (green curve) accounting for the dipolar *and* exchange interactions (solid curves) and for dipolar interactions only (dashed curves) for typical values of a 80 nm thick Permalloy© film (Vansteenkiste, et al., 2014) ($\gamma = 1.76 \cdot 10^{11}$ (sT)$^{-1}$, $A_{\mathrm{ex}} = 1.2 \cdot 10^{-11}$Jm^{-1}, $M_{\mathrm{S}} = 7.4 \cdot 10^{5}$Am^{-1}) and $H_{\mathrm{DC}} = 74$ kAm^{-1}, approximately equivalent to 93 mT in air. It is worth to note the different manifolds for each type of magnetostatic spin wave, since the internal field is different for FVSW (for which we assume $H_{\mathrm{i}} = M_{\mathrm{S}}$ for a normally magnetised film of thickness 80 nm) than for BVSW and MSSW ($H_{\mathrm{i}} = H_{\mathrm{DC}}$ for an in-plane magnetised infinite extent film).

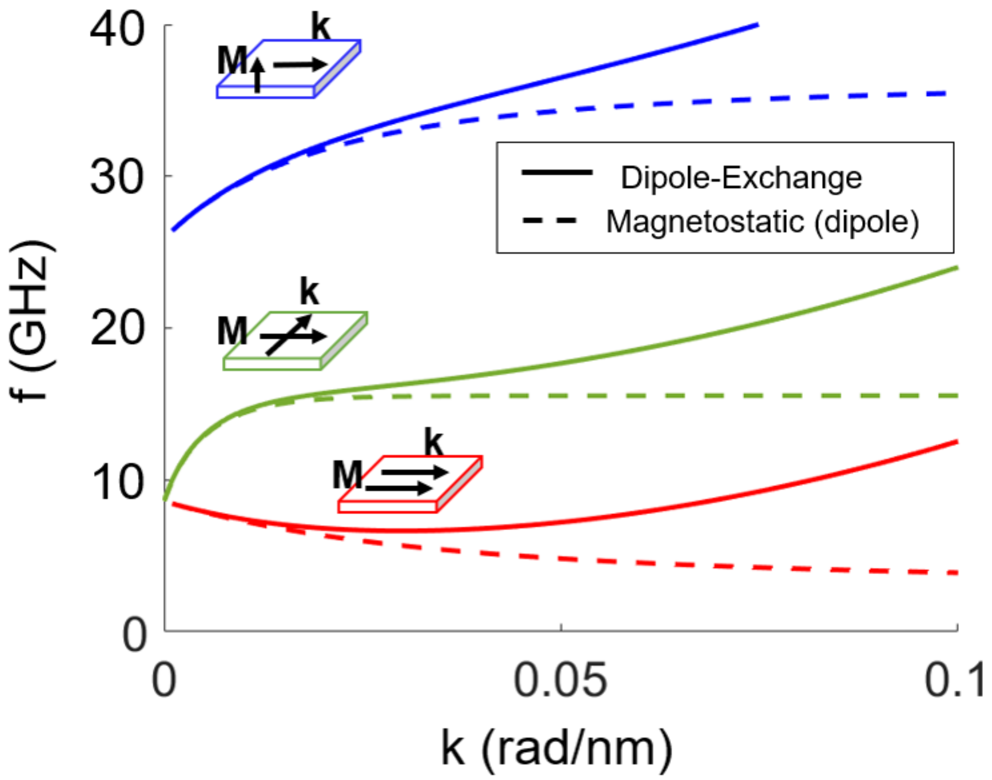

Figure 2.5. Dispersion relations from Kalinikos *et al.* for FVSW (blue curve), BVSW (red curve) and SSW (green curve) for the material specifications of Permalloy© and bias field (see main text) and bias field of 750 kAm^{-1}, in

the dipolar (dashed curves) and dipolar-exchange regime (solid curves). Insets show the geometrical relation between **k** and **M** for each type of spin wave.

For the magnetostatic modes described by Kalinikos we are assuming a 'dipolar regime', where **k** is low enough to not consider the exchange phenomena between magnetic moments. When the **k** vector is larger, we step into the 'exchange regime'. To include this behaviour, ω_H can be modified in the previous dispersion relations as in,

$$\omega_H \rightarrow \omega_H + \omega_M \lambda_{ex} k^2 \,. \tag{2.41}$$

This quadratic dependence becomes dominant in the dispersion behaviour for large enough **k** vectors, or equivalently, for short wavelength spin waves, typically in the order of nanometres. This is the spin wave regime in which the work shown in this Thesis is developed.

2.11 Spin Waves in Confined Structures

One of the main consequences of limiting lateral dimensions of a sample is the quantization of spin waves' spectra, in a similar way for perpendicular standing spin waves in thin films. Moreover, finiteness in all directions leads to modifications in the internal magnetic field that results into more complex modes and the existence of spin wave wells at specific regions of the shape, such as the edges, which leads to localized spin waves' modes. This has some resemblance with mechanical vibrational systems such as plates with sprinkled sand and excited by acoustic waves. Therefore, the variety of eigenmodes shows the need of using numerical methods for describing modes in these complex structures. An ellipsoidal shape is an exception since its internal field is uniform (Gurevich, et al., 1996) and therefore its eigenmodes are analytically easier to calculate.

Regarding magnetisation dynamics, complexity increases when the structure is in a non-saturated state because of the arising of magnetic inhomogeneities such as vortex cores or domain walls (Yan, et al., 2006). In the past, work has been done in order to explain the source of spin waves in patterned magnetic structures in multidomain and saturated states (Bailleul, et al., 2006; Yan, et al., 2006; Bailleul, et al., 2007) in terms of local ferromagnetic resonances, for simpler elements such as thin stripes or circular disks (Aliev, et al., 2009; Davies, et al., 2017; Mushenok, et al., 2017; Novosad, et al., 2002) to multilayer structures (Wintz, et al., 2016) in an equilibrium state. Results show the relevance of shape and edges of the sample, since spin waves can be excited from vortex cores and internal inhomogeneities at low frequencies but especially from the edges at high frequencies, forming a final in-plane standing wave pattern in some cases. Inhomogeneities have been proved to be sources of spin waves (Whitehead, et al., 2017) as well as reflectors or absorbers (Pirro, et al., 2015). These inhomogeneities of the self-demagnetizing field could be present in the form of vortex cores, antidots (Davies, et al., 2015) or domain walls, with two different polarity and circulation (or vorticity) numbers and, in the case of domain walls, two possible configurations, Neel or Bloch walls, and even combinations of both (Torok, et al., 1965). This shows, once again, the huge variety of possible structures to be useful in technology based on localised spin dynamics.

2.12 Dynamics in Non-Saturated Ferromagnets

Shape anisotropy (see section 2.7.2) introduces further complexity to the magnonic landscape when the sample is non-saturated, due to the arising of magnetic inhomogeneities such as domain walls. The equation of motion still applies and therefore, the dynamics in these scenarios can still be regarded as a result of the turns of the magnetisation vectors in regions with in-homogenous internal fields. The two naturally formed regions typically are: The domain wall/magnetic inhomogeneity and the magnetic domain (regarded as a quasi-saturated/saturated region). Spin wave dynamics in these environments strongly depend on inhomogeneous internal fields and therefore, propagation of spin waves can be very difficult to model analytically unless an accurate description of those fields is given. Further reading on this topic can be found in Ref. (Gurevich, et al., 1996). Just as an introduction to the topic, basic considerations on the two most common dynamical processes are addressed here, these are: domain wall oscillations and ferromagnetic resonances in a quasi-saturated sample. Other well-known dynamics related to magnetic inhomogeneities are vortex core gyrotropic motion, polarity reversal or motion of sub-structures within and along domain walls such as Bloch points or Bloch lines.

In general, under the influence of a small external fields, the main dynamic process is the growing of the aligned domain following a ‘displacement’ of the domain wall or any magnetic inhomogeneity. Rotation of magnetisation vectors still happen until they are aligned with the external field. A full rotation process may be dominant instead if the field is large and not aligned with the magnetic domain from start. Spin wave modes in such scenario are a result of a complex interplay between the size and thickness of the sample, oscillating field frequency and the sample material. All these parameters determine the local dynamic susceptibility in the region and thus, the local ferromagnetic resonance.

Ferromagnetic resonances in the presence of domains are dominated by the demagnetising fields, due to the macroscopic nature of magnetic domains. Again, equation of motion for magnetisation vectors still apply. One can approach the problem from the perspective of a standard magnetostatic problem, defining the magnetic potential of the dominant demagnetising fields in the sample at the domain boundaries or inhomogeneous regions. This approach usually starts from the boundary condition of magnetic induction component normal to the domain boundary,

$$\mathbf{H_1 n_0} - \mathbf{H_2 n_0} = -4\pi(\mathbf{M_1 n_0} - \mathbf{M_2 n_0}) \, , \tag{2.42}$$

where the indices 1 and 2 correspond to the neighbouring domains and $\mathbf{n_0}$ is unit vector normal to the boundary. However, the problem can easily turn out very complicated and in order to obtain practical solutions, simple assumptions must be taken considering the scenario under study.

For instance, in simple shapes such as spheres or ellipsoids, where the demagnetising fields are easier to calculate, the linearized equations of motion lead to two natural eigenfrequencies. These ferromagnetic natural resonances correspond to two general uniform modes in a non-saturated sample, one being excited by the parallel component of the oscillating field to the external field and the second, by the perpendicular component. As expected, in the saturation regime, the perpendicular mode transitions into the FMR main mode, following Kittel's equation, and the parallel mode disappears after going to zero (Gurevich, et al., 1996).

As in saturated samples, standard shapes such as ellipsoids or spheres are studied predominantly due to the simplifications in calculations which, otherwise, do not allow to obtain a practical analytical solution to the problem. Therefore, the shape of the sample can also add considerable complexity to the problem. In addition to this, for a more rigorous study, oscillations of domain walls should also be considered simultaneously, which illustrates the high complexity of the dynamics in non-saturated samples. Not only that, an even more rigorous solution of the equation of motion, including non-linear effects of stronger external fields would be required, but this is not in the scope of this chapter and further reading is refer to Ref. (Gurevich, et al., 1996).

Spin wave modes and nonuniform modes are more difficult to find unless further simplifications are considered, since the demagnetising field tensor yields very complicated integro-differential equations. Typically, approximated analytical solutions can be found when a relation in magnitudes between the spin wave wavelength λ, the thickness *t* of the sample and the domain wall width Δ is assumed. For example, for exchange dominated spin waves, it can be assumed that $\lambda \ll t \approx \Delta$ which, to obtain a practical analytical solution, implies that dynamics at the top and bottom boundaries/surfaces in the sample can be reasonably neglected in order to study the dynamics at the centre or far enough from the surfaces.

Due to the inhomogeneous internal fields in the sample, propagation of spin waves can become very complicated to model and control. For a given frequency, the wavevector $\boldsymbol{k}$ of a spin wave propagating in a ferromagnet with variable internal field will continuously change in space (Schlömann, 1964). If the change of the internal field is slow enough, this condition can be written as (Gurevich, et al., 1996) (p.198),

$$|\nabla \mathrm{H_i}| \ll |\boldsymbol{k}| \mathrm{H_i} \,, \tag{2.43}$$

which may also help to simplify calculations by assuming high order differential terms not very influential. Note that, for exchange dominated spin waves where $\boldsymbol{k}$ is large enough, Eq. (2.43) can, in principle, be easily satisfied along a slow-variating internal field path. In electromagnetics, bespoke steering of waves in inhomogeneous media can be achieved by engineering the refraction of the transmission media, usually leading to the field of transformation optics and metamaterials (Pendry, 2000; Kang, et al., 2008; Rinkevich, et al., 2015). Some metamaterial media can also show ferromagnetic behaviour to further tailor their refraction properties, focusing on re-configuring its effective magnetic permeability (Enkrich, et al., 2005; Lei, et al., 2016). In a similar way to metamaterials, an array of magnetic elements shows different magnetic and electromagnetic behaviour than the single elements alone, mainly due to dipolar interactions between the elements, something that has been widely studied (Awad, et al., 2010; K Y Guslienko, 2014; Lisenkov, et al., 2015; Sukhov, et al., 2014). Due to the different dispersion relations of spin waves and high tunability properties, similar principles are interesting to implement in a non-saturated magnetic structure, where inhomogeneous demagnetising fields modify local ferromagnetic resonances.

The interest is to engineer the propagation characteristics of spin waves to develop magnonic devices. The term ‘Magnonics’ illustrates the idea of using spin waves or their quasi-particle equivalent, magnons, in the same way of what electrons are to electronics. Most of the efforts of the research in magnonics is to come up with practical logic devices based on spin waves, which would pave the way up to magnonic computers as an ideal last stage.

2.13 Summary

The basic principles of Magnetism related to this Thesis have been reviewed. The chapter unfolds from the basic magnetism towards the main sub-topic of this Thesis, which is Magnonics, with a special focus on ferromagnetic resonances and the potential application of non-saturated ferromagnets. The next chapter explains the basics of the numerical and experimental techniques used in this Thesis.

Chapter 3 Numerical methods and experimental techniques

3.1 Introduction

In this chapter, the basics of the simulation and experimental techniques that have been used in the thesis are explained, as well as the fabrication process of samples. The magnetic material under study is Permalloy©, an alloy of Nickel and Iron ($Ni_{80}Fe_{20}$)[5] that presents soft magnetic properties (i.e., small coercivity) and high magnetic permeability (typically about 100.000). This material has been frequently chosen for spin wave transmission due to its low Gilbert's damping term ($\alpha = 0.008$), which allows spin waves to propagate long distances in the order of a few microns. A low damping also reduces experimental absorption linewidths. The specific Permalloy© samples used in this Thesis are described in more detail in section 3.3. The experimental data shown in this chapter is for illustrative purposes only, in which case details of the sample will be given. The most significant software scripts for the micromagnetic simulations can be found in Appendix A.

3.2 Numerical simulation methods

The software used in this thesis to run micromagnetic simulations is the general package Mumax3© (Vansteenkiste, et al., 2014). This software is an open-source, GPU-accelerated micromagnetic simulator to solve the Landau-Lifshitz equation of motion. There are other

---

[5] Other compositions of Permalloy are available, typically denoting its composition in Nickel by a prefix (i.e., 45 Permalloy means $Ni_{45}Fe_{55}$). An alloy with high concentrations of Nickel (~70%) is usually called Supermalloy.

open-source packages such as OOMMF© (1998 release) (Donahue & Porter, n.d.) or Grace© (Zhu, 2015), but these typically run on the PC's CPU. Mumax3© running on GPU exploits the potential of parallel calculations, and therefore extensive simulations can be done at reasonable computational times. In addition to its free cost and a user-friendlier graphical user interface (GUI), this is the main reason why we choose Mumax3© as our numerical solver to run micromagnetic simulations. Mumax3© uses the finite-difference (FD) method, which magnitudes are approximated by discrete values and their derivatives as finite differences in a spatial grid. Other free solvers such as marpag© (Scholz, et al., 2003) and Nmag© (Fischbacher, et al., 2007) use the finite-element (FE) method, which subdivides the model in smaller finite elements and each of those is assigned with a linear local description of one (or more) general equation of physics. The total contribution of each discretised element leads to the macroscopic behaviour of the model. This method is useful for multi-physics simulations which require solving together more than one equation (magnetisation and fluid dynamics equations, for example), such as COMSOL© (which however runs on CPU). While the discretisation method (FE or FD) itself was not a crucial aspect on choosing Mumax3© over other solvers, our study only requires a focus on the physics dictated by the LLG equation, hence the election of a micromagnetic only solver.

For this section, only the most relevant aspects of Mumax3 to the work shown in this thesis are addressed below, although a more exhaustive description of the design and general considerations of Mumax3 can be found in Ref. (Vansteenkiste, et al., 2014). Any specific design or parameter used in this thesis is addressed and further explained in its corresponding chapter. Some examples of the scripts used for Mumax3 can be found in Appendix A. All results from simulations were imported and treated through MATLAB. The MATLAB script for post-processing simulation results consists of a collection of functions for importing, treating, and visualising data. It was initially developed by Dr. Fedor Mushenok and more functions and modifications to it were incorporated by me.

3.2.1 Model Design and Spatial Discretisation

According to the finite-difference method, the geometry of the model in Mumax3 is discretised in equally sized hexahedral cells (along x, y and z directions), each of those with the assigned material parameters (such as saturation magnetisation M_{S}, exchange constant A_{ex} or Gilbert's damping term α) and magnitudes such as magnetisation **M** or the effective field $\mathbf{H_{eff}}$. A finite (discretised) Landau-Lifshitz equation is then solved for every cell and their neighbouring cells. Many magnetic parameters and scalar or vector magnitudes can be recorded during simulation-time either as spatially averaged values (stored in a table-like text file) or as x-, y-, z-spatial dependent matrices files (as open virtual format .OVF).

Since the discretisation is performed in hexahedral cells, circular or curved geometries can be approximated with the built-in function 'EdgeSmooth'. However, this is not the main consideration regarding discretisation. The spin wave dynamics studied in this work are mainly exchange dominated, which means that the exchange interaction must be 'felt' between cells. In other words, the cells size must be less than the exchange length of the material, for example approximately 5.3 nm for Permalloy© (Wang, et al., 2017). Also, cell size dictates the minimum spatial feature (including spin wave wavelengths), so cells as small as half the length of the minimum wavelength are desired. Making smaller cells would not be a problem if simulation time and memory space did not come into play. GPU's RAM is critical for simulations speed and PC's RAM for data storage which, depending on the discretisation of the model, may reach hours of computation time and tens of Gigabytes, respectively. The simulated samples are typically hundreds of nanometres size which means that, under these considerations, the number of cells in just one direction can easily get out of hand and impractical for use. Therefore, a trade-off between number of cells, cells size and model size must be addressed in every simulation but always to keep the cell size smaller than the exchange length of the material. Usually, for every simulation shown in this thesis, given the model size in one dimension ($\mathrm{L}_{x,y,z}$) for a specific magnetic material (through its exchange length λ_{ex}), the number of cells in the same dimension ($\mathrm{N}_{x,y,z}$) has been chosen under the following criterion:

$$\frac{\mathrm{L}_{x,y,z}}{\mathrm{N}_{x,y,z}} < \lambda_{\mathrm{ex}} \tag{3.1}$$

Some techniques to reduce the simulation time and the size of the saved files are considered, such as saving only one layer from the entire model after simulating the entire structure. This reduces the size of the final OVF files by the number of total layers. Simulating only one layer from the beginning is not advisable since exchange interactions between layers must be considered in the final results. Also, for computational efficiency, the number of cells that make up the grid must be set as powers of 2 in every direction.

3.2.2 Dynamic Response

Once the grid of the model in Mumax3 is made, excitation and/or biasing fields can be applied to the model. Also, one can define volumetric parameters (such as magnetisation, biasing fields, damping…) in specific regions only, which is a very useful feature of Mumax3 to study local dynamics in the nanostructure. Prior to every simulation, the equilibrium magnetisation state of minimum energy of the sample must be obtained. To do so, Mumax3 has built-in functions for evolving magnetisation until a minimum energy state is reached. In this work we combine one of these functions with long running time simulation for optimising the result. The stopping criterion is found in the maximum Landau-Lifshitz torque/γ normalised over all cells magnetic moments (so in units of T) which must be minimised (around the value 10^{-7} T) indicating convergence and the achievement of the equilibrium state. Once the equilibrium state is obtained, the spin configuration is saved as initial magnetisation state for simulations with a magnetic field excitation.

The typical excitation signals applied in this work to magnetically probe the response of our structure are either continuous wave (CW) excitation, to study time evolution and *sinc* pulses, for finding the frequency response. Obviously, every time a biasing (DC) field is applied, the same relaxation process must be performed to obtain the new equilibrium state before any oscillating magnetic probe field. The amplitude of the oscillating signal is always chosen so the magnetic configuration is not significantly altered, or modes remain in their linear regimes. Typically, this is considered in the order of less than 1% the saturation field of the corresponding material.

Sampling in time is another important aspect in simulations. The magnetisation under study are recorded at a series of time steps. A small time-step (i.e., high sampling frequency) then, is desired to avoid aliasing effects. However, very small steps may lead to unnecessary large and unmanageable amounts of data stored in memory. Nyquist theorem requires a sampling frequency of, at least, twice the maximum frequency of the dynamic range under study (Nyquist, 1928). While this criterion is satisfied, dynamic phenomena will be clear to observe in time sequences and, reciprocally, no aliasing effects will happen in the frequency spectrum. The same applies to the spatial frequency spectra and visualisation of modes in the real space. Analogously to the sampling frequency and the running time of the simulation, smaller cells (spatial ‘sampling frequency’) and larger model sizes will work better for visualising spatial modes and frequencies in the k-space. Again, we encounter a problem of balance between spatial/time resolution and computational efficiency. In this work, the sampling frequency is typically chosen as four times the excitation frequency. The Nvidia GeForce GTX 1080 Ti graphic card is used to run the micromagnetic simulations. Examples of typical scripts for running Mumax3 simulations can be found in Appendix A.

3.3 Sample Fabrication and Experimental Techniques

In this section, the fabrication process and cleanroom techniques are explained, as well as the experiment setup and techniques for measuring the dynamical magnetic characteristics.

3.3.1 Fabrication process

The samples studied in this thesis are ferromagnetic (Permalloy©, $Ni_{80}Fe_{20}$) nanothickness elements (or dots or patches) of various geometries patterned, or written, by Electron Beam Lithography (EBL) on a Silica (SiO_2) substrate. Fig. 3.1 shows a flow diagram of the standard fabrication process.

Figure 3.1. Flow diagram of the standarised fabrication process of the patterned ferromagnetic sample.

Sample substrates used in this thesis are silica square substrate of 10 mm × 10 mm × 1 mm. After sonicating the substrate in acetone for 2 minutes and cleaning with Isopropyl Alcohol (IPA), Polymethyl-methacrylate (PMMA 950K A4-Neat) photoresist is applied, and spin coated on one surface of the substrate to get a consistent and equally distributed thickness on the substrate. Prior to writing the pattern, a heating (or 'baking') process of 4 minutes on a hot (160°) plate is performed to the sample for a uniform distribution of PMMA. The standard nanofabrication process followed in this thesis for patterning is Electron Beam Lithography (or EBL), which allows writing patterns in the micro and nanoscale, down to tens of nanometers on unmasked PMMA (Broers, 1988) due to the short wavelength of accelerated electrons (Jones, 1987; Rosenfield, 1987). For a more accurate description of this technique and examples of typical setups, the reader is referred to Ref. (Martinez-Chapa, et al., 2016).

Typically, patterned elements are no smaller than a few hundred of nanometers, however, sharp features such as corners need to be more carefully written. In these cases, for the current density to remain constant, a smaller beam current (I) is applied to the corner region (usually a smaller area A) to obtain an acute angle, for example of 60°, present in 'teardrop' shapes (as the ones used in Chapter 7) or triangles (see Fig.3.2(a)), in detriment of the writing time (T) which increases proportionally. Also, to penetrate the entire thickness of the photoresist layer (typically about 80 nm), a larger current dose (D) is used. This also increases the total writing time, according to the relation: $D \cdot A = T \cdot I$, (Parker, et al., 2000). The electron beam changes the solubility of the photoresist, which after the writing process can be removed through chemical removal or 'developing'. The PMMA photoresist used is a positive photoresist, which means that the exposed areas will be removed. Developing time is crucial. Overdeveloping can erase the sharp contour of the shape by removing too much photoresist at the edges and sub-developing may not give enough time for the developer to reach the total depth of the exposed hole, which flaws the sample for the sputter deposition. The chemical developer used is a mix of chemical solvents in the following proportions: IPA (30 mL), Methyl isobutyl ketone (MIBK, 10 mL) and Methyl ethyl ketone (MEK, 2 mL). The developing time for our samples is usually about 30 seconds and then about 1 minute immersed in IPA for cleaning the sample surface. Fig. 3.2(a) shows an optical image of typical sample arrays (of teardrop and triangular shaped elements) after cleaning. Differences in colour between images are due to the different light intensity applied in an optical microscope, although the written pattern (light grey) can be easily identified in the PMMA matrix (blueish/darker grey).

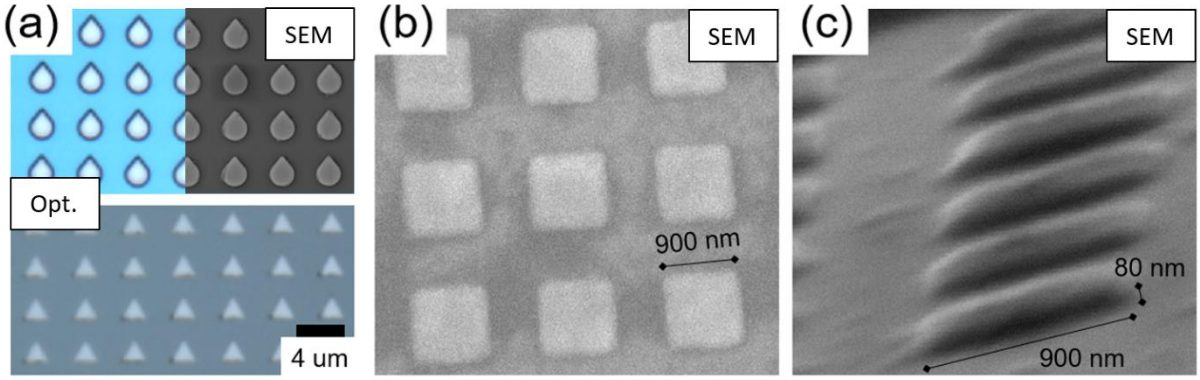

Figure 3.2. Examples of optical (Opt.) and Scanning Electron Microscopy (SEM) images of different arrays of samples, teardrop and equilateral triangular shapes of 2 um width and 2 um separation (a) and SEM images of an array of ferromagnetic squares of 900 nm size and 80 nm thick viewed from the top (b) and from a lateral view (zenith angle of 85 degrees) (c).

After the sputtering of a Permalloy layer on the whole surface of the sample (task performed by my colleague Dr. Erick Burgos), the areas on the substrate with photoresist must be removed so only the ferromagnetic pattern remains. This is done by a standard lift-off or removal process. Thus, the sample is pre-heated again at 70° on a hot plate for 45 minutes so the PMMA is loose enough for a proper removal. The sample is then immersed in a glass petri dish filled with acetone and pumped with a pipette until the flow removes the remaining photoresist, usually after 3- or 4-minutes pumping. Sonicating the sample is also advisable for a better removal. After this process, the sample is cleaned by immersion in IPA and dried with N_2 gun. The sample quality and its topological profile can be easily inspected by means of Scanning Electron Microscopy (SEM) in different angle perspectives. Fig. 3.2(b) and (c) show a SEM capture of a fabricated array of squares from the top and from almost a lateral view, respectively. Samples with the ferromagnetic pattern are now ready for measurements.

3.3.2 Vector Network Analyzer – Ferromagnetic Resonance (VNA-FMR)

The main experimental technique used in this thesis is the Vector network analyser – ferromagnetic resonance (VNA-FMR). This frequency domain technique indirectly provides information of dynamic phenomena through the amplitude and phase signals in a microwave absorption spectrum. There are other techniques for measuring in the frequency domain, such as Brillouin Light Scattering (BLS). However, the main advantage of VNA-FMR is its relative low cost, information obtained from both magnitude and phase, and easy to build setup which consists primarily of a Vector Network Analyser (explained in the next paragraph), a U-shaped Coplanar Waveguide (CPW) (see inset in Fig. 3.3), which provides the oscillating field ($\mathrm{h_{ac}}$) and an electromagnet, which provides an external biasing field ($\mathrm{h_{bias}}$).

The Vector Network Analyser (VNA) is a system that enables the measurement of performance of RF and microwave devices in terms of a two-port network *scattering parameters* in a wide range of frequencies, acting as source and receiver. We use the Anritsu® MS46122B Vector Network Analyzer (Anon., n.d.), which performs in a wide range of frequencies up to 20 GHz, enough for the phenomena explored in this thesis. The whole system forms a two-port network where the *scattering parameters* (S) describe the input/output relationships of power signals between ports. Therefore, in a passive two port network, transmission (linear) gain through the device under test (this is, anything between ports) is described by $\mathrm{T} = |\mathrm{S}_{21}|^{2} = |\mathrm{S}_{12}|^{2}$ (transmission from port 1 to port 2 or viceversa due to reciprocity). Signal reflections can be described by the input port reflection coefficient $\Gamma = \mathrm{S}_{11}$ (or S_{22} for output port), which is also related to impedance matching to the nominal impedance of the system. These parameters are typically expressed in decibels as $\mathrm{T} = 20\log_{10}|\mathrm{S}_{21}|$ for transmission gain (or insertion loss $\mathrm{IL} = -\mathrm{T}$) and the input return loss $\mathrm{L} = -20\log_{10}|\mathrm{S}_{11}|$. The magnetic characteristics of the sample are related to the transmission absorption peaks or losses through the imaginary part of its magnetic dynamic susceptibility. For further reading on the fundamental physics of ferromagnetic resonance we refer to Chapter 2, section 2.9. Here we focus in explaining the experimental setup for generic measurements. Any specific design or measurement particularity used in this thesis is addressed and further explained in its corresponding chapter.

Fig. 3.3 shows a schematic diagram of the employed VNA-FMR setup. The VNA is connected to the CPW through standard K-connector cables, up to 40 GHz, of 72 inches long in a line as straight as possible to avoid high frequency reflections. Sample substrate (light blue square in Fig. 3.3) is placed on top of the CPW, usually with the sample face down on the surface for maximum in-plane uniformity of magnetic field from the CPW central conductor. A CPW provides with an almost uniform in-plane oscillating magnetic field $\mathbf{h_{ac}} = \mathrm{h_{ac}}\hat{\boldsymbol{y}}$ to the magnetic pattern in the sample (see black dashed arrow and dark blue area in inset from Fig. 3.3), where, depending on the orientation of the sample with respect to the biasing field, it will be parallel ($\mathrm{h_{ac}} // \mathrm{H_{bias}}$) or perpendicular ($\mathrm{h_{ac}} \perp \mathrm{H_{bias}}$). Parallel or perpendicular configurations can be obtained by placing the sample on the long path or the short path of the U-shaped CPW, respectively. This leads to two different VNA-FMR measuring configurations which are useful to excite different dynamic phenomena (see Chapter 2 and results from Chapter 4 and 7). However, two experimental general conditions must be always met to excite (condition 1) and detect (condition 2) spin wave modes:

1) The pumping field must have a non-zero component perpendicular to the static magnetization: $\mathbf{M} \times \mathbf{h_{ac}} \neq 0$
2) The total dynamic moment ($\boldsymbol{\Delta}\mathbf{M}$) must have a non-zero projection in the direction of the pumping field for the time-averaged absorbed power to be non-zero: $\langle \boldsymbol{\Delta}\mathbf{M} \cdot \mathbf{h_{ac}} \rangle \neq 0$

The reflection (scattering parameter S_{11}) and transmission (scattering parameter S_{21}) coefficients are then determined by the VNA either at a fixed frequency whilst the magnetic field is swept or at a fixed field whilst the frequency is swept. To find the frequency dependence of the magnetisation dynamics, we follow the latter configuration. After every frequency sweep, a LABVIEW PC program[6], controlling the power supply of the electromagnet, sweeps the biasing field to a maximum (or minimum) value. For a proper data acquisition timing, the reading and writing data (T) and retrace (τ) times in the VNA must be considered with great importance, so the bias field changes only after the writing data period. Typically, $T \gg \tau$ in most cases. The writing and retracing times are not easy to find theoretically and to be generically applied to any measurement, since the data transmitted by the VNA includes data headers and more extra information apart from the measurement data. Therefore, typically, the value of T is found empirically for each particular VNA-FMR setup. In our setup, we consider an optimistic-case scenario where time between acquisitions is set to be twice the sweeping time (T) of the entire frequency range. This value must be input in the LABVIEW program accordingly.

---

[6] The LABVIEW PC program was made by me and intercommunicates the PC with the power supply through a GPIB (IEEE-488 digital communications interface bus) and with the VNA through an Ethernet Bus.

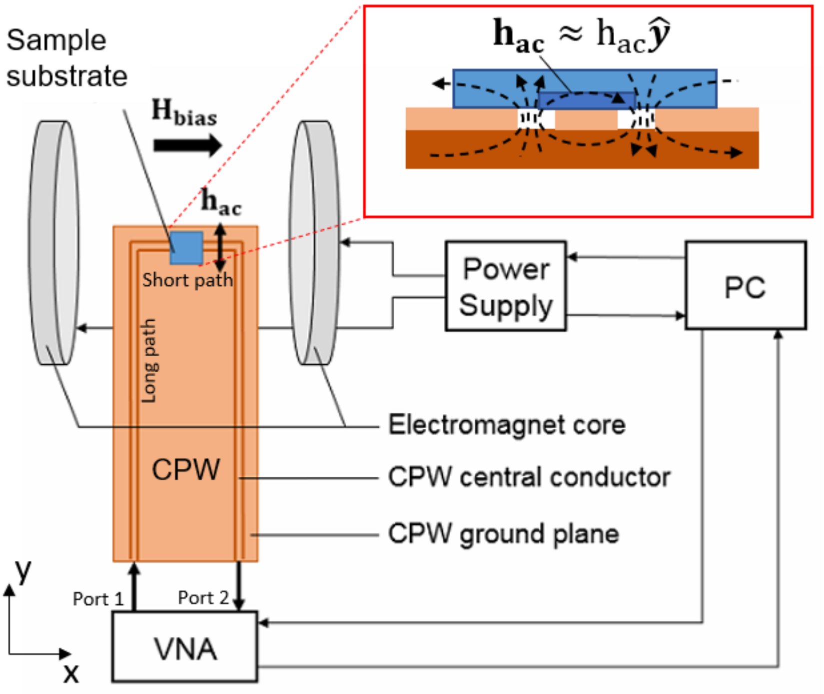

Figure 3.3. Schematic diagram of the VNA-FMR setup used in experiments with a sample placed on the short path of the CPW. Inset shows a schematic of the magnetic field distribution in the sample substrate (light blue area) and in the patterned magnetic structure (dark blue area).

We also use the Southwest® 292-04A-6 End Launch SuperSMA 27 GHz Jack (Female) Standard Block adapters clamped to the CPW. A careful design of the RF components and connections is critical to the success of these measurements since parasitic reflections, which distort the signal, are often present. For spin wave dynamics or higher order ferromagnetic resonance modes these effects are particularly problematic since their signals are of very low amplitude and can be shadowed by spurious signals or even background noise due to the low signal to noise ratio. One way to mitigate against these effects is by averaging measurements. This increases the global signal to noise ratio, since averaging background white noise will approximate it to its mean value or zero whereas any resonance signal would, in principle, remain unaltered between sweeps. The LABVIEW program is designed accordingly so it measures applying several times the same field sweeping on the sample. Therefore, the resulting file can be split in as many ‘cycles’ as repetitions, for a simple post-processing averaging through MATLAB. Also, averaging per frequency point (typically 6 measurements per point) for every single field sweep is activated in the VNA panel control. Another last method is followed to improve the quality of the final plots. At high fields, absorption peaks related to ferromagnetic resonances are expected to be moved up to very high frequencies, leaving the background signal only at lower frequencies, where the dynamics of interest appear at low fields. Therefore, to remove the common background signal as much as possible for every frequency in the field sweep, a highest field measurement is subtracted from all the others as a typical normalisation.

Fig. 3.4 shows a typical measurement of a magnetic (Permalloy©) film of 80 nm thickness. Following Kittel's formula (Kittel, 1948), the quadratic dependence of the FMR frequency with the biasing field can be easily identified (blue curve), along with other less intense higher order modes in saturation and smaller resonances in the multidomain state (as well as spurious signals at high frequencies, >15 GHz). Other material parameters can be inferred from these measurements, such as the Gilbert damping term from the linewidth of the resonance peak, or the g-factor, related with the gyromagnetic ratio. The FMR main mode can be easily found using this technique, however, other dynamics such as spin waves, higher order modes or edge modes might be more challenging to measure, especially in non-saturated nanomagnets. This is due to their less intense magnetic signal and to potential signal compensations due to the VNA-FMR spatial averaging.

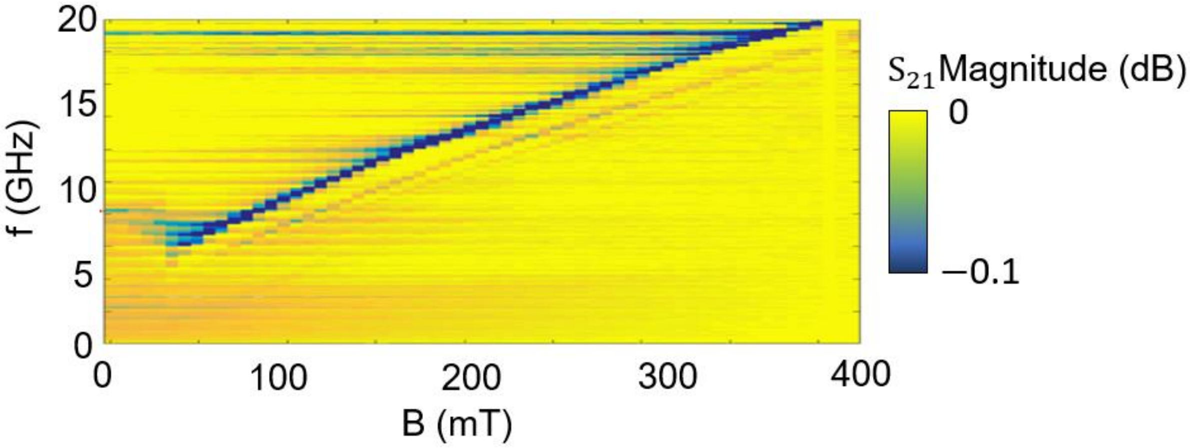

Figure 3.4. Example of a VNA-FMR measurement on the transmission coefficient in a decibel scale for a Permalloy thin film on a CPW. The FMR main mode can be easily identified (blue curve).

3.3.3 Time Resolved Scanning Kerr Microscopy (TRSKM)

Another relevant technique, used in chapter 5, is 'Time resolved scanning Kerr microscopy'. Experiments and results based on this technique were performed and obtained by Dr. Paul Keatley. This section aims to be an introduction to the Magneto-optical Kerr effect and the basics of TRSKM although more details about the technique can be found in Ref. (Keatley, et al., 2009) and in the corresponding chapter in this Thesis.

In contrast to VNA-FMR, this time domain technique provides spatial information and direct visualisation of the spin dynamics in the sample. In this setup, the spin wave excitation and probing could be both achieved by ultrafast laser pulse, although it could be used for probing only. Fig. 3.5 shows a schematic of a typical TRSKM setup for probing only.

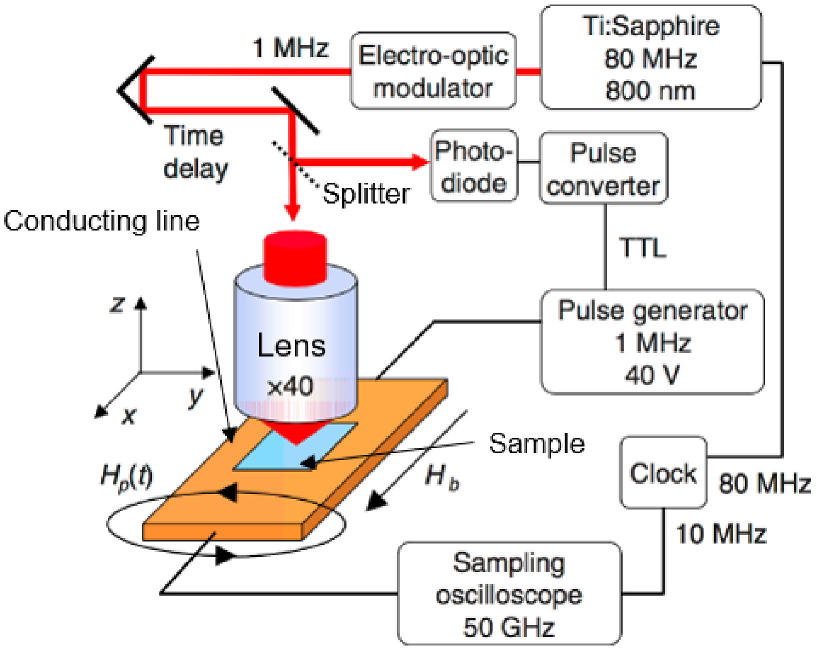

Figure 3.5. Schematic diagram of the TRSKM setup used in experiments, taken from (Keatley, et al., 2009).

In this case, a CPW provides the alternating magnetic field (shown in Fig.3.5 as $H_p(t)$) to excite spin waves in the sample. A circularly polarised probe laser beam, synchronised by phase locking with the oscillating magnetic field, detects the dynamic component in magnetisation through the Magneto-optical Kerr effect (MOKE) (Qiu & Bader, 2000; Kerr, 1877). This effect is similar to the Faraday effect, which describes changes to light transmitted through a magnetic material. The Magneto-optical Kerr effect describes changes in light reflected from the surface of a magnetic sample. A change in any combination of the following may occur: Kerr rotation, Kerr ellipticity, or polarized amplitude, depending on the geometry between magnetisation and polarisation of the incident light. These changes in light are possible due to the anisotropic dielectric permittivity of the material, since off-diagonal elements of the dielectric tensor determine the magneto-optical properties of the material (Kimel & Zvezdin, 2015). Since the speed of light depends on permittivity, changes in the phase of the reflected beam can be detected and interpreted in terms of regions of different permittivity and thus, of different magnetisation.

A detailed understanding of the effect of magneto-optical interaction requires considering quantum phenomena, which is not in the scope of this section. However, MOKE can be easily understood from a classical perspective. For example, for a circular polarised light, the electrons on the surface will be driven by a circular electric field. Local magnetisation will induce a Lorentz force, which will introduce changes in the electron's trajectory[7], as described before. Therefore, magnetisation dynamics can be mapped after performing the right conversion of these changes into intensity Kerr signals, usually by means of photodiodes. The photodiodes receive the original incident light (using a 50:50 beam splitter) and the reflected signal, from which a differential measurement can be taken to detect the Kerr polarization, ellipticity or rotation.

Due to the light wavelength of the laser beam, a spatial resolution of hundreds of nanometres is possible (Keatley, et al., 2009). The probing can be repeated in femtosecond timescales, allowing a clear and direct visualisation of the magnetization dynamics happening in the sample, typically in the order of nanoseconds.

3.4 Summary

In this chapter, the simulation methods, experimental techniques used in this Thesis and their underlying physics have been reviewed and described in a general way. Numerical and experimental details for particular studies are addressed and further described in their respective chapters. This combined work of simulations and experiments aims to give an accurate description of the magnetisation dynamics phenomena studied in this Thesis.

---

[7] As in the previous Chapter, it is worth noting that this is a classical interpretation of the phenomenon. Obviously, electrons movement cannot be described entirely by a 'trajectory' in the classical sense, and quantum physics need to be accounted for a more complete description.

Chapter 4 Dynamics of spiral spin waves

4.1 Introduction

Spin waves in confined structures have been a subject of interest with the view of their potential applications in the field of computing and data storage (V V Kruglyak, et al., 2010; Chumak, et al., 2015; Hoffmann & Bader, 2015; Krawczyk & Grundler, 2014). Due to a competition between dipolar and exchange energies in such structures, a range of relaxed states can be achieved, dependent on the shape and the dimensions of the structures. Most of these magnetization states will have a preferred in-plane magnetization with inhomogeneities arising at the boundaries or high symmetry points, leading to magnetization singularities such as magnetic domain walls and vortex configurations. It has been reported that, due to the confinement or the natural magnetic state of the sample, inhomogeneities of the internal magnetic field can be sources of spin waves due to a graded index in the magnonic landscape (Whitehead, et al., 2018; Davies, et al., 2017). Several studies have focused on characterizing and explaining the source of spin waves in confined micron and sub-micron structures for different magnetic domain configurations and saturated states (Bailleul, et al., 2006; Bailleul, et al., 2007; Perzlmaier, et al., 2005). Due to the finite size of the structures, dispersion relations of spin waves are expected to be discrete in contrast to a continuum spectrum for spin waves in infinite films (Schlömann, 1964). Spin wave propagation along the edges and emission from edges and local regions in the magnet have also been proved through micromagnetic simulations and direct imaging (Lara, et al., 2013; Mushenok, et al., 2017; Davies, et al., 2017). Moreover, in circular disks, depending on the orientation of the oscillating field, i.e. transverse or normal to the plane, a spiral or circular standing pattern can be formed, respectively.

In some applications based on confined magnetic structures like nano-dots, the existence of spin waves is usually a non-desirable phenomenon, as their frequencies lay in the GHz range and potentially interfere with writing or reading operations in magnetic memories. On the other hand, spin waves may play a central role in future communication technologies.

For example, previous works have reported conceptual ideas and realizations of several magnonic devices, logic gates (Kostylev, et al., 2005; Lee & Kim, 2008) and information processing components such as transistors or diodes (Chumak, et al., 2014; Lan, et al., 2015) which, in addition to an effective control on redirection along magnetic tracks (Vogt, et al., 2012; Xing, et al., 2013), can lead to more complex and practical magnonic logic circuitry. Hence, discovering new ways to effectively source and control spin wave propagation can make a significant impact on realization of such applications.

In this chapter we focus on the problem of spin-wave emission of thick magnetic elements with vortex singularities. The understanding of the origin of these modes is, by itself, an interesting topic and consequently led to several subsequent studies, for example by Kammerer et al. (Kammerer, et al., 2011) and Stoll et al. (Stoll, et al., 2015). However, these studies mainly focused on stationary modes and core reversal, with the formation of a dynamic double core or ‘dip’. A similar explanation was offered by Verba et al. (Verba, et al., 2016), but through a different approach: varying thickness to compare different hybridizations in thin and thick samples. Wintz et al. (Wintz, et al., 2016) demonstrated recently that a vortex core can serve as a source of spin wave coherent emission in ferromagnetic bilayer elements, with the ability of tuning the spin wave frequency and propagation direction, inwards towards, or outwards from the core. They reported large amplitude spin wave modes with spiral wavefront. A further work by the same team has also reported spiral spin waves in monolayered nano disks, which were explained as a result of hybridization with first order standing spin waves across the thickness of the disk (Dieterle, et al., 2019).

Our present study explores the formation of spiral-spin waves in thicker samples using both numerical simulations and experimental results. Starting from the principle formalism of dynamics described by the Landau-Lifshitz equation of motion we consider the different energy contributions and their influence in thin and thick elements. We consider the dispersion of the supported spin-wave and study the influence of thickness on the intensity enhancement of these spiral modes. We also provide insight into the way that the element shape affects the magnetization distribution by making comparisons between a square sample and the original circular one. We study the arising of confined modes in different types of patches, which can lead to further enhancement of the spiral wave and turning the magnetic patch into a more reliable and complex spin wave emitter. We experimentally characterize these spin wave modes using a standard VNA-FMR ('Vector Network Analyzer - Ferromagnetic Resonance') setup, in contrast to the more complex imaging techniques such as space resolved Kerr microscopy, used by Neudecker et al. (Neudecker, et al., 2006). Our findings may lead to the development of new types of efficient spin wave emitters for information technologies, potentially useful as simple, tunable and high-intensity source units in larger magnonic circuitry.

In section 4.2, we describe our numerical model, and in section 4.3, we show our experimental and numerical results, including evidence illustrating the spiral character of the mode propagation, its dispersion relations (for both circular and square geometries).

4.2 Numerical and experimental details

In order to understand the dynamics of spiral spin waves, a set of micromagnetic simulations using Mumax3 software (Vansteenkiste, et al., 2014) have been undertaken. The typical material parameters of Permalloy elements at room temperature were (Vansteenkiste, et al., 2014): saturation magnetization $\mathrm{M_S} = 8 \times 10^5$ Am^{-1}, exchange constant $\mathrm{A_{ex}} = 1.3 \times 10^{11}$ Jm^{-1} and Gilbert damping constant $\alpha = 0.008$. All simulations, as well as the experimental conditions, assume room temperature parameters. Simulations were performed using a hexaedral grid for the samples with the following geometric parameters of the elements and the corresponding cell sizes: Circular (square) samples have a diameter *d* (side length *L*) of 900 nm and different thicknesses *t* of 20 and 80 nm. With a fixed size cell along z ($\mathrm{N_{c,z}}$) of 5 nm for the thick samples and 2 nm for the thin, the grid is discretized in the *x, y, z* space into $256{\times}256{\times}t/\mathrm{N_{c,z}}$ cells. Therefore, the number of cells in *z* is 10 (*t* = 20 nm) and 16 (*t* = 80 nm). Cell size along *x* and *y* is 3.5 nm. Size cell along three dimensions is always kept smaller than the exchange length of Permalloy (~5.5 nm). To verify that the cell size is not affecting the results, several simulations were performed with reduced dimensions keeping the size of the elements fixed. Following the common practice (Vansteenkiste, et al., 2014), the number of cells were chosen to be powers of 2 to maintain the computational efficiency. In circular disks, we also set a ‘smooth edges’ condition with value 8. A key point for most micromagnetic simulations is to achieve a stable magnetization ground state. This was achieved by firstly setting an artificial vortex state with polarity (i.e., vortex core pointing either ‘down’, 1, or ‘up’, -1) and chirality or ‘circulation’ (i.e., in-plane magnetisation circulating counter-clockwise, 1, or clockwise, -1) numbers of (1, 1) and then running the simulation with high damping term ($\alpha = 1$) to relax the magnetization until the maximum averaged Landau-Lifshitz torque of all magnetic moments in the sample, normalised to the gyromagnetic ratio γ and therefore, in units of Teslas (as it is defined as ‘maxTorque’ parameter in Mumax3) is at the level of 10^{-7} T. Numerical value oscillates around a specific value, which indicates convergence and the effective achievement of a magnetization ground state as the averaged precessional motion of magnetic moments is effectively zero. A typical time to achieve this is of the order of 100 ns, which has no physical meaning due to the artificially set high damping. Once the ground state is obtained the whole magnetization configuration is stored and then used for the simulations with the dynamic activation. To achieve an equal excitation across a desired frequency range in the dispersion diagram, a sinc-shaped magnetic pulse has been used, ($B_1(t)$):

$$B_1(t) = A_1 \mathrm{sinc}(2\pi f_c(t - t_d)) \tag{4.1}$$

where fc is the cut-off frequency, set to 30 GHz, and A_1 = 10 mT is the pulse amplitude. Using this activation, each mode is equivalently fed with an AC magnetic field of 0.3 mT in amplitude. This field is small enough to remain in the linear regime of activation and to avoid any static changes in the magnetic domain structure of the samples. The delay time t_d = 5 ns provides a reasonable offset to the peak of the pulse, allowing a gradual increase of the amplitude from the beginning of the simulation. In another scenario, for analyzing time evolution of the magnetic signal, we apply a continuous wave (CW) excitation with a magnetic field B_2 at a specific frequency f_0:

$$B_2(t) = A_2 \sin(2\pi f_0 t) \tag{4.2}$$

Like with the sinc pulse, each mode is excited with a relatively small oscillating field. Equivalently to the previous case, A_2 is chosen to be 0.3 mT to obtain a good magnetic contrast in the time domain.

We use a sampling period of T_s =25 ps and record up to 1024 frames in space and time. With these parameters, simulation time is long enough (up to 50 ns) to get a reasonably good Fourier resolution of 78 MHz per frequency bin. For computational efficiency, we use a power of 2 for the number of time samples for faster Fourier transformation in analysis. The simulated spin wave spectrum is calculated from the absolute amplitude of all modes averaged for every cell in the model.

In the experiment, these spectra are compared to the absorption intensity, visualized through the real part of magnetic susceptibility (χ'). Experimental results were obtained by measuring a transmission spectrum of a sample in a coplanar waveguide geometry by means of a Vector Network Analyzer ferromagnetic resonance (VNA-FMR) setup. We use wide frequency band VNA-FMR technique in a lower range of frequencies, where many waveguides operate with higher reliability. In our measurements we used a set of samples fabricated using standard EBL techniques, with different parameters of shapes and dimensions. To enhance the RF response the elements were grouped in square lattices with the separation equal to the size of the element, assuming no or very limited inter-action between the elements. We tested arrays of thick (t = 80 nm) disks and squares with diameter and side lengths ranging from 500 nm to 900 nm. Since the arrays of samples are placed on top of a Coplanar Waveguide (CPW), the pumping magnetic field provided by the CPW is applied parallel to the sample plane and, in the case of square elements, parallel to one side of the square lattice. The sample is placed on the short path of a U-shaped CPW, and so, a perpendicular pumping with respect to the biasing field is applied (H_{bias} perpendicular to h_{rf}) (Aliev, et al., 2009). The experiments were carried out in the range of - 70 mT to 70 mT, which was enough to cover the vortex structure regime in the elements as well as saturation, in steps of 2 mT. Each spectrum was reduced by subtracting a signal produced at a highest field, and then averaged over 10 measurements. This helped to remove the larger background signal related to the transmission line noise and allowed us to amplify the magnetic response which is normally much smaller than other electromagnetic components.

4.3 Influence of Thickness and Shape

In this section we explore spiral spin waves propagating outwards from the vortex core region. We analyse their dispersion characteristics for circular and square discs and provide an explanation from the point of view of dipolar and exchange energies and their balance.

4.3.1 Dispersion characteristics

We start with the analysis of circular discs. Spin wave spectra of circular nanodots has been studied intensively in the past (Taurel, et al., 2016; Kakazei, et al., 2004). When applying an in-plane excitation, the lowest state mode that can be observed is related to a gyrotropic motion of the vortex core, with the frequency of gyration highly dependent on the aspect ratio of the dot (Guslienko, et al., 2002). With increase of frequency, higher order gyrotropic modes (Ding, et al., 2014; Guslienko, et al., 2015) and a complete set of modes related to azimuthal and radial spin waves can be obtained (Taurel, et al., 2016). The last type of spin waves is intuitively related to the well-known Damon-Eshbach modes in magnetized thin films, in the sense that radial k vectors are always perpendicular to M in a vortex core configuration (Eshbach & Damon, 1960). Depending on the thickness and more generally, on physical dimensions, the spectra of these waves can drastically change.

In our study, we firstly proceed to obtain dispersion relations for Permalloy circular disks with a relatively high aspect ratio (see section 4.2). To understand their dynamic properties here, we explore their dispersion relations. Because of the circular geometry, which does not allow to take advantage of periodic boundary conditions (PBC), we have also built rectangular structures, setting an equivalence between the radius of the disk and the lateral dimension of the rectangular stripe. PBC along y axis of the stripe structure are set, this provides a similar dependence but in a much clear representation. Their magnetization distribution along x-direction is the same as in the circular disk whereas an infinite Bloch wall, similar to the one studied in Ref. (Krawczyk & Grundler, 2014), plays an equivalent role to that of the vortex core in discs.

Figure 4.1 (a) shows a comparison of the simulated spin wave spectra for a 20 nm and 80 nm thick discs as well as the semi-infinite rectangles of the same thickness, and their dispersion relations (See Fig.4.1(b) and Fig.4.1(c)). Although both systems show more intense modes above 6 GHz, there are some small discrepancies between the resonance spectrum which could be due to the differences in shape anisotropy and the implications on the internal effective field and the local FMR (Mushenok, et al., 2017). However, the difference between relative larger peaks when the size is reduced (from d = 900 nm to 600 nm) remains the same (f = 0.77 GHz) for the disk and our stripe model, which suggests that this mode is of the same nature in both shapes and equally influenced by the cavity length of the shape.

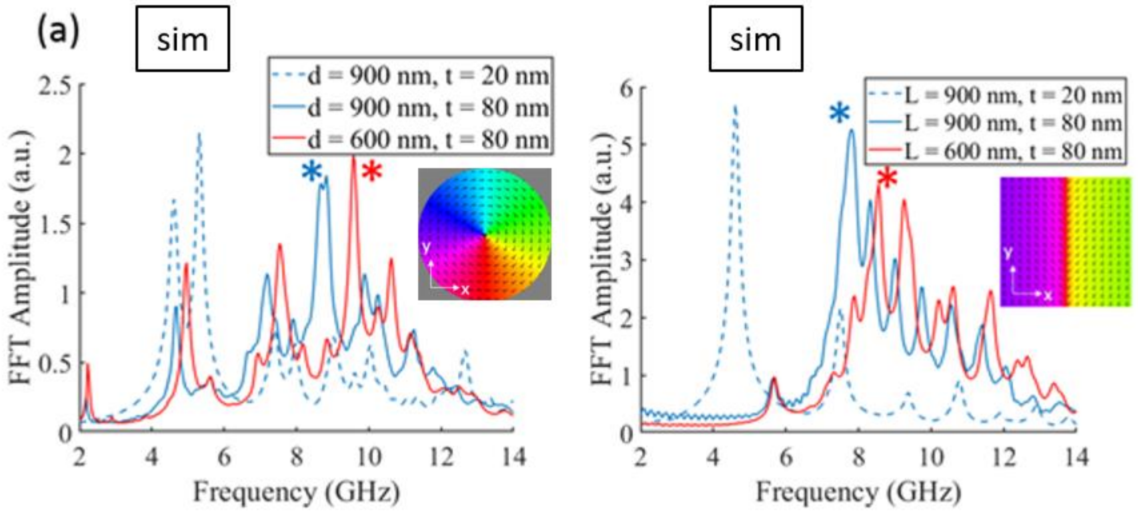

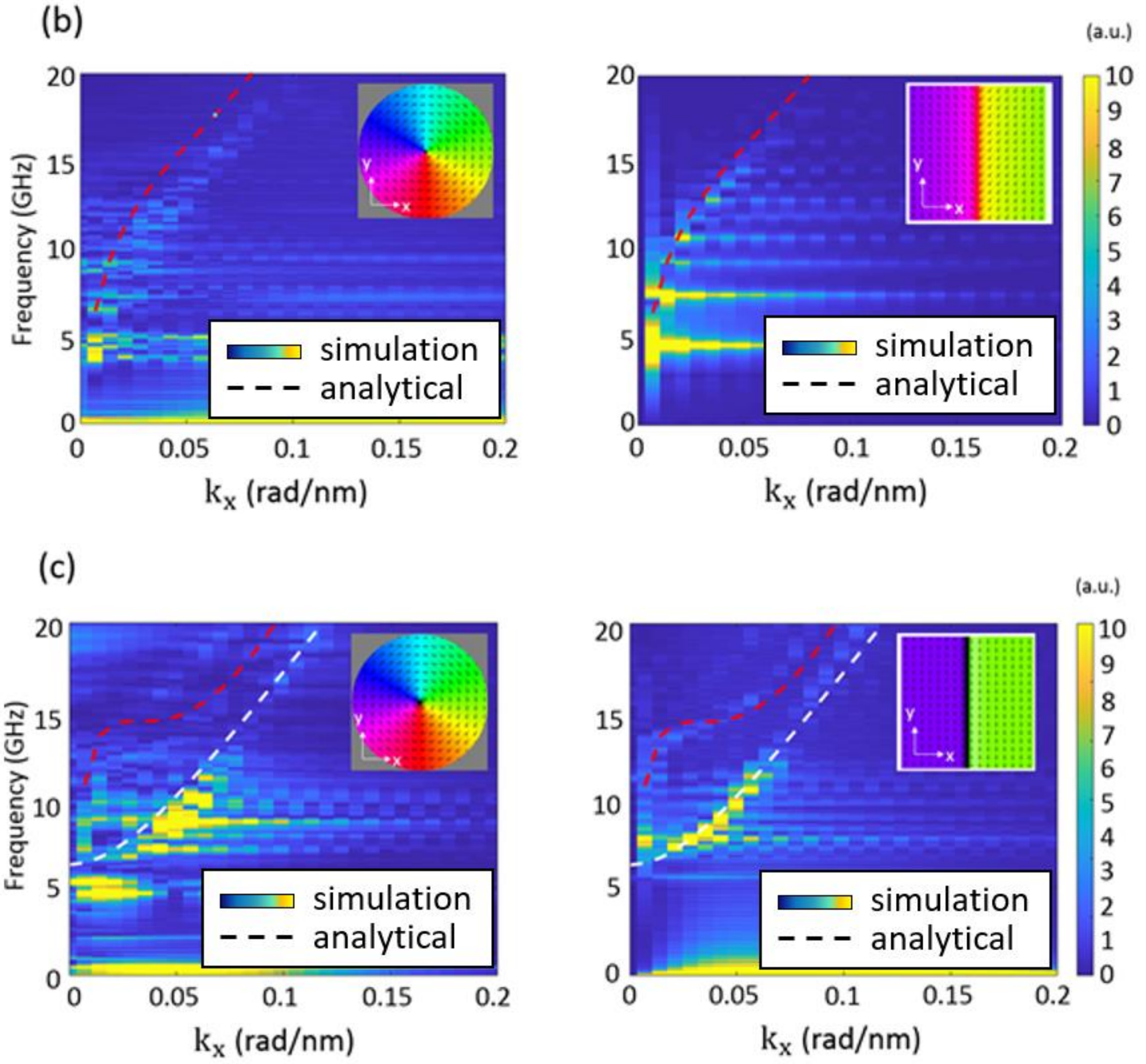

Figure 4.1. (a) Spin wave simulated spectra for thick and thin circular disks (left) and semi-infinite stripes (right),. The main peak has been marked with a star. Insets in (a) show the simulated model for thin structures as examples. Dispersion diagrams in x direction, i.e., across the center for thin (b) and thick (c) discs and stripes of equal length along x (L = 900 nm) are shown. Color scale shows the module of each mode. The change in width of the vortex core can be easily spotted in the insets. Red dash line shows the analytical equation for a Damon Eshbach mode from (Brächer, et al., 2017) and white dashed line the analytical model from (Kalinikos & Slavin, 1986) assuming unpinned moments.

All the above suggests that this mode is not excited from the edges but rather, from the central region of the shape, i.e., from the vicinity of the vortex core (see Fig.4.2) and, equivalently, from the vicinity of the Bloch wall in the semi-infinite stripe. The latter is supported by results from (Whitehead, et al., 2017), suggesting that the inhomogeneity at the core region can be treated as an equivalent source of spin wave. For thicker disks, this implies that there is a multi-mode regime above a certain frequency, where the spin waves are being excited from both the edge and from the core, like it was found in (Mushenok, et al., 2017). However, in our case, the waves originating from the core significantly prevail in amplitude. The obtained dispersion relations, help to understand the spectra in more detail, see Fig. 4.1. For thin (20 nm) disks (Fig. 4.1(b)), we can clearly see that the only mode excited at frequencies above 5 GHz is originating from the edges (see Fig. 4.2(a)), in accordance with the analytical model for spin waves in a Damon-Eshbach configuration from (Brächer, et al., 2017), which takes into account the finiteness of the element. This is also consistent with previous results where the edges act as spin wave emitters (Mushenok, et al., 2017). In thicker disks (Fig. 4.1(c)), the lower branch mode can be analytically described assuming un-pinned magnetic moments conditions, i.e., free surface boundary conditions for first higher order modes (Kalinikos & Slavin, 1986; Dieterle, et al., 2019) (see Fig. 4.1).

Here we reproduce some results for thin circular disks for the comparison with our thicker samples. As previously reported for this case, an in-plane CW excitation gives rise to an inwards propagating wave which generates a spiralling wavefront. It is worth to note that this case is realized for the excitation in-plane, in comparison to radial waves which can be also produced with out-of-plane pumping (Mushenok, et al., 2017).

Looking at the thicker 80 nm disks we can clearly see the following factors in Fig. 4.2(b). If we excite a wave with an in-plane CW magnetic signal at the resonance condition of 8.7 GHz, we can observe the formation of a spiral pattern which is clearly emanating from the vortex core region of the disk. The spin wave's wavefront is attenuated along the direction of excitation y, that we believe is due to the destructive interference with the weaker oscillations coming from the edges, which are also excited along that direction. As expected from the dispersion relations, we get similar spiral patterns at different CW frequencies that fall into the excitation range of the lower branch (see Fig.4.2(c) and (d)). Also, the wavelength of these waves can be easily tuned changing the frequency of the driving field, similarly as it was reported in (Wintz, et al., 2016). Further simulations (not shown here) show that if the pumping field is applied out of plane, the outward propagating spiral wave turns into a circular wave. At higher frequencies, waves from the core become weaker and spin waves from the edges are now more efficiently excited. Another important feature of the spiral wave is that it is still excited at the resonance frequency even if the vortex core is shifted by applying a biasing external field, where the limit is saturation field.

Similar investigation was carried out in 80 nm thick Permalloy square elements. This shape shows a richer collection of modes due to the formation of domain walls, which provides additional topological confinement. They can serve as the channels for spin wave propagation, when the sample's magnetization configuration is in its ground state of closed leaf, Landau pattern (Perzlmaier, et al., 2005; Wagner, et al., 2016). Due to the Landau pattern, separation between the triangular domains in the square dot will give rise to 90 degrees domain walls. From this point, every mention in the paper to 'domain walls' in the studied samples or as spin wave channels will be implicitly referring to this type of domain wall, unless it is indicated otherwise (as in '180 degrees Bloch wall'). To visualize the spin wave dynamics here we demonstrate the results of excitation only of the central core region of the square in a single Landau ground state. This helps to avoid other dynamic effects such as domain wall oscillations and radiation of spin waves from the edges. However, it can be shown that such limitation does not undermine the effect and, even when the whole element is exposed to uniform magnetic field, the same processes can be easily observed (see Fig. 4.2(b)). Figure 4.3 shows examples of magnetization configuration at different times after exposing the square elements to a continuous periodic field h_{ac}. It can be clearly seen that as the time progresses the phase of the oscillation becomes asymmetrically distorted forming a spiral wavefront. Compared to the circular elements however, where the formed spiral is radially uniform, in squares the shape of the front is significantly distorted.

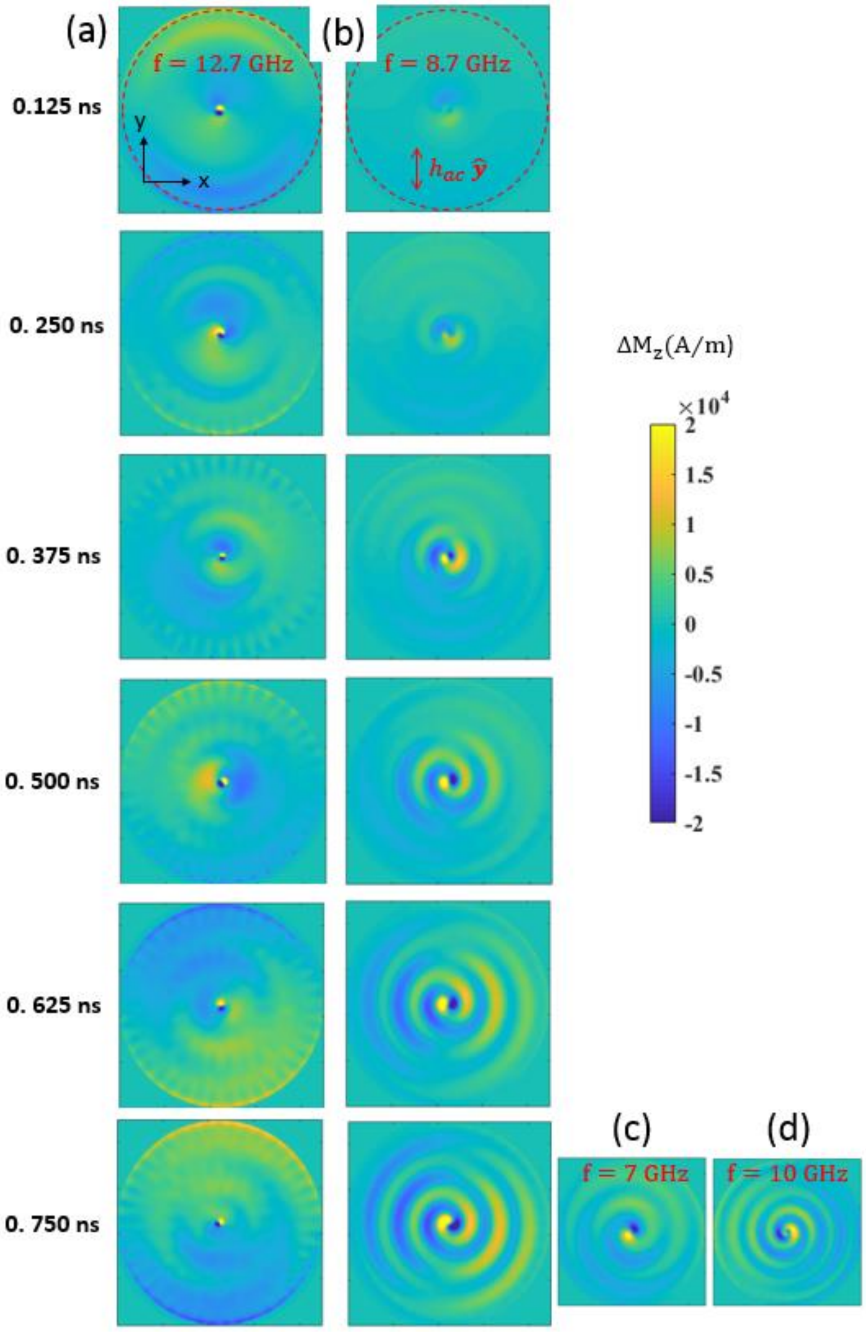

Figure 4.2. Snapshots of the dynamic out-of-plane component of magnetization for thin circular disks, d = 900 nm, applying a CW in-plane excitation of 12.7 GHz (a) and for thick circular disks applying 8.7 GHz (b), 7 GHz

(c) and 10 GHz (d) to the whole shape. While in thin disks the excited wave propa-gates inwards (a), on the thick disk the spin wave propagates outwards with more intensity (b).

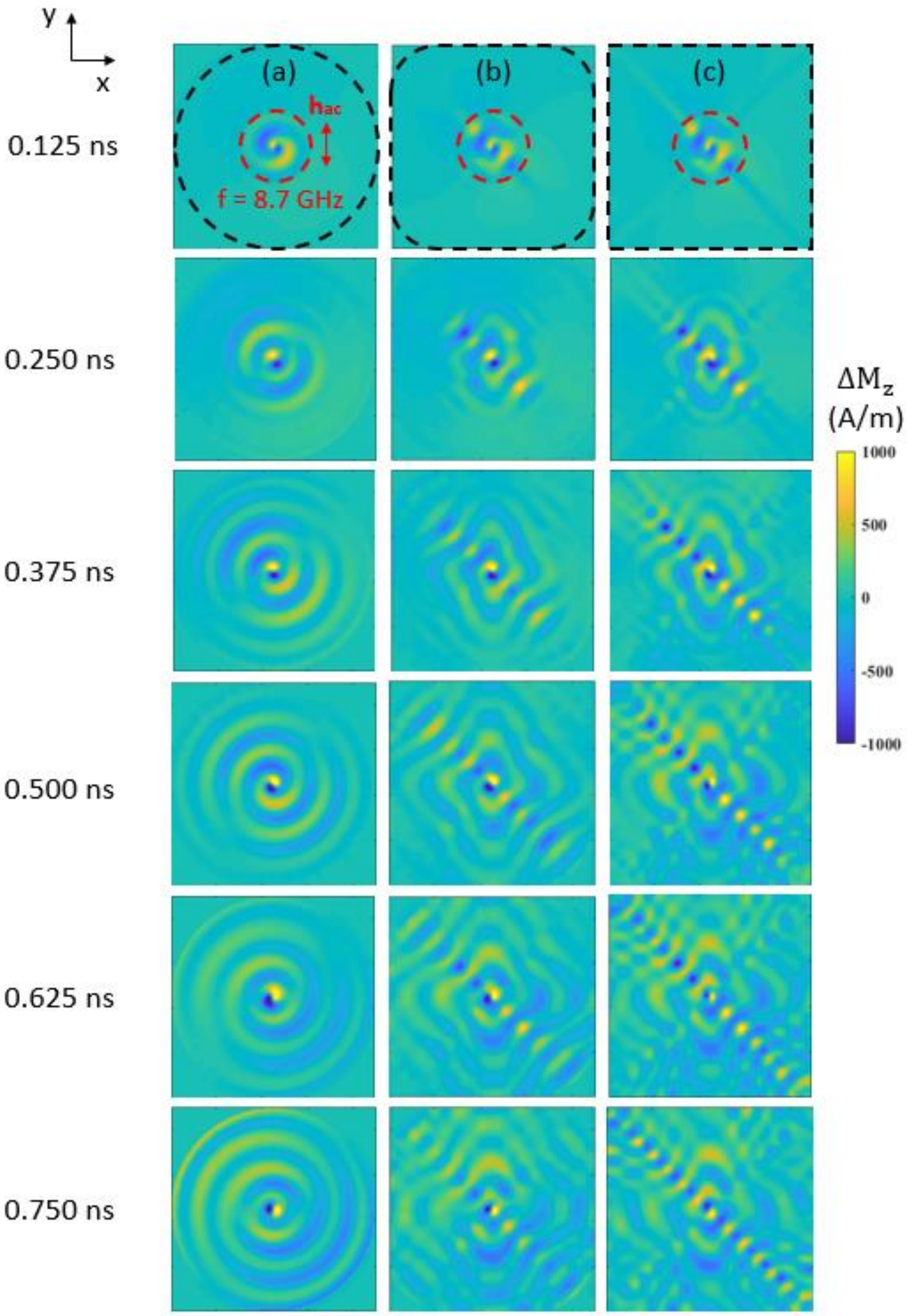

Figure 4.3. Snapshots of the dynamic out-of-plane component of magnetization for thick circular disks ($d = 900$ nm) (a), rounded squared disks (b) and squared disks (c) applying a 8.7 GHz CW excitation at the core region

($d = 100$ nm). Black dashed contours for each shape are plotted and curvature of the chamfered corner is equal to one quarter of the side length.

As well as the geometric constraints of the shape, the wave propagation is affected by the presence of the domain walls. In both thin and thick elements, the walls primarily lead to distortion in local demagnetizing field and thus modifying the dispersion properties. For thicker elements this is a more profound effect, because above a certain limit (approx. 50 nm) the transverse profile of the wall changes significantly, leading to a Bloch type structures with a non-zero out-of-plane component. A more (significant/interesting) effect however comes from the dynamics of the walls themselves. Even though the walls are stationary at this frequency range, due to their confined nature they can host a range of transverse oscillations for the perpendicular component of magnetization alongside the wall. This can lead to a formation of propagating spin-wave modes along the domain walls, or so-called Winters modes (Winter, 1961). Our simulations show that the intensity of these modes can be significantly higher than any other dynamic modes, and thus significantly affect the formation of the spiral waves. Previously it was shown that these modes can arise from the topological in-homogeneities in the sample (e.g. corners or edges) (Aliev, et al., 2011). In our case, this is very well seen that they originate directly from the core region and propagate with a shorter wavelength, almost twice smaller (see Fig. 4.3(c)) than the spiral spin waves radiated into the triangular domains of the Landau pattern. The confined spin waves - Winter's magnons - also show opposite phase propagation along the different sides across the core. This later factor helps to couple the spiral waves in the triangular domains together with the magnons in the domain walls. However, the difference in the wave numbers leads to a different propagation velocity and consequently the distortion in the circular spiral wavefront that become reminiscent of the geometric shape structure. It can be shown that this works not only for squares, but for shapes of any number of corners, as long as the corners are sharp enough to produce a reasonably confined domain wall. Figures 4.3 (b) and (c) show how the effect is changing when reducing the angle of the corner. It is interesting to note, that one diagonal seems to be better excited than the other. Numerical results show that in the frequency range where only Winter's magnons are excited, both diagonals show spin waves of similar amplitude. Therefore, the enhancement (attenuation) along one diagonal may be related to constructive (destructive) interference with the corresponding spiral spin waves along the given diagonals or any other standing pattern in the triangular domains, as seen in Fig. 4.8(b) (both insets).

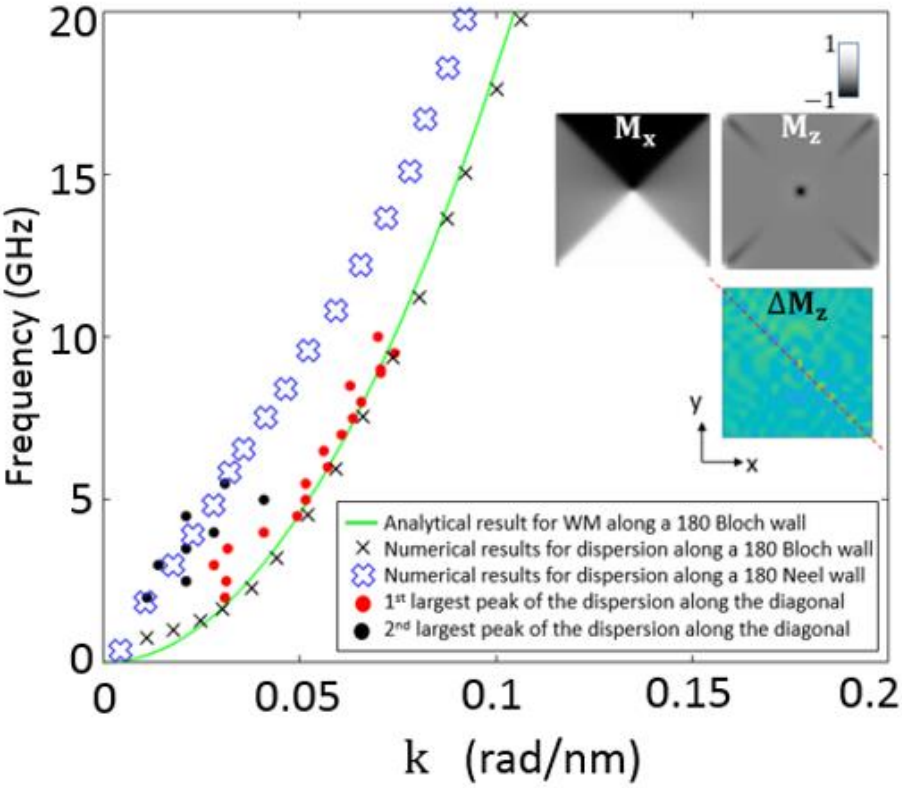

Figure 4.4. Dispersion relation from of the mode traveling along the domain wall in the square (red dots). Numerical results from the dispersion along the diagonal of the square (red dots) agree nicely with the theoretical equation of a Winter's magnon along a 180 degrees Bloch wall (green solid line) in the exchange regime (Garcia-Sanchez, et al., 2015) at large **k** and show a mixing of two behaviors with the dispersion along a Neel wall at lower **k** and bloch at larger **k**. Insets show components of static magnetization demonstrating the mixed Bloch and Neel wall behavior along the diagonal of the square.

To clarify these findings, we used the analytical dispersion relation from (Garcia-Sanchez, et al., 2015) for a Winter's magnon propagating in a Bloch wall. In this case, any intrinsic anisotropy is negligible. We also consider pinned boundary conditions at the edges and the core and assumed an effective internal field value of $H_{eff} = 0$ A/m at the region surrounding the core. Fig. 4.4 shows a comparison between the dispersion relation along one of the diagonals of the square and that of a Winter's magnon propagating along a 180 (degrees) Bloch wall, defined only by the interplay between exchange and anisotropy. Excitation is applied parallel to one of the edges of the square. As can be seen from the dispersion, there is a significant mismatch at low ***k*** values between the analytical solution (solid green line) for a 180 degrees Bloch wall and numerical results from our Landau pattern. We believe this could be since the domain wall in the Landau pattern is not entirely a Bloch type wall. Base on the magnetization profile, the region closer to the core shows a reduced out-of-plane component and therefore, closer to a Neel wall configuration (see inset of Fig. 4.4). In fact, if we consider the propagation of waves in the Neel walls from (Garcia-Sanchez, et al., 2015), its dispersion relation is growing faster than that of a Bloch wall. As a result, there is a certain mixing of two regimes, with Neel wall dispersion dominating at low ***k*** and Bloch wall dispersion at higher ***k***. A non-zero dipolar field transversal to the square's domain walls, due to the 90 degrees turning as it is suggested in (Lara, et al., 2017), could also contribute to the mismatches at very low ***k*** values.

We continue with the analysis of the effects of rounded corners. This shape is closer in geometry to the real sample, assuming imperfections at the sharp corners happened during fabrication. In such a case, the wavefront becomes modified when approaching the corners (see Fig. 4.3). The exchange energy density is reduced, and the shape anisotropy becomes dominant, resulting in a confined wave with similar wavelength to that of the spiral radiated into the triangular domains. This shows an effective spatial down-chirping of the Winter's magnons wavelength caused by the geometry of the corners. From Fig.4.1 and Fig.4.4 we see that the wavelength of Winter's modes is smaller than that of the spiral spin wave ($k_{\mathrm{WM}} > k_{\mathrm{d}}$), up to a certain frequency. At a frequency close to 19 GHz, it can be deduced that the wavefront becomes a circular spiral, since both wave vectors match ($k_{\mathrm{WM}} = k_{\mathrm{d}} = 0.1$ rad/nm). This implies that the spiral spin wave can also be modified by just applying oscillating fields of higher frequencies. We ran micromagnetic simulations at 20 GHz CW excitation (not shown here) confirming the latter. Previous works have also suggested to apply biasing fields to modify further the width of the domain walls or 'exchange channels' for the Winter's magnons (Lara, et al., 2017). In the next section, we provide a simple physical explanation of the arising of these characteristic waves in thicker samples.

4.3.2 Balance between Dipolar and Exchange Energy

In finite magnetic elements in absence of biasing fields, the domain wall formation is mainly governed by their shape and magnetic anisotropy, leading to specific magnetic configuration. Depending on the thickness, either Bloch or Neel walls are preferable because of a competition between magnetostatic and exchange energy. This can be intuitively understood as follows: In thin films, out-of-plane rotation of magnetic moments between domains is energetically expensive because of high demagnetizing fields. When the thickness is increased, the demagnetizing field is reduced initially at the points of higher magnetic gradients such as boundaries and magnetic singularities, leading to increased out-of-plane components. The same happens with a Neel wall, which at certain thickness (typically around 50 nm for Permalloy) starts transferring into a Bloch wall.

Now let us consider an in-plane excitation applied to circular discs. To get a better view on the magnetostatic relations behind these processes, we record the magnitude of magnetization, dipolar and exchange fields across the diameter of the disc. Here we take two case scenarios for a Permalloy nano-disc with thicknesses of 20 nm and 80 nm, where the vortex configuration is reached after relaxation in both situations. Our simulations show a more pronounced out of plane turning in the thicker discs. Interestingly, the orientation of magnetization vectors in thin and thick discs in the ground state resembles the distribution for Neel and Bloch walls, respectively. These differences on the initial distribution contribute to a better excitation of spin waves at the vicinity of the core in thicker discs. From Landau-Lifshitz-Gilbert (LLG) equation (Landau & Lifshits, 1935), applying an in-plane excitation to magnetic moments in a thick disc near the core, will enhance the exerted torque. Therefore, spin waves from the vortex core region are not that much excited in thinner discs. These different configurations can also explain why the vortex core diameter becomes larger in thicker samples. In thick discs, since the out of plane rotation of magnetization happens more gradually than in thin samples, the vortex core becomes wider.

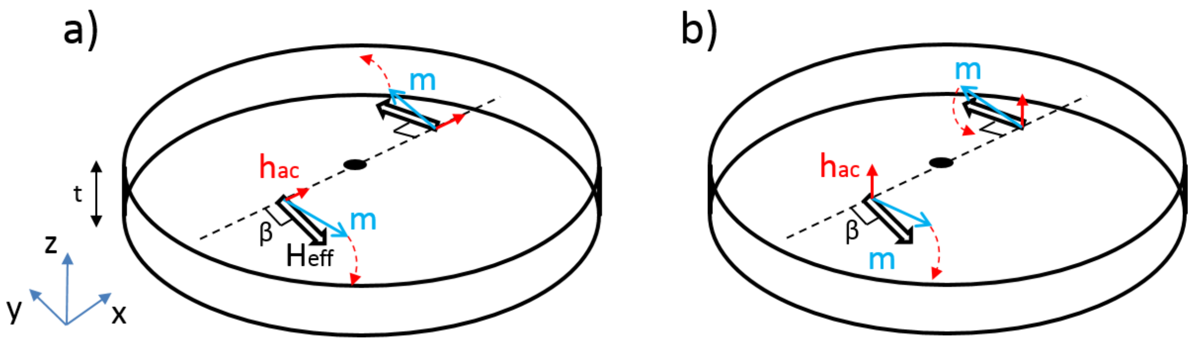

Figure 4.5. Schematic of a thick disc (t = 80 nm) with in-plane (a) and out of plane (b) excitation showing counterclockwise precession of magnetic moments (blue arrows) around the effective field (white arrows) at opposite positions referenced to the vortex core (black dot). Dotted red arrow shows the sense of rotation due to the exerted torque according to LLG equation, where the out of plane component of magnetization can be deduced to be out of phase by (in-phase) when an in-plane (out of plane) excitation is applied. Vectors are magnified and not scaled for sake of clarity.

The characteristic wavefront of the spiral spin wave can also be easily understood from LLG equation, which dictates the counterclockwise sense of Larmor precession of magnetization $\mathbf{M}$ around $\mathbf{H}_{\mathbf{eff}}$ (see Fig.4.5). For two vectors in the vicinity of the core, the excitation of applied in-plane field will lead to out-of-phase precessions on opposite sides of the core, thus leading to the spiral nature of the phase. In case of the out-of-plane excitation, the clockwise rotation leads to in-phase precession of both vectors, which is then resulted in a radial wave propagation. The asymmetric phase of precession can also explain the existence of the gyrating ‘dip’, reported in other studies on thinner films (Kammerer, et al., 2011).

Fig. 4.6 shows the module of dipolar and exchange field at the points surrounding the vortex core in its equilibrium position, x_c, (from numerical results not shown here, we define that region as $|x - x_c| < 50$ nm, with $x_c = 450$ nm) for thick and thin circular discs ((a) and (b), respectively) and for thick and thin square patches ((c) and (d)). Due to circular (90 degrees) symmetry in the discs (square patches) we only consider the x-direction for the following analysis. Firstly, results are similar if not identical, so we can infer that similar dynamical behaviour will be found in both element shapes along that direction (perpendicular to the patch edge, circular or square). From Fig. 4.6 we can see that, in contrast to the thin discs, dipolar field is drastically reduced in the bulk of the thick discs. From these results, we can infer the following: 1. A weaker demagnetizing field allows magnetic moments to precess out-of-plane with more freedom than when being closer to the surfaces (blue line). This also explains why the spiral spin wave is more intense in the bulk of the thick disc, due to the effective non influence of surface anisotropy and pinning; 2. Dipolar field in the bulk of the thick disc is near to zero. This implies that dipolar interaction with the surfaces is minimal, while exchange interaction in the core region is dominant allowing the exchange-dominated spiral spin waves to occur; 3. Away from the core region and closer to the surfaces, values of the exchange field for thin and thick discs are similar and are very low in contrast to the core region. This suggests that, via exchange interactions, the spiral spin wave is originated in the middle layers and gets coupled more easily to the neighbouring layers. This also supports the uniformity in phase of the spiral wave across the thickness, which is observed in simulations. In summary, the significant weakening of the demagnetizing field in thicker discs allows the core vicinity in the bulk of the disk to act as a better source for exchange dominated spin waves.

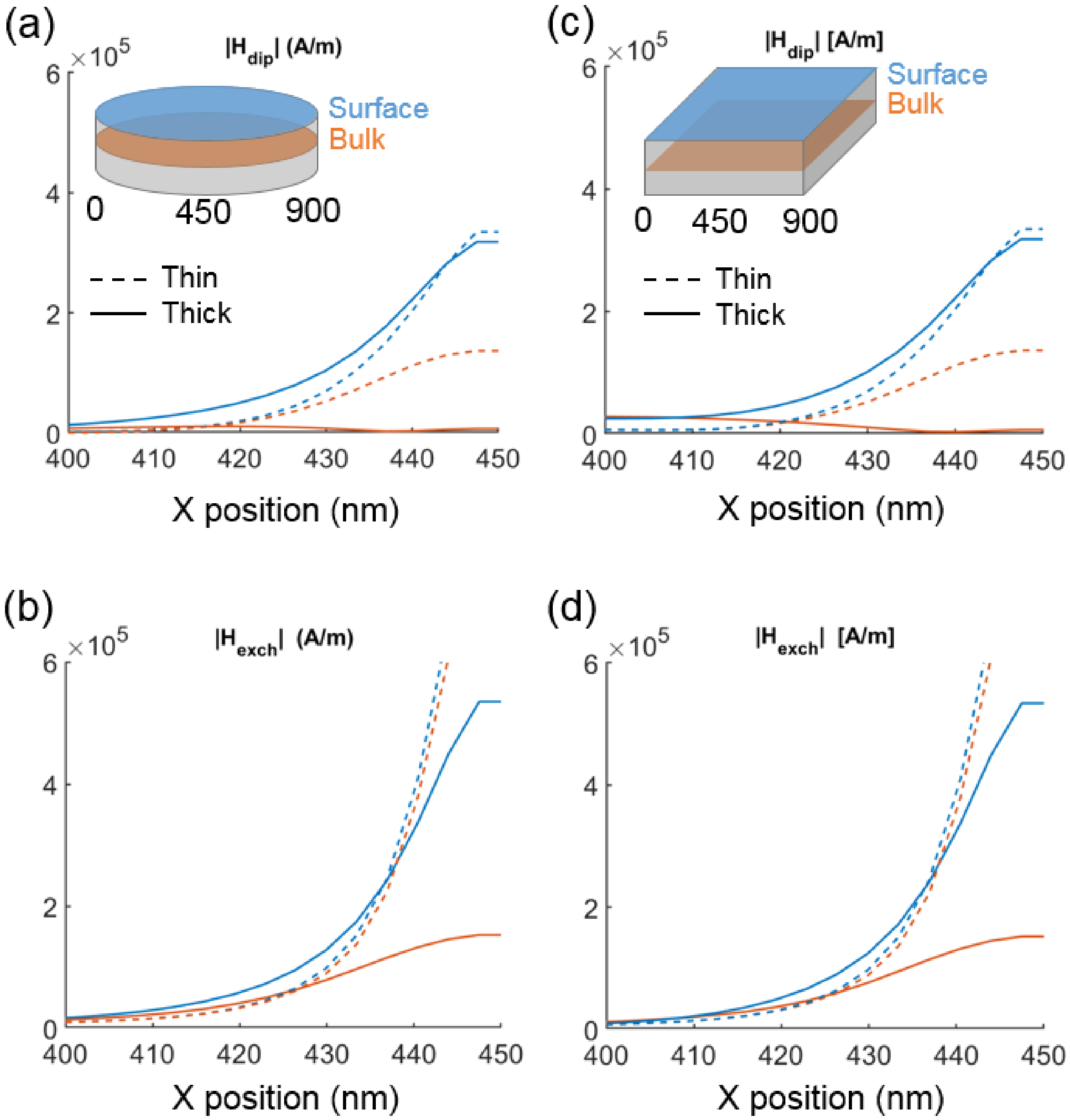

Figure 4.6. Module of magnetostatic and exchange fields in x direction across the center for circular discs ((a) and (b)) and square elements ((c) and (d)) of 900 nm diameter and thicknesses 80 nm (solid lines) and 20 nm (dashed lines). Insets show a reference for the sectional cuts for the top and middle layer in thick and thin discs. The x axis direction is chosen to be radial in the circular disks and perpendicular to one edge in the square patch.

4.4 VNA-FMR Measurements

In the previous section, we showed that the spiral spin wave emanating from the core is more intense for thicker nano-patches, always assuming a single vortex state configuration as starting point. Hence, in thick samples, the footprint of these propagating modes is more susceptible of being measured through standard RF techniques.

4.4.1 Circular discs

Figure 4.7(a) shows the experimental absorption spectra and the characteristic absorption peaks from the contribution of the real part of microwave permeability in 80 nm thick discs of 900 nm diameter. The main absorption peaks are present at the frequencies where spiral spin waves can be efficiently excited (these modes are numbered in Fig. 4.7 as I, II and III), which are in good agreement with our simulated spectra. There are some slight discrepancies, of 4% at 7 GHz and 5% at 10 GHz, which can be due to imperfections at the edges which normally lead to a smaller effective sample size.

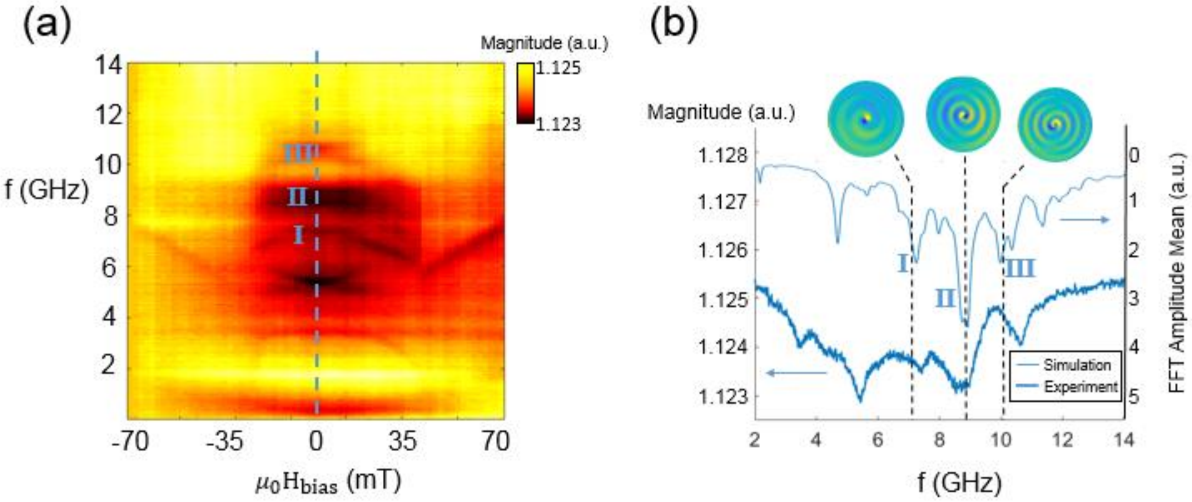

Figure 4.7. VNA-FMR results for circular discs (a) of thickness 80 nm. The FMR main mode can be spotted as well as other low field resonances related with the simulated spiral spin waves (insets in (b)). Cut at zero applied

field (dark blue line) compared with the simulated spin wave absorption spectra of a centered vortex (light blue line) (b).

Qualitatively, we observe that some resonances seem to remain stable in a wide range of fields (up to 25 - 30 mT) and therefore, not much influenced by biasing field or dipolar-dipolar interactions between discs and thus ensures that we are observing characteristic modes from the single dots. This follows up from numerical results, where the spiral wave exists as long as the vortex core is not self-annihilated when reaching the edge of the element. In Fig.4.7(b), the amplitude of the main peak at 8.7 GHz (mode II) corresponds to a standing wave condition in the disk: From numerical simulation (see Fig. 4.1(b)), we can see that the wavelength of the spiral spin wave at that frequency is 125.6 nm. Considering one half of the disk as a resonant Fabry-Perot cavity, the resonant length (L) condition for a set of standing modes of order n would be satisfied given: $L = n\lambda_c/2$ where λ_c is the spin wave wavelength. From Fig. 4.3(c), for the given wavelength at a frequency of 8.7 GHz and the length of the cavity, the number of anti-nodes found is n = 7 which gives a resonant length of L = 440 nm. This is in good agreement with the radius of the disk (r = d/2 =450 nm). It is worth to note that a more realistic 'cavity length' will be shorter due to the width of the vortex core, therefore shorter than the radius of the disk. Similarly, if we repeat for frequencies of 7 GHz and 10 GHz (n = 5, mode I; and n = 9, mode III respectively), and assuming a resonant cavity length of L = 450 nm, we obtain the same k-vectors (or equivalent wavelengths) as in the lower branch of the dispersion diagram from Fig. 4.1(b), 0.034 rad/nm and 0.069 rad/nm respectively. We also note the consecutive odd values (n = 2k +1) of the measured modes. These are the modes susceptible for activation since the even modes (n = 2k) across thickness may not be seen due to the symmetry of the signal in the CPW (Khivintsev, et al., 2010). Therefore, we can confidently correlate the measured modes above 6 GHz to the spiral spin waves emitted from the core vicinity.

4.4.2 Squares

Analogously to Section 4.4.1, Fig. 4.8 shows the experimental results for squares and a comparison with numerical results. From the measured absorption spectra, we can also observe a large resonance peak at 8.8 GHz for a square of dimensions (L) 900 nm by (t) 80 nm, which it is also in very good agreement with our simulations. Its frequency position falls almost exactly into that of a circular disc of equivalent dimensions where, according to numerical results (see Fig. 4.2), we are expecting propagation of an intense spiral spin wave. When compared to the resonance frequency of a perfect square, it is worth to note that there will be an expected frequency mismatch mainly because of imperfections made during the fabrication process, which include more rounded corners and a longer side length than expected. All these factors may contribute to a frequency down shift which could explain the mismatch and a closer matching to the resonance frequency from the circular disk of 900 nm diameter.

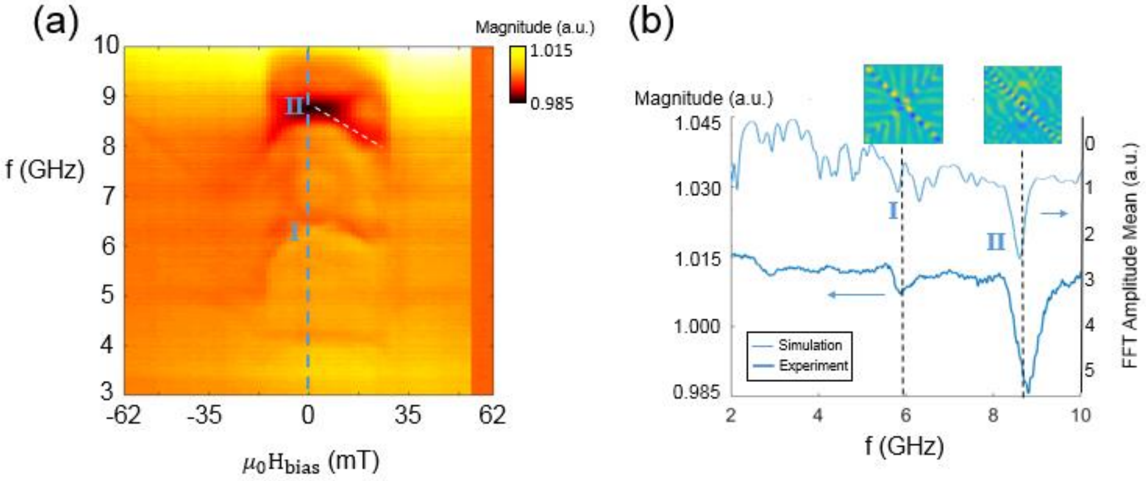

Figure 4.8. VNA-FMR results for square elements (a) of thickness 80 nm. The FMR main mode can be spotted as well as other low field resonances related with the simulated spiral spin waves and Winter's magnons (insets in (b)). (a) shows the splitting of the main resonance peak and white dashed line shows the analytical slope for the downshifted peak. Cut at zero applied field (dark blue line) is compared with the simulated spin wave absorption spectra of a centered vortex (light blue line) (b).

It is interesting that, the resonance peak here is stronger and wider than those found in circular arrays. As previously discussed in section 4.3, this could be related to the formation of 90 degrees domain walls in the sample, characteristic of a Landau pattern, and thus the stronger confinement of the spiral spin waves propagating in them. Considering the spin wave's wavelength from the dispersion diagram in Fig.4.4 (λ_d = 88.8 nm) and check the resonance condition in a domain wall of length $l_{dw} = \sqrt{2}L/2 = 636$ nm, we will obtain, for n = 14, a resonant length of L = 622 nm which well agrees with the length of half the diagonal of the square. As it happened in the circular discs, a more realistic domain wall length will be always less than half the diagonal of the square. If we repeat the process for the next largest peak, at 6 GHz (n = 11 and n = 8, respectively, see Fig.4.8(b)), we obtain an optimal resonant lengths of L = 602 nm, which is also in good agreement with half the length of the diagonal, with relative errors of 5% ($0.38\lambda_0$). Again, considering a shorter effective length of the domain wall due to the width of the vortex core, the error is even smaller ($0.18\lambda_0$). Considering all this, the largest measured resonance can be associated with the Winter's propagating modes coherently emitted with the spiral spin wave. The lowest peaks are related with only lower resonances of the Winter's magnons in the domain walls, but not necessarily matched with the spiral spin wave from the core, especially at the lowest frequencies, where the spiral from the core is not excited.

Other reported works have shown previously the splitting of azimuthal spin waves in circular shapes when the vortex core is displaced (Neudecker, et al., 2006; Aliev, et al., 2009). By applying a biasing field parallel to one side of the square, we can shorten or increase the length of opposite domain walls, which splits the resonance into a lower and upper frequency due to the broken symmetry. If the domain walls are of the same length (this is, at $\mathrm{B_{bias}}$ = 0 mT), the resonance peaks add up and can also match with the absorption peak related to the spiral spin wave radiated into the domains. This enhances the total absorption at that specific frequency (see Fig. 4.8). We show experimental results of this phenomenon for the largest sample (L = 900 nm). For this sample, we obtain an experimental average value of the *frequency shift to bias ratio*, $\frac{\Delta \mathrm{f}}{\Delta \mathrm{B}} = -0.049$ GHz/mT for the peak that shifts down (see Fig. 4.8(a)). To confirm this analytically, we make the following approximation: If the biasing field is small, i.e. $\mathrm{B_{bias}} \ll \mathrm{B_{sat}}$, we can consider the variation of domain wall length approximately equal to the vortex core displacement ($\Delta \mathrm{s}$), $\Delta \mathrm{l_{dw}} \approx \Delta \mathrm{s}$. We can also put $\Delta \mathrm{f}/\Delta \mathrm{B}$ as $(\Delta \mathrm{f}/\Delta \mathrm{s})(\Delta \mathrm{s}/\Delta \mathrm{B})$. From numerical results on thick square patches, we obtained a vortex displacement to biasing field ratio of $\Delta \mathrm{s}/\Delta \mathrm{B}$ = 8.59 nm/mT. Then, we can obtain the relation $\Delta \mathrm{f}/\Delta \mathrm{s} \approx \Delta \mathrm{f}/\Delta l_{dw}$ from the dispersion relation of discretised spin waves in a normally magnetised film:

$$\mathrm{f}_n = \mathrm{f}_0 + \mathrm{f}_{\mathrm{M}}\lambda_{ex}\left(\frac{n\pi}{l_{dw}}\right)^2 \tag{4.3}$$

From numerical results, we obtain a vortex core half-width of 50 nm, we can calculate an effective domain wall length ($l'_{dw} = \left(\frac{L}{\sqrt{2}}\right) - 50 = 586$ nm), n = 13 for a driving frequency of f = 8.7 GHz (see Fig.4.5(b)) we derive Eq.(4.3) with respect to l_{dw} and substitute the corresponding values, obtaining: $\Delta \mathrm{f}/\Delta l_{dw} = 0.0052$ GHz/nm. Finally, and under all the previous approaches, we obtain an analytical value for $\Delta\mathrm{f}/\Delta\mathrm{B} = -0.045$ GHz/mT, which is in good agreement with the measured value, with a tolerable error of 9%. While the agreement at low external fields is very good, mismatches at larger biasing fields can be explained since the assumption $\Delta\mathrm{l}_{\mathrm{dw}} \approx \Delta\mathrm{s}$ may no longer hold. By considering this similar variation in the eigen-frequencies for this mode, both in the experiment and the analytical approximation, we can confidently say that the frequency down-shift due to applying larger biasing fields is a consequence of the standing wave condition of Winter's magnons in the domain walls of square patches. Figure 4.9 shows more results on arrays of square elements with smaller length (L) at a fixed thickness (t = 80 nm): L = 600 nm and 500 nm. It was confirmed through electron microscopy (SEM) that the samples had the same separation length, similar to the side length, to avoid dipolar coupling and magnetic interferences among them. It was found that, although the resonance peak shifted to higher frequencies, we also observed that the down shift dependence on the biasing field of the main peak follows as well a similar if not identical slope to the one analytically found for the largest square. From numerical results, the number of nodes found along half the diagonal of the 600 (500) nm square is 9 (8). Given the wavelength of the Winter's magnon excited at frequencies 9.1 (9.4) GHz (see Fig. 4.4), the optimal resonant length of the domain wall was 399 (338) nm, which was again in good agreement with the ideal length of half the diagonal of the square, 424.3 (353) nm. This gives a tolerable error of 6% (4%), i.e., an error of 0.28 ($0.18\lambda_0$), which is even smaller if we consider a more realistic shorter domain wall length due to the width of the vortex core region.

For smaller sizes such as the 500 nm and 600 nm squares, reduction of side length in steps of 100 nm (i.e. a reduction of half the diagonal of 70.7 nm), is almost equivalent to eliminating two nodes, i.e. one wavelength (88.8 nm), therefore it seems reasonable that the numbers of the modes are close and consecutive. Assuming that imperfections during fabrication happened regularly for every array and taking all the above into account, we can confidently say that the measured resonances, in thick samples, are associated with the spiral wave emanating from the core vicinity in coherence with Winter's magnons propagating in domain walls.

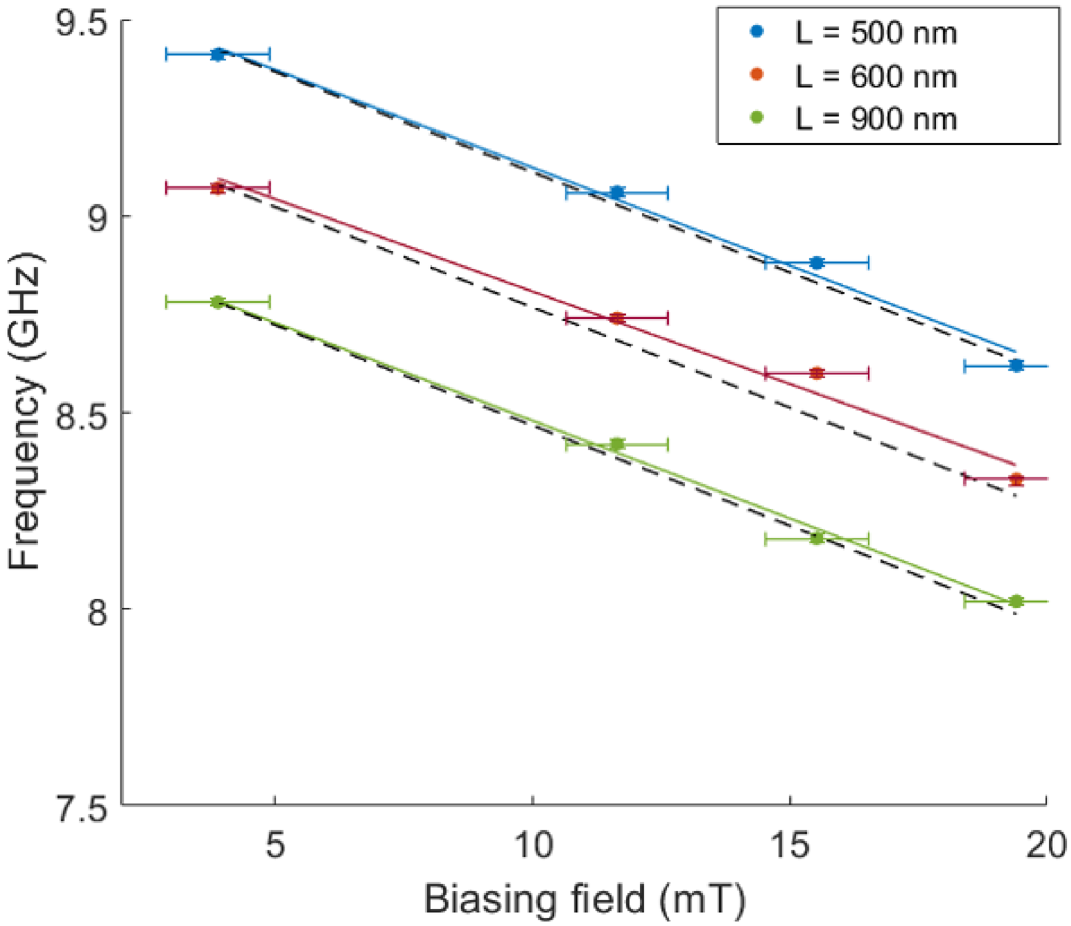

Figure 4.9. VNA-FMR results for squared thick discs of side lengths 900 nm (a), 600 nm (b) and 500 nm (c) applying different biasing fields. Solid lines show a linear fitting to experimental data and the error bars are the

steps (20 G = 2 mT) of the sweeping of the biasing field. Dashed line is the analytical slope for the downshifted peak.

4.5 Mathematical modelling of the radial wavefront in n-vertices patches

In the past, a vast work on analytical modelling has dealt with magnetically non-saturated structures presenting domain walls. Some examples are spin wave emission from Bloch domain walls (Dejong & Livesey, 2015; Whitehead, et al., 2017), reflection and transmission across domain walls (Chang, et al., 2018) or magnetic configuration in a transition between domain walls types (Wang, et al., 2013). These models help to provide insight into the dynamics and a tool for modelling spin wave phenomena in confined structures that show a more complex magnonic landscape than saturated dots. In this work we report on a model for the observed wavefront of spin waves emitted from an almost punctual source (e.g., a vortex core) in any n-vertex patch, which implies the existence of domain walls, azimuthally distributed across the geometry. The final expression is derived from a generalisation of the dispersion relation of a first higher order spin wave mode in a Damon-Eshbach (DE) configuration for an arbitrary angle between magnetisation **M** and wavenumber **k**. For $n > 2$, the patch adopts the form of a regular polygon, for $n = 2$ and $n = 1$, the model considers two or one single vertices. Finally, $n = 0$ implies a circular disc. The obtained curves from the models agree well with numerical results. We describe our models and the numerical method used for their validation. Later, we provide with a comparative between the models and their validation through numerical simulations as well as discussion of results. This model can help on the description of complex spin wave wavefronts in non-saturated elements, which avoids running numerical simulations for particular shapes.

It is worth to note that, in practice, the models lose accuracy for large values of n, since the formation of Bloch domain walls between the vortex core and a corner is assumed, regardless of n. Obviously, this is not the case for a large n. If n is large enough, the straight edges of the shape become shorter and the dot shape tends to that of a circular disk. For large n values and close to the core region, effects of shape anisotropy are less pronounced and Bloch domain walls are not likely to be formed, forcing magnetisation to lay entirely in-plane around the core, as in circular discs. This implies there will be an internal region around the core, modelled in polar coordinates as $r < r_0$, where the spin wave wavelength will be azimuthally constant: $\lambda(\theta) = \lambda_{\mathrm{DE}}$. The limiting radius r_0 can be trivially found using basic trigonometry for overlapping domain walls of width Δ for $n > 2$. Thus, the limiting radius can be calculated as $r_0 = \frac{\pi}{n}\Delta$. However, regarding potential applications of these dots as spin wave emitters, the interest is on the wavefront distribution closer to the edge of the dot. Therefore, for nanometre sized patches, we are only interested in low n values.

Regarding magnetic configuration in equilibrium after a relaxation process, and assuming a centred vortex core, n triangular domains and n domain walls will form in the patch. In contrast to the circular dot, the azimuthal distributed domain walls will distort the wavefront of the propagating spin wave from the core region, introducing an azimuthal dependence (or equivalently, $n -$ dependence) to the wavelength of the radial wave ($\lambda(\theta)$). Also, two known values for the spin wave wavelength can be analytically deduced for any n-corner patch: the characteristic wavelength of an exchange dominated short spin wave emitted from the core in a DE configuration (λ_{DE}), when **k** is perpendicular to **M** (this is, when the spin wave propagates into the domain), and the characteristic wavelength of the confined spin wave along the domain wall (λ_{WM}), also known as Winter's magnon.

4.5.1 Description of the models

For this study, we mathematically infer a fitting model from numerical results on some of the first obtained shapes when n = 0, 1, 2, 3, 4..., and so on. We then generalize it to any n-vertex patch.

For the case of $n = 1$ we take an internal angle assumed to be $\pi/3$ and only one domain wall is present, resembling the patch to a ‘teardrop’ shape. For $n = 2$, we also make a similar assumption, and the patch resembles to a ‘double teardrop’ shape.

Geometrically, for any polygonal shaped dot of n corners, these corners (and therefore the domain walls) will be distributed at every ${}^{2\pi}/_{n}$ angle, assuming a first corner as reference always placed at the topmost of the shape (zero angle). For sake of completeness of the model, for the case of $n = 1$ there is only one corner whose internal angle is assumed to be $\pi/3$. For $n = 2$, we also make the same assumption. For the following values of n, the internal angles of the corners are the internal angles of the regular polygons, defined as: $\frac{2\pi(n-2)}{n}$.

After relaxation, and assuming a centred vortex configuration, n triangular domains and n domain walls will rise in the dot. In contrast to the circular dot, these azimuthal and regularly distributed non uniformities will distort the wavefront of the propagating spiral spin wave from the core, introducing an azimuthal (and equivalently, number of corners) dependence to the wavelength of the radial wave (as seen for squares in section 4.4.2). Also, two known values for the spin wave wavelength can be deduced for any n-corner patch: the characteristic wavelength of an exchange-dominated short spin wave emitted from the core in a DE configuration (λ_{DE}), this is when **k** is perpendicular to **M**, and the characteristic wavelength of the confined spin wave along the domain wall (λ_{WM}), also known as Winter magnon. These two values can be well known beforehand given their respective dispersion relations.

As a first approach, from numerical results on $n = 0, 1, 2, 3, 4, \ldots$ vertices, extrapolating for a generalized n-vertex patch we mathematically infer the collection of functions of the form:

$$\mathrm{g}(\theta, n) = 1 - \cos(n\theta + \varphi_0) \ , \tag{4.4}$$

$$\mathrm{h}(\theta, n) = \mathrm{g}(\theta + \pi/n, n) \, , \tag{4.5}$$

which plot n number of lobes and n zeroes (these are along the domain walls direction). n is the number of vertices of the patch and φ_0 is an arbitrary phase which sets the relative position of the dot, so the lobes from function g 'aim' towards the magnetic domains (see Fig. 4.10). Assuming a sharp corner always at the topmost of an n-corner patch, this phase term can always be expressed as: $\varphi_0(n) = (1 + (-1)^n)\,\pi/4$. On the other hand, the phase shift of θ/n in $\mathrm{h}(\theta, n)$ will accordingly rotate $\mathrm{h}(\theta, n)$ so it aims into the domain walls. For $n = 0$, function $\mathrm{h}(\theta, n)$ is not defined and the wavelength corresponds to the one obtained from function $\mathrm{g}(\theta, n)$, as expected for a circular disk. Thus, the defined functions are self-consistent, and we can model the wavelength as:

$$\lambda(\theta, n) = \lambda_{\mathrm{DE}}\mathrm{g}(\theta, n) + \lambda_{\mathrm{WM}}\mathrm{h}(\theta, n) \tag{4.6}$$

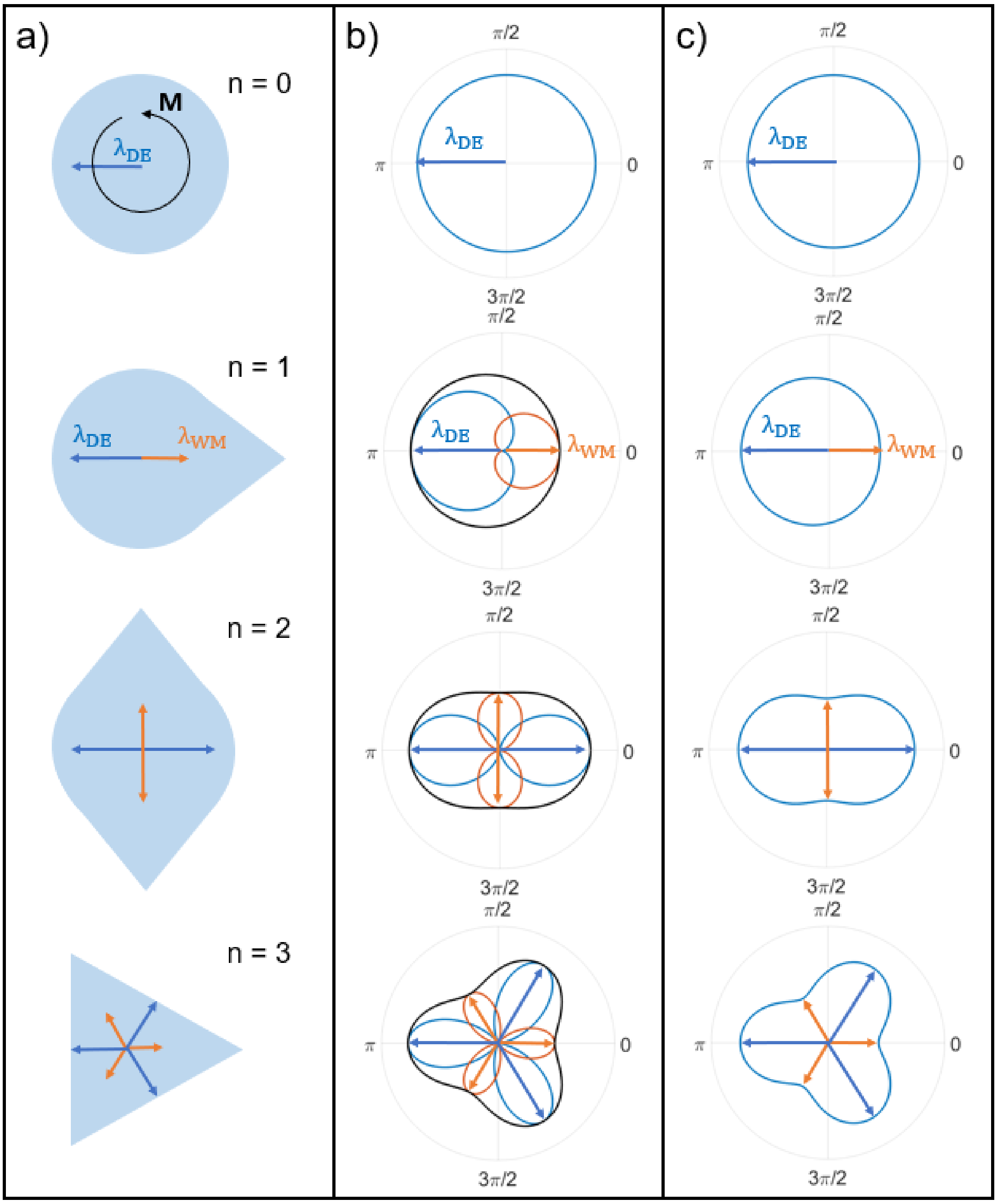

Figure 4.10. (a) Schematic of the various magnetic patches depending of the number of vertices ‘n'. (b) Polar representation of weighing functions g (blue curve) and h (orange curve) from Eq. (4.4) and (4.5) showing the

global azimuthal variation of wavelength in the shape (Eq(4.6), black solid line). Radial amplitudes are normalized for each function. Polygonal shapes for n > 3 are not shown but can be inferred from these examples, following a ‘petal’ structure. (c) Polar representation of the Hippopede curves equation.

This collection of curves resembles to the geometrical family of ‘sinusoidal spirals’, which in polar coordinates, lead to n numbers of lobes azimuthal equally distributed, see Fig.4.10(a). Function $\mathrm{h}(\theta, n)$ avoids the azimuthal zeroes found from $\mathrm{g}(\theta, n)$ and both functions define a cosine-like transition between two finite values of wavelength although, at a first glance, these functions seem to have no connection with the physics from the problem scenario. Also, these equations apparently lack connection with any known equation of magnetisation dynamics. Therefore, despite their apparent utility for modelling purposes, a more refined second approach is taken in the next step.

The next proposed model is based on the mathematical expressions of a family of curves known as ‘hippopedes’. Since the polar representation of these curves allow a smooth azimuthal transition from a certain wavelength (maximal) to another finite value (minimal), these curves can be used here as a generalization of the problem scenario. By applying these expressions to a magnetic patch with regularly distributed corners and domain walls, a simple expression for the spin wave wavelength can be obtained. If a circle, defined with radius a, is rotated about an axis at distance b from its center, then the generic equation of the resulting hippopede in polar coordinates is,

$$f(\theta) = 2\sqrt{b}\sqrt{a - b \cdot \sin^2(\theta \frac{n}{2} + \varphi_0)}\,, \tag{4.7}$$

where the phase parameter φ_0 sets an initial rotation angle for the patch. For $n = 2$ and $b = 2a$, Eq. (4.7) leads to a special case known as Bernoulli's Lemniscate. In fact, a whole family of lemniscates can be obtained from the hippopedes if $b > a$. The ‘hippopedes’ when $b < a$, known as Booth's ovals, allow a transition from a finite wavelength maximum value (λ_{DE}) to another non-zero minimum value λ_{WM}, see Fig.4.10(c). The particular values of the geometrical parameters a and b can be found from the ‘hippopede’ general equation particularized to the wavelength limiting conditions of a maximum λ_{DE} at every $2\pi/n$ angle and a minimum λ_{WM}

at every $\frac{2\pi}{n} + \frac{\pi}{n}$ angle. An initial rotation angle of $\varphi_0 = 0$ is assumed. The ratio b/a is found to be,

$$\frac{b}{a} = 1 - \frac{{\lambda_{\mathrm{DE}}}^2}{{\lambda_{\mathrm{WM}}}^2}. \tag{4.8}$$

In the range of frequencies under study, $\lambda_{\mathrm{DE}} > \lambda_{\mathrm{WM}}$ is satisfied, so this implies we can model our system with hippopede curves where $b < a$. The initial phase rotation φ_0 in Fig. 4.10(c) (and hereafter) is chosen so it properly coincides with the numerically modelled patch. Therefore, a more complete expression for our model is:

$$\lambda(\theta, n) = \lambda_{\mathrm{WM}} \sqrt{1 - \left(1 - \frac{{\lambda_{\mathrm{DE}}}^2}{{\lambda_{\mathrm{WM}}}^2}\right) \cdot \sin^2(\theta \frac{n}{2} + \varphi_0)}, \tag{4.9}$$

Fig.4.10(c) shows a collection of results from Eq.(4.9) for different number of vertices n, where φ_0 is properly chosen so it agrees with the orientation of the patch shown in Fig.4.10(a). Following from the magnetic configuration of the patch in the vortex state and assuming for example $\lambda_{\mathrm{DE}} = 2\lambda_{\mathrm{WM}}$, which yields a ratio $b/a = 0.75$ $(b < a)$, results qualitatively show an azimuthal changing wavelength around the centre of the shape, according to a hippopede curve, and very similar to results from the first model.

So far, the two proposed models describe a transition between two finite values of wavelength, although they lack connection with fundamental physics of magnetisation dynamics. The third proposed model yields a connection with the fundamental physics and allow us to link all results together.

In this case, we start from the analytical expression of the dispersion relation of spin waves given an arbitrary angle between **M** and **k**. Damon and Eshbach (Eshbach & Damon, 1960) found an expression for the dispersion relation of spin waves for arbitrary angles α and β, being α the angle between the ferromagnetic planar body surface and effective field $\mathbf{H_i}$ and β the angle between the orthogonal direction of that effective field and wavenumber **k**. Extended to the exchange regime, it can be expressed as,

$$\omega = \frac{\gamma H_i}{2\cos(\alpha)\cos(\beta)} + \frac{\gamma B_i}{2}\cos(\alpha)\cos(\beta) + \omega_M \lambda_{ex} k^2 \ . \tag{4.10}$$

In non-saturated samples, Eq.(4.10) can be reduced by specifying only in-plane magnetization ($\alpha = 0$), assuming the internal field in the magnetic domain is $\mathbf{H_i} = -\mathbf{M_S}$ (therefore, $\mathbf{B_i} = 0$) in absence of an external biasing field. For $\beta = 0$, $\mathbf{k}$ is perpendicular to $\mathbf{M}$ and therefore, $\lambda = \lambda_{\mathrm{DE}}$. Hence, for a specific excitation frequency $\omega = \omega_0$ we can rewrite Eq.(4.10) in terms of a variable wavelength ($\lambda = 2\pi/k$) in the azimuthal direction θ as,

$$\lambda(\theta) = \lambda_{\mathrm{DE}}\sqrt{\frac{(1-p)\cos(\beta)}{\cos(\beta)-p}} = \lambda_{\mathrm{DE}}\sqrt{\frac{(1-p)\sin(\theta)}{\sin(\theta)-p}} \ , \tag{4.11}$$

where $\beta = \theta - \pi/2$, being β the angle between the spin wave wavevector and the direction of magnetization $\mathbf{M}$ which sets the reference for an azimuthal dependence of $\mathbf{k}$ at $\theta = 0$, and $p = {}^{\omega_M}/_{2\omega_0}$, where $\omega_M = \gamma M_S$. A classical dispersion behavior of a spin wave in the Damon-Eshbach configuration (λ_{DE}) is obtained when $\theta = \pi/2$. The initial arbitrary rotation phase of the patch can be conveniently chosen as $\varphi_0 = \pi/2$ so a DE spin wave wavelength can be obtained for $\theta = 0$ instead, as reference point. This implies we can substitute $\sin(\theta) \rightarrow \cos(\theta)$ which keeps the reference $\lambda(0) = \lambda_{\mathrm{DE}}$ consistent. Eq.(4.10) implies a decreasing wavelength as the angle θ increases. For a flux closure magnetisation in the patch, the reference angle coincides with the direction of propagation into a first magnetic domain.

In the model, parameter $p = {}^{\omega_M}/_{2\omega_0}$ yields a connection between the observed radial wavefront in simulations and the magnetic properties of the material but sets an upper frequency bound for the model, which is not physically meaningful. The model from Eq.(4.11), after the $\sin(\theta) \rightarrow \cos(\theta)$ substitution, yields imaginary values for $\cos(\theta) < p \leq 1$ and therefore, it would only be applicable for $\omega_0 \leq {}^{\omega_M}/_2$ and for certain azimuthal directions. Eq.(4.11) would still be applicable as a model for the scenario of a magnetic patch for small deviations of θ from 0, although it does not apply when $\theta \rightarrow \pi/2$, where backward volume spin wave propagates instead of spin waves in a Damon-Eshbach configuration according to Ref. (Eshbach & Damon, 1960).

Also, this preliminary model assumes in-plane magnetisation for all azimuthal directions, so it does not consider effects of magnetic inhomogeneities, i.e., the domain walls. Fig. 4.11 shows a collection of curves from Eq.(4.11), illustrating a periodic effect when an n number of corners is included ($\theta \rightarrow \theta\, {}^{n}\!/_{2}$). In Fig. 4.11, only the rightmost lobe would be strictly represented by Eq.(4.11).

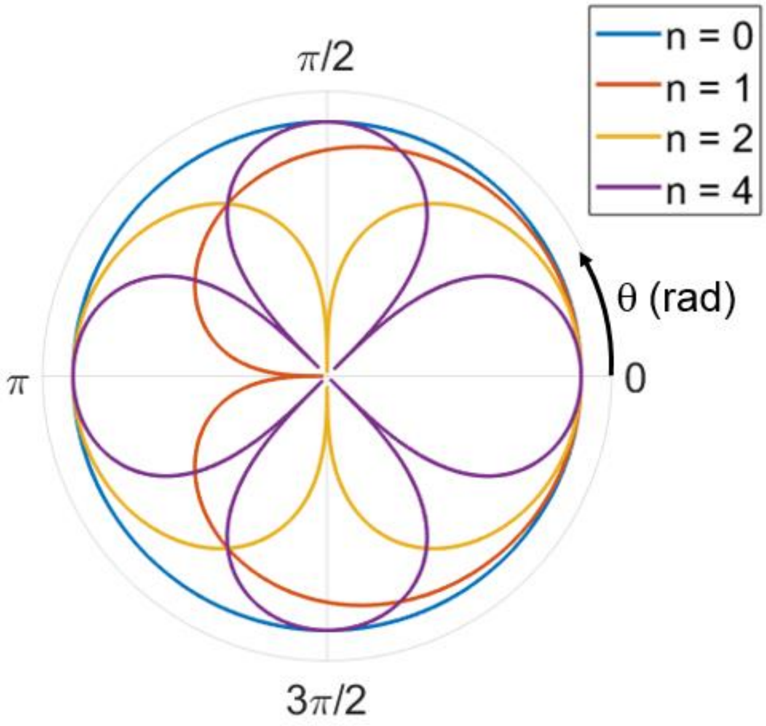

Figure 4.11. Collection of curves from Eq.(4.11) for $n = 0, 1, 2$ and 4. Curves for $n = 3$ and higher orders ($n > 4$) can be easily inferred. Physically non-realizable zeroes are placed at every π/n angle.

As stated above, imaginary values and zeroes of Eq.(4.11) due to the frequency dependence and geometry, are not physically meaningful in our scenario. This is due to the imposed lower frequency gap for the FMR in the disc and the presence of domain walls, respectively. To include these phenomena and avoid the zeroes in the model, Eq.(4.11) has to be generalised with the undefined parameter σ and re-scaling factor ε so the expression is extended as,

$$\lambda(\theta, \mathrm{n}) = \varepsilon \cdot \lambda_{\mathrm{DE}} \sqrt{\sigma + \frac{(1-p)\cos\left(\theta \frac{n}{2}\right)}{\cos\left(\theta \frac{n}{2}\right) - p}} \ . \tag{4.12}$$

In an n-corner patch, the spin wave shows a wavelength of λ_{DE} at every $\frac{2\pi}{n}$ angle and of λ_{WM} at every $\frac{\pi}{n}$ angle. These limiting conditions allow to find the values of parameters ε and σ. These values are found to be:

$$\varepsilon = \frac{\sqrt{{\lambda_{\mathrm{DE}}}^2 - {\lambda_{\mathrm{WM}}}^2}}{\lambda_{\mathrm{DE}}} \ , \tag{4.13}$$

$$\sigma = \frac{{\lambda_{\mathrm{WM}}}^2}{{\lambda_{\mathrm{DE}}}^2 - {\lambda_{\mathrm{WM}}}^2} \ , \tag{4.14}$$

which simplified for $\lambda_{\mathrm{WM}} = 0$, lead to the equation from Ref. (Eshbach & Damon, 1960). Due to the azimuthal periodicity every π/n in the patch (in contrast to the scenario described in Ref. (Eshbach & Damon, 1960)), cosine terms in Eq.(4.12) must only take positive values. Also, since taking their absolute values would yield a non-differentiable function at the angle where the domain wall is encountered, the cosine terms are replaced by their squared values. Assuming $\lambda_{\mathrm{WM}} \neq 0$ and after algebraic transformations, the modified equation is:

$$\lambda(\theta, n) = \lambda_{\mathrm{WM}} \sqrt{1 - \left(1 - \frac{{\lambda_{\mathrm{DE}}}^2}{{\lambda_{\mathrm{WM}}}^2}\right) \frac{(1-p)}{\cos^2\left(\theta \frac{n}{2}\right) - p} \cos^2\left(\theta \frac{n}{2}\right)} \ , \tag{4.15}$$

where $p = {}^{\omega_M}/_{2\omega_0}$. The key result is found if $p \gg 1$, and therefore, $(1-p)/\left(\cos^2\left(\theta \frac{n}{2}\right) - p\right) \approx 1$. Then, the resultant equation is indeed the Hippopede curve equation (assumed $\varphi_0 = \pi/2n$, so the directions for λ_{WM} and λ_{DE} are exchanged)), described previously, which explains the good fitting to these curves at low frequencies $\omega_0 \leq {}^{\omega_M}\!/_2$. Therefore, the azimuthal change of wavelength for a spin wave emitted from the core in an n-corners magnetic patch in the vortex configuration is fully described by Hippopede curves.

Fig. 4.12 (left inset) shows a collection of curves obtained from Eq.(4.15) normalized to λ_{DE}, assuming again $\lambda_{\mathrm{DE}} = 2\lambda_{\mathrm{WM}}$. In the right inset, a particular case for $n = 4$ is shown in comparison with the respective solution from Eq.(4.11) and the relative error between both equations for all angles between 0 and $\frac{\pi}{n}$, normalised to the number of vertices n for a value $p \approx 1.75$ (black solid curve), obtained from assuming $\omega_0/2\pi = 8.8$ GHz and from Permalloy material properties, $\omega_M/2\pi \approx 27$ GHz. For a large enough value of p, assumed to be six times larger ($p \approx 10.75$), and therefore $p \gg 1$, results show indeed a minimal difference (red solid curve) with the Hippopede curves, almost negligible away from the domain wall regions.

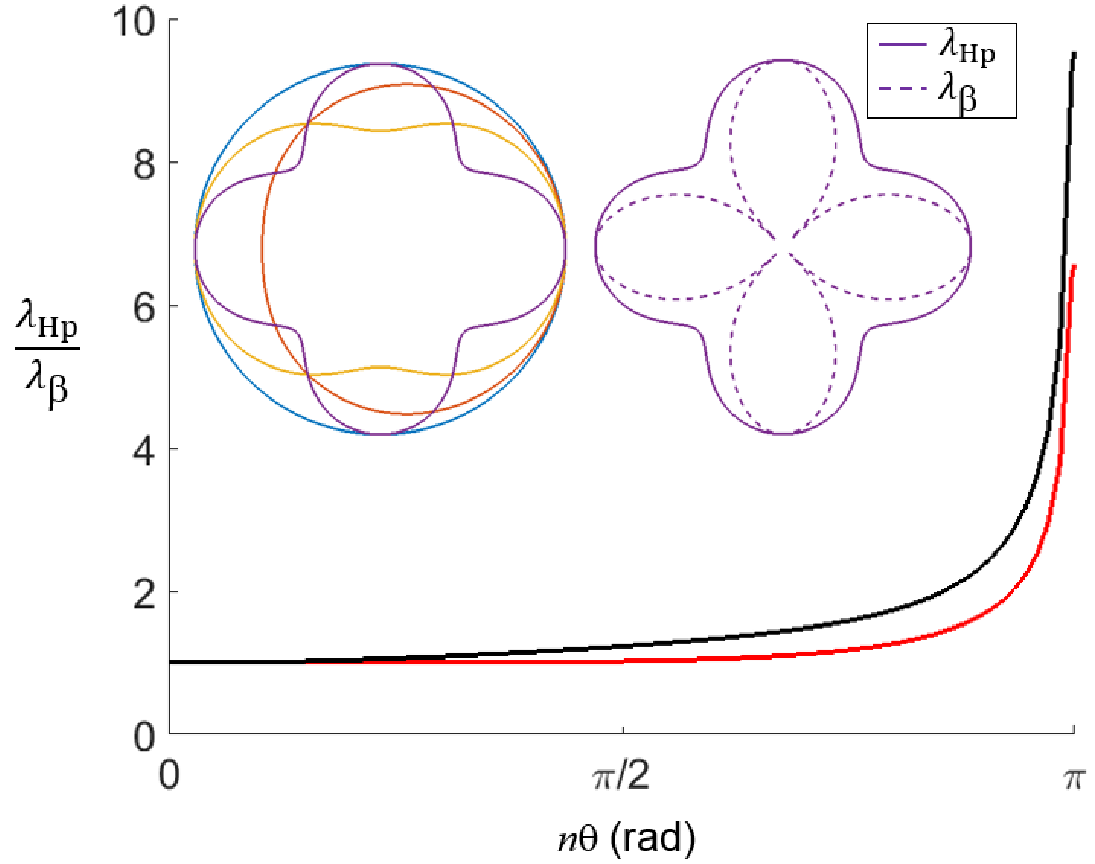

Figure 4.12. Ratio between wavelengths obtained from the dispersion relation from (Eshbach & Damon, 1960) (λ_β) and from the extended model linked to the Hippopedes (λ_{Hp}) for $p \approx 1.75$ (for $\frac{\omega_0}{2\pi} = 8.8$ GHz and Permalloy material properties) (black solid curve) showing good agreement, and practically no deviation from unity at any angle (apart from the domain wall region) for $p \approx 10.75 \gg 1$ (red solid curve). Inset (left): Normalised results from Eq.(4.15) adding azimuthal periodicity for a number of corners $n = 0$ (blue), $n = 1$ (red), $n = 2$ (yellow) and $n = 4$ (purple). Inset (right): Comparison of the normalised results from Eq.(4.11) (λ_β, solid purple curve) and Eq.(4.15) (λ_{Hp}, dashed purple curve) for $n = 4$ and $p \approx 1.75$.

The proposed model, as an extension of Eq.(4.11), avoids the azimuthal zeroes and shows a minimal difference with the values from the dispersion relation of spin waves in a generalised Damon-Eshbach configuration. Therefore, Eq.(4.15) is a suitable model, derived as a generalization from Eq.(4.11).

4.5.2 Numerical validation

In this section we compare the models previously described to numerical micromagnetic simulations to validate them. Radial spin waves with a spiral profile from the core region can also propagate when the excitation signal is applied in-plane of the patch (Davies, et al., 2015). This effect can be added to the model in terms of a normalised azimuthal factor which creates a counterclockwise spiralling effect as observed in the simulated wavefronts ($\lambda \rightarrow \frac{\theta}{2\pi}\lambda$). In micromagnetic simulations, a continuous out-of-plane wave excitation of frequency $\mathrm{f}_0 = \frac{\omega_0}{2\pi} = 8.8\ \mathrm{GHz}$ is applied to the core region. The excitation frequency is chosen so the radial spin wave shows a clear wavefront for the given dimensions and material of the magnetic patch (see section 4.3). From numerical in section 4.3, the wavelengths of the spin wave into the domain and the confined mode are chosen as $\lambda_{\mathrm{DE}} = 126$ nm and $\lambda_{\mathrm{WM}} = 89$ nm.

We need to address that the main objective is to test the relative change between these two wavelengths, regardless of their absolute values. Fig. 4.13(a) shows snapshots of the dynamic out-of-plane magnetisation from micromagnetic simulations of two different shapes, a ‘double teardrop’ shape (two vertices) and a square (four vertices). Their respective k-space maps from each image are shown on the right, where the white arrows indicate the propagation of the main modes, first higher order spin wave modes in the DE configuration and Winter's magnons. The images are interpolated for clarity. Before performing a spatial FFT, a Hamming window of 256 points is applied to the data set to avoid image artifacts due to reflections at the edges and spurious high frequency values.

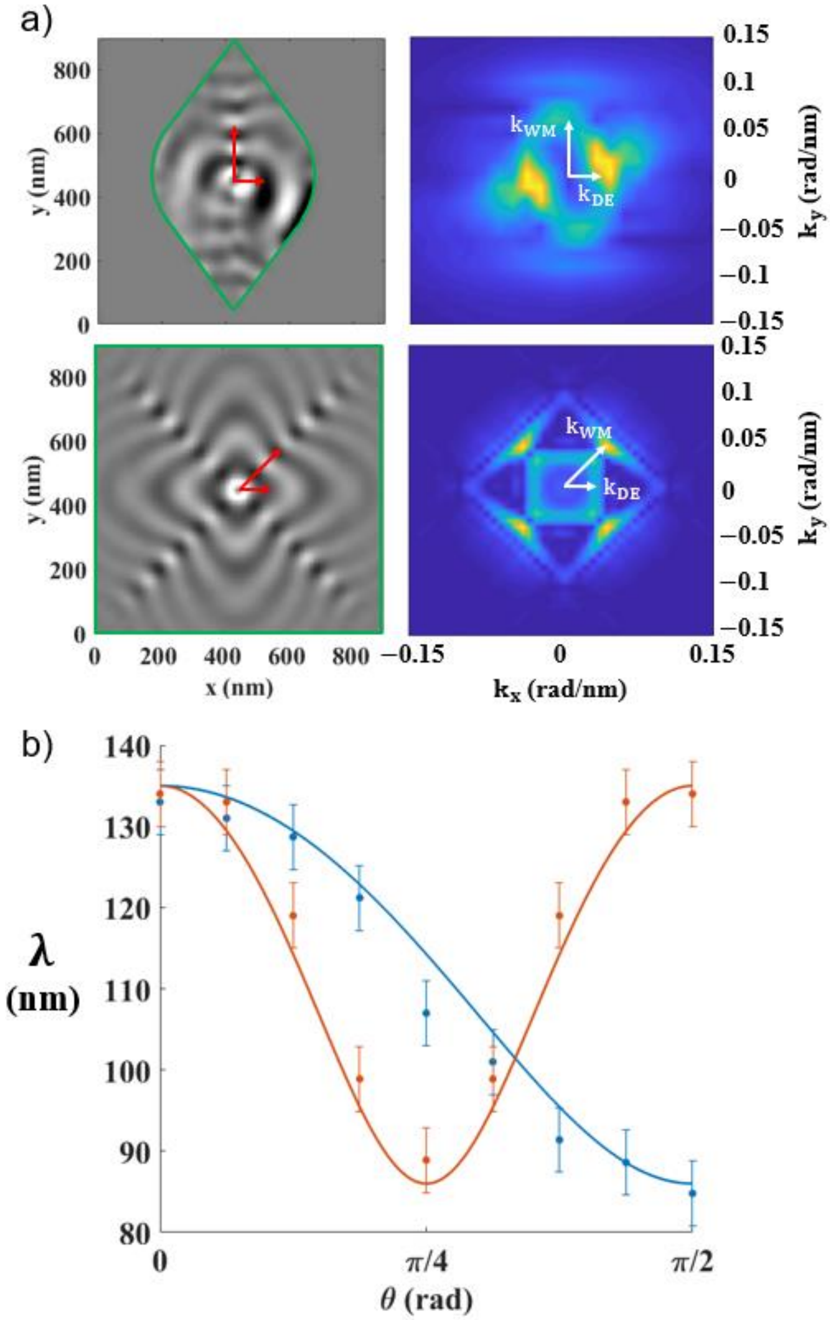

Figure 4.13. (a) (Left) Snapshots of numerical results for a teardrop shape ($n = 1$) and a square ($n = 4$). Red arrows indicate the direction of propagation of the two main modes (short waves emitted from the core in a DE configuration and Winter's magnon). (Right) k-space of the snapshots where the wavenumber profile (inverse of the wavelength profile) is shown. Results are interpolated to 5 extra points between data points for a better clarity. White arrows indicate the direction of propagation of the main modes. (b) Comparison of the maximum values of $\lambda = 2\pi/k$ found in (a) for the teardrop shape (blue) and the square (orange) with the results from Eq.(4.15) where

λ_{DE} = 126 nm and λ_{WM} = 89 nm found from numerical results at f_0 = 8.8 GHz an $p \approx 1.75$. Error bars are found after the interpolation process, which introduces a measured error of approximately 8 nm.

Values of wavelength are extracted from the simulated k-space images at angles from 0 radians to $\pi/2$ radians in the teardrop shape and from 0 radians to $\pi/4$ in the square in steps of $\pi/16$. The error bars are found after interpolation, yielding an error in wavelength of approximately 8 nm. The change in wavelength given by the model shows very good agreement with numerical results and follow the predicted trend. The analytical results can easily be extrapolated to any n-corner shape. Taking this into account, we can confidently say that the proposed model describes the spin wave wavefront of an emitted spin wave from the core in any n-corner shape with accuracy.

Finally, in any n-corners shape presenting angular periodicity, the azimuthal transition from a short wave emitted from the core, in a DE configuration, of wavelength λ_1 into that of a confined mode along a domain wall $\lambda_2 < \lambda_1$ is of the form of an Hippopede curve or, more generalised,

$$\lambda(\lambda_1, \lambda_2, \theta, \mathrm{n}) = \lambda_1 \mathrm{D}(\lambda_1, \lambda_2, \theta, n)\sqrt{1 + \mathrm{E}(\lambda_1, \lambda_2)\cos\,(\theta\frac{n}{2})} \tag{4.16}$$

As a suggested improvement to the model, a radial dependence could be included into Eq.(4.15). The radial dependence should consider that, as n increases, the domain walls will merge closer to the core region, which implies no azimuthal gradient and the wavefront profile will be that of a disc (equivalent to $n = 0$) under a critical effective radius. As stated at the beginning of section 4.5, this effective radius can be modelled as $r_0 = \frac{\pi}{n}\Delta$ for $n > 2$, where Δ is the domain wall width.

The Hippopede curves are obtained from Eq.(4.15) under the condition: $p \gg 1$. It is worth to note that the condition $\sqrt{2}\lambda_{\mathrm{WM}} > \lambda_{\mathrm{DE}} > \lambda_{\mathrm{WM}}$, which implies an ‘hippopede wavefront’ with geometrical parameters $b < a$, is not necessary satisfied for all values of $\lambda(\theta)$ at every ω_0, as explained before. There is a lower frequency bound from which only spin waves will be radiated into the domains from the core due to the non-zero internal field there. In contrast, a gapless mode can propagate in the domain walls (Garcia-Sanchez, et al., 2015). As ω_0 increases, at the limit when $\lambda_{\mathrm{DE}} \approx \lambda_{\mathrm{WM}}$, the radial wavefront tends to a circular profile, as explained in section 4.4 and as Eq.(4.15) consistently predicts. This frequency dependence is already implicit in the model in parameter $p = {}^{\omega_M}/_{2\omega_0}$.

At high frequencies where $\omega_0 \approx \omega_M/2$ and therefore $p \approx 1$ (so $p >> 1$ is not hold), assuming $\lambda_{\mathrm{DE}} \approx \lambda_{\mathrm{WM}}$, Eq.(4.15) effectively yields a wavelength of $\lambda(\theta, n) = \lambda_{\mathrm{DE}}$, this is, a circular wavefront. At even higher frequencies ($\omega_0 \gg \omega_M$), $p \ll 1$ and therefore: $(1-p)/(p - \cos^2(n\theta/2)) \approx 1/\cos^2(n\theta/2)$. In that case, Eq.(4.15) leads again to $\lambda(\theta) = \lambda_{\mathrm{DE}}$, regardless of λ_{DE} and λ_{WM} absolute values. This implies that Eq.(4.15) is still a valid model even for $p \approx 1$ or $p \ll 1$, or in other words, it does not show an upper frequency bound for radial waves either. This is consistent with the physical scenario to describe and previous work on radial propagating spin waves.

4.6 Summary

The competition between minimization of exchange and dipolar energies dictates the different dynamics and the configuration of the internal magnetic field in the sample with a strong dependence of the thickness of the sample. As in the formation of different types of domain walls, we showed the rising of different spin wave modes near a vortex core inhomogeneity and gave an explanation from the perspective of a balance between magnetic energies and the distribution of magnetization vectors.

In the bulk of a thick disc, intensity of dipolar fields is reduced, and exchange fields are enhanced in the vicinity of the vortex core. This creates new magnetization inhomogeneities which causes an outward propagating wave from the vortex core region. If the excitation is applied in-plane, the spin wave shows an out of phase wavefront on opposite sides of the core and hence, conforming a spiral wavefront. In thin disks, the arrangement of magnetic moments and surface pinning effects reduce considerably the intensity of the generated spin wave. When the pumping field is applied out of plane, a circular wavefront is launched outwards from the core vicinity. In this report, all these scenarios have been explained based on relations used in Landau-Lifshitz equation of motion. Dispersion relations give more in-sight of the landscape of the excitable modes in circular disks and squares, where the collection of modes is richer due to the formation of domain walls.

We showed the possibility of enhancing the amplitude of spiral spin waves in thick nano-patches, improving their detection by means of standard RF techniques such as VNA-FMR. Through this technique, we also show experimental demonstration of absorption peaks related to Winter's magnons traveling along the diagonals of square elements and how the absorption can be enhanced by exciting simultaneously the spiral spin wave from the core.

In addition to this, we have used geometrical expressions to successfully model radially propagating spin waves from the vortex core in n-corner elements. These elements show a magnetic flux closure configuration where domain walls are present. Three types of models are proposed and all show very good agreement with numerical results. The equations can be generalised to any n-corner shape, including non-regular shapes such as a teardrop shape (one vertex) and a double teardrop shape (two vertices). A first approach is based on two functions that, depending on the azimuthal direction, weight two limiting wavelengths (which can be known beforehand) in a non-homogeneous patch in the vortex configuration. This approach accurately describes the change from one wavelength to another in an azimuthal direction about the core. A second model is based on a special case of the 'Hippopede' curves, known as Booth's ovals, since they allow smooth transitions between two known wavelength values.

A more exact model is obtained straight from generalising the fundamental equation of spin wave dispersion in a DE configuration, which can be retrieved by setting $\lambda_{\mathrm{WM}} = 0$. This more compact model describes the spin wave wavefront accurately at positions far from the core and especially, close to the inhomogeneous areas (i.e., domain walls). Interestingly, through algebraic transformations, the final equation of the model (where $\lambda_{\mathrm{WM}} \neq 0$ and $p >> 1$), is identical to the 'hippopede' curve. The result connects the mathematical model with the physical parameters of the material and proves the 'hippopede curves' as the most accurate mathematical description of the transition between one wavelength and the other. Reciprocally, the magnetic properties of the material (through λ_{DE} and λ_{WM}) can be retrieved from the geometrical parameters of the plotted Hippopede curve (a and b) through a fitting process. Given the frequency of the oscillating field ω_0, parameter p and therefore ω_M and M_s can also be retrieved.

The model from Eq.(4.15) also takes into account the frequency dependence of the oscillating field. At lower frequencies, the model yields hippopede curves for the spin wave wavefront profile. At higher frequencies, it effectively leads to circular wavefronts, as confirmed by micromagnetic results.

The models can also be applied on spiral wavefronts, although they are originally defined for 'in-phase' wavefronts, which makes them suitable for also describing circular/non-spiralling wavefronts. For modelling spiral wavefronts, the model equation can be modified accordingly by simply introducing a normalised spiralling effect factor, $\lambda(\theta) \rightarrow \frac{\theta}{2\pi}\lambda(\theta)$.

We hope these results help to better understand the sources of spiral spin waves in confined structures and how to control their dynamical properties. The core vicinity can act as a quasi-punctual source of spiral spin waves, among other shapes of wavefronts, offering a new variety of potential applications for magnetic nanostructures.

Chapter 5 Imaging the curling eigenmodes of a confined magnetic vortex and their connection to propagating spiral spin waves from the core[8]

5.1 Introduction

Vortex states confined to thin film ferromagnetic discs generate negligible stray field at the edge of the disc, exhibit stability without the need for a biasing magnetic field, and can support a rich spectrum of spin waves making them attractive elements for high density, low energy, microwave frequency magnetic devices. Spin waves are eagerly anticipated as an energy efficient carrier of information in tunable micron and sub-micron scale magnonic circuits for magnetic logic, memory, and oscillator applications (V V Kruglyak, et al., 2010; Hoffmann & Bader, 2015; Chumak, et al., 2014; Lan, et al., 2015; Xing, et al., 2013; Kostylev, et al., 2005; Lee & Kim, 2008). For this purpose, the magnetization dynamics of circular ferromagnetic discs with a vortex equilibrium state have being studied intensively, from works to acquire a greater understanding of the gyrotropic core dynamics (Guslienko, et al., 2002; Park, et al., 2003; Park & Crowell, 2005) to emerging signal processing applications, such as tuneable microwave emission of a spin torque vortex oscillator (STVO) (Pufall, et al., 2007). For applications, phase locking of multiple oscillators is required in order to enhance microwave emission to a technologically useful level (Ruotolo, et al., 2009; Dussaux, et al.,

---

[8] At the time of submission of this Thesis, this research was an ongoing work and under peer review. It has been enriched and modified with new results and analysis since then. As of October 2020, an updated version of this research work can be found in: https://arxiv.org/abs/2007.02043v2

2011; Belanovsky, et al., 2012). One approach is to simply couple isolated oscillators in an array by dipolar interaction (Belanovsky, et al., 2012). However, an understanding of the magnetization dynamics of the individual oscillator elements is an essential prerequisite to understand the collective modes.

Spiralling spin waves found in vortex configurations have been previously explained as the hybridization of a stationary azimuthal mode and a higher order gyrotropic mode that shows no radial propagation, or alternatively as a burst of incoherent spin wave emission during a vortex core reversal (Kammerer, et al., 2011; Stoll, et al., 2015). It is well known that microscale confinement can lead to a non-uniform magnetization such as the vortex state (Shinjo, et al., 2000) or S and C single domain states (Fruchart & Thiaville, 2005).

Related inhomogeneity of the internal magnetic field in the region of the vortex core, or in the vicinity of edges perpendicular to an applied magnetic field, have been recently shown to be sources of spin waves due to a gradient in the magnonic refractive index. Such spin wave emission from these regions has been demonstrated using micromagnetic simulations and direct imaging techniques (Davies, et al., 2017; Mushenok, et al., 2017).

In the frequency domain, techniques such as Brillouin light scattering (BLS) and vector network analyzer ferromagnetic resonance (VNA-FMR) can be used to acquire the spin wave spectra of confined nanostructures. In spatially resolved BLS microscopy (micro-BLS), the amplitude of excited spin waves can be directly imaged in individual discs with < 300 nm resolution (Bayer, et al., 2005; Demidov, et al., 2009; Haidar, et al., 2019), and phase-resolved micro-BLS can be implemented by using extensions such as interference-based techniques (Demidov, et al., 2011; Vogt, et al., 2009). On the other hand VNA-FMR can provide amplitude and phase, but no spatial information and typically averages the response of an array of discs (Aliev, et al., 2009; Lara, et al., 2013). In the time domain, time-resolved scanning transmission x-ray microscopy (TR-STXM) has been used to directly image spiral spin waves in circular discs (Davies, et al., 2015; Wintz, et al., 2016; Dieterle, et al., 2019). In Ref. (Dieterle, et al., 2019) the authors claim that there would be a hybridization between core gyration and laterally propagating, perpendicular standing spin waves. At lower frequency, time-resolved scanning Kerr microscopy (TRSKM) can be used to image the spatial character of spin waves with wavelength larger than the diffraction limited optical spatial resolution (Neudecker, et al., 2006; Park, et al., 2003; Keatley, et al., 2017; Yu, et al., 2015). Other scanning probe techniques based on FMR force microscopy or magnetic resonance force microscopy (Obukhov, et al., 2008; Lee, et al., 2010) have proven useful for detecting highly spatially localised magnetization dynamics (Bhallamudi, et al., 2013; Urban, et al., 2006) as well as magnetic and electrical device characterization (Lee, et al., 2012; Berger, et al., 2014) in the nanoscale.

In this work we report on the direct observation and micromagnetic simulation of the curling nature of magnetization dynamics of the in-plane magnetized region of the disc that leads to an hybridization at low and high frequencies (~ 5GHz and ~10 GHz) and superposition at intermediate frequencies (6 GHz – 9 GHz) of azimuthal and radial modes with the gyrotropic modes of the core. We identify from simulations propagating short wavelength spiral spin wave are activated, simultaneous to the curling, and emitted from the core due to the excitation of the core region by the oscillating field. We note that the short wavelength spiral spin waves emitted by the core and the curling, spiral nature of the azimuthal and radial modes may become confused. Here on in, we therefore refer to these modes as ‘propagating spiral spin waves from the core’ and ‘curling azimuthal and radial modes’ respectively.

A sufficiently large disc thickness was chosen to yield a rich mode spectrum, while our results are reported over a broad frequency range that captures both azimuthal and radial modes and their interaction with different orders of the gyrotropic mode. TRSKM with a spatial resolution of ~300 nm was used to image the curling modes in a NiFe 2 um diameter and 40 nm thickness disc over a frequency range extending from 4 GHz to over 10 GHz. The simulations reveal that at low frequencies, the observed curling wave patterns can be described as a superposition between azimuthal modes with core dynamics, which also activate short wavelength spiral spin waves emitted by the core, showing the same azimuthal sense of spiralling as the driven core gyration. While the short spiral waves cannot be spatially resolved experimentally, micromagnetic simulations with fixed core spins demonstrate that the short wavelength modes are no longer emitted, and the curling nature vanishes, highlighting the dependencies of both phenomena with the core dynamics. The experimental observation of the curling using TRSKM thus provides an indirect confirmation of the emission of the short wavelength spiral spin waves from the core since our experimental measurements show very good agreement with the micromagnetic simulations. To understand the dynamics of the observed azimuthal and radial modes, we performed a set of micromagnetic simulations using Mumax3, as in previous chapters. A vortex state with counter-clockwise circulation (circulation index 1) and core polarization towards the substrate (polarization index -1) was manually set as the initial state. This particular configuration of core polarization and circulation reproduced the experimental findings as discussed in Section 5.3.

The disc studied in this work had a thickness ($t = 40$ nm) that has been predicted to coincide with a transition between two dynamical regimes, with different spin wave character excited in discs with diameter of 0.5 um (Noske, et al., 2016). In Ref. (Noske, et al., 2016), when the thickness is below the transition thickness, the frequency of the first order gyrotropic mode of the core, which has a $\sim 1/t^2$ dependence with thickness, is greater than both azimuthal modes with node index $m = \pm 1$ and forms an anticrossing (hybridization) with the higher frequency azimuthal mode ($m = +1$, counterclockwise, CCW), because of the same azimuthal sense of motion as the core gyration. Above the crossover thickness, the frequency of the first order gyromode becomes lower than the azimuthal modes and crosses the lower frequency azimuthal mode ($m = -1$, clockwise, CW). While the aspect ratio (thickness to diameter) of the disc studied in this work is one quarter that of the modelled disc in Ref. (Noske, et al., 2016), we can also relate the observed curling of the azimuthal mode, in similar terms as those discussed in Ref. (Noske, et al., 2016), to the core gyration of same sense of motion (in our case $m = -1$ instead of $m = +1$) and, additionally, to time correlated spatially unresolved core spiral spin waves.

5.2 Experimental details

Time-resolved scanning Kerr microscopy (TRSKM) was used to image the spin wave modes within a single NiFe disc with diameter of 2 um and thickness 40 nm. The spin waves were imaged at remanence (<10 Oe) and in response to a uniform RF magnetic field applied in the plane of the disc.

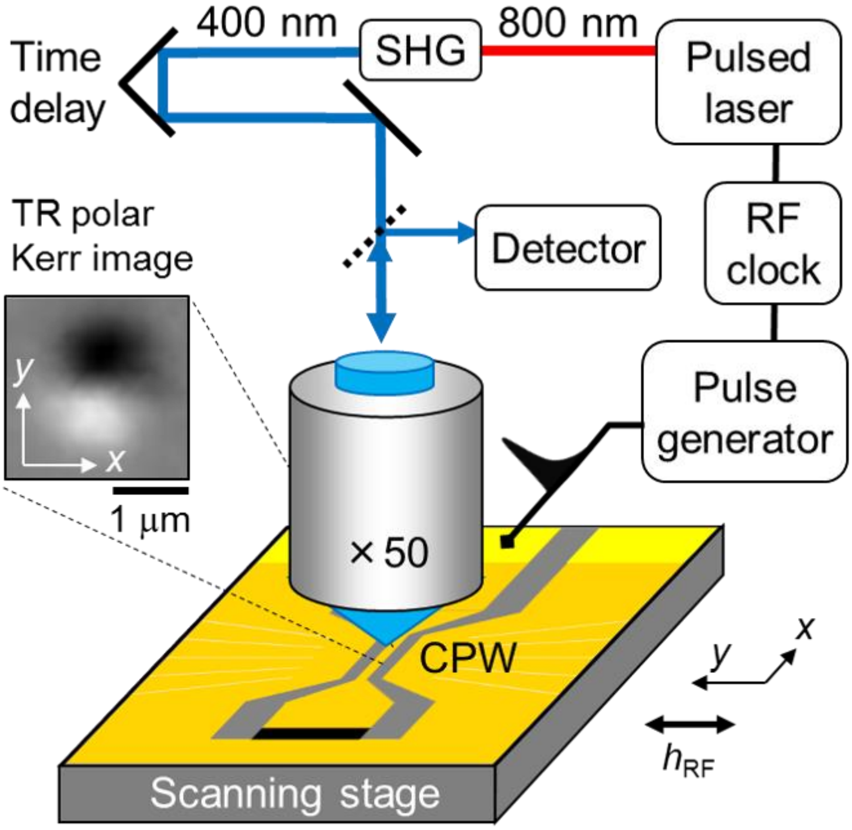

Figure 5.1. A schematic of the time-resolved scanning Kerr microscope featuring second harmonic generation (SHG) and an optical time delay for ~300 nm spatial resolution and picosecond temporal resolution. The microscale disc was fabricated on the central conductor of a constricted section of coplanar waveguide (CPW, not to scale) where the RF field (h_{RF}) was enhanced, in-plane, and perpendicular to the conductor. Images of magnetization dynamics (e.g. inset) correspond to the measured TR polar Kerr signal as the disc is scanned beneath the focused laser spot at a fixed time delay (phase) of the RF field excitation. A ~50 Ω NiCr resistor (black rectangle) was incorporated into the end of the CPW to attenuate the time-varying RF current and minimise multiple reflections.

The RF excitation was generated using a 50 Ω impedance matched coplanar waveguide (CPW). The CPW and NiFe disc were fabricated from a multilayer stack of composition Ta(5)/Cu(25)/[Ta(3)/Cu(25)]$_3$/Ta(10)/Ru(5)/ Ni$_{81}$Fe$_{19}$(40)/Al(1.5) (thicknesses in nm) as described in more detail elsewhere (Yu, et al., 2015). TRSKM was carried out using a Ti:sapphire mode locked laser to generate ~100 fs pulses with 800 nm wavelength at a repetition rate of 80 MHz. Second harmonic generation was then used to generate pulses with 400 nm wavelength that were passed along a 4 ns optical delay line, expanded by a factor of 5 and linearly polarized, before being focused to a diffraction limited spot onto the disc using an high numerical aperture (NA) microscope objective lens (NA 0.6, ×50). The beam was filtered to remove residual 800 nm and attenuated so that less than 200 μW average power was incident on the disc. The reflected light was collected by the same objective lens so that changes in the polarization resulting from polar magneto-optical Kerr effect could be analysed using a polarizing balanced photodiode detector.

Two types of measurement were performed. First, a time-resolved (TR) scan was performed. The laser spot was positioned 0.5 um from the centre of the disc along the y-direction parallel to the RF magnetic field. In this region the RF excitation of the in-plane equilibrium magnetization is expected to be maximum. The polar Kerr signal was recorded while the time delay was scanned yielding a sinusoidal response corresponding to Δm_{z} as the magnetization precesses, Fig.5.2(a). In the second measurement the time delay was fixed at a particular time delay of interest, and then the disc was scanned in the xy-plane beneath the laser spot to acquire a polar Kerr image corresponding to Δm_{z}, e.g. see the inset of Fig.5.2(b) for polar Kerr images of the disc acquired at opposite $(+, -)$ antinodes of the TR signal (red curve and open symbols) in Fig.5.2(a). For all RF frequencies used, time delays were selected so that images were acquired at similar increments in phase throughout a single RF cycle, e.g. see phases indicated by open symbols overlaid on the red curve in Fig.5.2(a). The resulting images were then drift-corrected and arranged according to their time delay to construct movies of a particular spin wave.

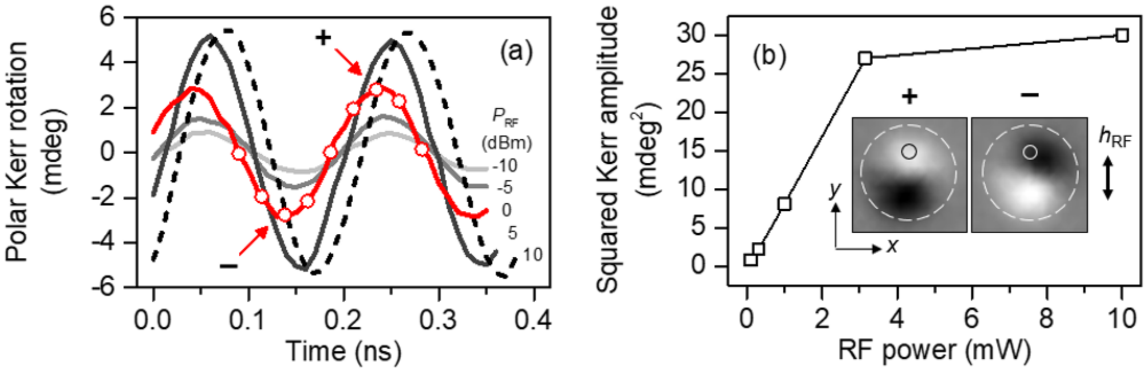

Figure 5.2. (a) TR polar Kerr signals for an RF frequency of 5.2 GHz and RF power (P_{RF}) ranging from -10 dBm (light grey trace) to 10 dBm (black dashed trace). (b) The squared Kerr amplitude as a function of P_{RF} (in mW) showing a linear dependence up to 3.3 mW (5 dBm). Inset in (b) are polar Kerr images corresponding to the antinodes (+,—) of the mode excited by a RF field h_{RF} with frequency 5.2 GHz and power $P_{\mathrm{RF}} = 0$ dBm (1 mW, red trace and symbols in (a)). The TR signals in (a) were acquired from the right hand side of the 2 um disc (large dashed circle overlaid on inset of (b)) from a small circular region corresponding to the optical spatial resolution (solid circle in inset of (b)). For all modes imaged, the symbols on the red trace in (a) indicate the relative phase at which Kerr images were acquired.

Individual spin wave modes of the vortex state were excited using RF frequencies ranging from 4.24 GHz to 10.24 GHz. The frequencies were selected from the Fourier spectrum of a TR scan acquired from the same point in the disc, but in response to a broadband pulse excitation, Fig.5.3(a). A pulse generator with ~30 ps rise time and ~70 ps duration was used to excite all modes that would couple to a uniform in-plane excitation field on picosecond timescales. The frequency and power of the excited modes was then identified from the spectrum. To excite these modes individually for TRSKM imaging the RF excitation (previously described) was applied with frequency equal to an integer multiple of the laser repetition rate, and with RF power adjusted to compensate for the lower power of some of the modes observed in the spectrum, e.g. particularly at higher frequency, see Fig.5.3(b). Such modes were excited with an RF power that was enhanced by the approximate difference in power with respect to that of the highest power mode at 5.2 GHz.

To confirm that all modes were imaged within a linear regime of the RF excitation, the RF power dependence was explored for the largest amplitude mode at 5.2 GHz, which was identified from the FFT spectrum corresponding to the broadband pulse excitation (Fig.5.3(b)).

The RF power dependent TR signal are shown in Fig.5.3(b). At 1 mW (0 dBm) the mode excitation was within the linear regime. This suggests that the excitation of modes with lower amplitude identified in the FFT spectrum of Fig.5.3(b) will also be excited within the linear regime, even when the excitation power is increase to compensate for the diminution of the mode amplitude in the spectrum.

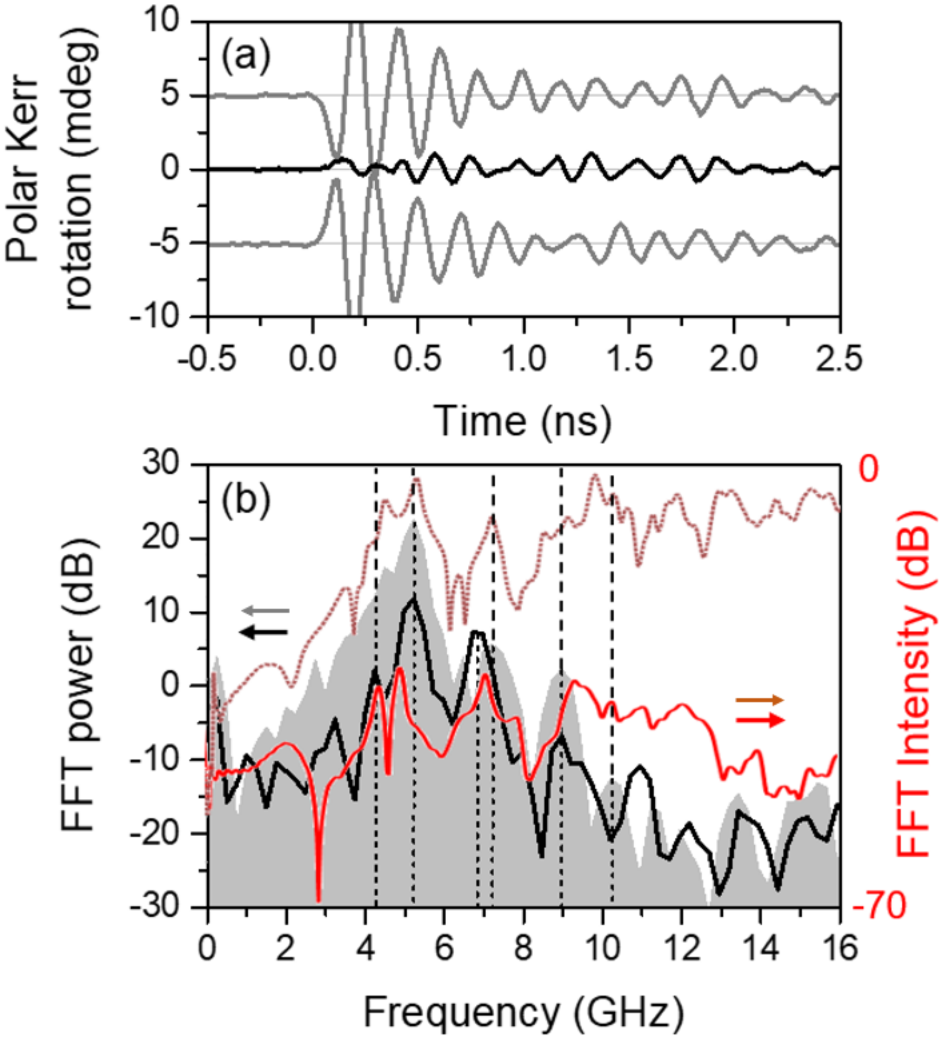

Figure 5.3. (a) TR polar Kerr signals, excited by a 70 ps pulsed magnetic field, acquired from the right hand side of the disc (top), centre of the disc (middle), and left hand side of the disc (bottom). (b) The fast Fourier transform spectra of the TR signals in (a) acquired from the right hand side (grey shaded spectrum) and the centre of the disc (black curve). Simulated spectra for the response extracted from the centre (solid red curve) and right hand side

(dashed red curve) of the disc are overlaid. Mode frequencies identified from the measured spectra are 4.24, 5.2, 6.8, 7.2, 8.96, and 10.24 GHz.

Slow phase drift of the microwave synthesiser waveform on timescales similar to that required for image acquisition can lead to mismatched spatial character of the spin wave at subsequent phases. To minimize this, repeated TR signals were acquired from the same position in the right hand side of the disc (~ +0.5 um from center of disc) to ensure the phase (time delay) was correctly set. Multiple images were acquired to ensure repeatability, and TR images were acquired in a non-sequential order to avoid a systematic accumulation of phase drift (nodal points imaged first, antinodes next, then intermediate phases to complete the series of images). Furthermore, the magneto-optical Kerr effect probes only the average response of the magnetization within the optical skin depth (~20 nm). In the simulations, variation in the phase across the thickness of the disc to a depth of 20 nm (top 5 layers of cells) was explored. It was confirmed that the phase was approximately uniform across the disc thickness far from the vortex core.

5.3 TRSKM measurements and discussion

The TR Kerr signals acquired in response to a pulsed magnetic field, exhibit an almost identical response 0.5 um to the left and to the right of the center of the disc, but have opposite sign, Fig.5.3(a). This is the expected dynamic response of regions of circulating in-plane equilibrium magnetization that lie perpendicular to the pulsed magnetic field. Since these regions to either side of the vortex core have antiparallel magnetization, the initial torque exerted by the pulsed magnetic field will have opposite sign, leading to the observed signals in Fig. 5.3(a). Clear beating of the TR signals indicates a multi-mode excitation in these regions. The average response of the core probed by the same ~300 nm focused laser spot positioned at the center shows a response that has reduced amplitude and more complicated beating.

Comparison of the FFT spectra of the response detected at the centre of the disc (black curve) and in the right hand side of the disc (grey shaded) are shown in Figure 5.3(b). Simulated spectra (red and brown curves) extracted from similar regions of the simulated disc in response to a sinc pulse have been overlaid with the measured spectra. While the complete spectral responses of measured and simulated spectra show differences, there is good agreement of some of the spectral peaks identified from the experimental spectra and the simulated spectra. The differences in the magnitude of the simulated and measured spectral response is due to the uniform power delivered at all frequencies in the simulations, while the power dependence is known to be non-uniform in such experiments, e.g. see reference (Keatley, et al., 2008). In particular, the shoulder below 5.2 GHz in the measured spectra is supported by the simulations which reveal at least one additional mode between 4 and 5 GHz. At around 7 and 9 GHz the simulated spectral response from the center (solid red curve) exhibits peaks that coincide with those of the measured spectrum from the center. On the other hand, a mode at ~10 GHz may be seen in the simulated spectral response away from the center (dashed brown curve). The simulated mode at around 10 GHz is not well resolved from neighbouring peaks but does support the identification of a mode at 10.24 GHz in the measured spectrum away from the center. The frequencies identified from the experimental spectra alone are indicated by the vertical dashed lines in Fig. 5.3(b). We note these frequencies, especially the modes with radial numbers $n = 1$ and $n = 3$ (at 5.2 GHz and 8.96 GHz, respectively), are similarly spaced (~ 3.5 GHz spacing) to those detected in Ref. (Vogt, et al., 2011) for a single disc of same dimensions (1 um radius and 40 nm thick) and an out-of-plane excitation, although slightly downshifted in frequency compared to our measurements, perhaps due to dipolar interaction between discs in the array or a slightly different thickness due to fabrication errors. In our case, azimuthal features in the profiles are also expected instead due to the in-plane excitation.

It will be shown that the hybridized or superposed mode character observed at different frequencies, is well reproduced by the micromagnetic simulations. The simulations confirm that the character of the observed dynamics changes with frequency since gyrotropic modes may only hybridize with azimuthal modes at low frequency, while at higher frequency, hybridization may instead take place between a higher order gyrotropic mode and a radial mode. The discussion that follows in this section is split into two parts which address (A) the low frequency regime, and (B) the high frequency regime. This criterion is chosen from our observations, where we observe features of azimuthal curling motion only for the studied modes at 4.24 GHz, 5.2 GHz, 6.8 GHz and 8.96 GHz (with identified radial and azimuthal numbers (1,+1), (1,$-$1), (2,+1) and (3,+1), respectively), and a more marked and single radial feature for the mode at 10.24 GHz (4,±1).

5.3.1 Low frequency regime

In Fig.5.3(b) the most prominent spectral peaks are found in the low frequency regime for which simulations predict that spiral spin waves emitted from the core have the largest amplitude. In Fig. 5.4(d), 5.4(e), and 5.5(a) and 5.5(b), the TR spatial character of the modes is shown for frequencies of 5.2 GHz, 4.24 GHz, 6.8 GHz, and 8.96 GHz, respectively. Notably, Fig. 5.4(c) and 5.4(d) reveal good agreement of the measured and simulated spatial character of the curling azimuthal mode as a function of time.

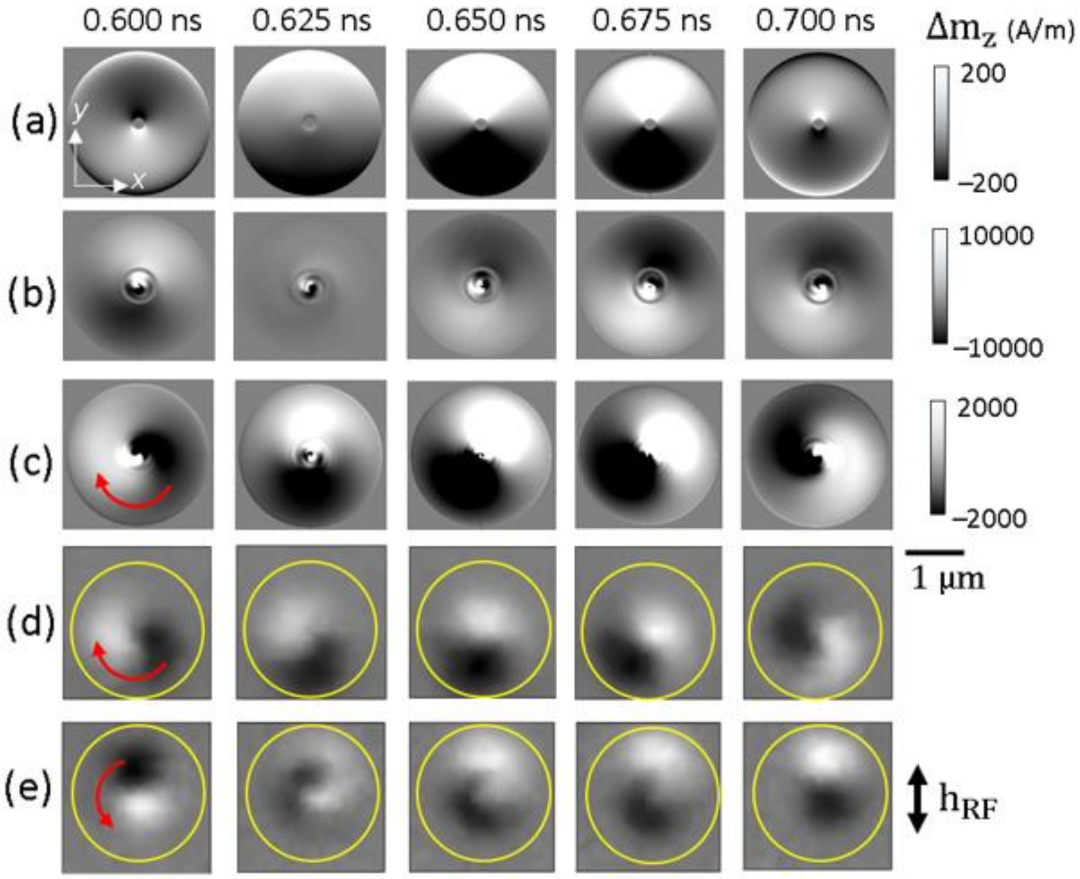

Figure 5.4. Simulated (a, b and c) and measured (d) TR images corresponding to the out-of-plane component of the dynamic magnetization in response to an in-plane excitation of 5.2 GHz frequency. In (e) measured images are

also shown for an excitation frequency of 4.24 GHz. In (a, b and c) the m_z component is extracted from the second layer of cells from the top surface of the disc. The spins in the vicinity of the core are fixed in (a) an in a ring around it in (b) and are free to precess in (c). In (d and e) the disc perimeter is indicated by the overlaid yellow circle.

In the low frequency regime, a whole set of azimuthal spin wave modes can arise (Park & Crowell, 2005). At an appropriate thickness (Noske, et al., 2016), core dynamics may hybridize with a curling mode leading to the observed dynamic pattern at a certain frequency way above the standing azimuthal mode. Such hybridization may only be observed above a threshold thickness (Verba, et al., 2016). To demonstrate that the curling effect is linked to the core dynamics, an equivalent disc was simulated with the spins of the core region fixed using the ‘frozenSpins’ function in Mumax3 (Vansteenkiste, et al., 2014). Fig.5.4(a) reveals that, when the spins are fixed, short wavelength spiral spin waves are no longer emitted by the core and the problem is almost equivalent to that of a ring structure, where no curling has been observed but the degenerate static azimuthal mode (Noske, et al., 2016). The spatial character of the azimuthal mode then remains static and does not exhibit the curling, spiral nature observed in the experiments and in the simulations where the core is free to gyrate (Fig.5.4(c) and 5.4(d)). Additional simulations (Fig.5.4(b)) in which spins are fixed in a concentric ring-shaped region around the core, show that the spiral spin waves are emitted by the core but do not propagate through the ring to reach the standing azimuthal mode and the curling of the azimuthal mode does not occur. In this case, the modelled disc can be regarded as a combination of a disc of smaller diameter (region enclosed by the frozen ring) plus a concentric magnetic ring (i.e., rest of the disc). In the equivalent ‘smaller disc’, similar dynamics to those observed for the original disc (Fig. 5.4(c)) can be observed. On the other hand, the concentric ring shows no curling. Therefore, the curling is undoubtedly linked to the existence of a vortex core, breaking the top-bottom symmetry of the disc. This suggests that the observed curling is linked to the core dynamics that also activate the propagating spiral spin waves as well emitted by the core.

At 5.2 GHz (Fig. 5.4(d)) and 4.24 GHz (Fig. 5.4(e)) the curling of the azimuthal mode is found to be in the opposite sense about the core. Ref. (Noske, et al., 2016) suggests that the driven core may hybridise with the curling mode of favourable sense to the gyration and similar profile across thickness, lifting its frequency above the other curling mode. This is observed in our measurements, where the CW curling mode is above the CCW mode. This idea is supported by additional simulations which show evidence of the fundamental gyromode profile, at 4.24 GHz, gyrating CW sense (see Fig. 5.6(d)).

At higher frequency, hybridization of the azimuthal mode and first order gyrotropic mode may only take place when their azimuthal motion is of the same sense (Noske, et al., 2016). The sense of gyration, and therefore polarization, may then be inferred from TR images of azimuthal modes hybridized at higher frequency, such as those identified in Fig. 5.3(b). The work from Noske *et al.* suggests that a significant frequency gap can be expected in the spectrum where the first order gyrotropic mode is hybridized with the higher frequency azimuthal mode, which means that the hybridized azimuthal mode may be observed at a frequency lower than that predicted for the first-order gyrotropic mode.

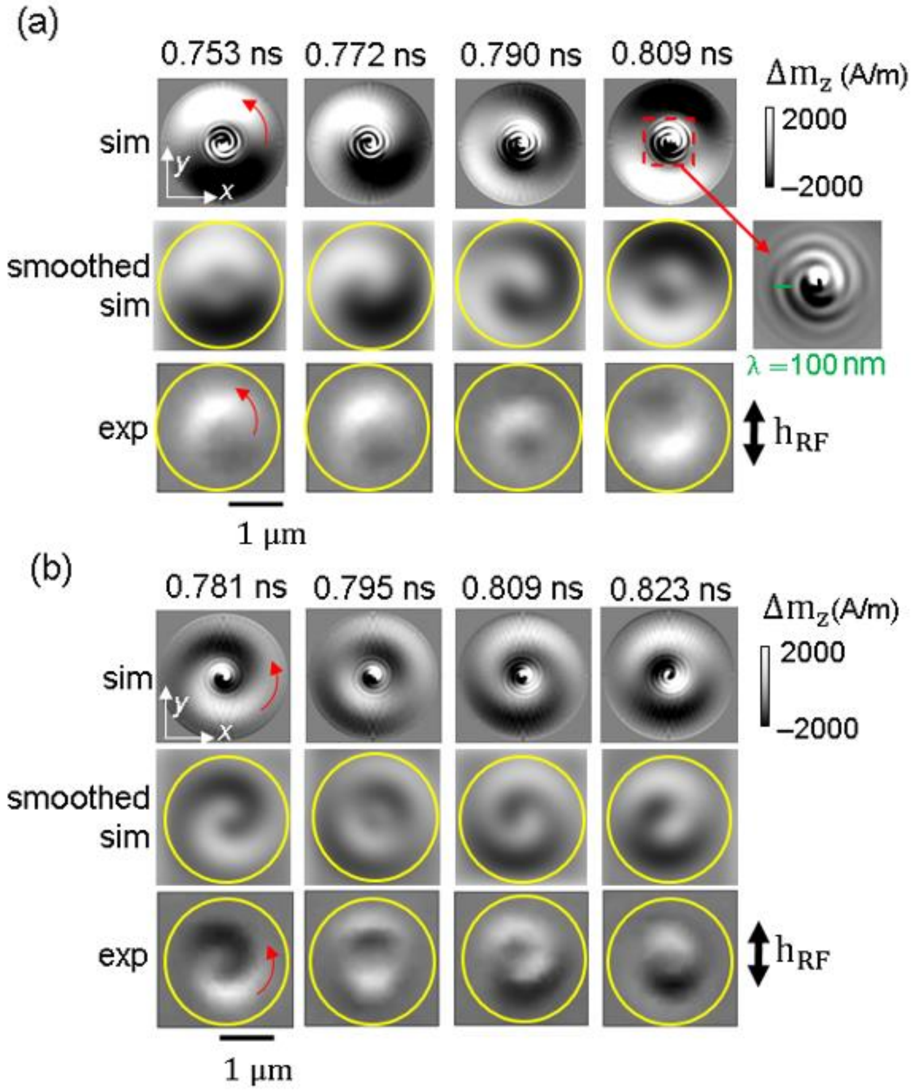

Figure 5.5. Simulated (sim) and measured (exp) TR images corresponding to the out-of-plane component of the dynamic magnetization in response to an in-plane excitation of 6.8 GHz (a) and 8.96 GHz (b). Simulated effects of a limited spatial resolution of 300 nm are shown in the second row in (a). The m_z component shown in the simulated images was extracted from the second layer of cells from the top surface of the disc. In (a) the inset shows the outwards propagating spiral spin wave from the core region in a larger color scale.

The simulated images of Figures 5.4(c) (5.2 GHz), 5.5(a) (6.8 GHz) and 5.5(b) (8.96 GHz) clearly show the emission of a shorter wavelength spiral spin wave from the core. In Fig.5(a) a snapshot of the simulated core region (dashed red square) at 0.809 ns is shown in more detail (inset right), where a 'two-arms' spiral can be observed. In contrast to one-arm spirals previously reported (Wintz, et al., 2016), the formation of a dynamical double-dip in the core region, given the right combination of the gyrotropic and the azimuthal modes curling senses of motion (Kammerer, et al., 2011), may explain the emission of a double-arm spiral instead of a single-arm spiral. Spiral spin wave emission from the core was also observed in simulations at 4.24 GHz (not shown). The spatial resolution of the experimental technique prevents the direct visualisation of these spin waves. To demonstrate this, the top row of simulated images in Fig.5.5(a) have been spatially down-sampled using Gaussian smoothing with a width corresponding to the optical spatial resolution of ~300 nm. The smoothed simulated images (smoothed sim) are shown in the center row in Fig.5.5(a) and reveal greater similarity with the measured images where the short wavelength spiral spin waves emitted from the core are not resolved and lead to a reduction of the net signal in the core region..

The TR polar Kerr images of Figures 5.4(e) (4.24 GHz), 5.5(a) (6.8 GHz), and 5.5(b) (8.96 GHz) all exhibit a curling motion with the same counter-clockwise sense, but with varying degrees of the spiral nature. This is due to the excitation of higher order radial-azimuthal modes of different order, increasing with frequency and a driven gyration of the core. Ref. (Noske, et al., 2016) suggests that the spiral character of the hybridized mode is more marked when the azimuthal mode is hybridized with the first-order gyrotropic mode at higher frequency. In this work at 8.96 GHz, the hybridized azimuthal mode exhibits the strongest spiral spatial character observed at any of the studied frequencies (Fig. 5.5(b)) due to his high radial number ($n = 3$). Furthermore, the hybridized mode at 8.96 GHz is observed at a frequency within 2 GHz of the first-order gyrotropic mode frequency. For the dimensions (2000 nm × 40 nm) and material parameters of the disc, the analytical dispersion relation from (Ding, et al., 2014) yields an eigenfrequency of 10.69 GHz for the first order gyrotropic mode ($n = 1$). When it is considered that the linewidth of the mode at 8.96 GHz is ~1 GHz, that a sizable frequency gap (> 1 GHz) opens in the spectrum because of hybridization (at a higher frequency close to 10.69 GHz), and that the frequencies of the azimuthal and gyrotropic modes only need be close to hybridize, the TR spatial character of the observed dynamics in Fig. 5.5(b) provides compelling evidence that the mode at 8.96 GHz is an ‘overlapping’ to a first-order gyrotropic mode profile, lower than its expected frequency, as a consequence of an hybridization between the first higher order gyromode and a higher order ($n > 3$) radial-azimuthal mode (Jorzick, et al., 1999). This mode will be explored in more detail in the next section. This idea is also supported by simulations which show evidence of the excitation of the first order gyromode profile at 8.96 GHz (Fig. 5.6(b)). Previous work has also shown the first order gyrotropic mode and related antisymmetric dynamical magnetization combined with a uniform profile in the core region at frequencies as low as 6.8 GHz in discs of the same thickness (40 nm) (Verba, et al., 2016). Since the sense of gyration of the first order gyromode is CW (see Fig.5.6(d)) and the sense of the curling wave is CCW (see red arrow in Fig. 5.5(b)), the observed patterns in the disc can be a result of superposition rather than hybridisation. The short spiral spin wave 'spirals out' in a CW sense at 6.8 GHz, which coherently matches with the sense of the first order (and fundamental) gyromode and confirms further its gyration sense to be opposite to the curling.

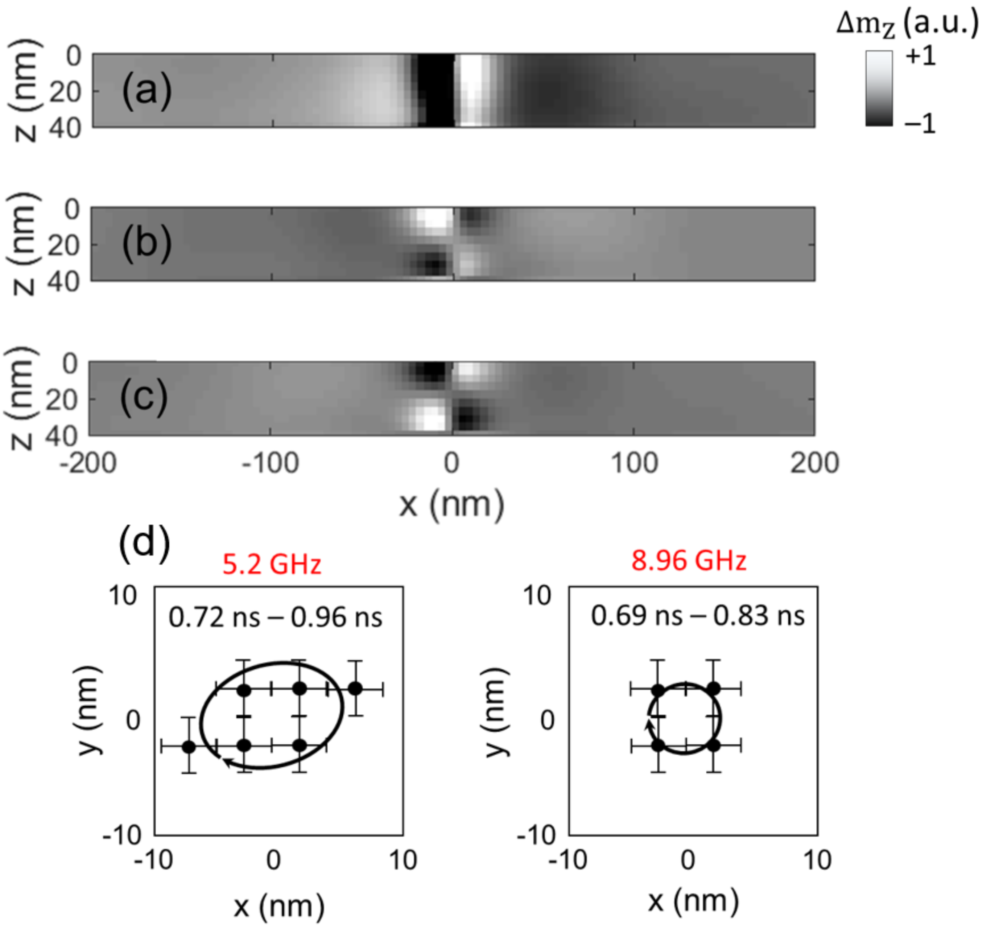

Figure 5.6. Simulated TR images of a cross section across the thickness of the disc passing through the core region. The contrast corresponds to the normalised out-of-plane component of the dynamic magnetization in response to

an in-plane excitation of 4.24 GHz (a), 8.96 GHz (b) and 10.24 GHz (c). The characteristic profile of the fundamental gyromode and that of the first higher order gyromode can be easily identified in (a), and (b) and (c), respectively. The vortex core equilibrium position is centered at x = 0 nm. The dynamic core profile of a x-z cross section obtained at 5.2 GHz is similar to that shown in (a) while the profile at 6.8 GHz is also similar to that shown in (b). (d) Vortex core positions at ~10 nm deep from the top surface relative to the equilibrium position from simulations (black dots) for a time interval approximately equal to a period of an excitation frequency of 5.2 GHz (left) and 8.96 GHz (right). Error bars length is equal to the cell-size of the model (~3.9 nm). Black arrows are only for guiding the eye showing an approximate trajectory of the simulated core motion in the x-y plane. The CW motion was observed in the animated simulation (not shown here).

To get insight of the relation between the curling wave and the short spiral spin waves observed in simulations, radial profiles of the simulated out-of-plane component of the magnetization dynamics at 6.8 GHz are shown in Fig. 5.7 as a function of time. The profiles in Fig. 5.7(a) and 5.7(b) were extracted from the middle layer of cells along the y- and x-direction respectively. The temporal evolution of the radial profiles reveals the onset of the spiral spin wave emission from the core, followed by the subsequent curling of the azimuthal mode. In the first 300 ps, the azimuthal mode remains spatially stationary and exhibits the expected maximum amplitude along the y-direction where the in-plane equilibrium magnetization is perpendicular to the RF field. The initial standing nature of the azimuthal mode is confirmed by the absence of its oscillation along the orthogonal x-direction at time delays < 300 ps, and beyond a radius of 300 nm from the core where the azimuthal mode is expected. This standing azimuthal mode exhibits almost constant amplitude across most of the disc radius in the y-direction where the equilibrium magnetization lies in-plane and orthogonal to the RF field. At the same time, and within 50 nm of the center of the disc, core dynamics with a phase difference of approximately $\pi/2$ with respect to the azimuthal mode can be seen. These core dynamics act as the source of the radially propagating short wavelength spiral spin wave, as discussed in the previous chapter.

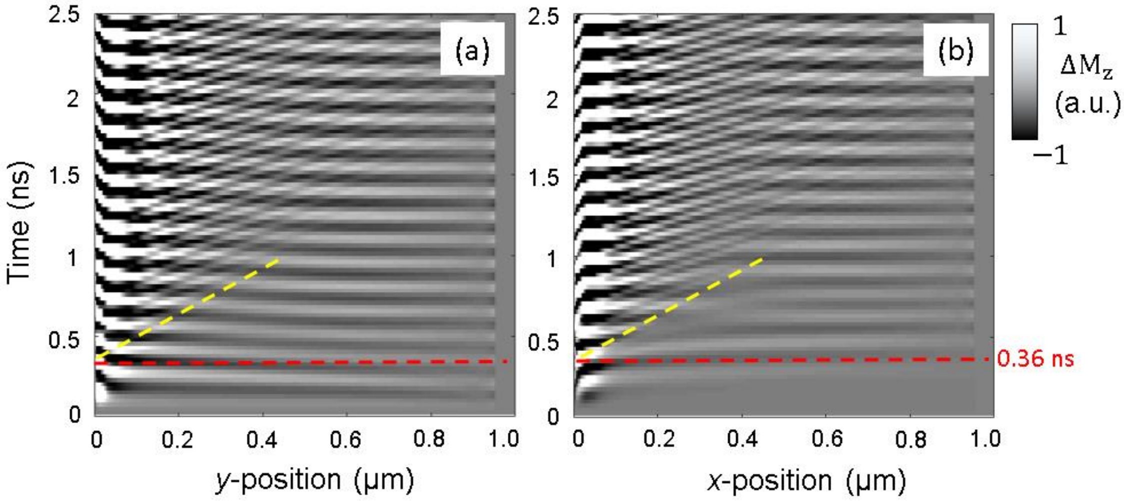

Figure 5.7. The temporal evolution of the magnetization dynamics is shown along the radial (a) y- and (b) x-directions from the centre of the disc to its edge. The contrast corresponds to the out-of-plane component of the magnetisation dynamics in response to the in-plane RF magnetic field with frequency of 6.8 GHz applied along the x-direction. The red dashed line highlights the time at which the curling makes one quarter of an azimuthal cycle and the yellow dashed line the wavefront of the propagating spiral spin wave emitted from the core.

Propagating spiral spin waves are coherently emitted from a gradient in the internal field close to the core, which perturbs the core from its equilibrium position (Wintz, et al., 2016). A correlation between the propagating spiral and the curling of the azimuthal mode is observed, as the curling starts when the wavefront of the emitted spiral spin wave starts ‘radiating’ into the in-plane circulating magnetisation region of the disc. This occurs at ~360 ps (dashed red line in Fig. 5.7(a) and 5.7(b)) and indicated by the onset of oscillations as a function of time along the x-direction with constant amplitude and phase over almost the entire radius of the disc. At larger time delay the gentle curvature of the white and black contrast indicates that, at a particular time, the contrast will slowly change from white to black as a function of spatial coordinate. This is most clearly seen in Fig. 5.7(a) from ~1.5 ns and between 0.2 to 0.6 um. This is observed as the ‘spiral’ nature of the curling azimuthal mode in the TR images and may be thought of as a time-delayed dragging of the azimuthal wavefront by the exchange interaction with the propagating spiral spin wave from the core. Micromagnetic simulations of a nominally identical disc, but with fixed core spins, strongly support this interpretation. When the core spins are fixed, the azimuthal mode remains as a standing mode in the absence of the core dynamics, that are revealed as the common activator of both the curling and the emission of short spiral spin waves (yellow dashed line in Fig. 5.7), setting a correlation between them.

The emission of a short wavelength spiral spin wave from the vortex core is predicted by micromagnetic simulations over the frequency range explored experimentally. The spiral spin wave propagates away from the core as time progresses and appears as a diagonal propagation wavefront in the space-time plots of Fig. 5.7 (see yellow dashed). Marked changes in the contrast as a function of x can be observed for x between 100 nm and the spiral spin wave propagating wavefront (dashed yellow line). Beyond this wavefront the contrast is almost constant, which demonstrates how the spiral spin wave, emitted from the core, and interacts with the azimuthal mode and modifies its spatial character. The wavelength of the emitted spiral spin wave at 6.8 GHz is ~100 nm (see Fig. 5.5(a)), corresponding to a k-vector of 0.06 rad nm^{-1}. Experimentally it is not possible to resolve spin waves with a half-wavelength shorter than the spatial resolution of 300 nm. Furthermore, as this spin wave propagates between 0.2 um and 0.5 um from the core, a phase mismatch occurs between the emitted spin wave and the curling motion of the azimuthal mode, see Fig. 5.7(b). This leads to an apparent reduction in the amplitude of the dynamics within ~300 nm of the core where the spiral spin waves exhibit their largest amplitude, but are averaged to a weak net signal by the limited spatial resolution of the laser spot. Consequently, these dynamics are not spatially resolved in the experiments, which can be confirmed by applying Gaussian smoothing with a full-width-half-maximum of 300 nm to the simulated images, Fig. 5.5(a).

The measured TR images of the curling azimuthal mode, and the understanding of its origin from micromagnetic simulations, allows us to unambiguously confirm that short wavelength spiral spin waves are emitted from the core, propagate radially outwards, and being correlated with the curling (statistical necessary condition but not sufficient for being the cause of the curling), they are present in the thick disc as long as core dynamics are activated, despite the insufficient spatial resolution for their direct observation. It should be noted that the onset of interaction discussed with reference to Fig. 5.7 can only be observed in the simulations since the TR images are acquired by integrating the polar Kerr signal at each pixel for at least 1 s while the dynamics in the disc are driven through more than 10^9 cycles in that time, which averages out transient dynamics. However, the observation of the subsequent steady state dynamics, i.e. the curling of the azimuthal mode, confirms that the spiral spin waves must have taken place.

5.3.2 High frequency regime

Previous studies have demonstrated that in addition to the core, other nanoscale regions of inhomogeneity of the equilibrium magnetic state can act as sources of high frequency spin waves (Davies, et al., 2017). In this work, a higher frequency excitation of 10.24 GHz, revealed magnetization dynamics that extend to the very edge of the disc. In contrast, at the lower frequencies already discussed, there is a diminution of the Kerr signal in the vicinity of the disc perimeter. This suggests that at the higher frequency of 10.24 GHz, the edge of the disc is also a source of spin waves, in addition to the core.

Micromagnetic simulations shown in Fig. 5.8 predict that at 10.24 GHz an antisymmetric radial mode is excited. The asymmetry is due to the opposite torque acting on the antiparallel in-plane equilibrium magnetization to either side of the core. The spatial character therefore appears as the superposition of a high order radial mode with 3 nodes (4 nodes including the core and the perimeter of the disc) and an azimuthal mode with nodal line perpendicular to the RF field and passing through the centre of the disc (Lupo, et al., 2015). This character is most clearly seen in Fig. 5.8(a) at 1.1712 ns and 1.22 ns when the spins of the core are fixed. When the spins of the core are free to precess, the radial-azimuthal mode appears to propagate from the edge of the disc (Davies, et al., 2017) towards the center exhibiting a spiral character that curls about the centre of the disc. The TR simulated images reveal an apparent reverse in chirality (chirality indexes +1 or −1) of the spiral pattern due to the asymmetry of the radial mode, e.g. compare simulated images in Fig. 5.8(b) at 1.1468 ns and 1.1712 ns.

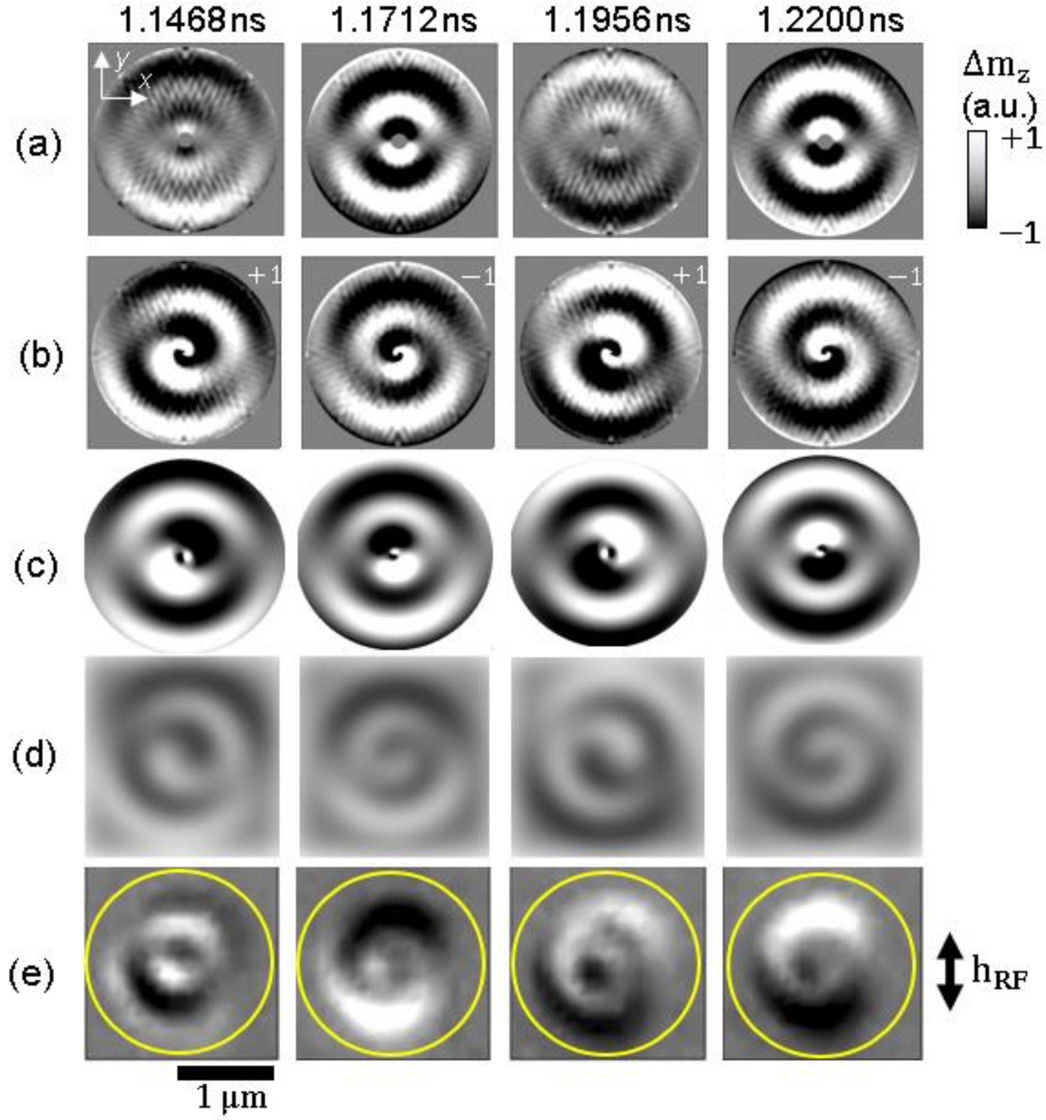

Figure 5.8. Simulated (a, b, and d) and measured (e) TR images corresponding to the out-of-plane component of the dynamic magnetization in response to an in-plane excitation of 10.24 GHz. In (a, b, and d) the m_z component was extracted from the second-from-the-top layer of simulated cells. The spins in the vicinity of the core are fixed in (a) and are free to precess in (b). The simulated effect of a spatial resolution of 300 nm is shown in (d). In (c) TR images calculated from a pseudo-analytical model from Eq.(5.1) and Eq.(5.2) and separated by $T/4$ ns.

In a similar mechanism that led to the observed curling characters at lower frequency, the excitation of the first order gyrotropic mode leads to an interaction with the high order radial mode. This TR spatial character is due to a time-delayed dragging of the radial mode wavefronts as the core dynamics, interpreted as an azimuthal-like wave, ‘curl’ about the core. The propagating spin wave interacts with subsequent wavefronts at increasing time delay, and with reduced coupling, far from the dynamical core. This interaction may be interpreted as an hybridisation since, for the aspect ratio of the given disc, the 1st order gyromode profile is found at lower frequencies than those predicted by theory (~ 10.69 GHz) (Ding, et al., 2014) and the interacting modes' frequencies are close enough (Jorzick, et al., 1999). The hybridized radial mode exhibits additional complexity whereby the tight spiral structure close to the core appears to separate to allow for the propagation of the next radial wavefront with opposite sign of m_{z}, but then merges with the subsequent wavefront with the same sign of m_{z}. The result is an apparent alternating chirality of the hybridized curling radial mode. Parallel emission of short spiral spin waves is also observed, but these are very attenuated compared to the radial spin waves, we believe due to an excitation frequency far from the local FMR condition near the core (Davies, et al., 2017).

Fig. 5.9 shows the simulated amplitude of the out-of-plane component of the dynamic magnetization as a function of time extracted from three positions: approximately 70 nm (in the core region), 140 nm (at the perimeter of the core) and 210 nm (within the in-plane magnetised region) from the vortex core. The core width is approximately 300 nm and was extracted from the simulated equilibrium vortex state (see inset of Fig. 5.9). The traces show that the core gyration is delayed by $\pi/4$ radians with respect to the radial wave at the perimeter of the vortex core. After ~0.175 ns, the radial wave interacts with the core and the phase delay is introduced (see black dashed line in Fig. 5.9).

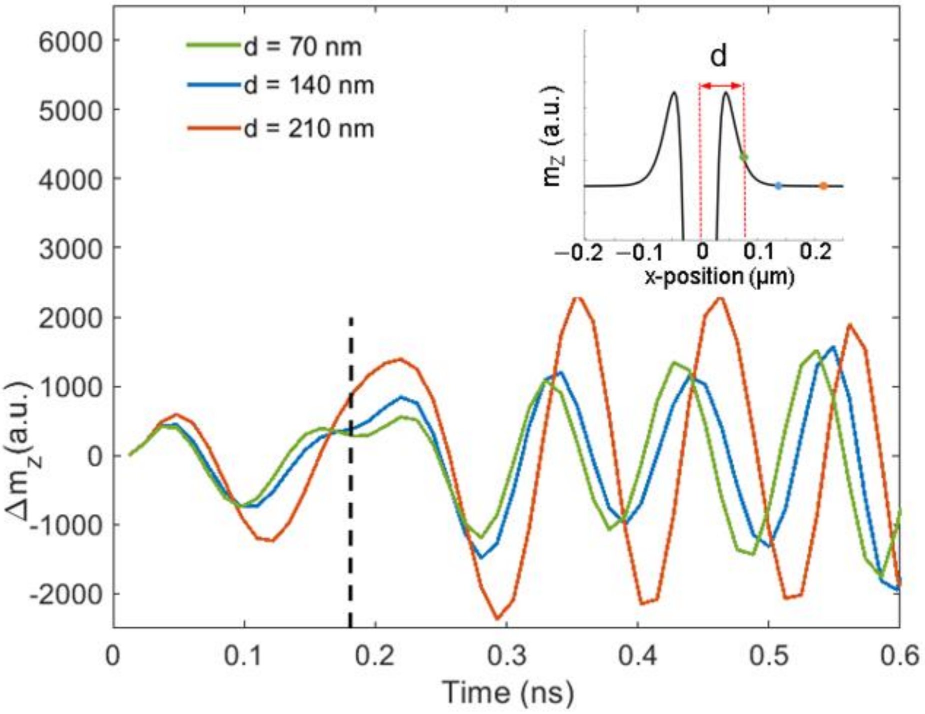

Figure 5.9. Simulated TR traces for the dynamic out-of-plane component of magnetization extracted from the selected positions. Inset shows the core profile at *t* = 0 ns and the positions where magnetization is recorded as a function of time. The black dashed line highlights the time when the interaction between the radial mode and core dynamics starts.

The dynamic out-of-plane component of magnetization of the radial spin wave (m_r) and of the core clockwise gyration ($m_{\Delta\mathrm{g}}$) at high frequencies can be naively described in polar coordinates,

$$m_\mathrm{r}(\rho,\theta,t) = m_0\sin(\theta)\sin\left(k_\rho\rho+\omega_0 t\right), \tag{5.1}$$

$$\begin{aligned} m_{\Delta\mathrm{g}}(\rho,\theta,t) = {} & m_0\sin(\theta-\omega_0 t-\varphi_0-\varphi_1)e^{-\rho/\delta_0} \\ & -2m_0\sin(\theta-\omega_0 t-\varphi_0)e^{-\rho/\delta_1}, \end{aligned} \tag{5.2}$$

where ρ and θ are the radial and azimuthal coordinates respectively, t is time, and ω_0 is the angular frequency of the microwave excitation. The phase difference assumed between the core and the curling radial mode is $\varphi_0=\pi/4$ (identified from Fig. 5.9) and k_ρ is the radial mode wavevector. The amplitude m_0 is assumed to be identical in both expressions while the core dynamics are modelled as the gyration of a 'double-dip' bipolar profile in m_z. The double dip profile has oppositely polarized regions that exist close to the moving vortex core with position described by δ_0 $(+m_z)$ and δ_1 $(-m_z)$, a phase difference φ_1 between them (Kammerer, et al., 2011) and with a radially decaying function since it is limited to the core region. The formation of such a double-dip may also explain the emission of a double-arm spiral spin wave as observed in Fig.5.5.

From micromagnetic simulations of the equilibrium vortex state, the core region is estimated to be approximately $|\rho| < \delta_0 \approx 0.15$ um (see inset in Fig. 5.9). The outermost part of the 'double-dip' is delayed $\varphi_1 = \pi/8$ with respect to the innermost part of the profile ($|\rho| < \delta_1 = 0.06$ um) to mimic a dragging effect around the core. Assuming superposition of both waves inside the core region ($|\rho| \ll \delta_0$), the final pattern exhibits a spiral-like profile that appears to change chirality with time at the centre. Fig. 5.8(c) shows results from this pseudo-analytical model at time frames separated by *T*/4 ns, where *T* is the period of the microwave excitation ($T = 1/f_o$). While this analytical model does not account for the 'dragging' effect due to hybridization, it does provide insight into the change in chirality of the spiral character of the hybridized mode (Fig. 5.8(b)) as it curls around the core due to the significant phase difference between the core dynamics and the radial mode.

Given a generic function in polar coordinates $f(\rho, \theta)$, the reverse of chirality can be described as the even symmetry $f(\theta) = f(-\theta)$. Through algebraic transformations and assuming that $|\rho| \ll \delta_0$ and φ_1 is negligible, it can be trivially shown that Eq.(5.2) satisfies the condition $m_{\Delta g}(\rho, \theta, t) = m_{\Delta g}(\rho, -\theta, t + T/4)$, only if $\varphi_0 = \pi/4$. Together with numerical results from Fig. 5.8, this reveals that the phase delay between the radial mode and the core dynamics reverses chirality every *T*/4 ns. Fig. 5.8(d) shows the simulated images of Fig. 5.8(b) after Gaussian smoothing has been applied to reproduce the 300 nm spatial resolution of the optical measurements. While the high resolution of the core dynamics in the simulated images is lost as a result of the smoothing the smoothed images yield an accurate reproduction of the measured images in Fig. 5.8(e).

The understanding gained from the analytical model and micromagnetic simulations allows us to conclude that the observed TR spatial character is a hybridization of a higher order gyrotropic mode of the core and a higher order radial spin wave in the disc. From the dispersion relation in (Ding, et al., 2014), and the size and material parameters of the disc in this work, the first-order gyropotropic mode has frequency 10.69 GHz, which lies within the line width of the observed mode at 10.24 GHz (Fig. 5.3(b)). Simulated profiles across the thickness and through the vortex core (Fig. 5.6(c)) show the characteristic first higher order gyrotropic mode profile for that excitation frequency and partial features of it for lower frequencies, exhibiting a single node at the centre of the disc thickness and maximum amplitude of precession close to the surfaces, but with opposite phase at the opposite surfaces at the same polar coordinate. The detailed micromagnetic and analytical analysis provides evidence to support our interpretation that the experimentally imaged mode at 10.24 GHz is a hybridization of a higher order vortex radial mode with the first order gyrotropic mode of the core.

5.4 Summary

We have used TRSKM to image magnetisation dynamics of the vortex state in a microscale disc that exhibit curling, spiral nature as a result of interactions between azimuthal and radial modes with gyrotropic modes of the core. Micromagnetic simulations predict the emission of short wavelength spiral spin waves from the core that cannot be observed in the measurements due to the limited spatial resolution. However, micromagnetic simulations with frozen core spins demonstrate that the curling of the azimuthal and radial modes cannot be initiated without the emission of the short wavelength spin waves from the core. This suggests that these two phenomena are time correlated and activated by the presence of a dynamical core. Therefore, the experimental observation of the curling nature in response to a microwave excitation is indirect evidence of the emission of spiral spin waves from the core with wavelength beyond the experimental resolution. The imaged curling modes can provide information about the core such as core polarity and vorticity and also, due to its correlation, about the beginning of the emission and ‘chirality’ of the emitted short wavelength spiral spin waves from the core.

At low frequencies, the clockwise and counter-clockwise curling of the azimuthal mode hybridized with the fundamental gyrotropic mode has been observed, while at high frequency both an azimuthal and a higher-order radial mode showed evidence of hybridization with the first-order gyrotropic mode of the core. At intermediate frequencies, other azimuthal-radial modes are apparently not hybridized but only superposed to the gyromodes due to their opposite senses of motion. Unlike the azimuthal modes, the higher-order radial mode also showed spin wave excitation at the edges of the disc. Micromagnetic simulations reveal that the spin waves can propagate towards the core to establish the standing radial mode and form part of the hybridised radial mode dynamics.

This work provides detailed insight into the hybridised nature of azimuthal and radial vortex modes with gyrotropic modes of the core, and its connection to short wavelength spiral spin wave emission from the core, which cannot be observed using a pulsed excitation alone, but by continuous excitation at microwave frequencies. These results will permit further understanding for the control of spin wave emission from the core of a vortex and their interaction with other modes of confined magnetic elements. Such understanding will be important for the design of magnetic nanotechnologies for high frequency logic and oscillator applications.

Chapter 6 Graded index confined modes in Bloch domain walls

6.1 Introduction

Graded index media for wave propagation have been widely studied especially in electromagnetics, in the field known as transformation optics (Kang, et al., 2008; Rinkevich, et al., 2015; Pendry, 2000). The development of structures ranging from nanometre size to centimetres, have proved interesting properties not shown in nature, leading to the application of novel graded-index (GRIN) lenses in an extremely wide range of frequencies, from microwaves to visible light.

In the field of magnonics, graded index magnetic media serve to similar purposes, taking advantage of the high anisotropic behaviour of spin waves (Davies, et al., 2015; Davies & Kruglyak, 2015). For example, tailoring the spin wave propagation in magnetic domains, allow the development of lenses for spin waves (Toedt, et al., 2016; Whitehead, et al., 2018; Whitehead, et al., 2019). Regarding uni-directional propagation in domain walls, previous studies have dealt mainly with redirection and steering the spin wave path (Hämäläinen, et al., 2018; Albisetti, et al., 2018), inducing phase changes (Bayer, et al., 2005; Wang & Wang, 2015) or non-reciprocal paths by means of non-linear effects (Garcia-Sanchez, et al., 2015).

However, anisotropic magnetic media can not only modify direction, intensity, or temporal frequency of the spin wave. Spatial frequency modulation or ‘spatial chirping’ is a technique widely used in telecommunication engineering and photonics, for example, to use in fibre-Bragg gratings or other chirped mirrors as filters, where wavenumber or equivalently, wavelength ($\lambda = 2\pi/\mathrm{k}$), spatially changes. Analysis of spatially chirped signals can be extended even to the processing of images where periodic features are visualised in perspective. The graded-index technique for EM waves could also have its equivalent for spin waves, and therefore, mathematical tools are required to control this feature. Using the non-uniform demagnetising field in a saturated YIG non-ellipsoidal rod, the pioneer work from Schlömann (Schlömann, 1964) for Backward Volume Spin waves and from Stancil (Stancil & Morgenthaler, 1983) for Surface Spin waves and further experimental results using spatially varying external fields (Smith, et al., 2008) confirmed the realization of this technique for spin waves. A change of wavelength has also been observed by using tapered saturated magnonic waveguides (Demidov, et al., 2011). In this chapter, we demonstrate a spatially dependent wavenumber (spatial dispersion) of confined modes in domain walls (and therefore, in non-saturated films), providing with an equation that allows to model their local wavenumber and propagation properties.

6.2 Spatially dependent wavenumber for confined spin waves: An analytical model

In the next section, we focus on controlling the spatial frequency of the confined modes along domain walls. As previously shown in Chapter 4, the confined mode in a domain wall will show a certain wavelength according to the Winter's magnons dispersion relation. Following on from chapter 4 and 5, the interest here is on how to predict and control spin wave propagation in a more complex scenario, which includes inhomogeneities in the domain walls and variable domain angles. These spatial changes in the internal field in the wall, can be a result of an irregular shape of the patch for example, external biasing fields or other local inhomogeneities. All this will lead to a spatial dispersive behaviour for the spin wave wavenumber propagating in the wall.

6.2.1 Description of the model

As a first step to a reliable model and similarly to what is done in (Bayer, et al., 2005), we search for an expression of a spatially dependent wavelength for a spin wave travelling in a domain wall, based on a Wentzel-Kramers-Brillouin (WKB) approximation (Zil, et al., 1995). Assuming a Neel domain wall along the x-direction, this implies that dynamic magnetization components at its centre can be expressed as: $\{m_\mathrm{x} = m_0 e^{i\omega t},\ m_\mathrm{y} = \mathrm{M_S},\ m_\mathrm{z} = m_0 e^{i\omega t} e^{ik(x)t}\}$. This description of static and dynamic magnetization is still approximately correct even for a Bloch wall of an arbitrary angle and suitable, at least, for the in-plane component of magnetization. If we assume an internal magnetic field perpendicular to the wall and only related to dipolar and exchange interactions, $\mathbf{H_i} = (\mathrm{H_d} + \mathrm{H_{ex}})\hat{\mathbf{y}}$, where the exchange field $\mathrm{H_{ex}} = \mathrm{H_{ex}}(x) = \frac{2\mathrm{A}}{\mu_0 \mathrm{M_s}} \nabla^2 \mathrm{m}$, and the magnitude of the demagnetizing field $\mathrm{H_d} = \mathrm{H_d}(x)$, the linearized Bloch equations of motion (Bayer, et al., 2005) yield:

$$\begin{cases} i\dfrac{\omega}{|\gamma|} m_\mathrm{z} = m_\mathrm{x}(\mathrm{H_d} + \mathrm{H_{ex}}) = m_\mathrm{x}\mathrm{H_d} + \dfrac{2A}{\mu_0 \mathrm{M_s}} \dfrac{\partial^2}{\partial x^2}(m_\mathrm{x}) \\ \dfrac{\omega}{|\gamma|} m_\mathrm{x} = i\, m_\mathrm{z}(\mathrm{H_d} + \mathrm{H_{ex}}) = i m_\mathrm{z}\mathrm{H_d} + i\dfrac{2A}{\mu_0 \mathrm{M_s}} \dfrac{\partial^2}{\partial x^2}(m_\mathrm{z})\,. \end{cases} \tag{6.2.1}$$

As in Ref. (Bayer, et al., 2005), we define a compact expression of magnetization including m_x and m_z as in $\varphi = m_x + \mathrm{i} m_z$, which reduces the system of equations to:

$$\frac{\omega}{|\gamma|}\varphi = \left(\mathrm{H_d} + \frac{2A}{\mu_0 \mathrm{M_s}} \frac{\partial^2}{\partial x^2}\right)\varphi\,. \tag{6.2.2}$$

Assuming $\varphi \sim \varphi_0 e^{ik(x)x}$, Eq. (6.2.2) can be extended to:

$$\frac{\omega}{|\gamma|} = \mathrm{H_d} + \frac{2A}{\mu_0 \mathrm{M_s}}\left(ixk'' + x^2(k')^2 + 2xk' - 2ik' + k^2\right). \tag{6.2.3}$$

As a first approach to solve this differential equation, we can naively assume that variations of spin wave wavelength along the domain wall will be smooth, since no sudden changes in the demagnetizing field along the longitudinal direction are expected in a straight domain wall configuration. Thus, satisfying the condition from Eq. (2.43) (see chapter 2, section 2.12). This implies that the first and second derivative with respect to *x* can be neglected: $k' \approx k'' \approx 0$, which eventually leads to,

$$\frac{\omega}{|\gamma|} = \mathrm{H_d} + \frac{2A}{\mu_0 M_s} k^2 \,. \tag{6.2.4}$$

Similarly to Schlömann's work (Schlömann, 1964), this gives an approximate description for a spatially dependent wavenumber, as a function of the module of the demagnetizing field in the wall,

$$k(x) = \sqrt{\frac{\mu_0 M_s}{2A|\gamma|}\omega - \frac{\mu_0 M_s}{2A}\mathrm{H_d}(x)} = \sqrt{k_0^2 - \frac{\mu_0 M_s}{2A}\mathrm{H_d}(x)}\,, \tag{6.2.5}$$

where $k_0 = \sqrt{\frac{\mu_0 M_s}{2A|\gamma|}\omega_0}$ is the wavenumber for a confined spin wave of frequency ω_0 when the transversal in-plane demagnetizing field is zero, or in other words, in a 180 degrees Bloch domain wall (Garcia-Sanchez, et al., 2015). Therefore, k_0 can be found from the dispersion relation of Winter's magnons given an excitation frequency ω_0.

Eq. (6.2.5) is a general expression for a spatially dependent wavenumber (wavelength) as a function of the transversal demagnetizing field in the domain wall. As shown in Chapter 2, finding a general demagnetizing field expression in a non-saturated ferromagnet of a non-ellipsoidal, arbitrary shape can be a very tough task. To address this, we first provide a magnetostatic first approach for such a scenario based on how in-plane magnetization transversally changes through the wall, this is, from one domain into the other. In other words, we aim to establish a link between the Eq. (6.2.5) and the angle (α) between domains.

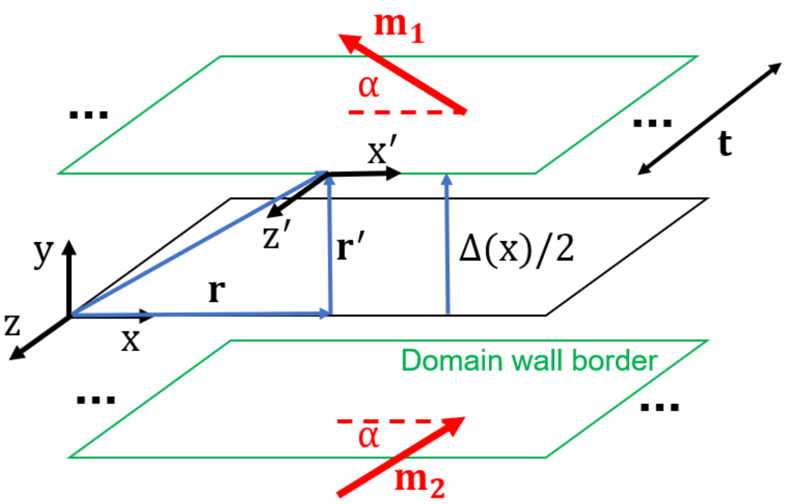

Figure 6.1 Schematic of a domain wall in terms of the domain magnetisation (red arrows) and their angle (α) with respect to the domain wall of initial width $\Delta(0) = \Delta_0$ in a sample of thickness t. The domain wall borders (green areas) and the domain wall centre (black area) are shown. The absolute and relative coordinate systems, chosen for the calculations, are also shown.

Let us assume the scenario from Fig. (6.1) for the domain wall of initially constant width $\Delta(x) = \Delta_0$ and angle α that magnetisation **m** makes with the domain wall. Solving the static Landau-Lifshitz-Gilbert equation yields the Walker's profiles across the domain wall (Stancil & Prabhakar, 2009). Below a critical angle α_c, a mixed Bloch-Neel behaviour of the wall is obtained, where the Neel component is always dominant if $t \sim \Delta_0$ (Torok, et al., 1965). A sin(α)-dependent coefficient is naively added to the magnetisation in-plane components transversal to the wall (m_y) to consistently model the angle dependence of a mixed wall. Following similar calculations to those shown in Ref. (Hubert & Schäfer, 1998), chapter 3.9 (a more detailed mathematical description of the model can be found in Appendix B.2), and considering that $M_s = |\boldsymbol{m}|$ must be satisfied for every y-position across the domain wall, the three components of magnetisation in the wall region can be regarded as,

$$\begin{cases} m_{\mathrm{x}} = M_s\sqrt{1-\sin^2(\alpha)\,\mathrm{sech}^2\left(\dfrac{y}{\Delta_0}\right)-\dfrac{\cos^2(\alpha)}{(1-\sin(\alpha))^2}\xi(\alpha,y)^2} \\ m_{\mathrm{y}} = M_s\sin(\alpha)\mathrm{sech}\,(\dfrac{y}{\Delta_0}) \\ m_{\mathrm{z}} = M_s\dfrac{\cos(\alpha)}{1-\sin(\alpha)}\xi(\alpha,y)\,, \end{cases} \tag{6.2.6}$$

where

$$\xi(\alpha,y) = \left(\frac{1+\sin(\alpha)\cosh\left(\cos(\alpha)\frac{y}{\Delta_0}\right)}{\sin(\alpha)+\cosh\left(\cos(\alpha)\frac{y}{\Delta_0}\right)} - \sin(\alpha)\right). \tag{6.2.7}$$

Therefore, the derivative of the dynamic magnetization transversal to the domain wall is,

$$\frac{\partial m_{\mathrm{y}}}{\partial y} \approx \frac{\partial m_{\mathrm{y,Neel}}}{\partial y} = \frac{-M_s\sin(\alpha)\tanh\left(\frac{y}{\Delta_0}\right)\mathrm{sech}\left(\frac{y}{\Delta_0}\right)}{\Delta_0}\,. \tag{6.2.8}$$

This expression implies a slow variation for the demagnetizing field at the central region of the domain wall ($y \to 0$). Following a magnetostatic approach and assuming $\frac{\partial m_x}{\partial x} = \frac{\partial m_z}{\partial z} = 0$, a bulk magnetic density charge can be found:

$$\rho_{\mathrm{m}}(\mathbf{r}') = \nabla\mathbf{M}(\mathbf{r}') = \frac{\partial m_x}{\partial x} + \frac{\partial m_y}{\partial y} + \frac{\partial m_z}{\partial z} = \frac{-\mathrm{M_s}\sin(\alpha)\tanh\left(\frac{y}{\Delta_0}\right)\mathrm{sech}\left(\frac{y}{\Delta_0}\right)}{\Delta_0}\,. \tag{6.2.9}$$

Notice that if $\alpha = \alpha(x)$, $\Delta_0 = \Delta_0(x)$ and a cross-tie wall were formed, the term $\frac{\partial m_x}{\partial x}$ is not zero, and therefore, it should count into the expression of bulk magnetic density charge,

$$\frac{\partial m_x}{\partial x} = \frac{{\mathrm{M_s}}^2}{2m_x}\left[2\sin\big(\alpha(x)\big)\cos\big(\alpha(x)\big)\,\mathrm{sech}^2\left(\frac{y}{\Delta_0(x)}\right)\frac{\partial\alpha(x)}{\partial x}\right. \tag{6.2.10}$$
$$+\,2\sin^2\big(\alpha(x)\big)\frac{y\dfrac{\partial\Delta_0(x)}{\partial x}\tanh\left(\dfrac{y}{\Delta_0(x)}\right)\mathrm{sech}^2\left(\dfrac{y}{\Delta_0(x)}\right)}{{\Delta_0}^2(x)}$$
$$\left.+\,\frac{\partial}{\partial x}\left(\frac{\cos^2\big(\alpha(x)\big)}{\Big(1-\sin\big(\alpha(x)\big)\Big)^2}\right)\xi^2(\alpha,y)+\frac{2\cos^2\big(\alpha(x)\big)}{\Big(1-\sin\big(\alpha(x)\big)\Big)^2}\frac{\partial\xi(\alpha,y)}{\partial x}\right].$$

However, for the sake of simplicity, in this case we consider slow variations of the domain angle and domain wall's width along the domain wall's length ($\partial\alpha/\partial x \approx \partial\Delta_0/\partial x \approx 0$) and no formation of a cross-tie profile. This implies that Eq. (6.2.10) is equal to 0. Also, a thick enough patch is considered, so at the central region of the patch, far enough from the surface pinning effects, variations of magnetization across the thickness can also be neglected $\left(\frac{\partial m_z}{\partial z} = 0\right)$ even considering the formation of a cross-tie wall (Metlov, 2001).

Under the above mentioned assumptions and due to the conservation of the transversal component in the domain wall border, surface magnetic charges can also be considered negligible: $\sigma_m(\mathbf{r}') = \mathrm{m_{y,2}} - \mathrm{m_{y,1}} = 0$. Choosing the right integration volume under reasonable assumptions (see Appendix B.3), we now use Eq. (2.14) and Eq. (2.15) to derive an expression of the demagnetizing field transversal to a domain wall of constant width Δ_0, which is,

$$\mathrm{H_d}(\alpha,y) = \frac{-\mathrm{t}\,\mathrm{M_s}\sin(\alpha)\tanh\left(\frac{y}{\Delta_0}\right)\mathrm{sech}\left(\frac{y}{\Delta_0}\right)}{4\pi y}\ . \tag{6.2.11}$$

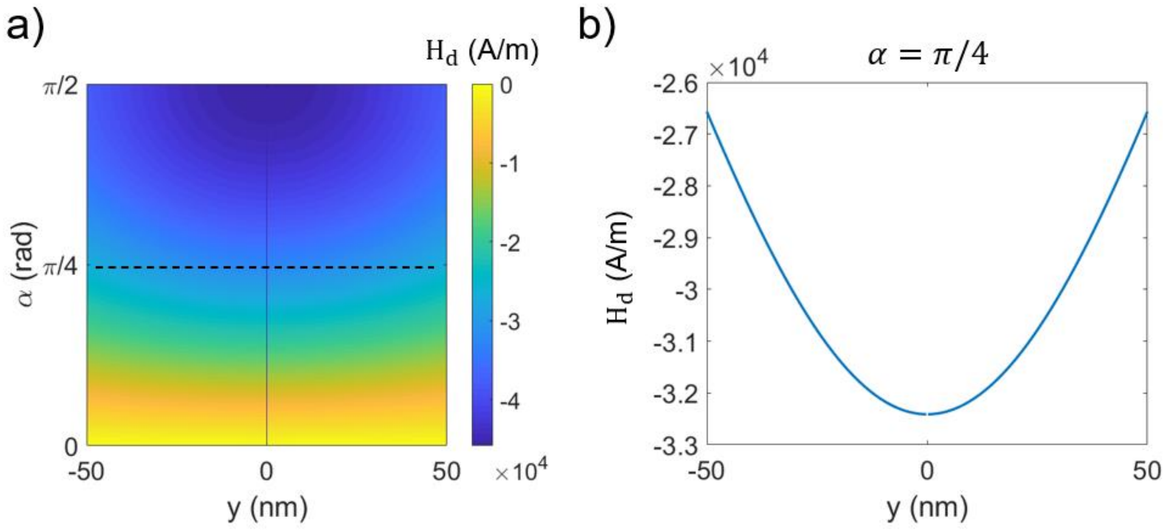

Figure 6.2 (a) Contour plot of Eq.(6.2.11) for a domain wall of width $\Delta_0 = 100$ nm and $M_S = 720\ \text{kA} \cdot \text{m}^{-1}$. (b) Horizontal cut at $\alpha = \pi/4$ (black dashed line in (a)) shows an indeterminate at y = 0, solved as a local maximum for the magnitude of the demagnetising field, at the centre of the domain wall.

Fig. 6.2(a) shows results of Eq. (6.2.11) for values of the angle of $0 < \alpha < {}^{\pi}/_{2}$ and for the width of ${}^{-\Delta_0}/_{2} < y < {}^{\Delta_0}/_{2}$. One must stress that, the main assumption for these results is that the demagnetising field is orientated, almost fully in-plane and perpendicular to the domain wall. This assumption is not far from reality, since it has been proved that, in intermediate domain walls (between 180°-Bloch and Neel wall), the Neel component is dominant. This behaviour is observed in arbitrary α-Bloch walls where $\alpha < 180°$. In fact, above a critical angle, the out-of-plane component of magnetisation vanishes, and the wall becomes essentially a Neel wall (Olson, et al., 1967). Not only that, argument is even more convincing for thicker samples, since the critical angle reduces when increasing thickness almost reaching zero when $t{\sim}\Delta_0$ (Torok, et al., 1965). Eq.(6.2.11) is consistent with these results, since it also reduces in magnitude as α reduces. The equation yields a numerical indeterminate at the centre of the wall although this is not a physically realisable solution. At the midwidth (taking the limit $y \to 0$) of the domain wall, where the confinement of the mode is strongest, and assuming $t{\sim}\Delta_0$ in a thick enough sample, Eq. (6.2.11) leads to (see Appendix B.3):

$$\mathrm{H_d}(\alpha) = \frac{-\mathrm{M_s}\sin(\alpha)}{4\pi} \quad , \tag{6.2.12}$$

which shows the maximum value of the transversal demagnetizing field in the wall, found at the centre. This equation allows to express the demagnetizing field perpendicular to the wall, in terms of the arbitrary angle α of magnetization between the magnetic domains and the wall. Moreover, it is also consistent with the assumption of a dominant Neel component in the domain wall profile.

It is worth to note that at an angle of $\alpha = \pi/2$, there is, by definition, no domain wall since magnetization between 'domains' is continuous. Therefore, the wall width is by definition zero width and Eq. (6.2.11) may no longer apply. The competition between dipolar and exchange energies means that this angle α will also determine the width of the domain wall. In other words, finding an expression for the demagnetising field as a function of the domain angles and the domain wall width is a self-consistent problem. The interrelation can be seen as in that the width of the wall Δ_0 decreases as α increases (see Appendix B.1).

In order to find a more complete and exact expression for $\mathrm{H_d}(\alpha)$, an additional demagnetising field should be derived from the respective magnetic potential, again derived from the magnetic density charges defined by $\frac{\partial m_x}{\partial x}$. Also, the constant term Δ_0 should be replaced by (see Appendix B.1 for calculations details): $\Delta(x) = \Delta_0 \frac{\pi-2\alpha}{\pi} \sqrt{\frac{\pi-2\alpha}{\cos(\alpha)(\sin(2\alpha)+\pi-2\alpha)}} \approx \Delta_0 \frac{\pi-2\alpha}{\pi}$. Note that, at the limit $\alpha = \pi/2$, the spatially dependent domain wall width is $\Delta = 0$. These other considerations add more complexity to the problem. However, as described before, the following reasonable assumptions can be made for sake of simplicity in our approximate model:

1. $\frac{y}{\Delta_0} \ll 1$: Since the maximum intensity of the confined mode will be at the centre of the domain wall ($y \to 0$), this quotient is very small regardless of the domain wall width if $\Delta_0 > 0$. Replacing this factor in the equation avoids the dependence on the wall width ($y/\Delta_0 \to y$).

2. $\Delta_0 = 0$ is not physically defined. Even in the case of small domain wall widths that may contradict the first assumption, a domain wall width of zero, as it has been explained before, is a mathematical consequence of the equation with no physical sense. In fact, by linking the domain wall width with the angle α, we can explicitly avoid the width parameter in the demagnetizing field expression. The fact that the demagnetising field increases when the domain wall width reduces, is indirectly modelled already by the $\sin(\alpha)$ factor for $\alpha < \pi/2$.

After all these considerations, we need to stress, once again, that finding an exact solution for a local demagnetising field is very often, a very complicated task for non-ellipsoidal shapes, even in saturation or quasi-saturation (Osborn, 1945; Berkov & Gorn, 2005). When not found numerically through micromagnetic simulations, approximate analytical approaches are usually taken under reasonable assumptions (see Chapter 2). For all this and realizing that Eq. (6.2.12) is a physically consistent model for the defined scenario, we consider it from now on, as a valid first approximation for the transversal demagnetising field along a domain wall of variable domain angle. Therefore, this expression can be combined with Eq. (6.2.5) to give a new one where the dependence is now with the variable angle between magnetic domains:

$$\mathrm{k}(\alpha) = \sqrt{\mathrm{k}_0^2 - \frac{\mu_0 \mathrm{M}_\mathrm{S}^2}{8\pi \mathrm{A}_{ex}} \sin(\alpha)}\,. \tag{6.2.13}$$

This equation relies on an initial $\mathbf{k}$ ($\mathrm{k}_0\hat{\boldsymbol{x}}$) which is found to be the wavenumber of a Winter's magnon for a frequency ω_0 through a 180° domain wall (i.e., when $\alpha = 0$). Regarding this, through the dispersion relation of Winter's magnons, a spatial index of refraction can be defined as $n(x, \mathrm{k}_0) = {}^{\mathrm{k}(x)}/_{\mathrm{k}_0}$,

$$n(x) = \sqrt{1 - \frac{|\gamma|}{\omega_0} \mathrm{H}_\mathrm{d}(x)}\,. \tag{6.2.14}$$

Equivalently, replacing the demagnetising field by Eq. (6.2.12) leads to:

$$n(\alpha) = \sqrt{1 - \frac{\omega_M}{4\pi\omega_0}\sin(\alpha)}\,. \tag{6.2.15}$$

This equation predicts the *change* in wavenumber (or wavelength) from a given k_0 along the domain wall. In other words, a different initial k_0 will give different values of local wavenumbers, but always varying in accordance to this model. Therefore, this applies as well to the index of refraction if we assume an index of unity for an arbitrary initial k_0. Fig.6.3(a) shows a contour plot of Eq. (6.2.14) as a function of $|\mathrm{H_d}|$ and $\omega_0 = 2\pi f$. It clearly shows, for the right combination for excitation frequency and a generic demagnetising field magnitude, the different values for the real part of the index of refraction (dark blue area shows an entirely imaginary index). Most importantly, it shows how at lower frequencies, the change in wavenumber is more sensitive to the transversal demagnetising field than at higher frequencies. Fig. 6.3(b) shows the same behaviour even when Eq. (6.2.12) is introduced into Eq. (6.2.14), which reflects now the dependence on the angle α.

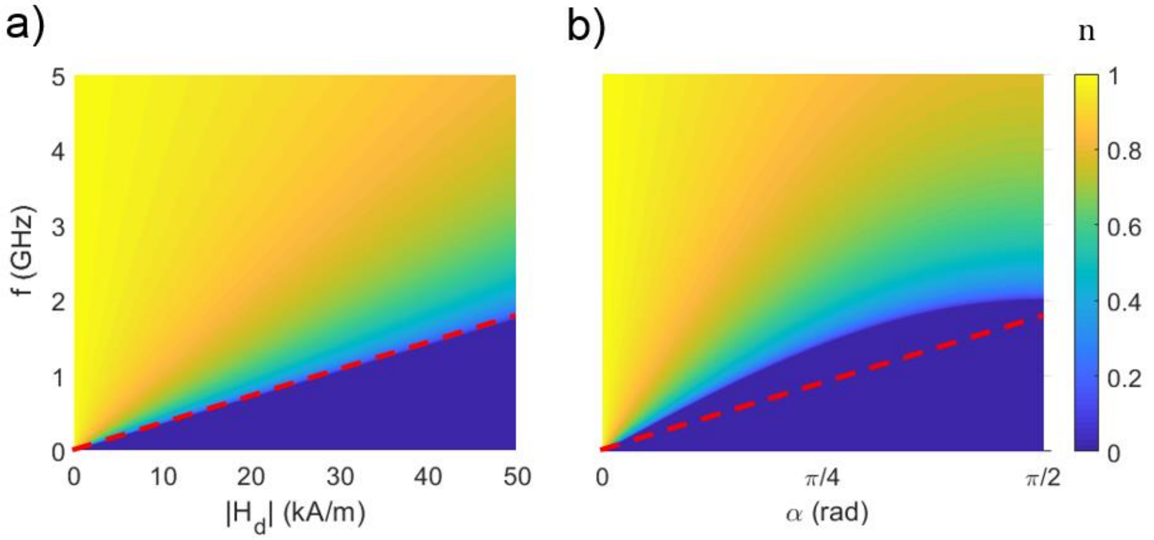

Figure 6.3 Contour plots showing the real part of (a) Eq. (6.2.14) and (b) Eq. (6.2.15) for $M_S = 720$ kA · m^{-1}, a gyromagnetic ratio $\gamma = 2.2 \times 10^5$ Hz(Am)$^{-1}$ and $A_{\mathrm{ex}} = 1.3 \times 10^{-11}$ Jm^{-1}. Red dashed line with slope γ shows the n = 0 condition in (a).

6.2.2 Numerical validation

A mathematical model is only as good as the assumptions. In order to validate our model, micromagnetic simulations on the magnetic structure shown in Fig.6.4 are performed and recorded for comparison with the analytical model. Since it is inevitable to start from an angle of approximately $\pi/4$ at the source (the vortex core), the shape of this structure has been chosen so because it allows to cover the widest range of values of α and therefore of n, see Fig.6.3. Therefore, for the shape of this patch, the demagnetizing field transversal to the wall is not constant along its length: The angle between magnetic moments at both sides of the wall changes from $\pi/4$ at the core region to 0 at the centre of the shape and to $\pi/4$ back again.

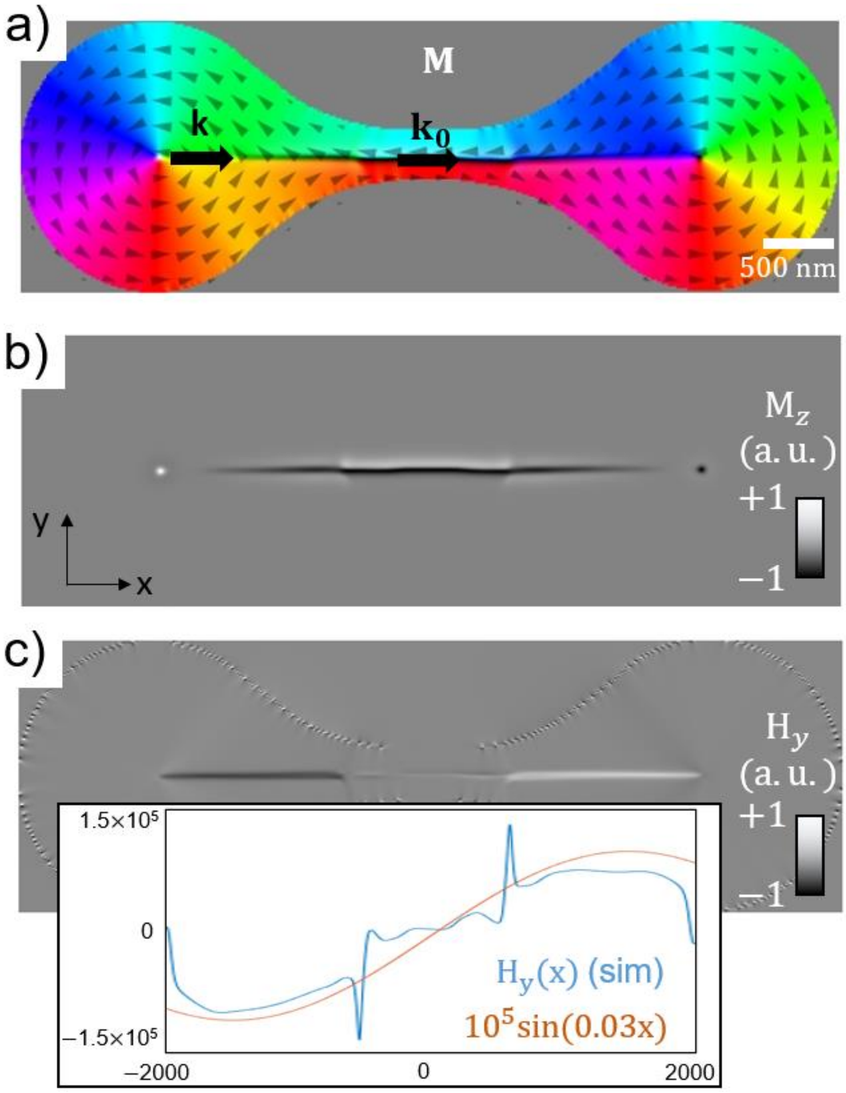

Figure 6.4 (a) Schematic of the proposed structure of 2000 nm × 6000 nm × 80 nm. A Bloch domain wall is induced and left to relax before running dynamic excitations.(b) Normalised out-of-plane component of magnetisation is shown, demonstrating the formation of a Bloch domain wall in the middle of the structure. (c) Normalised in-plane y-component of the demagnetising field, showing a reduction in magnitude in the centre of the structure. Inset in (c) shows the magnitude of the in-plane component of the demagnetising field, perpendicular to the wall, at the center of the wall obtained from micromagnetic simulations (blue curve) and a sinusoidal dependence with x-position between the two vortex core positions (x = 2000 nm and x = −2000 nm), in qualitative good agreement with the proposed model from Eq. (6.2.12). The spatial frequency of 0.03 (nm^{-1}) is obtained from the spatially-dependent angle α between magnetic moments in the shape (Fig. 6.5(a)).

Notice that, as reference, an index of refraction of unity midway between the vortex cores, in a 180° Bloch wall, is considered. The reference wavenumber k_0 is that of a Winter's magnon along a 180° Bloch wall. For a spin wave propagating from one of the core regions, reduction in α (or equivalently, reduction in the transversal demagnetizing field, see Fig.6.4(c)) implies an increase in the local wavenumber. From numerical results on this particular shape, small and smooth variations of the angle are considered far from the core regions, so the assumption $\alpha'(x) \approx \Delta_0'(x) \approx 0$ is still hold and therefore: $\frac{\partial m}{\partial y} \approx \frac{\partial m_y}{\partial y}$. Close to the core regions, the domain wall angle is large enough to assume the domain wall Neel component to be dominant (Olson, et al., 1967) and therefore, $\frac{\partial m}{\partial y} = \frac{\partial m_y}{\partial y}$ is also satisfied at the centre of the domain wall. In other words, the assumptions held in the previous section are still valid as well as the derived model for the demagnetising field transversal to the wall.

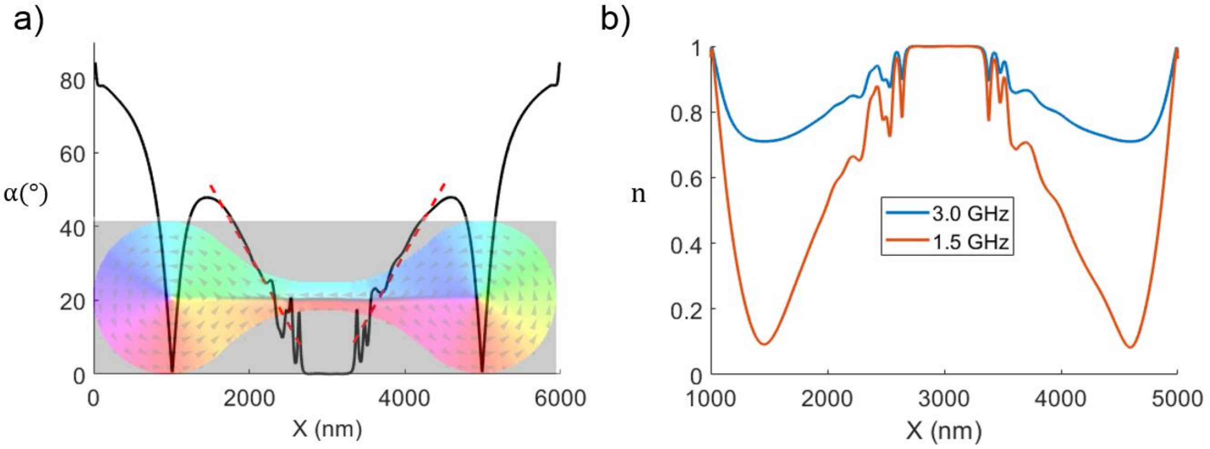

Figure 6.5 (a) Angle profile for the structure calculated as atan($\mathrm{m_y}/\mathrm{m_x}$) along a line, parallel to the wall, at 50 nm from the domain wall centre. Red dotted line is a linear fit to the values from the vortex core region to the centre of the structure. (b) Local index of refraction from Eq. (6.2.15) with the wavelength of a Winter's magnon in a 180° Bloch wall as reference for 3 GHz and 1.5 GHz.

Fig. 6.5(a) shows the spatial position profile of α parallel to the domain wall at 50 nm from the centre of the wall, calculated as $\tan^{-1}(\mathrm{m_y}/\mathrm{m_x})$, where the components of magnetisation are extracted from numerical simulations and magnetisation is assumed in-plane. The ripples close to the central region come from the numerically obtained equilibrium state of magnetic moments. More specifically, from those in the region where the curved contour is closer to the straight domain wall, which makes magnetization to not smoothly follow the contour neither the domain wall in a straight line but rather, in an apparent ‘zig-zagging’ path as a middle-ground solution. This alters the calculation of the angle α ($\alpha = \tan^{-1}(\mathrm{m_y}/\mathrm{m_x})$), introducing the rippling. Ideally, this should not be happening, and magnetisation should be laying completely in-plane and smoothly following the shape contour even close to the domain wall. Still, the shape of the structure allows to approximate the dependence of angle α with x by a fitting linear dependence $\alpha(\mathrm{x}) \approx -0.029\mathrm{x} + 87$, see red dotted line in Fig.6.5(a), making it closer to the ideal case. Including this linear fitting into the proposed model for the demagnetising field (Eq. 6.2.12) shows also good qualitative agreement with the values obtained from simulations (see inset in Fig. 6.4(c)). Quantitatively, result from simulation fits better to a sinusoidal function with a maximum value of 10^5Am^{-1}. While in the same order of magnitude, this value is about three times the maximum of the model from Eq. (6.2.12) for $\alpha = {}^{\pi}/_{4}$, ~$0.32 \cdot 10^5$Am^{-1} ($M_s \sin\left({}^{\pi}/_{4}\right)/4\pi$, for a saturation magnetisation of $7.2 \cdot 10^5$Am^{-1}, see Fig. 6.2). This can be explained by the neglection of other components of the magnetostatic potential in the model (which leads to a ‘weaker’ demagnetising field than in reality, due to fewer contributions), that should be accounted for a more accurate description. Fig.6.5(b) shows the analytical index of refraction from Eq. (6.2.15) with the obtained values of α as inputs for the excitation frequencies of 1.5 GHz and 3 GHz. This agrees with analytical results from Fig.6.3 which show that the wavevector can be reduced as much as approximately 0.7 times the reference wavevector k_0 (i.e., $n = 0.7$) when the spin wave approaches the core regions (at 900 nm from the vortex core) and α is approximately $\pi/4.8 \approx 0.205\pi$ radians (i.e., 37°, see Fig.6.5(a)).

To numerically check this change in wavelength, we run micromagnetic simulations with an excitation frequency of 1.5 GHz and 3 GHz so Winter’s magnons can be efficiently launched from the core region and travel along the domain wall. Numerical results for the spatially dependent wavelength (λ(x)) are obtained from the time-averaged spectrograms of the channelled spin wave profiles using a Hanning window of 128 FFT points and 100 overlapping points. Since the spatial wavelength is constantly changing along the domain wall length, a fixed width of the window will introduce a trade-off between spatial frequency resolution and position accuracy in the x-direction. A wider spatial window yields less position accuracy to the wavenumber and a very narrow window cannot properly resolve the spatial frequency at large wavelengths, leading to spatial frequency leakage per frequency bin. The chosen parameters of window width and overlapping points are obtained after an optimisation process considering several different outcomes. Another solution could be using a width-variable window as described in (Nisar, et al., 2016).

Fig.6.6(a) shows the wave profile of the propagating mode and the respective wavelengths found in the respective regions I and II. Fig.6.6(b) shows the index of refraction profiles for 1.5 GHz and 3 GHz (solid lines) obtained from Eq.(6.2.15), with the range of angles found from simulations as input, and numerical results (dots) for the spatial frequency in the x-direction, normalised to the value at 3000 nm (or in other words, the simulated spatial index of refraction). Numerical results confirm what the equation predicted: The change in wavenumber is more pronounced, and more sensitive to the transversal demagnetising field (or equivalently, to the domain angle α) when the frequency is smaller. Therefore, the covered graded-index profile is wider at lower frequencies. Also, as expected from the model, the values of the obtained index of refraction from simulations agrees with the predicted values from Eq. (6.2.15) with the specified angle $\alpha = 37°$ at the corresponding position ($\mathrm{x} = 1900\ \mathrm{nm}$) in the shape ($n \approx 0.7$ at 3 GHz and $n \approx 0.4$ at 1.5 GHz).

In conclusion, Eq. (6.2.12) or its generic form Eq. (6.2.5) is proposed as a valid model for finding the local wavenumber (and Eq. (6.2.15) for the local index of refraction) of a spin wave along domain walls under the influence of different demagnetising fields or shape contour effects. The model helps to predict how these effects modify the wavelength of a confined mode in a domain wall.

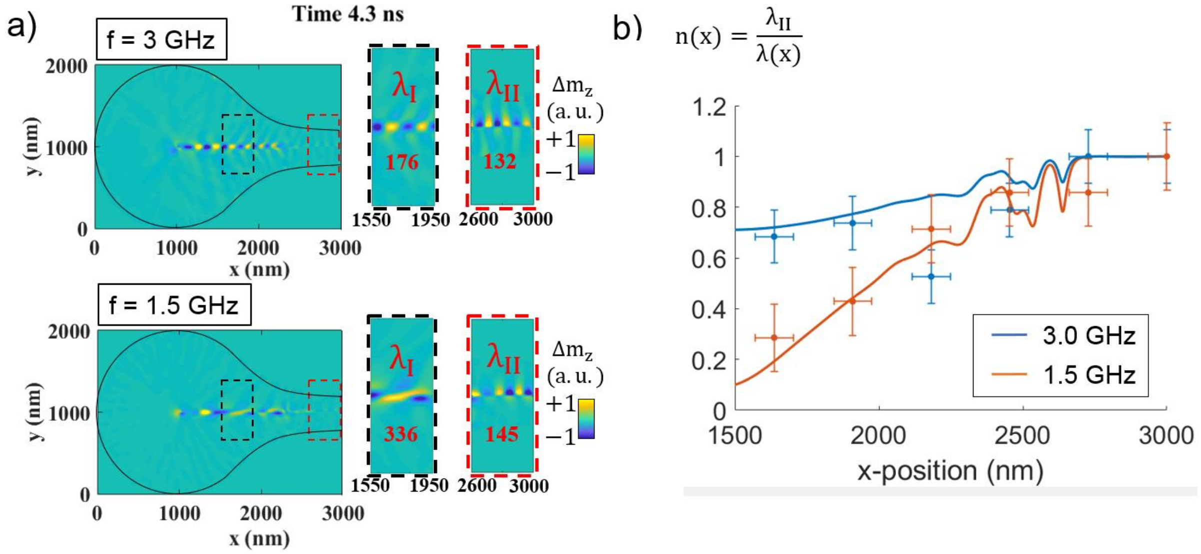

Figure 6.6 (a) Simulated wave profiles for an excitation frequency of 3 GHz and 1.5 GHz, with the chosen regions highlighted in dashed lines (they are not representing the Hanning window): Region I centred around x=1900 nm and region II centred around x=2800 nm, showing the spin wave profile in one half of the structure. The local wavelengths are indicated in the insets, along a length of 400 nm.(b) Results from the analytical model from Eq.(6.2.15) for 1.5 GHz and 3 GHz (solid lines) and the ratios λ_{II}/λ_{I} from micromagnetic simulations (dots) for each frequency and per Hanning window.

6.3 Zero and near zero index spin waves

An interesting property arises from the definition of this effective index of refraction. In Fig.6.3, a contour plot of Eq. (6.2.14) as a function of $|H_d|$ and ω_0 was shown. The set of values indicated by the red dashed line yields the ratio of demagnetizing field and frequency that leads to an effective zero index of refraction. Moreover, the same mathematics of Eq.(6.2.14) yield that any combination below that border line should give an *imaginary* index of refraction and by definition, *evanescent spin waves* in the domain wall. These interesting scenarios are analytically and numerically explored in more detail in the next sections.

6.3.1 Connection with the FMR main mode

It can be inferred from Eq.(6.2.14) that, in absence of a biasing field, there is an upper limit for the frequency at which an index of refraction of zero can be obtained. This maximum is reached when the demagnetizing field is maximal. In terms of the magnetic moments' orientation, this is when $\alpha = {}^{\pi}/_{2}$. However, once this condition is reached, the effective field can be enhanced by applying biasing fields parallel to the orientation of the magnetic moments which will now be always aligned. Notice that, in this situation, the definition of domain wall is meaningless. The scenario would imply the vanishing of the domain wall into a saturated region (i.e., magnetic domain). In that region, Eq.(6.2.14) is modified as in,

$$\mathrm{n}(x) = \sqrt{1 - \frac{|\gamma|}{\omega_0}\left(\frac{\mathrm{M_S}}{4\pi} + |\mathrm{H_{bias}}|\right)} = \sqrt{1 - \frac{|\gamma|}{\omega_0}\mathrm{H_i}}\ . \tag{6.2.16}$$

In other words, if the domain wall transitions into a uniformly magnetised region, applying a biasing field aligned with that domain would bring lower the index of refraction even further for a given frequency of excitation. Eq.(6.2.16) implies that an index of refraction of zero would be obtained at $\omega_0 = |\gamma|\mathrm{H_i}$, which is actually the *ferromagnetic resonance* main mode (i.e., all precessions in phase) of a saturated film for a given internal field $\mathrm{H_i}$. This result agrees with the wave perspective of a uniform FMR precession, which lays a wavenumber of $k = 0$ (infinite wavelength and $\mathrm{n} = 0$). Fig.6.7(b) shows that the zero-index condition can be extended to higher frequencies by applying external biasing fields.

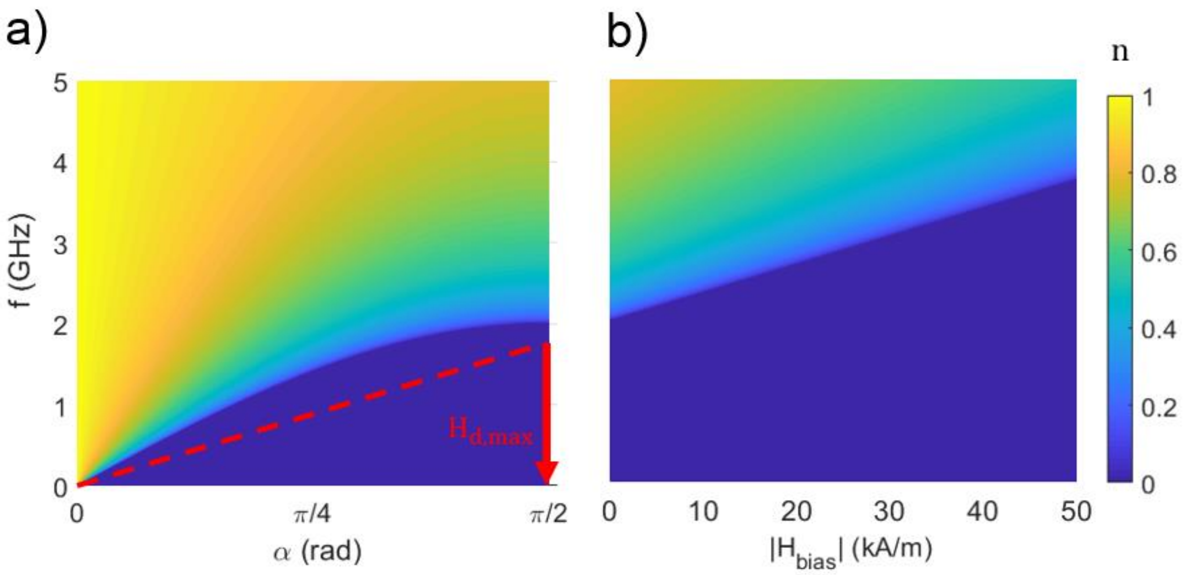

Figure 6.7 Contour plots showing the real part of Eq.(6.2.15) and Eq.(6.2.16) assuming M_s = 720 kA/m and a gyromagnetic ratio $\gamma = 2.2 \times 10^5$ Hz/Am. Red dashed line shows the slope γ/ω_0 which represents n = 0.

By applying biasing fields, 'zero index spin waves' are not limited to the maximum demagnetizing field transversal to the wall. A biasing field should be applied in the orientation of magnetization **M**, which accordingly fixes $\alpha = \pi/2$. This external field is considered negative as it is antiparallel to the demagnetizing field. In the next section, we numerically demonstrate this behaviour in a magnetic structure with a shape specifically designed for this test.

6.3.2 Numerical validation

Analogously to section 6.2.2, in order to confirm the behaviour of a spin wave propagating through a medium of *zero index of refraction*, we tailor a structure to show the required magnonic landscape, this is, a magnetic domain wall transitioning to a region where magnetization is uniform. The transition from one into the other must be smooth. Fig.6.8(a) shows a magnetic shape that satisfies these requirements showing a rectangular stripe infinitely long in y-direction and 500 microns wide in x-direction. In simulations, a periodicity along y-direction is imposed to model an effectively infinite stripe. Spin wave emission is launched from a magnetic vortex core in a teardrop shape (region I) and channelled along the domain wall towards a magnetized stripe (region II) perpendicular to the wall. The structure is symmetric, so a second teardrop shape is attached on the other side (region III). The shape works as the *inverse* of the shape shown in section 6.2.2, since the angle α increases from $^{\pi}/_{4}$ to $^{\pi}/_{2}$ at the centre of the structure and back to $^{\pi}/_{4}$ again. The biasing field, used for testing, is only applied in region II in the direction of magnetization.

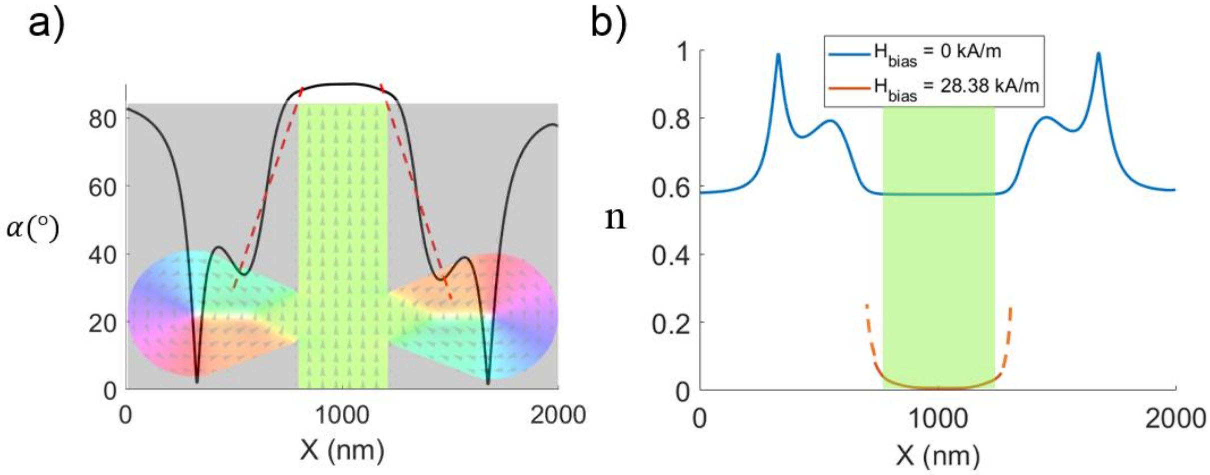

Figure 6.8 (a) Angle profile for the structure calculated as $\mathrm{atan}(m_y/m_x)$ along a parallel line at 50 nm from the domain wall centre. Red dotted line is a linear fit to the values from the vortex core region to the centre of the structure.The structure shape is shown overlapped. (b) Local index of refraction from the Eq.(6.2.16) with the wavelength of a confined mode in a 180° domain wall as reference for 3 GHz in absence of applied field (blue curve) and when a biasing field is applied (orange curve) only to the region in the middle (highlighted in green).

Fig.6.8(a) shows the profile of angle α and Eq. (6.2.15) applied to this variation in α. For an excitation signal of 3 GHz and using Permalloy© material, according to Eq. (6.2.16), a biasing field of about 28.38 kA/m (or equivalently, 35 mT in the air) in region II leads to an index of refraction as low as 0.0068 (with the wavelength of the confined mode close to the source as reference). In comparison to the obtained index at the same region in absence of biasing field (~0.6) this implies an approximately ×100 reduction in wavenumber. This extremely low index of refraction would imply a practically uniform oscillation of m_z (see Fig.6.8(b)), leading to an effective *near zero index of refraction* at the main mode FMR frequency. Fig. 6.9(a) shows time snapshots of the spin wave profile on a cut along the centre of the structure at 3 GHz. The time difference corresponds to practically half of the period of the excitation frequency (~0.16 ns). Results from simulations show uniform oscillation in the middle region of the structure (between 750 nm and 1250 nm). As in Section 6.2, a spectrogram of the confined spin wave is obtained to compare with the analytical results, with windows of width 128 cells and an overlapping of 100 cells, which leads to a total of 15 windows covering the entire x-range. Fig.6.9(b) shows the analytical results from Eq.(6.2.16) when no biasing field is applied to regions I and III (solid blue curve) and when a biasing field of 28.38 kA/m is applied in region II, (solid orange curve) along the length of the stripe. In simulations, we can apply different fields to selected regions in the model, therefore we only simulate a biasing field of the same magnitude in region II (750 nm < x < 1250 nm) to get the numerical results for the whole structure (black dots). The error bars in the y-axis are calculated as the half width amplitude of the main peak for each FFT from the windowed signals in the spectrogram. The error bars in the x-direction are calculated as half the width of the applied window. The good agreement between the analytical curves and the numerical results confirms that Eq.(6.2.16) can also be extended to model the local wavelength of confined spin waves, when external biasing fields are applied and reaching as low values as $k = 0$ (equivalently, $n = 0$).

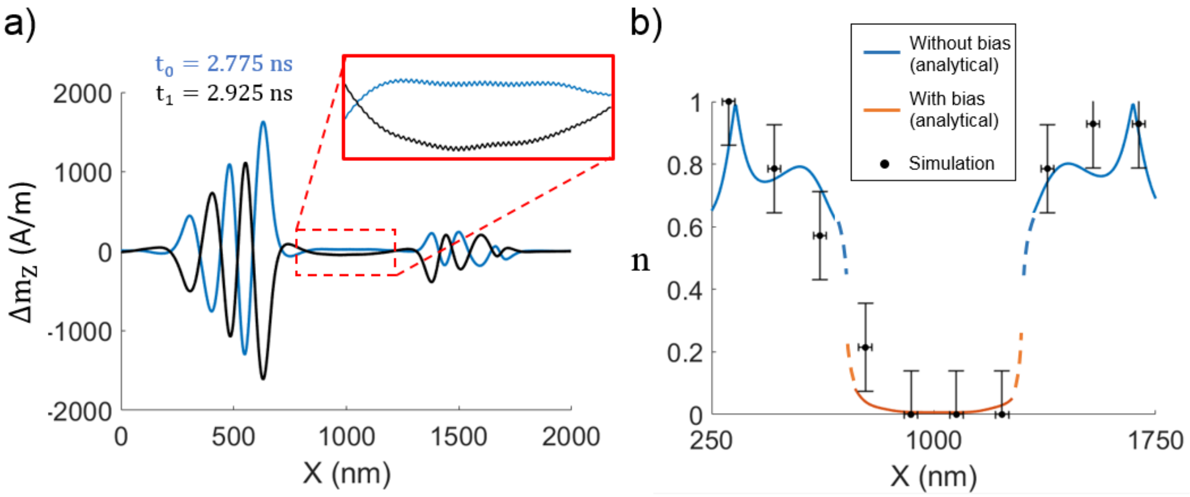

Figure 6.9 (a) Spin wave dynamic profile along the centre of the structure (y = 0) for two timestamps, separated by T/2 (blue and black curves). Inset shows a zoom in of the middle region, where a quasi-uniform oscillation can be observed. (b) Local index of refraction from Eq.(6.2.15) split between the two different regions, one without a biasing field applied (blue curve) and the middle region with a biasing field of 28.38 kA/m applied (orange curve).

Results from simulation (black dots) consider both scenarios in the structure at once and so they are overlapped. All results are shown for a excitation frequency of 3 GHz.

We must stress that uniform oscillation of Δm_{z} along the x-direction, for a given bias field, can also be observed at higher frequencies that, obviously, cannot correspond to the FMR main mode. How can this relate to the non-zero values of n obtained from Eq.(6.2.15)? The scenario where $\alpha = \frac{\pi}{2}$ is a particular one, since no domain wall is formed and therefore no effective channelling along the x-direction occur. It is worth noting that the proposed model applies to confined spin waves and therefore only to one-dimensional scenarios. The proposed model is a loose approximation to the scenario shown in Fig. 6.8 since it apparently works only in the x-direction. However, while the model effectively leads to a *zero wavenumber* along x-direction (and therefore, uniform oscillation in one dimension), this does not imply that the uniformly magnetised region cannot show spin wave modes with smaller wavelengths along other directions (such as the orthogonal y-direction). In fact, Fig.6.10(a) shows that at 5 GHz, a standing pattern of wavelength $\lambda_{\mathrm{II}} \sim 400$ nm can be observed along the vertical axis (y-direction) in the magnetised stripe, corresponding to a Magnetostatic Backward Volume Spin Wave (MSBVSW) configuration. Therefore, the structure seems to allow a partial conversion of a confined mode, propagating in the x-direction, into a BVSW mode in the y-direction, also implying a change in the direction of propagation.

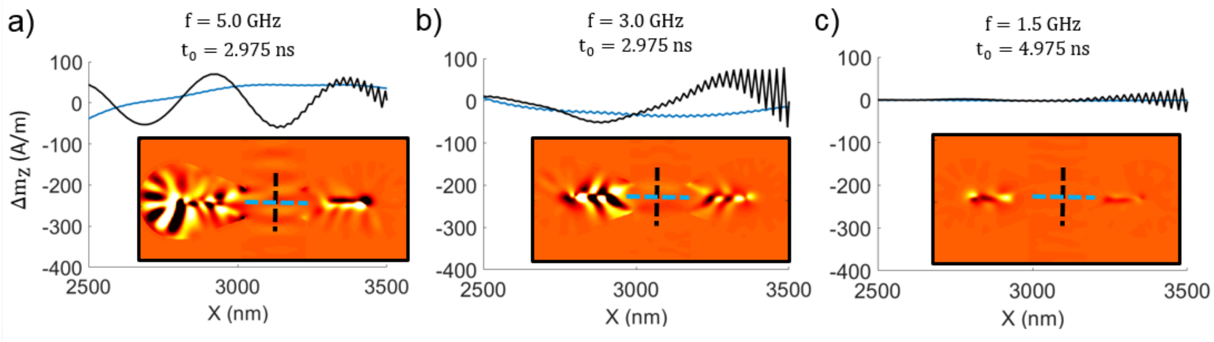

Figure 6.10 (a) Spin wave dynamic profile along the centre of the structure, x = 0 and y = 0 (blue and black curve, respectively) for two different timestamps at 5 GHz (a), at 3 GHz (b) and 1.5 GHz (c). Inset shows a zoom in of the middle region (not to scale) and where the x-cut (blue dashed line) and y-cut (black dashed line) are shown.

The two attached 'teardrop' shapes can alter the internal field and the eigenmodes of the rectangular magnetized region. In fact, a stronger confinement of the mode can be observed close to the sharp indentations of the shape. At 5 GHz, the channelled spin wave in the domain wall seems to split and follows an 'easy path' towards the indentations, accompanying the excitation of an azimuthal mode in the 'teardrop' shape. That confinement can be observed as a more intense signal at both sides of the indentation, in the teardrop shape and in the magnetised stripe (see insets in Fig. 6.10(a)). Previous work on other indented shapes such as crosses, show a mixed behaviour of Damon-Eshbach and Backward Volume modes at higher frequencies, showing even fully azimuthal distribution (in this case, constant phase along x-direction), instead of the expected Damon-Eshbach configuration (Machida, et al., 2005; Adhikari, et al., 2018). As a matter of fact, the proposed structure can be regarded as a cross-like structure with tapered lateral arms where magnetization diverges from the straight arms of the cross due to the formation of the vortex cores. All this supports the idea that the sharp joints in the structure and the lateral confinement may also alter the natural spin wave modes of the stripe.

Nevertheless, all this would suggest a spin wave mode conversion between the confined spin wave mode and a MSBVSW mode in the magnetised region of the proposed structure. Considering this, for the case of $\alpha = \frac{\pi}{2}$, Eq. (6.2.16) can be physically interpreted as well as a 'spin wave matching' equation between different magnonic landscapes, i.e. confined spin waves in a domain wall and MSBVSW in a magnetised film. From this model, a zero index would still imply the excitation of the FMR main mode or at least, modes with no k_{x}, and therefore a ‘conversion’ of the channelled spin wave in the domain wall into magnetostatic BVSW modes in a uniformly magnetised region.

Below the ‘$n = 0$’ line (dark blue region in Fig.6.7(b)), the model predicts an *imaginary* index of refraction which would lead to, conceptually speaking, *evanescent spin waves*. Schlömann mentions the possibility of obtaining an imaginary wavenumber for spin waves ($k^2 < 0$) in Ref. (Schlömann, 1964) but this scenario is no longer explored in his work. In the model proposed here, we observe this is more of a mathematical consequence with no real physical meaning and therefore it is no longer explored in this chapter. However, this could physically relate to dipolar interactions between opposite sides of the magnetised stripe region. Fig.6.10(c) shows that at 1.5 GHz no oscillations in the middle are observed and no BVSW modes can be excited but large amplitude oscillations still occur in the second teardrop shape. We believe that at these low frequencies, a dipolar interaction between opposite sides of the magnetised stripe dominates due to the long wavelength. In conclusion, we consider the mathematical model physically consistent and valid to apply in different magnonic scenarios, as it has been proved in this chapter.

6.4 Summary

The main result of this Chapter is the proposed mathematical model for an effective spatial frequency dependence of confined spin waves in Bloch domain walls. The equation of the model is derived from the fundamental Bloch equations of motion and applied to a variety of magnonic scenarios. The model can be applied to straight domain walls of variable domain angles, which can be useful as a first approximation to the study of more complex scenarios such as spin waves in confined structures of arbitrary shapes showing magnetic domains. Reciprocally, the connection between the shape of the nanostructure and the induced demagnetising field transversal to the wall, showed by the model, allows to a proper design of the shape for a particularly desired channelled spin wave profile. The model also leads to conditions that have physical meaning such as the FMR main mode, and therefore further extending the applicability of the model to not localised modes in domain walls.

In summary, an equation for a spatial-dependent wavenumber for spin waves is proposed, performing as a good model for their propagating behaviour in domain walls. This result may help in the development of more complex models for spin wave propagation in non-saturated nanostructures, channelled along domain walls or propagating into magnetic domains.

Chapter 7 A uni-directional tuneable spin wave emitter based on a teardrop shape

7.1 Introduction

As it has been shown in the previous chapters, inhomogeneities such as vortex cores can act as spin waves emitters. These emitted waves can also be channelled along domain walls at low frequencies in the order of 0.2 GHz (Sluka, et al., 2019). Once the spin wave is emitted, an adequate control of its propagation is key for the developing of circuits that conduct the spin wave through these magnonic channels. Local excitation of spin waves and their spatial confinement has been widely studied in terms of local ferromagnetic resonances due to an inhomogeneous demagnetising field (Mushenok, et al., 2017; Davies, et al., 2017), more specifically confinement along the edges of magnetic triangular patches (Lara, et al., 2013; Lara, et al., 2017), along domain walls and by so-called Winter magnons (Winter, 1961) or other anisotropic ‘spin textures’ (Wang, et al., 2018; Sluka, et al., 2019). Domain walls act as natural channels for spin waves due to their energy well (Whitehead, et al., 2017), while Winter magnons are very useful for efficient spin wave channelling in a wide range of frequencies. The new degree of control has led to a new sub-field of magnetism, which has been termed ‘Topological Magnonics’ (Wang, et al., 2018).

Regarding control of spin wave propagation, localizing spin wave energy or confinement of the wave is a key point. Therefore, the interest is on spin waves emission along a single direction of propagation, showing a maximum confinement and directivity, ideally leading to a point-to-point spin wave transmission. Previous studies have shown the possibility of steering spin waves by using external biasing fields in Y-shaped structures which, while in a saturated state, allow propagation along different arms of the structure depending on magnetization orientation (Vogt, et al., 2014). This obviously requires external biasing and attached secondary structures to provide such a localized field, which makes designs/devices rather sub-optimal.

In this work we explore a simple way of achieving uni-directional propagation, based on *the simplest configuration possible*, consisting on a *single vortex core* and a *single domain wall* pinned at the shape's single corner. The required contour of the patch resembles a 'teardrop' or 'raindrop' shape. This is a simpler configuration than other implementations found in literature, mostly based on flux closure Landau patterns in square elements (Wagner, et al., 2016) or ellipses (Sluka, et al., 2019), or more complex nanodisc-film composite bi-layer structures (Chang, et al., 2020).

In absence of external biasing fields, the *single core and single domain wall* magnetic configuration is obtained in the 'teardrop' shape through the influence of shape anisotropy only and so, external fields are not required to retain such magnetic configuration. While a biasing field is unnecessary, its introduction leads to a different and tuneable behaviour of these confined modes. This structure can be regarded as the building block of simpler and more compact highly reconfigurable spin wave devices. The anisotropic behaviour of the teardrop shape is analytically and numerically studied, and experimentally proved by VNA-FMR measurements.

7.2 Simulation and experimental details

7.2.1 Methods

As in Chapter 4 and 5, in order to study the spin wave dynamics in the teardrop shape, different pulse configurations have been used for numerical results: A sinc-type pulse for studying the response in a wide range of frequencies and a sine pulse to get the time response at a particular frequency of excitation. The magnetic patch is initially uniformly saturated and left to relax without external influence until the equilibrium state is achieved.

To further characterize the channelled spin waves that we are looking for, an approximated simplified expression for the VNA-FMR plot from the dispersion relation of

Winter's magnons along a Bloch domain wall is also obtained. From micromagnetic simulations, Fig. 7.1 (a) shows the vortex core equilibrium position displacement to biasing field ratios for the most significant directions (towards the vertex and towards the curved edge, blue and red solid dots, respectively), showing an approximately linear behaviour with the magnitude of the bias field (fitting solid lines) (see Fig. 7.1(a)). The results agree with previous work (Yakata, et al., 2013), where the ratio is found to be more constant (a more linear displacement) when the core approaches a triangular vertex than the edge of a circular disc (where the displacement is non-linear and a linear fit yields a lower slope), due to the inhomogeneous demagnetising field in the shape. The 'teardrop' shape can be regarded as a combination of both scenarios. In a 'teardrop' shape, displacing the vortex core towards (or away from) the vertex by applying a biasing external field ($\mathrm{B_{ext}}$) perpendicular to the wall, implies a shortening (or elongation) of the domain wall length in initial equilibrium (l_0). We naively model this new domain wall length as: $l_{\mathrm{dw}} = l_0 + r\mathrm{B_{ext}}$. Similarly, if the field is applied parallel to the wall, the new length of the domain wall can be expressed as: $l_{\mathrm{dw}} = \sqrt{{l_0}^2 + (r\mathrm{B_{ext}})^2}$. Fig. 7.1 (b) and (c) show numerical results on how the domain wall moves according to these two expressions.

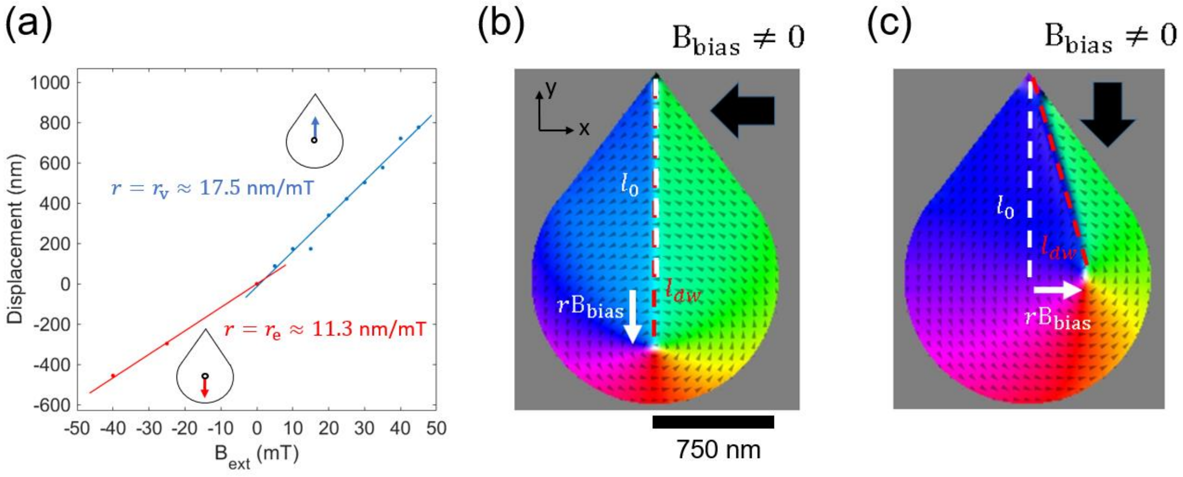

Figure 7.1 (a) Vortex core displacement versus biasing field magnitude for two opposite directions, towards the vertex (blue dots and blue fitting line) and towards the curved edge (red solid dots and red fitting line). Insets show an schematic of the core displacement and the obtained values for the slopes (ratios r_{v} and r_{e}) from a linear fitting to both datasets. Domain wall length (red dashed line) when a biasing field is applied perpendicular (b) and perpendicular (c) to the wall. White arrow shows the core displacement as a result of the biasing field. Colour scale

is the angle of in-plane magnetisation. White dashed line shows the domain wall length in the equilibrium state (l_0).

Replacing the respective final domain wall lengths (l_{dw}) into the dispersion relation of discretized exchange dominated Winter's magnons, and assuming a strong pinning of spins at the vortex core and at the vertex ($k = {}^{n\pi}/_{l_{\mathrm{dw}}}$), we obtain:

$$f_n = f_{\mathrm{M}}\lambda_{\mathrm{ex}}\left(\frac{n\pi}{l_0 + r\mathrm{B}_{\mathrm{ext}}}\right)^2, \tag{7.1}$$

$$f_n = f_{\mathrm{M}}\lambda_{\mathrm{ex}}\left(\frac{n\pi}{\sqrt{{l_0}^2 + (r\mathrm{B}_{\mathrm{ext}})^2}}\right)^2, \tag{7.2}$$

where $f_{\mathrm{M}} = \frac{\gamma}{2\pi}\mu_0 M_{\mathrm{S}}$. Eq. (7.1) and Eq. (7.2) are the dispersion relations of the mode under a perpendicular ($r = -r_{\mathrm{v}}$ when a positive sense and $r = r_{\mathrm{e}}$ when a negative sense, given the configuration in Fig.7.1) and parallel bias, respectively. These equations can be regarded as an approximate analytical model for the field dependent FMR plots for these modes, since $\mathrm{f}_n(\mathrm{B}_{\mathrm{ext}})$ (see Fig.7.2). These equations may be used as the base of a simple analytical model for Winter's Magnons in a Bloch wall and therefore easier to be implemented by computational methods. A more complex model was also proposed and used in Ref. (Aliev, et al., 2011) for Winter's Magnons in Neel walls under the assumption of thin circular discs, but not accounting for the influence of external biasing fields, and in principle not applicable to our thicker non-circular patches.

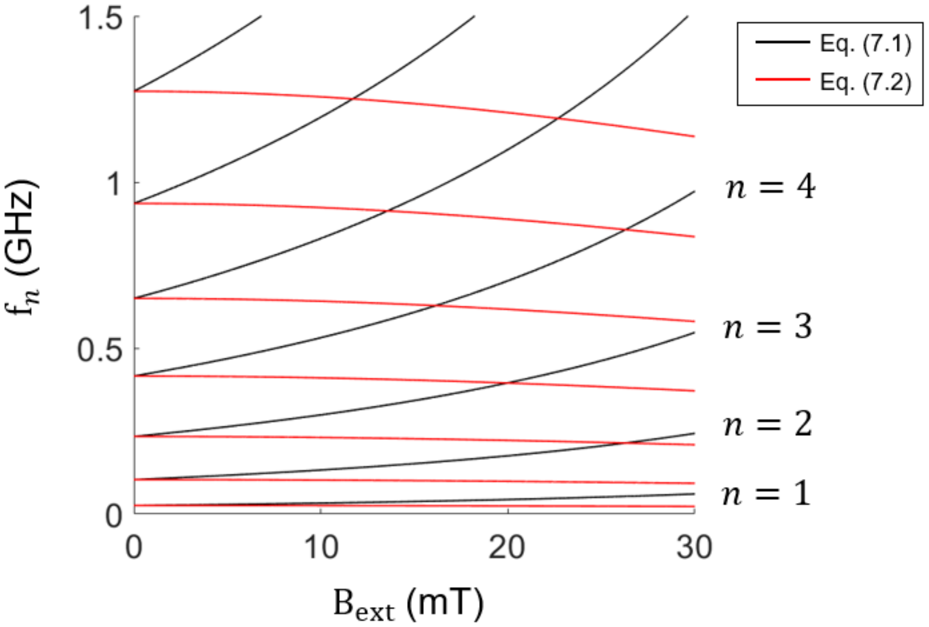

Figure 7.2 Basic modelling of the VNA-FMR plots for Winter's Magnons of different mode orders n using Eq. (7.1), representing a biasing field perpendicular to the wall and $r = -r_v$ (black curves) and Eq.(7.2), a field parallel to the wall (red curves). Pumping field is applied perpendicular to the wall in both cases. Results relate to higher order confined modes of nodal numbers from $n = 1$ to 7, in absence of additional phenomenological anisotropies.

The experimental setup for FMR measurements is the same as described in Chapter 3. However, before running measurements, some additional steps must be followed to match with the micromagnetic simulations, as indicated in the next section.

7.2.2 Additional considerations on the Teardrop shape

Fig. 7.3 shows the equilibrium state of a 750 nm wide (radius of the circumscribed circle), 2 μm high (from the base to the vertex) and 80 nm thick patch in the shape of a teardrop, with a corner angle of 60 degrees, after applying in-plane saturation along the x-direction and then being removed for relaxation of magnetisation. Note that, from numerical results, the obtained equilibrium state is not the single vortex state connected by a domain wall to the vertex of the shape. Instead, the domain wall ends at another vortex core close to the vertex. A 'Double Magnetic Vortex' (DMV) metastable state has been observed in thin enough circular patches (Vaz, et al., 2005; Aliev, et al., 2011). From Ref. (Vaz, et al., 2005), this metastable state should not be expected in circular patches as thick (80 nm) as the presented teardrop patch. However, introducing the sharp corner of the teardrop allows us to obtain an asymmetric DMV metastable state for thicker samples by breaking the top-bottom symmetry of the shape. This way, the DMV as equilibrium state seems to be allowed because it partially recovers the inversion symmetry (about a central point in the cyan domain, see Fig. 7.3) while minimising stray field. A similar behaviour was observed in elliptical shapes applying biasing fields along their short axes (Vavassori, et al., 2004).

However, to allow the Winter's magnon to reach the top vertex without impediments. a single vortex state and a single domain wall connecting with the vertex are required. To obtain a single centred magnetic vortex core state (SMV) without saturating the sample, the topmost vortex core must be 'expelled' by self-annihilation by applying a biasing field transversal to the wall. As a first step in numerical simulations, a biasing field of 40 mT, strong enough to expel the top vortex core and less than saturation magnetization to retain the centred vortex core, is applied. After the vortex core at the corner is self-annihilated, the external field is removed, and the shape is again left to reach a new relaxed state. This process is performed as first step and the obtained equilibrium state is saved as the initial magnetic configuration, before any dynamic excitation, see Fig.7.3. The same process is performed in experiments before taking measurements.

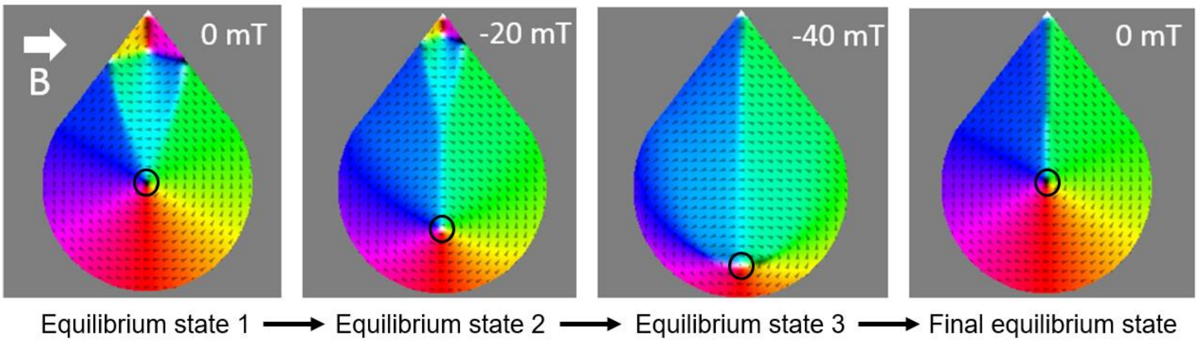

Equilibrium state 1 ⟶ Equilibrium state 2 ⟶ Equilibrium state 3 ⟶ Final equilibrium state

Figure 7.3 Simulated sequence (from left to right) of equilibrium states obtained after applying a smoothly varying sequence of biasing fields to a Double Vortex State in the teardrop shaped element. White arrow and values are the applied external biasing field before leaving the shape to relax in order to get a single vortex core, and single domain wall pinned at the vertex, as the desired final equilibrium state. Black solid circle illustrates where the vortex core is for each step.

It is worth noting that Eq. (7.1) and Eq. (7.2) are obtained under the assumption that the dispersion characteristics of the domain wall remain constant in its length and unaltered under application of transversal biasing fields of different magnitudes. All the analytical results shown in this Chapter are, unless indicated otherwise, obtained under this assumption as a first approach to the problem. In practice, however, we acknowledge there will be changes in the magnonic landscape in the domain wall when a biasing field is applied due to the variation of the internal field. For instance, Fig.7.4 shows how the domain wall changes type when elongated after applying a biasing field perpendicular to the wall. This is related to the difference between dipolar fields close to the core and close to the vertex, due to the influence of the straight edges (Yakata, et al., 2013). In a more realistic scenario, all these effects should be accounted for in Eq. (7.1) and Eq. (7.2), although for sake of simplicity this is not included in these equations. The implications from considering some of these effects were explored in more detail in the previous Chapter (*'Chapter 6. Graded index confined modes in Bloch domain walls'*).

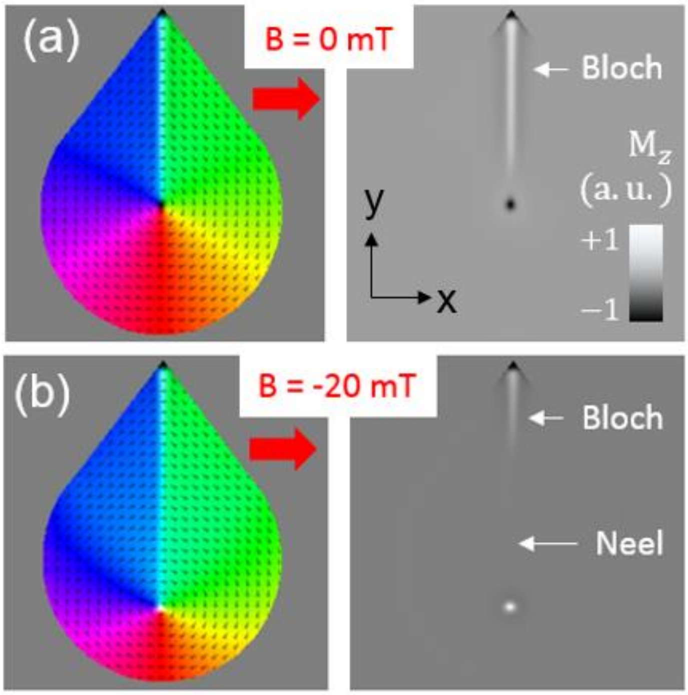

Figure 7.4 Magnetisation configuration for the teardrop shape in absence of biasing, showing the formation of a Bloch-type wall (a) and with −20 mT of biasing showing a mixed behavior in the wall (b).

Fig. 7.5 shows the simulated hysteresis loops for the teardrop shape in the SMV as initial state when the biasing field is applied perpendicular (a) and parallel to the domain wall (b). A sequence of sweeps from zero bias to saturation, back to zero and back to saturation again are indicated by the (i, ii and iii) indices, respectively. From these results, the main observations are: (1) The DMV appears naturally after relaxation of the saturated sample (descending hysteresis curve), implying that the SMV is a metastable state of the patch; (2) Both states, SMV and DMV, show very low remanence in the x-direction, -6261.7 Am^{-1} for the SMV state and -4639.14 Am^{-1} for the DMV state (8.4% and 5.9% of magnetisation saturation, respectively). Nucleation of a second vortex in the DMV state reduces magnetic remanence in approximately a 26%, compared to the SMV state; and (3) In a perpendicular biasing scheme, the 'returning path' (green solid arrow in Fig. 7.5(a)) from saturation shows the formation of a different configuration similar to a double *C* or 'buckling' state, where two opposite 'quasi vortex cores' or Bloch domain walls at the shape boundary are formed (Vaňatka M., 2017), retaining high in-plane magnetization in the x-direction and a left-right symmetry (see green contour inset at 36 mT in Fig. 7.5(a)) with further reduction. In-plane magnetisation is abruptly reduced around 30 mT, indicating a more abrupt nucleation in the sample than for the parallel biasing. This nucleation field indicates the beginning of the DMV state formation as confirmed by micromagnetic simulations (see Fig. 7.5(a) and the inset at 0 mT in (b)). Once the DMV is obtained, the initial SMV curve (red arrow) is lost and the upper branch of the loop indicates the new hysteresis ascendent path (green dashed arrow).

In a parallel biasing (see Fig. 7.5(b)), low hysteresis and Barkhausen jumps can be found before reaching saturation. These are associated with the magnetic inhomogeneities formed due to the Bloch domain wall pinning and unpinning at the shape boundary during the core shift (see inset at 20 mT in Fig. 7.5(b)).

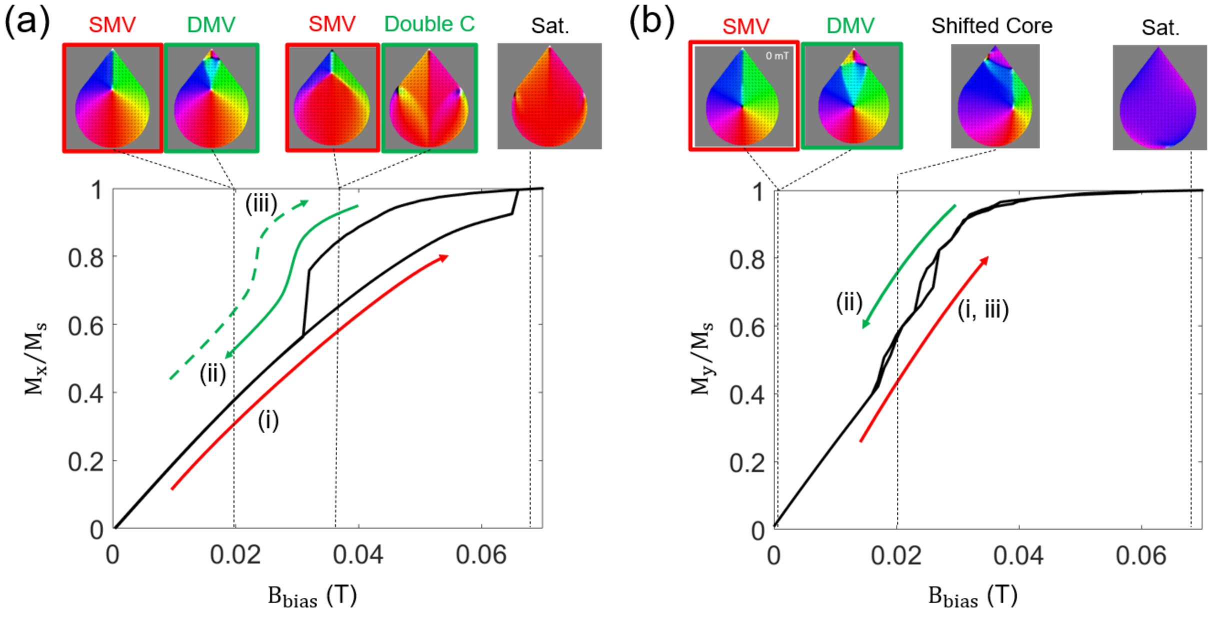

Figure 7.5 Simulations of a hysteresis half-loop for the teardrop shape starting from a SMV state with a biasing field applied perpendicular (a) and parallel (b) to the single domain wall. Insets show the magnetic configuration states at the indicated biasing fields (0 mT, 20 mT, 36 mT and 64 mT) for each hysteresis path (red or green arrows and contours) or both (no colour contour). Indices (i), (ii) and (iii) show a sequence of sweeps from zero bias to saturation, back to zero bias and back to saturation, respectively.

7.3 Tuning Winter's magnon's amplitude in the SMV state

As starting point, we investigate how a confined mode in the formed domain wall propagates in the 'teardrop' by micromagnetic simulations. Fig. 7.6 (a) illustrates the numerical dispersion relation of Winter's magnons (WM's) in the domain wall for a teardrop shape (colour plot), by Fourier transforming the time signals in the wall (black dashed line from the inset in Fig. 7.6(a)) and the analytical equation from (Garcia-Sanchez, et al., 2015) for a frequency gapless Winter's magnon mode in a 180 degrees Bloch wall (white dashed line), following on from Goldstone's theorem, which states the arising of a frequency gapless mode whenever the symmetry of the shape is spontaneously broken (Goldstone, et al., 1962; Sluka, et al., 2019). In the 'teardrop' ferromagnet, the symmetry is broken due to the fluctuation of the originally static domain wall. In the 'teardrop' shape there is a frequency gap at $k = 0$ due to the 60 degrees corner which, as mentioned before, introduces a transversal anisotropy to the confined wave. This shifts the minimum ($k = 0$) in the dispersion relation up in frequency as it is explained in more detail in Chapter 6, Section 6.2.1. If a transversal anisotropy term, obtained from Eq. (6.2.12) for $\alpha = 30°$ (half the vertex angle), and if we assume an effectively thinner shape of thickness $t/3$ (since we are only looking of the middle layers of the shape for more intense spin waves, see chapter 3 and 6), then the fitting to the analytical equation for WM's, to numerical results becomes more accurate (red dashed line). From Eq. (6.2.12) and assuming a generic anisotropy transversal to the wall due to the in-plane dipolar field $H_{\mathrm{d,y}}$, the additional anisotropy term can be defined as $K_{\mathrm{d}} = \frac{\mu_0 M_s}{2} H_{\mathrm{d,y}}$.

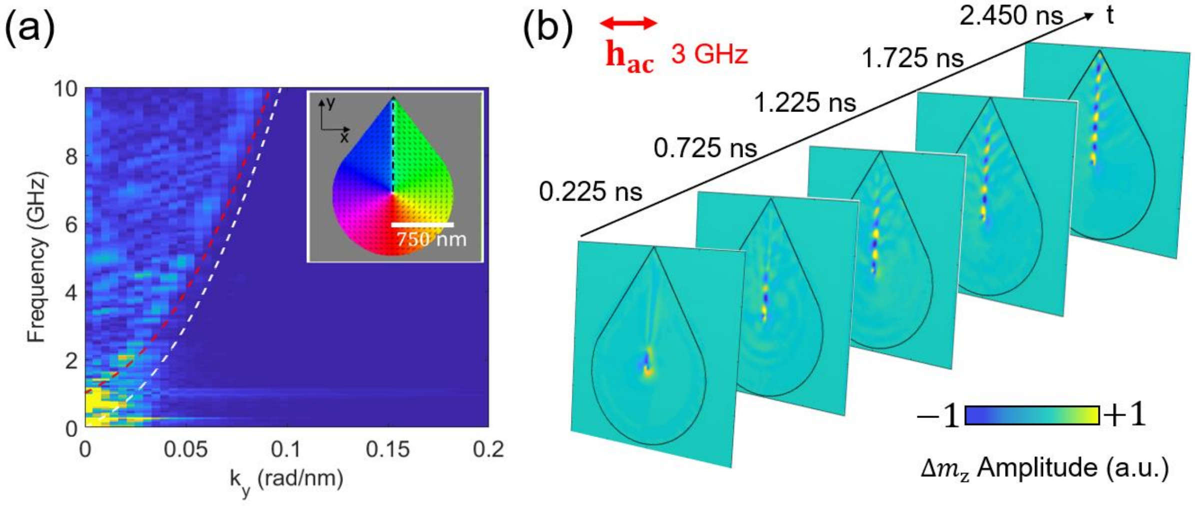

Figure 7.6 (a) Simulated dispersion relation along the domain wall (black dashed line in inset) in a teardrop shape of given dimensions (colour plot). Dispersion relations from a Winter's magnon a long a 180 degrees Bloch wall (white dashed line) and the same dispersion with an added anisotropy term based on the demagnetising field expression from Chapter 6 (red dashed line). (b) Simulated time sequence of the dynamical out-of-plane magnetisation for the middle layer of the micromagnetic model after applying an in-plane oscillating field of 3 GHz in the x-direction.

A confined mode will propagate in the domain wall if this is stable within a range of biasing fields (no larger than saturation fields), in a wide range of frequencies (from about 1 GHz to ideally above 10 GHz). For example, for an in-plane oscillating field with frequency 3 GHz applied to the whole shape along the x-direction, a strongly confined mode propagates in the domain wall from the core towards the vertex (see Fig. 7.6(a)). Since the excitation field is applied perpendicular to the wall, the origin of the confined mode can be regarded as a string-like resonance or flexural mode of the wall – or Winter's magnon – where the core acts as a 'free end' of that string, therefore acting as a source of the 1D propagating spin wave (Sluka, et al., 2019). Fig. 7.7 shows different wave profiles for different biasing fields transversal to the wall. In the range of biasing fields between 0 mT and −20 mT, one can see how the emitted spin wave amplitude does not notably decrease across the distance of the elongated domain wall (l_{DW}), therefore covering distances of about 8.2 times the mode's wavelength at 3 GHz (λ_{WM}, obtained from the dispersion relation in Fig. 7.6(a)). For more intense bias fields, one can see how the amplitude of the spin wave can be significantly enhanced or reduced depending on the intensity and orientation of the applied biasing field.

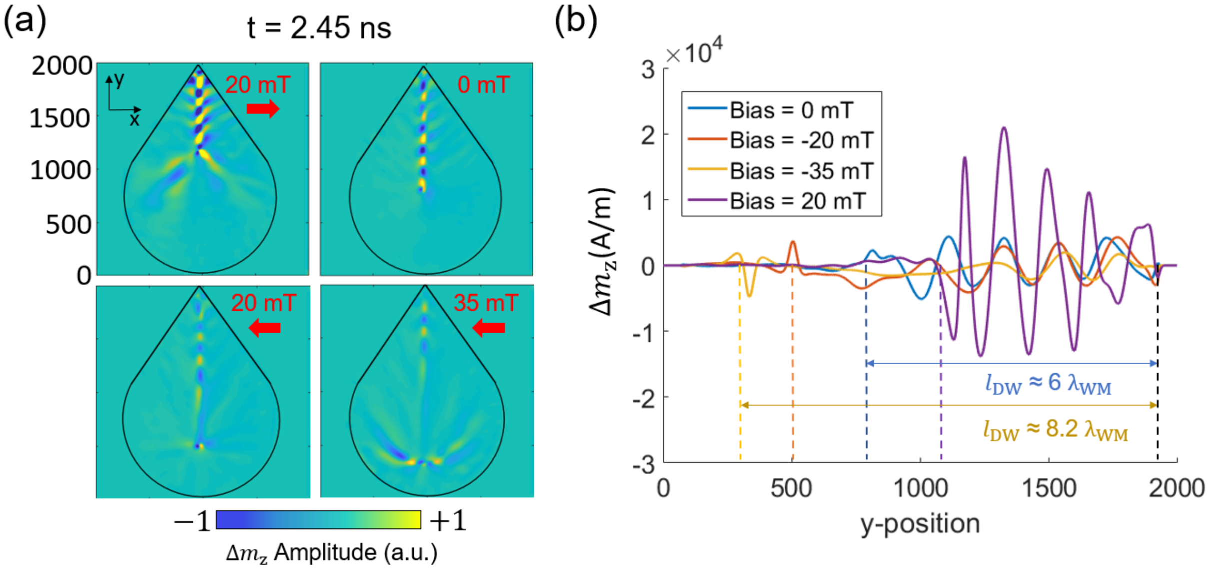

Figure 7.7 (a) Simulated spin wave profiles for the dynamic out-of-plane component of magnetization for different biasing fields for a given time. (b) Spin wave profiles and their amplitudes along the formed domain wall. The ratio between the domain wall length (l_{DW}) and the mode wavelength (λ_{WM}) at 3 GHz excitation frequency is shown at the bottom left for no bias (blue) and 35 mT bias. Dashed black line indicates the vertex position.

The spin wave lower amplitude at small and/or negative bias can be explained as the mismatch in the local effective magnetic field in the domain wall with its resonant modes (Van De Wiele, et al., 2016). However, in our scenario, other observed effects should be considered too: (1) The variation of the internal field due to the biasing fields (as explained in Chapter 6), and (2) the splitting of the domain wall into Neel and Bloch types due to the displacement of the vortex core. The latter situation can be regarded as a 1-D analogy to the scenario explored in Ref. (Chang, et al., 2018). Also, Fig. 7.4 shows that the vortex core can flip polarity when a biasing field is applied (from −1 to +1). In contrast, the polarity of the Bloch wall remains the same (+1). This implies a gradient in orientation of the out-of-plane component of magnetisation between both regions and therefore, of the demagnetising field too. We believe this relates to the different amplitudes of the confined spin wave at different biasing fields. This hypothesis may explain as well why the intensity increases when the wall is shortened, (i.e. at positive biasing fields) since there is less gradient along the direction connecting the core (polarity = +1) with the wall (polarity = +1), than at negative biasing fields. In this latter situation, even though the core polarity is the same as the wall polarity (+1), the Neel wall in between inhibits the emission of a large amplitude spin wave, since it introduces a gradient in magnetisation orientation, regardless of the vortex core polarity. Fig. 7.8(a) shows the in-plane component of the demagnetising field transversal to the wall for no biasing field (blue curve), and biasing fields of −20 mT (yellow curve) and +20 mT (orange curve). Fig. 7.8(b) does the equivalent for the out-of-plane component of the demagnetising field. From numerical results from Chapter 4 on 80 nm thick discs, the core width is assumed to be around 100 nm. The extent of the core region is therefore shaded in the respective colour of the bias. The beginning of a Bloch-type wall behaviour can be easily identified where the out-of-plane component of the demagnetising field becomes non-zero (see Fig.7.8(b)). At positive biasing field, one can see how the slope between the core region, i.e. source of the spin wave, and the domain wall region is minimal, implying similar values of the total demagnetising field and therefore, a ‘continuous medium’ for the spin wave transmission. As an example, these values are indicated with dashed lines for the case of positive biasing to show their minimal difference with respect to other bias fields.

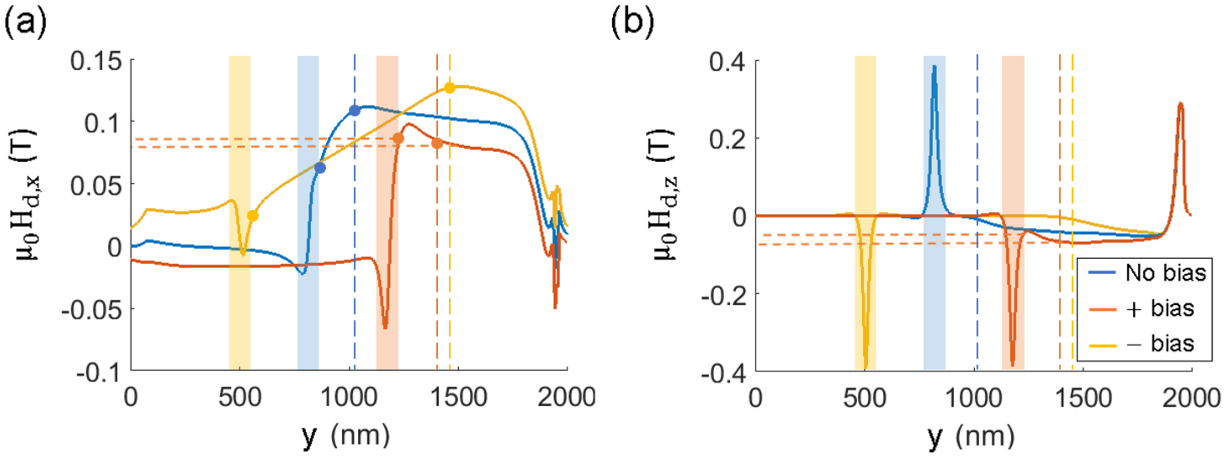

Figure 7.8 Simulated in-plane component of demagnetising field transversal to the wall (a) and the out-of-plane component (b) in absence of biasing (blue curve) and with +20 mT bias (orange curve) and −20 mT bias (yellow

curve). For the positive bias case, the orange dashed lines show the demagnetising field values for the border of the core region (right edge of the shaded area) and at the beginning of the Bloch domain wall (vertical long dashed lines for each bias). These values are more alike and their difference (the distance between coloured dots) reduces with increasing bias, improving the ‘mode shape matching’.

In other words, the attenuation or enhancement of the spin wave amplitude can be regarded as a sort of ‘mode shape mismatch’ problem between magnonic regions of different internal fields *in the domain wall*, for which the demagnetising field is the differentiator term (since if there is a biasing field, this is constant for the whole structure). This perspective of ‘mode shape mismatch’ can interestingly, but also naively, connect to a sort of ‘impedance matching’ scenario that implies the definition of a local ‘characteristic impedance’ for the spin wave propagating in the wall as in, $\mathrm{Z}(x) = \mathrm{Z}_0/n(x)$, where Z_0 is the reference impedance and $n(x)$ could be obtained from Eq.(6.2.13) (see chapter 6).

From the perspective of local ferromagnetic resonances, when the local demagnetising fields are not much different within the same region, the frequency of local FMRs are also alike (Davies, et al., 2017) and the spin wave is better transmitted along that path. Eq. (6.2.13) connects these two different perspectives by relating the index of refraction to the demagnetising field. We must stress that additional effects from the biasing fields will also modify the local ferromagnetic resonances, for which the same argument can work by using Eq. (6.2.15) instead. In summary, taking all this into account, the main reason behind a larger amplitude at positive biasing fields is because it provides a better matching with the local ferromagnetic resonance in the Bloch wall.

For the proposed geometry, the source at the vortex core region and the domain wall channel are shown to be highly tuneable by external biasing fields. Based on these numerical results, the teardrop shape in a Single Magnetic Vortex (SMV) state is proposed as a highly tuneable spin wave emitter with potential applications such as a spin wave valve. Unlike previous work, this device does not require any external attachments for exciting spin wave modes since it operates in the non-saturated regime while the vortex core configuration is stable. The key point for its operability is the formation and stabilisation of the SMV state in the structure.

7.4 VNA-FMR results

In section 7.3, we have numerically studied the behaviour of the confined modes or Winter's magnons in a domain wall in the teardrop shape. By applying external biasing fields, parallel or perpendicular to the domain wall, the confined waves can be controlled in the shape in a wide range of frequencies. Their resonant conditions can be analytically identified by Eq. (7.1) and Eq. (7.2). For example, for an excitation frequency of 3 GHz in absence of biasing fields, we count 10 anti-nodes (n) from Fig. 7.7 for the standing confined spin wave between the core and the vertex. The numerical dispersion relation of Winter's magnons from Fig. 7.4 yields a wavenumber of approximately k_0=0.025 rad·nm^{-1} or equivalently, a mode wavelength of $\lambda_0 = 251.2$ nm. From the resonant cavity condition (assuming pinned spins at both ends), $L = n\lambda/2$, these values yield a resonant cavity length of approximately 1256 nm. The domain wall length in absence of biasing fields is approximately 1250 nm (see Fig. 7.7(b)). Since the difference is about 6 nm ($\sim 0.024\,\lambda_0$), we could correlate the absorption peaks from a VNA-FMR plot at those RF frequencies with a discretised spectrum of a Winter's magnon propagating in the domain wall. The corresponding number of anti-nodes (n) to input into Eq. (7.1) and Eq. (7.2), can be obtained from numerical simulations. In the next sections we proceed to study the microwave features by means of the VNA-FMR technique, with the aim to confirm that the SMV state can indeed be obtained and stabilised, and therefore, the Winter's magnons modes in the 'teardrop' shape are susceptible for detection by this technique.

7.4.1 Numerical results on Winter's Magnons

We ran micromagnetic simulations to replicate the VNA-FMR measurement of a teardrop shape when a biasing field is applied perpendicular to the domain wall (each in a parallel VNA-FMR scheme). Only one single teardrop design of 80 nm thickness and 2000 nm diameter is simulated. Fig. 7.2 showed the approximate resonant curves for the first modes ($n = 1, 2, 3 \ldots$) from Eq. (7.1) and Eq. (7.2). Fig. 7.9 shows results from micromagnetic simulations for different biasing fields of 0 mT (blue curve), 10 mT (green curve) and 30 mT (orange curve), applied perpendicular to the domain wall in a parallel VNA-FMR scheme (bias parallel to oscillating field). The most significant peaks for the different confined modes are easily identified, from counting the number of antinodes especially in absence of biasing fields (0 mT). From the mode profiles at the frequencies of interest, one can see that on increase of the bias to high enough magnitude (i.e., 30 mT), the domain wall length is accordingly reduced, and the Winter's mode is excited (see Fig. 7.9(b)). The number of antinodes (n) to identify the mode order are only obtained along the single domain wall. A semi-numerical VNA-FMR plot (left panel in Fig. 7.9(a)) can be then obtained from tracking the corresponding mode in frequency. One can see that the peaks from the FFT spectra describe a monotonically increasing curve with increasing field (colour symbols, different colours for different bias fields), with a less pronounced slope for the lowest orders. This is in qualitatively good agreement with the analytically found expression for a discretised Winter's magnon along a bias-dependent domain wall length from Eq. (7.1) (see Fig. 7.2). However, there is a significant quantitative disagreement. When an additional anisotropic term, due to the sharp corner of the 'teardrop' is considered (as for the red dashed curve in its dispersion curve), Eq. (7.1) can be extended to an effective wavenumber in the wall as,

$$f_n = f_{\mathrm{M}}\lambda_{\mathrm{ex}}\left[\left(\frac{n\pi}{l_0 + r\mathrm{B}_{\mathrm{ext}}}\right)^2 + \frac{K_{\mathrm{d}}}{A_{\mathrm{ex}}}\right], \tag{7.3}$$

where K_{d} is the anisotropy constant defined in the beginning of section 7.3, l_0 is the domain wall length, assumed to be 1250 nm and $r = -r_{\mathrm{v}}$. Results from Eq. (7.3) are shown as black dashed curves in Fig. 7.9(a).

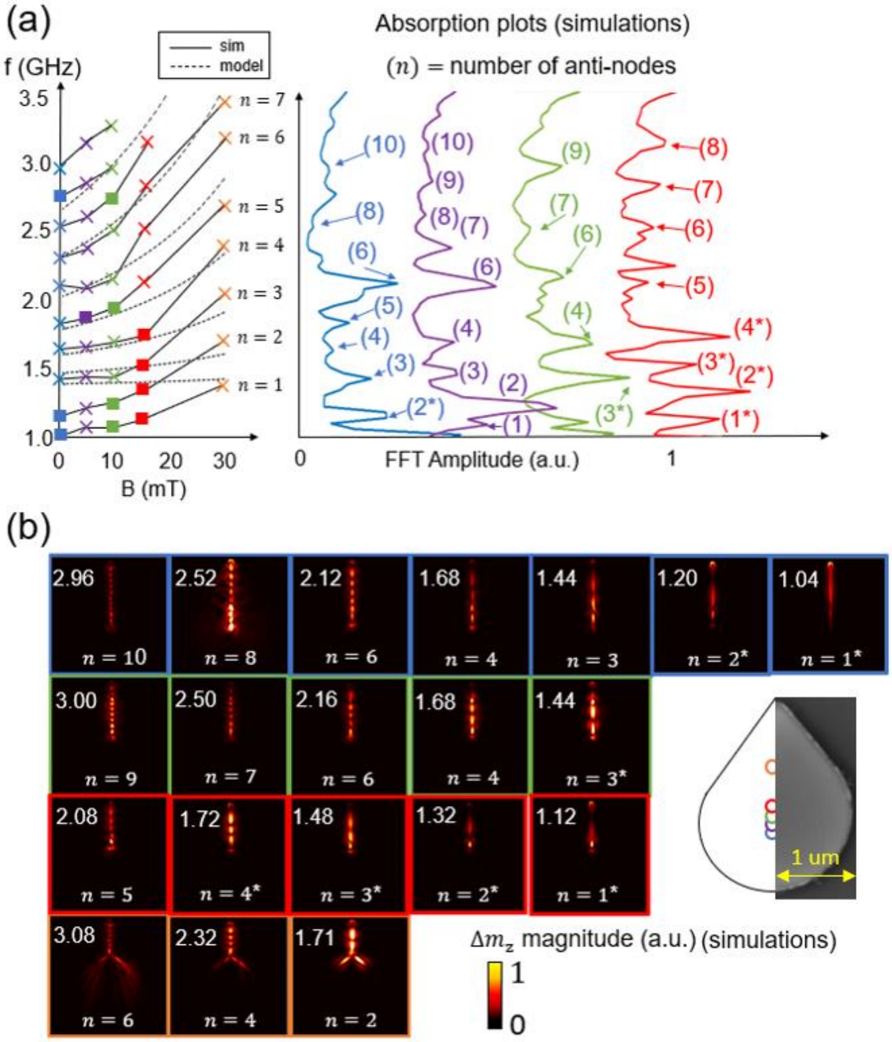

Figure 7.9 (a) Simulations results for a single teardrop shape, up to 30 mT that shows approximate mode curves (black solid lines are for guiding the eye) obtained from tracking the most significant peaks from the simulated FFT spectra for different bias fields (colour symbols), 0 mT (blue), 5 mT (purple), 10 mT (green) and 15 mT (red). Black dashed curves are results from Eq. (7.3). Crosses are succesfully identified peaks from the spectra (FFT spectra for 30 mT is not shown but identified peaks are also shown as orange crosses on the left), and correlated to the Winter's magnons, and squares are for the non-identified peaks in the spectrum (but expected halfway between two peaks) or Winter's magnons with a 'mixed' mode profile due to the mixed domain wall behavior. The simulated spectra are offset for clarity. (b) Simulations results for the magnitude and mode profile of various orders for some examples of bias fields and frequencies. Some modes show a wavelength dependence on the position in the wall due to its mixed profile, and their mode indices are indentified with an asterisk (*). Inset shows an schematic of the teardrop shape (not to scale) with the vortex core positions (exaggerated and not to scale) for each bias field and an SEM picture of (half of) a single fabricated element, as part of an array of elements (see chapter 3).

By considering this additional anisotropy due to the static dipolar field transversal to the wall, there is still not full agreement between Eq. (7.3) (black dashed curves in Fig. 7.9(a)) and numerical simulations (colour symbols). We believe this quantitative disagreement can be explained as follows.

At high positive bias fields, the applied field makes angle α smaller. This, in turn, reduces the demagnetising field in the wall, reduces K_d and increases the effective wavenumber of the Winter's magnon. To still satisfy the resonance condition in the wall, the now larger wavenumber should be obtained at a higher excitation frequency. Eq. (7.3) does not account for the effects of the bias fields and therefore it typically yields lower eigenfrequencies than the ones obtained from simulations (see orange crosses in Fig. 7.9(a)). At low frequencies (lower order modes) and small (or absence of) biasing fields, the mixed Bloch-Neel behaviour in the wall may also explain the differences between Eq. (7.3) and simulations. Due to their larger wavelengths, lower order modes are more sensitive than higher order modes to the differences in the local dipolar fields in the wall and therefore, an effective *constant* wavenumber in the entire length of the wall is difficult to define, due to the 'spatial chirping effect'. Unlike the effects induced by external fields, lower order modes naturally show a decrease in the effective wavenumber with respect to the local wavenumber close to the vertex. Red or blue contour insets in Fig. 7.9(b) show some examples for $n = 1, 2$ and 3 modes (indicated by an asterisk *), where an apparent 'chirping' effect on the mode's wavelength can be observed. This reduces the frequency at which such effective wavenumber is obtained for the lower order modes (potentially modelled by an additional anisotropy negative term $-K_\mathrm{c}$) and therefore, an apparent global linear behaviour with n is observed, rather than quadratic (as predicted by Eq. (7.3)), since this effect is less pronounced for higher order modes (see Fig. 7.9(b) for $n > 4$). This explains why, for low n and low bias, the simulated eigenfrequencies are typically placed below the ones predicted by Eq. (7.3) and for high bias, they are placed close or above the predicted ones, when both effects could, in principle, cancel each other ($K_\mathrm{d} \sim |K_\mathrm{c}|$). All these suggests that the effect of a mixed Bloch-Neel behaviour in the wall on the Winter's magnon local wavenumber is not that much pronounced for positive large biasing fields or high order modes, due to their smaller wavelengths. In fact, a more 'constant' wavelength for the confined mode in the wall can be observed for higher order modes, even in absence of bias fields (see mode profile images for $n > 4$ in Fig. 7.9(b)). Accounting for all these considerations, a more complete model for the propagation of Winter’s magnons in a ‘mixed’ domain wall can be developed, but this is not in the scope of this section.

Although we acknowledge that the model from Eq. (7.3) for the Winter’s magnons in the ‘teardrop’ shape is rather simplistic and shows poor quantitative agreement with simulations, we believe these additional effects (an additional anisotropy term due to external bias and a domain wall mixed profile) may explain the quantitative disagreement and can help to improve the model further. FFT spectra from Fig. 7.9 also show that the intensity of Winter’s magnons for high order modes is weak and low compared with the background signal and their linewidths are as small as 0.08 GHz, with a separation between peaks as small as of 0.02 GHz at 0 mT at lowest frequencies. Modes’ dispersion curves are highly ‘packed’, which can make their experimental detection a very difficult task when accounting for losses (which widen the linewidths).

Fig. 7.10 shows an absorption spectrum for no bias field from a parallel VNA-FMR scheme. To approximately retrieve the steady component of such low signal-to-noise ratio measurement, a high pass filter with a cut-off frequency of <1 GHz and a Savitzky-Golay (SG) finite impulse response smoothing filter (Savitzky & Golay, 1964) are used to post-process in MATLAB© the raw measurement. A Savitzky-Golay filter consists basically on a convolution by locally fitting a low-degree polynomial to sub-sets of data that yields a smoothed curve but preserving the local maxima and width of the most significant peaks. Prior to the Savitzky-Golay filter, a high-pass filter is applied to the data set to discriminate spurious low frequency periodic signals with significant amplitude from microwave reflections. This is done as a previous step, so they do not interfere with the steady component of the signal in the SG filtering stage. Fig. 7.10 (a) shows the simulated absorption spectrum (as it was shown in Fig.7.9) and (b) the resulting experimental spectrum after post-processing raw experimental data. Although the comparison between simulated and measured data is poor, the stochastic component from the measured data is minimised after the filtering process and some peaks can be more easily correlated with the simulated ones from their positions in frequency and their relative spacing. There is less agreement with the simulated peaks at higher orders (see absorption peaks above 2.5 GHz), perhaps due to the fact that their intensity is smaller compared with lower order modes, and they are more easily shadowed by other stationary but spurious signals from the VNA-FMR setup.

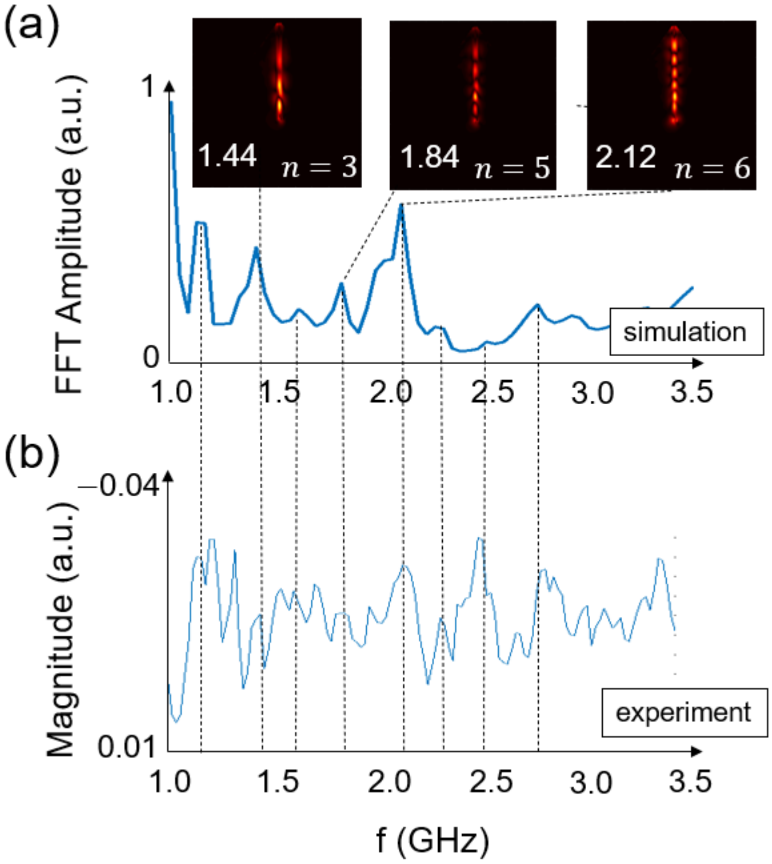

Figure 7.10 (a) Simulated FFT spectrum for a single teardrop shape for no bias field, B = 0 mT. As examples, insets show the mode intensity and anti-nodes number *n* at the selected frequency in GHz. (b) Absorption spectrum from a parallel VNA-FMR plot for no bias and after a high-pass and a Savitzky-Golay filtering.

The above results are obtained from a SMV assumed as initial state for the teardrop patch. The process described in Fig. 7.1 is replicated in experiments, which should lead to the required magnetic configuration that allows comparison of the experimental result from Fig. 7.10 with the results from micromagnetic simulations shown in Fig. 7.9. To confirm that the SMV was indeed obtained at the start (and our assumption is right), a more complete VNA-FMR study was conducted on the teardrop shape. The aim of the following section is to analyse and describe the differences in magnetization dynamics for two different VNA-FMR measurement orientations which, following from magnetostatic features shown in Fig. 7.4, should relate to two different stable states, i.e. the DMV and the SMV states.

7.4.2 Experimental results and confirmation of the Single Magnetic Vortex state

We use VNA-FMR technique to experimentally explore all the eigenmodes that appear in the teardrop shape for a perpendicular and parallel VNA-FMR scheme and to experimentally validate the formation of a Single Magnetic Vortex (SMV) configuration in the teardrop shape. Measurements and simulations are normalised by subtracting the average total response. The samples were fabricated following the same process, described in Chapter 3, for the samples used in Chapter 4 and 5. The sample can be rotated 90 degrees on the CPW, so the biasing field can be either parallel or perpendicular to the domain wall. We first describe results for a biasing field perpendicular to the domain wall.

Fig. 7.11 shows results from VNA-FMR measurements on an array of teardrop shapes equally spaced (2000 nm spacing), where the sample is placed on top of the short path of the U-shaped CPW, in a perpendicular VNA-FMR configuration and with the biasing field perpendicular to the domain wall.

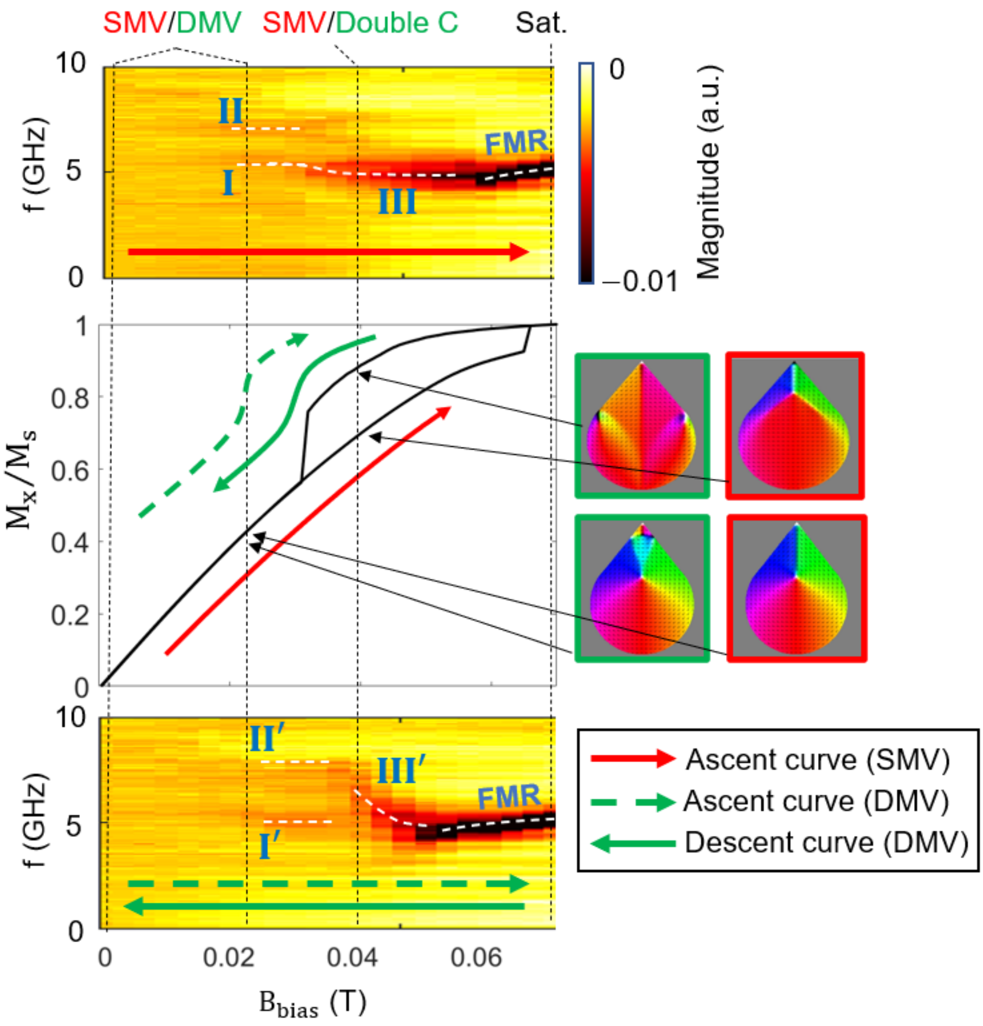

Figure 7.11 Experimental VNA-FMR results for teardrop shapes of thickness 80 nm and simulated hysteresis loop (black dashed lines indicate particular biasing fields of 0 mT, 21 mT, 36 mT and 70 mT). The FMR main mode can be spotted at highest fields as well as other low-field resonances (white dashed line are for guiding the eye) related with the simulated magnetic configurations, shown in the insets on the right. The hysteresis curves are labeled according to the initial equilibrium state at 0 mT (SMV or DMV).

Absorption plots are found to be asymmetric with respect to the maximum applied field (70 mT), which univocally relates to a different magnetic configuration after the biasing is reduced from saturation (see insets on the right in Fig. 7.11). This is in good agreement with the different curves in the simulated hysteresis loop. While modes I and II on the *ascent* curve (VNA-FRM plot at the top panel) are equivalent to modes I’ and II’ on the *descent* curve (VNA-FRM plot at the bottom panel) in the hysteresis loop, there is a clear frequency dependence and differences between modes III and III’, which may be characteristic of the SMV and the DMV states, respectively. On the ascent curve of hysteresis, one can see how mode I smoothly transitions into mode III and then transforms into the FMR main mode (see dashed white curve in the top panel of Fig. 7.11). However, on the descent curve, this transition does not happen. Instead, an abrupt transformation of mode III’ to modes I’ and II’ happens, which can relate to the nucleation process leading to the DMV state, as shown in the hysteresis loop from Fig. 7.5. The reversed process following the ascent hysteresis curve, once the DMV is obtained (green dashed line), can be related to the two vortex merging and self-annihilating to form the double C-like state in the patch (see green contour inset on the right in Fig. 7.11).

Fig. 7.12 shows a VNA-FMR cut at 21 mT from micromagnetic simulations and experimental results on the ascent curve of the hysteresis loop. Some peaks can be identified in the simulated and the experimental spectrum, which shows two mode profiles at around ~5 GHz correspond to localized modes near the core region (see yellow and purple domain regions in Fig. 7.5) and in the wall. It seems that there is a localised mode in the wall similar in nature to the Winter’s magnon, but from simulations in the time domain for a continuous wave excitation (not shown here), we can see that the apparent partial confinement in the wall is due to a spin wave radially emitted by the core region towards the in-plane magnetised regions and overlapping with reflected waves at the edges. At around ~6.5 GHz the modes are also emitted into the neighbouring domains. Their behaviour with frequency is therefore equivalent to a Bloch domain wall (Whitehead, et al., 2017), with bounded modes in the wall at lower frequencies and emission into the neighbouring domains at higher frequencies.

Modes I and II shown in Fig. 7.11 can therefore relate to similar dynamics too. Mode I can be related to a large excitation close to the vortex core and therefore, to localised modes, and mode II can relate to azimuthal-radial spin waves in the domains due to the broken symmetry of the ‘teardrop’ patch in a slightly shifted core configuration. This is equivalent to the I’ and II’ absorption regions and therefore, to the DMV state. Mode II’ appears higher in frequency than mode II maybe due to the formation of the second vortex, that significantly modifies the domain structure close to the vertex of the shape.

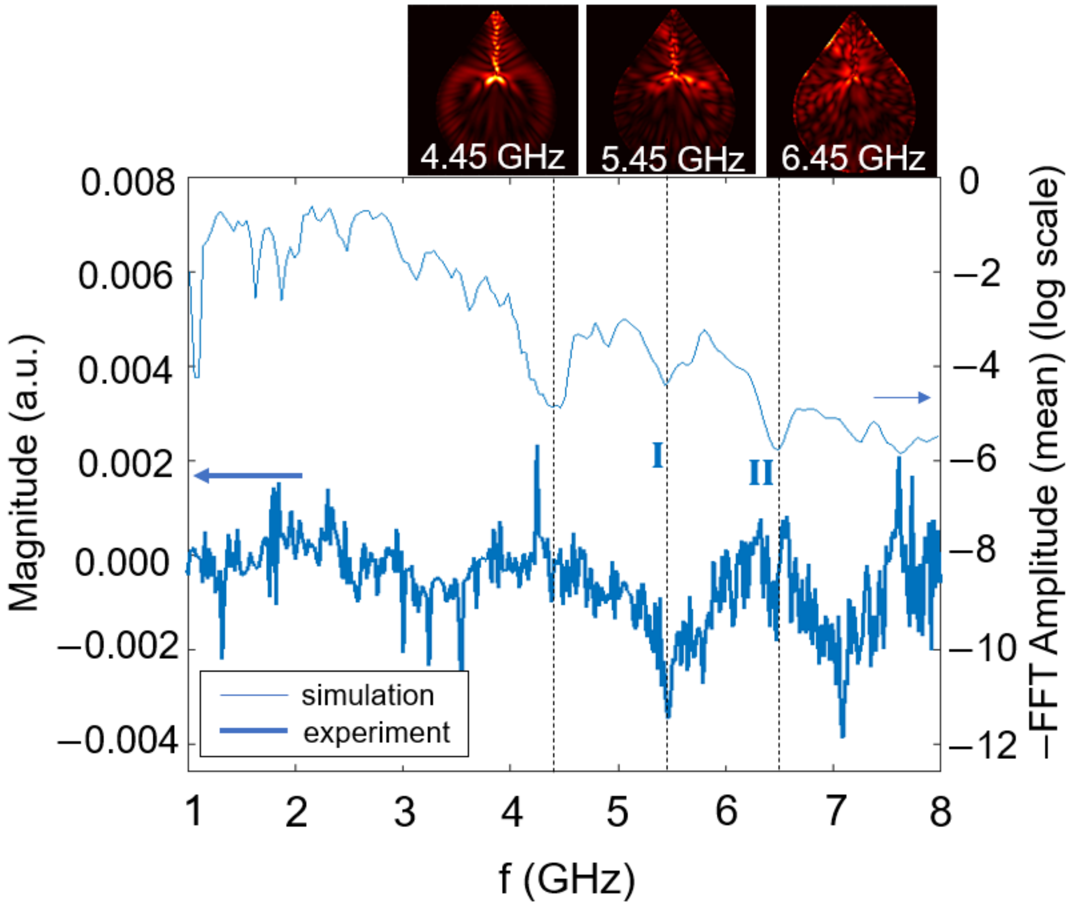

Figure 7.12 FFT spectrum from simulations and absorption spectrum from measurements with a bias field of 21 mT in a perpendicular VNA-FMR scheme, corresponding to the crescent curve of the hysteresis loop. Inset show the modes profiles from simulations at the selected frequencies.

These localized modes near the core around ~5 GHz and azimuthal patterns at higher frequencies were also observed in circular disks with non-centred magnetic cores, in a VNA-FMR parallel and perpendicular schemes, respectively (Aliev, et al., 2009). However, in the teardrop shape, the localized mode can remain more stable for larger biasing fields, due to the longer distance covered by the core towards the sharp corner (compared to towards the curved edge) and the formation of domain walls. Fig. 7.13 shows different simulated mode profiles at the chosen frequencies and bias field (blue dots) that suggest that this mode transforms from a localised mode in the ‘purple’ and ‘yellow’ domains (see insets in Fig. 7.11) into a ‘bulk-like’, ‘azimuthal-broken’ mode in the ‘red’ domain together with a highly-localised mode (identified as mode III in Fig. 7.11) in the now elongated, wall-like ‘purple’ and ‘yellow’ regions (see the inset at 35−50 mT in Fig. 7.13). Finally, it apparently converts into the FMR main mode with increasing bias field due to the continuously enlarging domain before full saturation and after the domain walls and vortex core self-annihilation takes place.

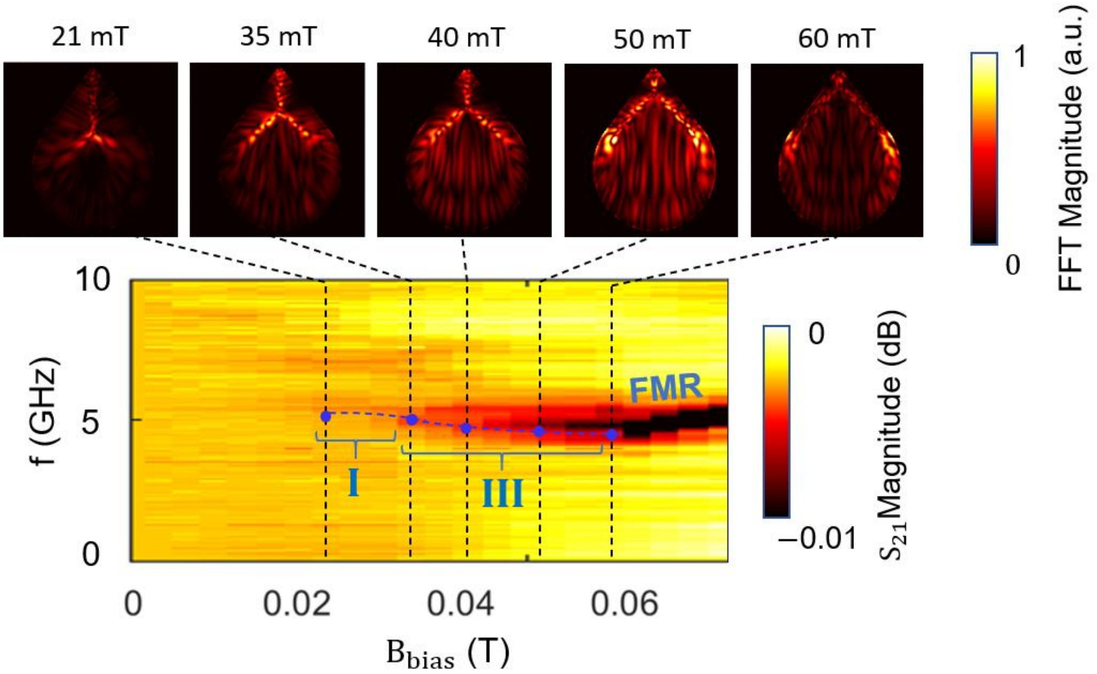

Figure 7.13 (Bottom) Measured VNA-FMR spectrum for a perpendicular biasing scheme (from Fig.7.11) and (top) simulated mode profiles at the selected combination of frequency and bias field (blue dots). The suggested mode conversion from mode I to mode III to FMR mode is shown. Blue dashed line is for guiding the eye.

Following on these results, the transition from the SMV state into the FMR main mode in saturation can be explained as follows: As the biasing field increases, the single core is displaced upwards until it is expelled at a higher annihilation field than in the DMV state. While this process occurs, the displaced core covers the longest distance in the shape since it does not encounter a second core on the way, while the domain wall remains pinned at the vertex. The domain at the ‘bottom’ (red colour domain) continuously and uninterruptedly enlarges, smoothly ‘assimilating’ the purple and yellow domains through a standard rotation process of their magnetic moments until the vortex core self-annihilates and the ‘purple’ and ‘yellow’ domains/walls vanish. As in Ref. (Aliev, et al., 2009), we can relate mode III with the ferromagnetic resonance frequency in the largest domain in a shifted core configuration, but in our case also coexisting with the highly confined mode in the formed domain walls in the shifted

SMV state (see insets in Fig.7.13). This is reflected in a single strong mode (mode III, between ~30 mT and ~60 mT) until full saturation is achieved.

Fig. 7.14 shows a VNA-FMR cut at 36 mT from micromagnetic simulations and experimental results on the *descent* curve of the hysteresis loop. It clearly shows a different magnetic configuration before the DMV is obtained than the one in Fig. 7.12. Several overlapped spin wave modes may explain the broad linewidth of the simulated and measured peak at around 6 GHz. At the selected biasing field, the collection of modes in region III' can be associated with localised and propagating spin waves from the magnetic inhomogeneities pinned at the sample's edges (identified as Bloch domain walls in the 'buckling' state) and the domain wall that splits along the middle of the shape. Mode profiles at some selected frequencies (see insets in Fig. 7.14) within the broad peak, confirm that those regions are acting as sources of those spin waves. Snapshots (not shown here) in the first stages in time at an excitation frequency of 5.75 GHz for a biasing field of 36 mT make clear that the excited spin waves emanate from the magnetic inhomogeneities, i.e., the domain wall in the middle and the Bloch walls at the sides, pinned at the curved edges. Their spin wave spectra are continuum which explains the broad absorption as a superposition of modes of different order.

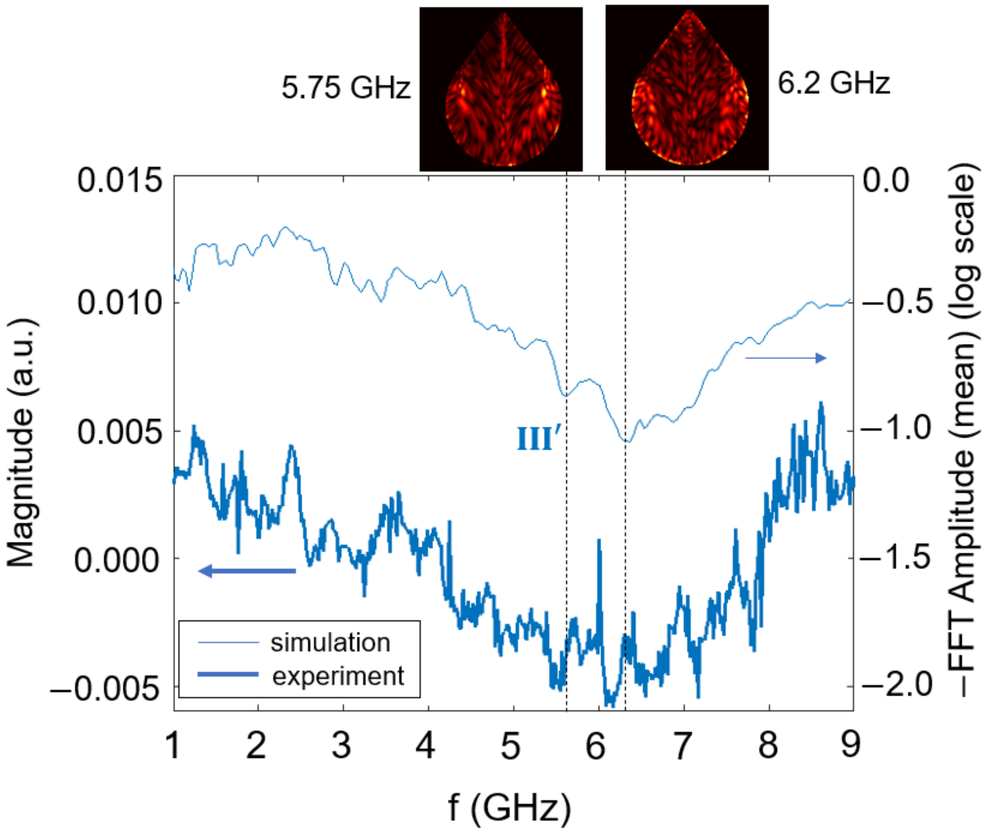

Figure 7.14 FFT spectrum from simulations and absorption spectrum from measurements with a bias field of 36 mT in a perpendicular VNA-FMR scheme, corresponding to the descent curve of the hysteresis loop. Inset show the modes profiles from simulations at the selected frequencies.

From these experimental observations and the simulated hysteresis loop, one can infer that the SMV state can be successfully obtained as an initial state prior to applying biasing fields. We can state that mode III and mode III' are characteristic of the SMV and the DMV states, respectively, and modes I/I' and II/II' are characteristic of the SMV as well as of the DMV state. To confirm the latter, we now run more experiments on a parallel biasing scheme.

As in the previous measurement, the sample starts in a SMV state but from the simulated hysteresis loop, it is expected to collapse into the DMV stable state after relaxation from saturation (see Fig. 7.5). Fig. 7.15 shows the experimental absorption spectrum sweeping to a maximum field value (70 mT) and reducing the field back to 0 mT.

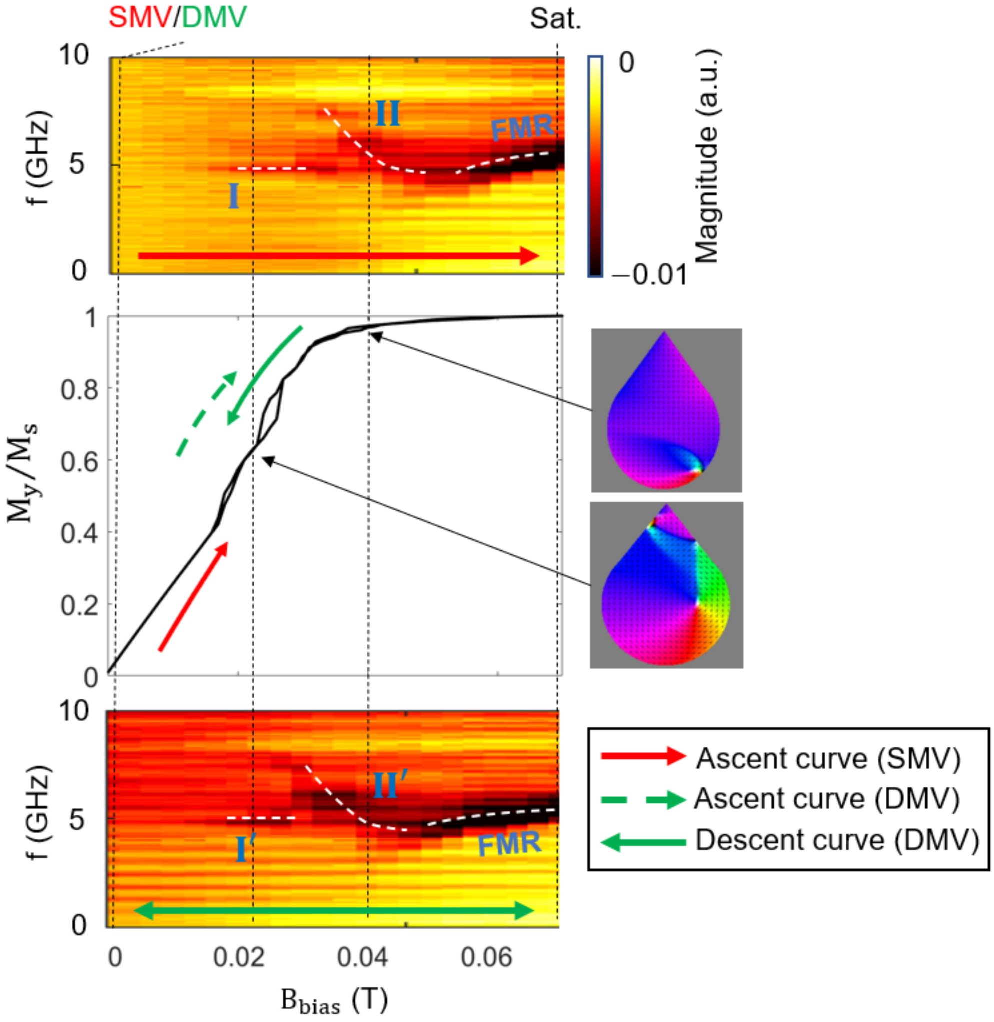

Figure 7.15 Experimental VNA-FMR results for teardrop shapes of thickness 80 nm and the simulated hysteresis loop (black dashed lines indicate particular biasing fields of 0 mT, 21 mT, 36 mT and 70 mT, and the magnetic configuration). The FMR main mode can be spotted at highest fields as well as other low-field resonances (white dashed line are for guiding the eye) related with the simulated magnetic configurations, shown in the insets on the right. The hysteresis curves are labeled according to the initial equilibrium state at 0 mT (SMV or DMV).

The resulting plot is found to lack a hysteretic behaviour and is symmetric with respect to the maximum field, meaning that modes I/I’ and II/II’ from Fig. 7.15 are characteristic of the SMV *and* the DMV states. Qualitatively, they are also very similar to the absorption spectrum observed in the perpendicular biasing configuration between saturation and the DMV state, where the measured modes I’ and III’ were related to the inhomogeneous areas near the core region. As in Fig. 7.12 for the perpendicular biasing, Fig. 7.16 shows the mode profile at 5.75

GHz, where different standing wave patterns can be easily spotted. These are more intense near the magnetic topological defects pinned at the sample edges (i.e., the triangular vertex and the Bloch domain wall pinned at the curved edge) diverging into the domain with some excitation along the edges. The several number of excited spin wave modes may explain again the broad linewidth of the simulated and measured absorption centred at around 5.5 GHz. Mode profiles at selected frequencies show the similarities of the excited modes (see insets in Fig. 7.16) highlighting their similar nature.

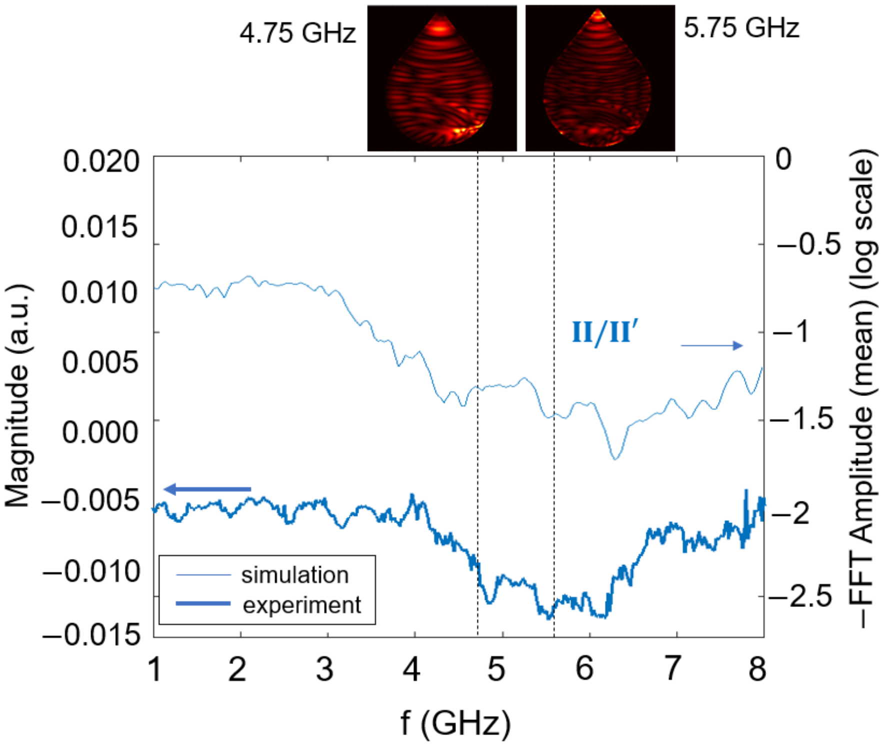

Figure 7.16 FFT spectrum from simulations and absorption spectrum from measurements with a bias field of 36 mT in a parallel VNA-FMR scheme, corresponding to the descent curve of the hysteresis loop. Inset show the modes profiles from simulations at the selected frequencies.

Snapshots (not shown here) in the first stages in time after applying a microwave excitation of 5.75 GHz perpendicular to the wall, for a biasing field of 36 mT, show that the excited spin waves emanate from the magnetic inhomogeneities, i.e., the sample edges, the top vertex of the shape and the Bloch domain wall at the bottom, pinned at the curved edge (notice the more intense areas in insets from Fig.7.16). The animation also shows edge spin waves emitted by the triangular vertex, sent down the straight edges of the shape, and edge spin waves from the Bloch domain wall along the curved edges and into the domains. Spin wave emission from a sharp corner was also found in triangular shapes (Lara, et al., 2013) in a B-state (quasi-saturated along one side of the triangle) and in the Y-state (quasi-saturated perpendicular to one side).

The teardrop shape can be regarded as a combination of a triangular shape and a circular disc and so, the B- or Y-states can be partially obtained from a perpendicular or parallel biasing VNA-FMR scheme, respectively. However, while the vertex position is fixed, the single Bloch domain wall in the teardrop shape can be pinned at different positions along the curved edge, since it is a consequence of a displaced single vortex core. This gives more degrees of freedom in using the teardrop shape as a spin wave emitter and a potential edge spin wave interferometer, due to the high configurability of the two sources (vertex and Bloch domain wall).

After identifying all the relevant eigenmodes of the sample for different magnetic configurations, we can confidently correlate the measured absorption peaks with spin wave modes in a variety of multidomain states. In the perpendicular biasing configuration, if the SMV state was initially formed, one of the modes related to resonance in a magnetic domain (mode I') is expected to be dominant until magnetic saturation, when it is converted into the FMR main mode. Under the right orientation of the bias field, the domain wall remains pinned at the vertex and therefore, modes related to other magnetic inhomogeneities 'pinned' at the edges, such as Bloch domain walls or the shape vertex should not dominate, in contrast to any other scenario. This behaviour has been observed in VNA-FMR measurements, which tells that the SMV configuration is achievable in practice, following the process shown in Fig. 7.3.

Once the SMV state is formed, the difficulty of measuring the confined modes along the domain wall in the SMV state (i.e., Winter's magnons) is mainly due to the modes' low amplitude, narrow linewidth, and small frequency separation. However, we can confidently correlate the measured absorptions with other spin wave modes in various multidomain states of the teardrop shape. After some filtering of the raw measurement, some absorption peaks may be correlated with the Winter's magnons' spectrum, which may show that these modes are measurable in practice in as thick samples as 80 nm thick on a VNA-FMR setup.

7.5 Summary

In this chapter we have studied the spin wave dynamics in a ‘teardrop’ shaped structure in the multidomain and vortex states. We have obtained approximated analytical and numerical VNA-FMR plots for the confined modes (Winter’s magnons) along the single domain wall, although there is a clear practical difficulty of detecting the out-of-plane signal of those modes, due to the small intensity of the magnetic signal. We have interpreted the asymmetric VNA-FMR plots in terms of different spin wave mode conversions from two different stable states, the Single Magnetic Vortex (SMV) and the Double Magnetic Vortex (DMV).

However, the main result of this work is not just the observation of the differences between the different VNA-FMR schemes on the teardrop shape or the different modes transformation between states, but also that we inferred that the SMV is achievable and stable (no biasing field to retain the magnetic configuration is required) in the non-saturated regime in a thick enough teardrop shape, which makes it suitable as a simple high-directional and highly reconfigurable spin wave emitter. Once this configuration is obtained, the effects of external biasing field, varying magnitude, and orientation, are explored in simulations, showing highly tuneable properties. We believe these results can help in the further development and improvement of highly reconfigurable spin wave emitters that do not require high biasing fields for operating.

Chapter 8 Future work involving novel spin wave devices

8.1 Introduction

The previous chapters of this Thesis have dealt with the study of spiral spin waves and control of confined modes in Bloch domain walls. These dynamics have been proved to be dominant in thick finite nanostructures in a flux closure domain. Therefore, they are strong candidates to become the base of magnonic devices that exploit these phenomena in absence of saturating fields. The aim of this chapter is to numerically give a proof-of-concept of these ideas which, aligned with the main objective of the Thesis, show the feasibility of designing effective spin wave devices based on non-saturated ferromagnetic nanostructures. Their implementation and further improvement are left open for future work.

In section 8.2, a conceptual spin wave phase shifter, based on the characteristic phase distribution of a spiral mode is shown. In section 8.3, a conceptual novel magnetic field nano-sensor based on spiral spin waves and the strong confinement of Winter's magnons is also shown. In section 8.4, a conceptual novel interferometer based on the dynamics on square patches is proposed.

8.2 A magnetically actuated phase-shifter based on spiral spin waves

In previous chapters, the sourcing of intense spiral spin waves from the core region has been studied. The outward propagation towards the edges, makes the magnetic patch an interesting emitter unit in a more complex magnonic circuit. The next step needed is 'extraction' or coupling to a secondary shape that acts as a channel and allows further propagation or processing of the spin wave. The system consisting of emitter and channel, may work as the basic unit in a magnonic circuit that does not require high external biasing fields. It can perform as a single spin wave device offering potential practical uses.

Here, a potential application as a magnetically actuated Spin Wave Phase Shifter is shown and explored by micromagnetic simulations, fully operational in the non-saturated regime. Other phase-shifting mechanisms, such as interaction of spin waves with magnetic inhomogeneities and domain walls (Hertel, et al., 2004; Vasiliev, et al., 2007; Chang, et al., 2018), self-biased large arrays with magnetic defects (Louis, et al., 2016) and bilayer structures (Au, et al., 2012), magnetoelectric structures (Khitun & Wang, 2011) or flow of electric current previously (Hansen, et al., 2009; Lee & Kim, 2008; Demidov, et al., 2009) have been explored. However, in most of the mentioned works, the existence of an emitted spin wave from a different structure is assumed or it requires externally attached microwave antennas for locally exciting the source spin wave at a fix position in the film. In contrast, a more compact, simpler design proposed here is based on the displacement of the wave source itself, in this case a well formed vortex core in a single film disk, with respect to the coupled output channel at the edge of the disk. This induces a phase delay when the emitted spin wave reaches the edge. The core displacement is achieved by means of a low intensity biasing field B_{bias} and no electrical currents or externally attached devices are required, which shows the simplicity of the structure.

Therefore, the proposed design is a magnetically actuated phase-shifter based on a Permalloy disk as those studied in Chapter 4, with diameter 900 nm and thickness 80 nm, and a straight film, 10 nm wide and 80 nm thick, coupled to the topmost edge of the disk. A width of 10 nm is chosen for practical purposes since a common limit in e-beam lithographic writing techniques on PMMA is of a few tens of nanometers (Broers, 1988), although features smaller than 10 nm can also be obtained using other resists such as hydrogen silsesquioxane (Cumming, et al., 1995; Manfrinato, et al., 2013). All micromagnetic simulation parameters are the same as in chapter 4. The straight film resembles more to a ‘wall’ due to the low width/thickness ratio.

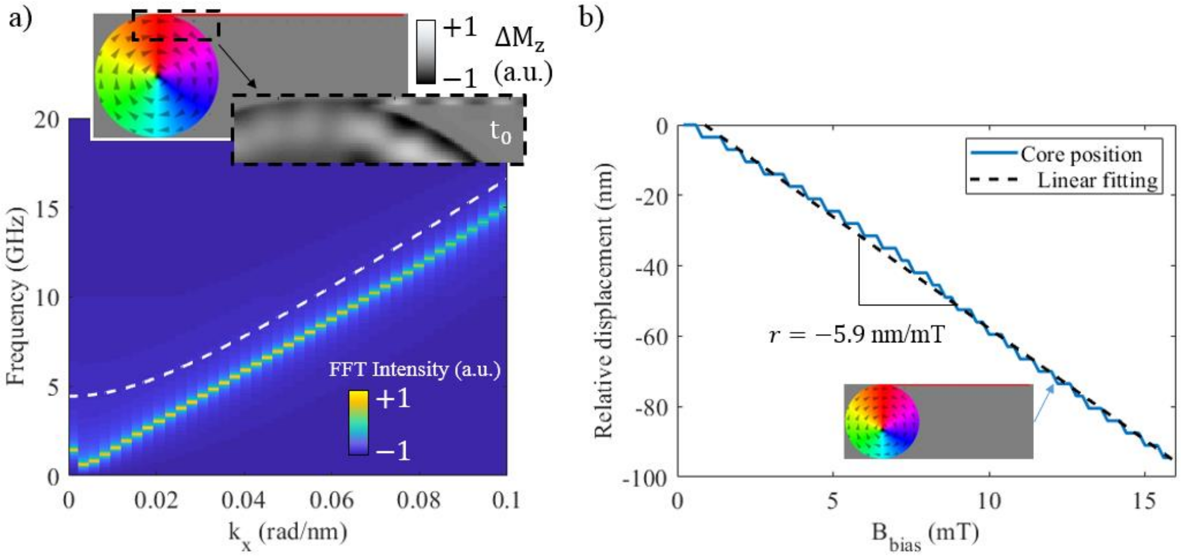

Figure 8.1 (a) (Top) Schematic of the proposed phase-shifter, the inset shows the coupled spin wave in the rectangular stripe attached to the edge of the disc and (below) dispersion relation inferred from the FFT normalised intensity plot for the rectangular stripe (colour plot) with the spiral spin wave dispersion overlapped (white dashed line). (b) Tracked core position from simulations for several biasing fields in steps of 0.5 mT, from which a linear fitting yields the core displacement to bias ratio *r*. Inset shows the magnetic configuration at 12 mT.

Fig. 8.1(a) shows the schematic of the structure and the analytical dispersion relation for the spiral mode from Chapter 4 and the simulated dispersion relation of the coupled 'wall'. For the given dimensions, Fig. 8.1(a) shows there is a wide range of frequencies, above ~7 GHz, where the mode coupling takes place, and the group velocity is approximately constant with a value of 125 m·s^{-1}. Theoretically, the coupling could be improved making the output magnonic waveguide narrower, but for practical reasons stated before, the minimum width is limited to 10 nm. The coupling is also expected to decrease (increase) if a biasing field is applied parallel (antiparallel) to the length of the 'wall'. This is inferred from the definition of a magnetostatic backward volume spin wave where, at the magnetostatic limit, $\lim_{k\to\infty} f(k) \to \omega_0$. An excitation frequency of $f_0 = 9$ GHz is chosen, which in absence of a biasing field, yields a k-vector for the spiral spin wave of approximately $k_0 = 0.05$ rad·nm^{-1}. Fig. 8.1(b) shows the displacement of the vortex core which yields a linear displacement to bias ratio $r = -5.9$ nm·mT^{-1} used in the following calculations of the phase delays. This agrees with previous works which shows an approximately linear displacement for low bias fields (< 15mT) (Yakata, et al., 2013).

The induced phase delay at a certain frequency can be expressed as $\Delta\varphi = k_0 d$, where $d = rB_{bias}$. A more realistic wavevector, slightly smaller, will introduce an error in the final phase delay, but allows us to extract a more physically consistent result from the model, since real wavenumber will be affected by external biasing. We set the effective wavenumber to $k_0 = 0.045$ rad·nm^{-1}, a 10% smaller than its original magnitude (see Fig. 8.1). This introduces a maximum error of 10% (0.005 rad·nm^{-1}) in our calculated phase delay in absence of biasing, but it will decrease as the biasing field increases. This altogether leads to a result of $\Delta\varphi \approx -0.27 \cdot B_{bias}$. This result implies that for a full π-delay ($\Delta\varphi = \pi$), a biasing field of approximately 11.8 mT is required. It is worth to point out again that this result is approximated and rounded down since k_0 will slightly reduce in magnitude as the biasing field increases.

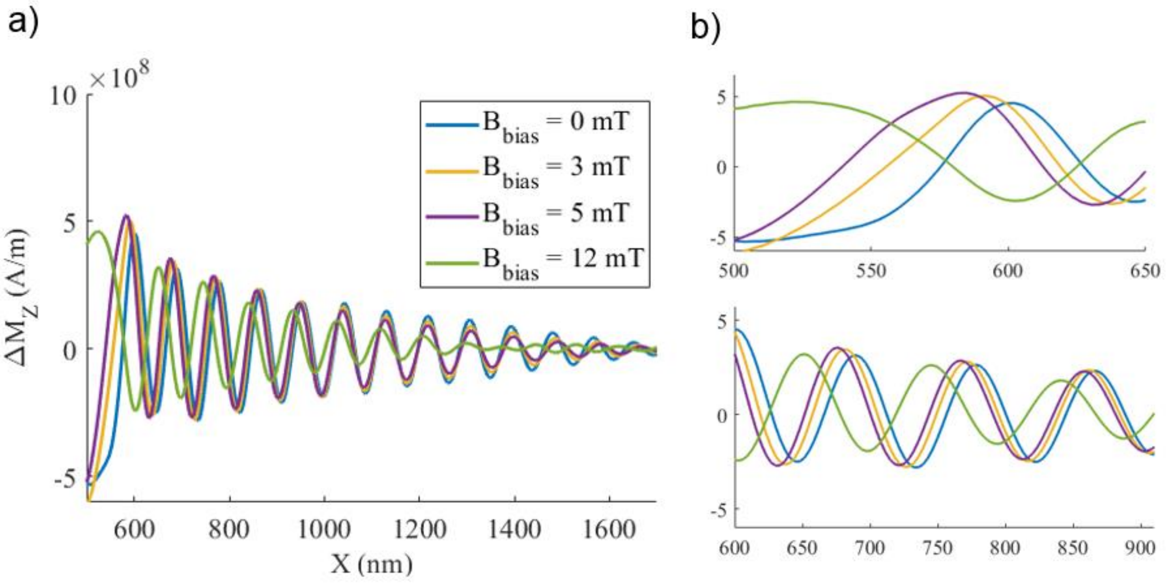

Figure 8.2 (a) Spin wave profile along the rectangular stripe for different biasing fields and (b) insets showing a closer look at (top) the joint position and (below) further in the stripe, showing a π-delay at 12 mT with respect to zero bias (see x = 600 nm) and different phase velocities for different biasing, respectively.

Fig. 8.2(a) shows the wave profile from numerical results at a certain time along the centre of the coupled stripe structure. The induced phase delays of $\pi/4$, $\pi/2$ and π in the 'output' channel for the applied biasing fields, 3 mT, 6 mT and 12 mT, respectively, show good agreement with the analytical result of $B_{bias} \approx 11.8$ mT, see Fig. 8.2(b). More importantly, at the chosen excitation frequency of 9 GHz, a full π-phase delay can be achieved with an external field ×4 times smaller than the saturation magnetisation of the structure ($\sim$50 mT), which allows it to operate with fields way below that limit and not introducing significant or irreversible changes in the magnetic domain configuration. It is worth noting that, at higher frequencies, the wavenumber will increase, and an even smaller biasing field will be required for a π-phase change. In addition to this, reversing the sense of the biasing field would cover the remaining phase delays up to 2π (0 rad), from 0 to $-\pi$, or equivalently reducing the field strength, from π to 0 radians again.

At long distances, Fig. 8.2(b) (below) also shows that phase velocity of the channelled wave increases when the biasing field is stronger. This can be explained by the effect of the biasing field on the internal magnetic field: In a thin film with tangential magnetisation, the biasing field dominates in the internal field expression. As field increases, the FMR frequency will also increase according to $\omega_0 = |\gamma|\mathrm{H_{Bias}}$. In the exchange dominated regime for Backward Volume Spin Waves, this implies that its wavenumber will accordingly be reduced in $\Delta\mathrm{k}$ to maintain a constant frequency, $\omega = \omega_0 + \omega_M \lambda_{ex} k^2 = \omega_0 + \Delta\omega_0 + \omega_M \lambda_{ex}(k + \Delta k)^2$, which explains the observed increase in phase velocity. The change in the FMR frequency can be regarded as $\Delta\omega_0 = |\gamma|(\Delta\mathrm{H_{Bias}})$, it can be trivially found from the previous dispersion relation that:

$$\Delta\omega_0 = 2\lambda_{ex}\omega_M \mathrm{k}_0 \Delta\mathrm{k} - \lambda_{ex}\omega_M(\Delta\mathrm{k})^2. \qquad (8.2.1)$$

In practice, since $2\mathrm{k}_0 \gg \Delta\mathrm{k}$ as variations of the k-vector with respect $\mathrm{k}_0$will be small, the quadratic term of the equation can be neglected. Fig. 8.3(a) shows $\Delta\mathrm{k}$ as a function of $\Delta\mathrm{H_{Bias}}$ taking into account that $\Delta\mathrm{H_{Bias}}$ is limited to be always less than the value of saturation field for Permalloy ($\mu_0\Delta\mathrm{H_{Bias}} < 50$ mT). For low values of $\Delta\mathrm{k}$ and within the range of ‘operational band’ of biasing fields ($\mu_0\Delta\mathrm{H_{Bias}} < 12$ mT), the expression can be approximately replaced by the linear term only. Therefore, the reduced phase velocity of the channelled spin wave can be regarded as,

$$v_p = \frac{2\pi f_0}{k_0 + \Delta k} = \frac{2\pi f_0}{k_0 + \frac{|\gamma|}{2\lambda_{ex}\omega_M \mathrm{k}_0}\Delta \mathrm{H}_{\mathrm{Bias}}}\ . \tag{8.2.2}$$

Fig. 8.3(b) shows a plot of Eq. 8.2.2 and the relative phase velocity of the spin wave obtained from micromagnetic simulations at 3 mT, 6 mT and 12 mT, calculated as the ratio of the periods completed within 300 nm distance along the output structure of the signal in absence of external field (blue curve in Fig. 8.2(b)) to those with bias (other curves in Fig. 8.2(b)). These ratios show good agreement with Eq. (8.2.2) and show a maximum reduction in phase velocity of approximately 6.2%, at the maximum phase shift of π radians (i.e., at 12 mT biasing field). Phase is traveling at 93.8% of its original velocity in absence of bias. Inverting the ratios $\left({}^{v_{p,0}}/_{v_p} = {}^{k}/_{k_0}\right)$, the equivalent maximum increase in wavenumber can be found, showing an approximate maximum 6.6% increase in wavenumber at the maximum phase shift of π radians. From this result, it can be seen that our approximation of considering an error of 10% in the wavenumber as the biasing field increases is tolerable, and even pessimistic perhaps, up to 20 mT, although this is over the ‘operational band’ of the phase-shifter for the chosen excitation frequency.

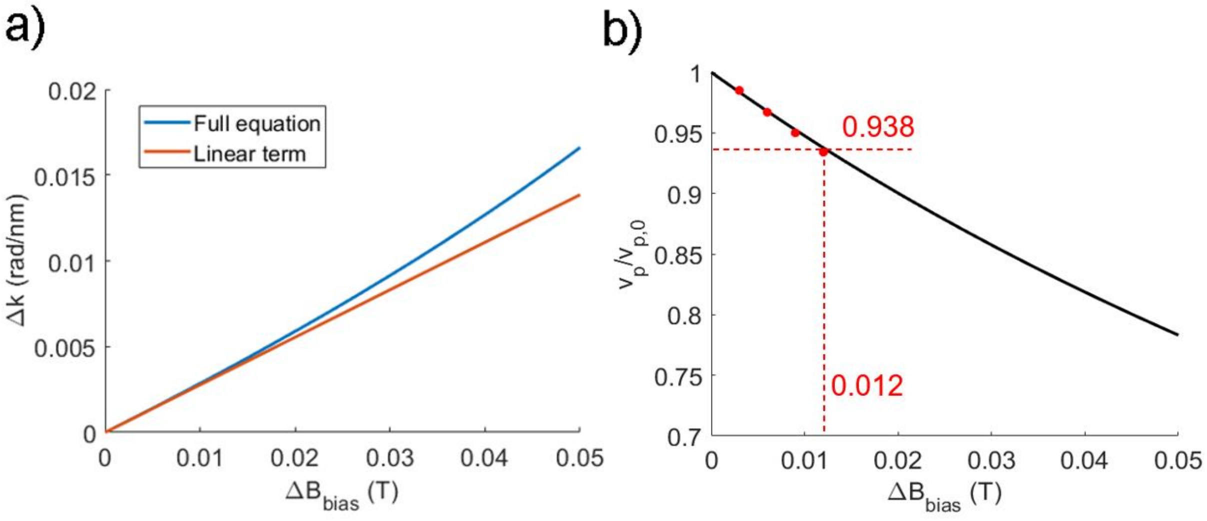

Figure 8.3 (a) Variations of wavenumber with respect of the biasing field described by the analytically obtained full equation Eq.(8.2.1) (blue curve) and its linear term only (orange curve) below saturation fields. (b) Normalised

phase velocity of the channeled wave with respect ot the biasing field, described by Eq. (8.2.2). Results from micromagnetic simulations and the maximum reduction relative to no bias (6.2%) at 12 mT is shown in red.

External biasing fields of different magnitude, required for the operation of the phase-shifter, will induce different phase velocities to the channelled waves. However, due to the good agreement with numerical results, Eq. (8.2.2) allows to predict how much the channelled waves will be affected by this aberration, helping on the control of the spin wave propagation.

The above calculations are done for an excitation frequency of 9 GHz. The lower limit of the operational frequency is obviously the lowest frequency at which the spiral spin wave can be excited and efficiently coupled to the structure, i.e., from respective dispersion diagrams, around 8~9 GHz. Ideally, there is no upper limit in frequency since the coupling and the spiral spin wave would still occur beyond that frequency. As stated before, at higher frequencies, the wavevector k_0 will increase which reduces even further the required biasing field for a complete $\Delta\varphi = \pi$ phase shift, ($\Delta\varphi = -r\Delta B_{bias} k_0$). However, concerning the propagation of pulses and therefore, the transmitted information, this will inevitably introduce a dispersive character for the phase shifts such as:

$$\Delta\varphi(\omega) = -r\Delta B_{bias}\omega\frac{\partial k}{\partial\omega}\,, \tag{8.2.3}$$

where, from Fig.8.1(a) at k > 0.05 rad nm^{-1}, a quick calculation of the slope yields $\frac{\partial\omega}{\partial k} \approx 1046.66$ m s^{-1}. This would lead to a pulse signal velocity of 1046.66 m s^{-1} and no group velocity dispersion, i.e. no effective pulse broadening of the signal for a pulse spectrum between approximately 9 GHz and 20 GHz at least. Fig. 8.4 shows the different operational bandwidths, phase shifts from 0 radians to π radians (grey shaded area) in frequency and biasing field (i.e., the controllable variables) from Eq. (8.2.3) for the proposed phase shifter. The maximum biasing field required for a full π-phase shift decreases with frequency. At very high frequency, 20 GHz, the model predicts that the required field for a complete π-phase shift is as small as 5 mT, this is about ten times below the saturation field. At the lowest frequency, around 8 GHz, that field is larger but still about four or five times below saturation fields. Therefore, the phase shifter performs well in the entire range of frequencies with only small bias field needed to obtain the necessary shifts.

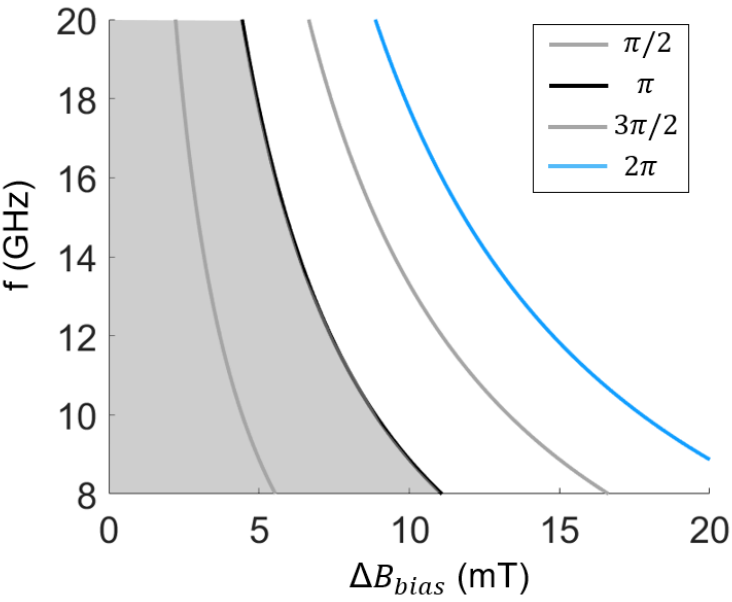

Figure 8.4 Results for frequency and biasing field from Eq. (8.2.3) for phase shifts of π/2 (grey curve on the left), π (black curve), 3π/2 (grey curve on the right) and 2π radians (blue curve). Grey shaded area shows the range of biasing fields that covers a whole excursion of π-phase shift for every frequency from 8 GHz to 20 GHz, i.e. the 'operational band' of the phase shifter.

Another key parameter is the operation speed of the device to set stationary states, in this case, coded into the phase of a spin wave emitted in different magnetic states of a displaced vortex core. Therefore, a transient time between states will set a limit to the maximum speed of operation. This transient time will be predominantly the time required for the core to displace to the new position (speed of core displacement) plus the time to bring the new magnetization state into a steady state. During that transient period, the displacement of the core is affected by the gyrotropic field (Thiele, 1973) and therefore, a non-straight trajectory, non-linearities (Guslienko, et al., 2006; Guslienko, et al., 2008) and incoherent spin wave emission may arise, making the device not operational while they last. For example, a 'transient time' of ~238 ns was measured before a displaced core is fully damped in square patches after a step function-like magnetic pulse is applied (Bukin, et al., 2016). In a binary digital transmission using a standard PSK (Phase Shift Keying) scheme, where the symbol rate is equivalent to the bit rate, based on the previous result from (Bukin, et al., 2016) a maximum bitrate of approximately 4.2 Mbps (calculated as the inverse of the 'transient time' for the PSK scheme) would be obtained in the worst-case scenario. Nevertheless, the bitrate limit can be pushed up by using other symbols based on more phase-shifted signals. For example, using four different spin waves with phase shifts of 0, π/2, π and 3π/2 (four symbols), theoretically doubles the bitrate up to 8.4 Mbps since it takes two binary digits to encode four states/symbols (‘00’, ‘01’, ‘10’ and ‘11’).

The transient time would set a major drawback for the design proposed here and for any fully magnonic device that requires changing magnetic static configuration, although it could be compensated using a different doped magnetic material to increase damping and thus reduce the transient time (Au, et al., 2012). In principle, this would drastically increase the bitrate of the device. Potential spin wave devices may be developed from this structure as a basic building unit, as shown in the next section. Moreover, following on from previous chapters, a richer collection of spin waves can be emitted in patches of different shapes, which enriches the potential applications.

8.3 A magnetic field nano-sized sensor based on a balanced phase shifter

A wide range of different DC-magnetic field sensors or magnetometers have been developed and commercialized including those based on solid state physics (Heremans, 1993), such as Giant Magneto-Resistance (GMR) (Reig, et al., 2009; Dogaru & Smith, 2001) or the Hall effect (Popović, 1989; Ramsden, 2006). Magnetic nanoparticles deposited on a YIG film have been proposed as gas sensors (Matatagui, et al., 2015; Ciprian, et al., 2016), fibre-optic and photonic interferometry based on Faraday or magneto-optical Kerr effect (Qiu & Bader, 2000) or magnetic fluids (Saker, et al., 2019; Dai, et al., 2011; Alberto, et al., 2018) have also been extensively studied. In magneto-optic sensors, the sensing of the external magnetic field is typically performed by changes in the index of refraction of the magnetically actuated material (the ferrofluid).

Fully magnonic magnetometers (for sensing static/quasi-static fields) or ‘susceptometers’ (oscillating fields) have not been that widespread, in part due to their early stage of development. Relevant research on these novel types of sensors has been conducted, principally susceptometers based on magnonic crystals of soft magnetic materials such as YIG (Atalay, et al., 2015; Inoue, et al., 2011), with sensitivities in the order of nanoteslas. These results make them interesting candidates for sensing magnetic fields due to their high compactness and very small size, in contrast to other more complex technologies such as SQUID (Superconducting QUantum Interference Devices) or GMI (Giant Magneto-Impedance). SQUID magnetometry holds nowadays a record in sensitivity in the order of nanoteslas and even femtoteslas (Buchner, et al., 2018) although the required materials and structure are complex, expensive to fabricate and potentially not operational at room temperature. Current GMI sensors also show low noise floor and very good sensitivity in the order of nanoteslas (Zhang, et al., 2017) and are used in a variety of fields such as biomolecules detection (Chiriac, et al., 2005), magnetocardiography and magnetoencephalography (Wang, et al., 2017; Karnaushenko, et al., 2015), accelerometery, geomagnetic measurements and much more (Asfour, 2017). However, their design and fabrication are generally more complex than a fully magnonic sensor.

It is not the aim of this section to summarize all the types of magnetometry and/or susceptometry but to put the focus on magnetometry performed by magnonic devices and show a proof of concept. In fact, not much work on full magnonic sensors can be easily found in the literature. Some of the examples include the work by Balinsky *et al.* (2017) (Balynsky, et al., 2017), which shows a cross-shaped interferometer where the sensing is performed by the changes in dispersion in both arms of the cross, due to the external field. It shows very good sensitivity, comparable to GMI sensors, and allows to detect magnitude and orientation of the bias field.

In this section, a nano-size magnetometer based on interferometry and spiral spin wave dynamics in a circular disc in the Single Magnetic Vortex state is explored and a proof-of-concept of its functionality is provided. The potential device is fully magnonic and does not require DC external fields, apart from the one to measure. Its design allows to sense not only magnitude but also orientation of the DC magnetic field.

Fig. 8.5(a) shows a schematic of the proposed structure from micromagnetic simulations. The device is based on a disc in the magnetic vortex state where the core acts as source of the spin waves, which are 'extracted' by mode coupling at two opposite positions (1) and (2) at the edge of the disc. Two thin magnetic tracks in a U-shape are attached to the output positions, and the reading-out point, or ‘detector position’, is the meeting point of the curved tracks.

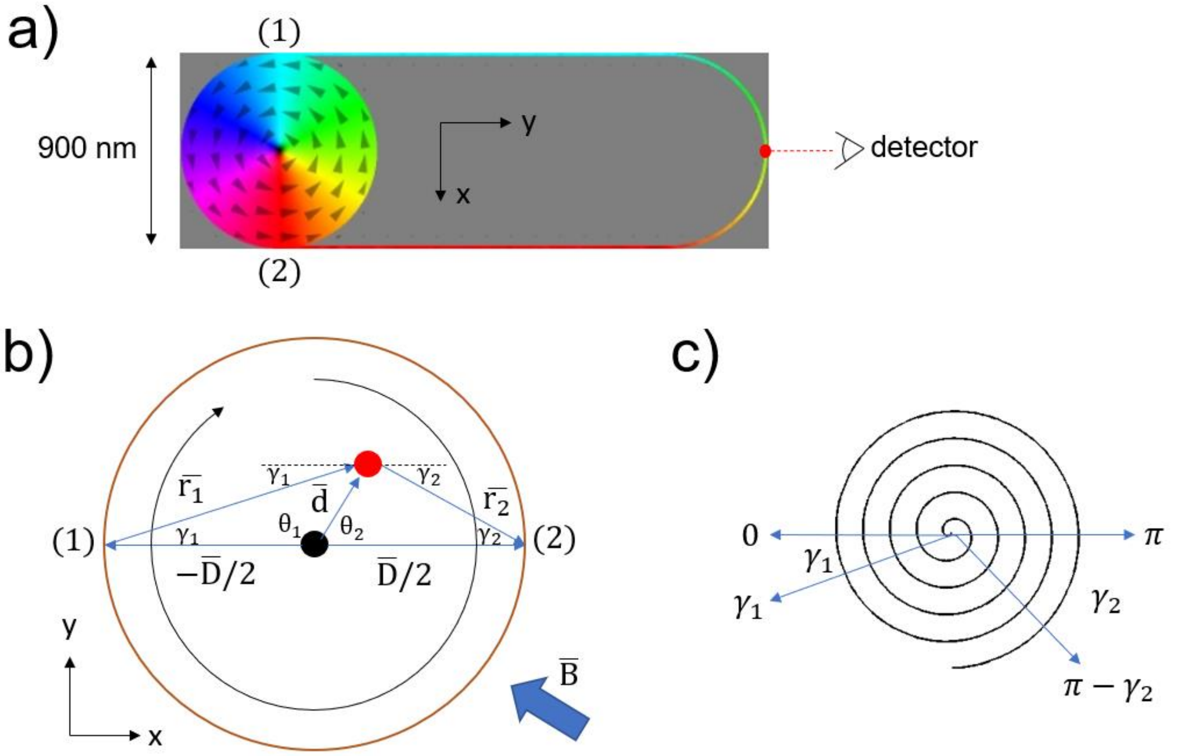

Figure 8.5 (a) Schematic of the proposed structure based on a 900 nm diameter and 80 nm thick disk. The red spot shows the detector position. (b) Schematic of the trigonometric relations of a displaced vortex core (red dot) and the coupling positions in the disc (1) and (2). (c) Schematic of phase for a spiral wavefront.

Firstly, a precise mathematical description of the output spin wave’s phase is required. Fig. 8.5(b) shows a schematic of the trigonometric relation between a displaced vortex core (red dot) and the ‘output’ positions in the disc (points (1) and (2)). The vortex core is assumed to have circulation number of $\mathrm{C} = -1$ which, in conjugation with the orientation of the external magnetic field, will dictate the direction of the core displacement, expressed as in

$$\mathbf{d} = \mathrm{C} \cdot \mathrm{r_d} \cdot \left(\mathbf{B_x} - \mathbf{B_y}\right), \tag{8.3.1}$$

where $r_d = -5.9\ \mathrm{nm} \cdot (\mathrm{mT})^{-1}$ is the displacement to bias ratio of the vortex core. From the trigonometrical relation between magnitudes, it can be trivially found that the distances $\mathbf{r_{1,2}}$ and angles $\theta_{1,2}$ are,

$$\mathbf{r_1} = -\mathbf{d} + \frac{\mathbf{D}}{2}\ , \tag{8.3.2}$$

$$\mathbf{r_2} = -\mathbf{d} - \frac{\mathbf{D}}{2}\ , \tag{8.3.3}$$

$$\theta_1 = \mathrm{atan}\left(\frac{-B_y}{B_x}\right)\ , \tag{8.3.4}$$

$$\theta_2 = \pi - \theta_1\ . \tag{8.3.5}$$

According to these formulas, the ‘output’ phases $\gamma_{1,2}$ at positions (1) and (2) are described by the equations,

$$\gamma_1 = \mathrm{asin}\left(\frac{d}{r_1}\sin\left(|\theta_1|\right)\right)\ , \tag{8.3.6}$$

$$\gamma_2 = \mathrm{asin}\left(\frac{d}{r_2}\sin\left(|\theta_2|\right)\right)\ , \tag{8.3.7}$$

Fig. 8.5(c) shows the case for an archimedean spiral wavefront, which must be accounted for in the ‘output’ phases at (1) and (2). This implies that the initial phase of the spin wave along the two different paths must be corrected as in $\varphi_1 = \gamma_1$ and $\varphi_2 = \pi - \gamma_2$. Additional delays along the paths inside the disk are described as $\Delta_{1,2} = k_0 \cdot r_{1,2}$, where k_0 is the spin wave wavenumber for a microwave excitation of frequency f_0. Therefore, the total phase at (1) and (2) will be $\varphi_{1,2} = \gamma_{1,2} + \Delta_{1,2}$.

Finally, at the ‘read-out’ point, the superposition of the two channelled spin waves will yield a final wave described by $m = e^{i(\varphi_1)} - e^{i(\varphi_2)} = e^{i(\gamma_1 + \Delta_1)} - e^{-i(\gamma_2 - \Delta_2)}$. Note that at this point, the damping along a longer path for one of the spin waves in the disc is not accounted for the final total amplitude and it is normalised to one. Neither attenuation along the parallel magnetic tracks nor phase delay along them is considered. The difference of travelled paths between the two waves is considered negligible since the device is balanced, and amplitudes of the two waves are assumed identical. The resulting superposition will give a total phase and maximum peak amplitude or magnitude for the out-of-plane component of magnetization ($|m_{\mathrm{p,z}}|$) and argument ($\arg(m_{\mathrm{p,z}})$),

$$|m_{\mathrm{p,z}}| = 2\left|\sin\left(\frac{\gamma_1 + \gamma_2 + \Delta_1 - \Delta_2}{2}\right)\right| \, , \tag{8.3.8}$$

$$\arg(m_{\mathrm{p,z}}) = -\mathrm{atan}\left(\mathrm{cotan}\left(\frac{\gamma_1 - \gamma_2 + \Delta_1 + \Delta_2}{2}\right)\right) \, . \tag{8.3.9}$$

These analytical equations yield amplitude and phase maps which relate the external biasing field (implicitly found in $\gamma_{1,2}$ and $\Delta_{1,2}$) and the 'read-out' magnitude and phase. Fig. 8.6 show the mapping between the 'read-out' magnitude and phase and the external field for magnitude and phase.

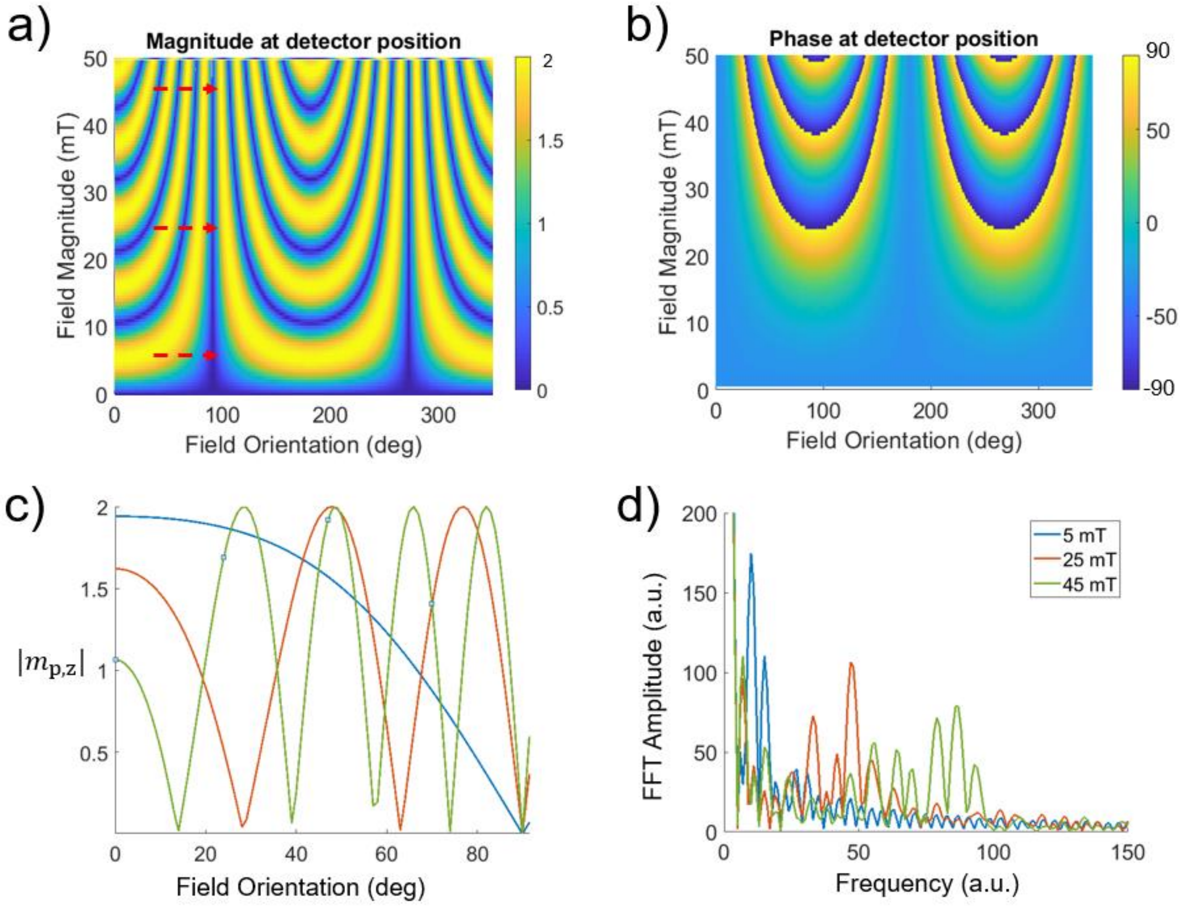

Figure 8.6 (a) Contour plot for the out-of-plane magnetization from Eq. (8.3.8) representing magnitude and (b) from Eq. (8.3.9) for phase at the 'detector position'. Red dashed line (and (c)) shows different gradients in out-of-plane magnetization magnitude for three different external field magnitudes of 5 mT, 25 mT and 45 mT but same range of field orientations. (d) Frequency analysis of the magnitudes recorded in (c).

Analytical results from Fig. 8.6(a) clearly show that the relation between the external field and the detected out-of-plane magnetization is not univocal. This is due to the non-bijectivity of the periodic source signal, which may complicate absolute measurements for inferring the actual magnitude and orientation of the external field.

Differential measurements can help to overcome this uncertainty. For example, varying the external field magnitude has an impact on the maximum detected magnetization in terms of a slow or fast variation (see red arrows in Fig. 8.6(a)) for the latter, which will give information about the field original orientation. Fig. 8.6(c) shows the detected spin wave peak amplitude against the field orientation for three different field magnitudes, 5 mT (blue curve), 25 mT (orange) and 45 mT (green). Vice versa and equivalently, by rotating the device while field magnitude remains unaltered, the relative phase to the external field orientation will be modified. This way, the speed of variation on the 'read-out' magnitudes can tell about the external magnetic field original orientation. In other words, by simply rotating the sensor, less than 90 degrees, the change in the 'read-out' magnitude, in terms of a larger or smaller gradient can help to locate the external field magnitude within a range of values in the order of tens of militeslas $(0\ \mathrm{mT} < \mathrm{B} < 10\ \mathrm{mT}, 10\ \mathrm{mT} < \mathrm{B} < 20\ \mathrm{mT}\ldots)$. The 'speed of variation' or 'frequency of change' can be easily found through frequency domain processing tools, as seen in Fig. 8.6(d), and therefore field magnitude range can be discriminated.

Once the range of the magnitude is narrowed down into approximately tens of militeslas, the absolute value of the field magnitude in units of militeslas is less uncertain, since in that scale, the relation between the measured amplitude and the field magnitude is found to be bijective (see Fig. 8.7(b)). In this case, if one property of the field is known (either magnitude or orientation), the other would be univocally deduced at least between 0 and 90 degrees of orientation. It is worth noting that this ranges vary depending on the frequency of oscillating field applied, due to the dispersion relation of the spiral spin wave, that dictates shorter wavelengths as frequency increases.

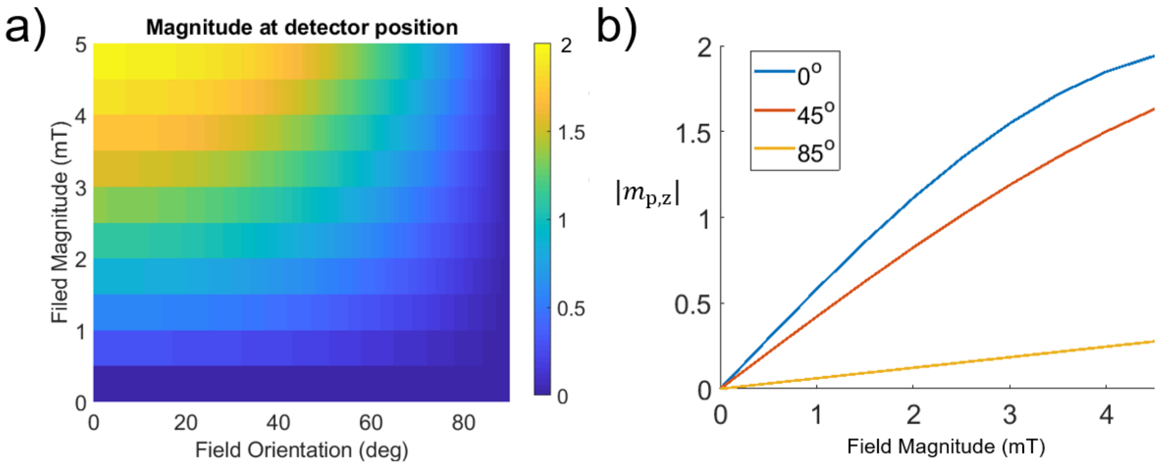

Figure 8.7 (a) Contour plot for a smaller range of field magnitude, between 0 mT and 5 mT and orientation, between 0 and 90 degrees. (b) Cut for a field orientation of 0, 45 and 85 degrees.

Adding extra sensors and placing them with a relative phase between each other will also help to measure the absolute value of the 'read-out' magnitude at once through differential measurements. This way, an estimation of the external biasing field can be inferred from the operation of the proposed magnetic field sensor.

In conclusion, the sensitivity of the conceptual magnetic sensor presented here is in the order of mT, which makes it a high-field full-magnonic magnetic sensor. It may operate in a similar sensitivity range where Hall-effect sensors typically operate. The proposed sensor is compact, small and as a novelty, fully magnonic.

8.4 A Mach-Zehnder interferometer based on spiral spin waves

Spin wave interferometry has been widely studied and regarded as a basic step towards developing more complex spin wave logic (Kanazawa, et al., 2016; Lee & Kim, 2008; Vasiliev, et al., 2007). A standard design is a Mach-Zehnder interferometer, typically based on interferometry of controlled phase delayed waves. Following from previous chapters, an interferometer based on the thick square patches studied in Chapter 4 and the phase-shifter from section 8.2 is proposed and explored by micromagnetic simulations. The structure is based on two square patches in a Landau state, whose vortex cores act as sources of the spin waves, and where the connecting elements are magnetic thin films, in-plane saturated, perpendicular to the plane of the squares, which resemble more to thin 'walls' in a Y-shaped interconnection. Another possible junction for combining the waveguides is in a circular shape to avoid magnetic frustration (Kim, et al., 2018). As in section 8.2, it is worth to note that the saturation in this Y-multiplexer is achieved by the intrinsic shape anisotropy of the structure and no external biasing field is applied. Two of its branches are directly attached to one corner in each square patch. Fig. 8.8(a) shows a schematic of the proposed structure from micromagnetic simulations, which resembles to a standard Mach-Zehnder interferometer.

The conversion between the square patch modes and the Backward Volume Spin Wave in the saturated 'stripe', facilitates propagation along the Y-shaped structure. This is achieved through an efficient coupling between the two shapes. Looking into the dispersion relations of both modes (see Fig. 4.4 for the Winter's Magnon and Fig. 8.1 for the Damon-Eshbach and

Backward Volume modes, an excitation frequency of 8.8 GHz is chosen for simulations, which yields a wavenumber of approximately 0.045 rad nm^{-1} for all modes.

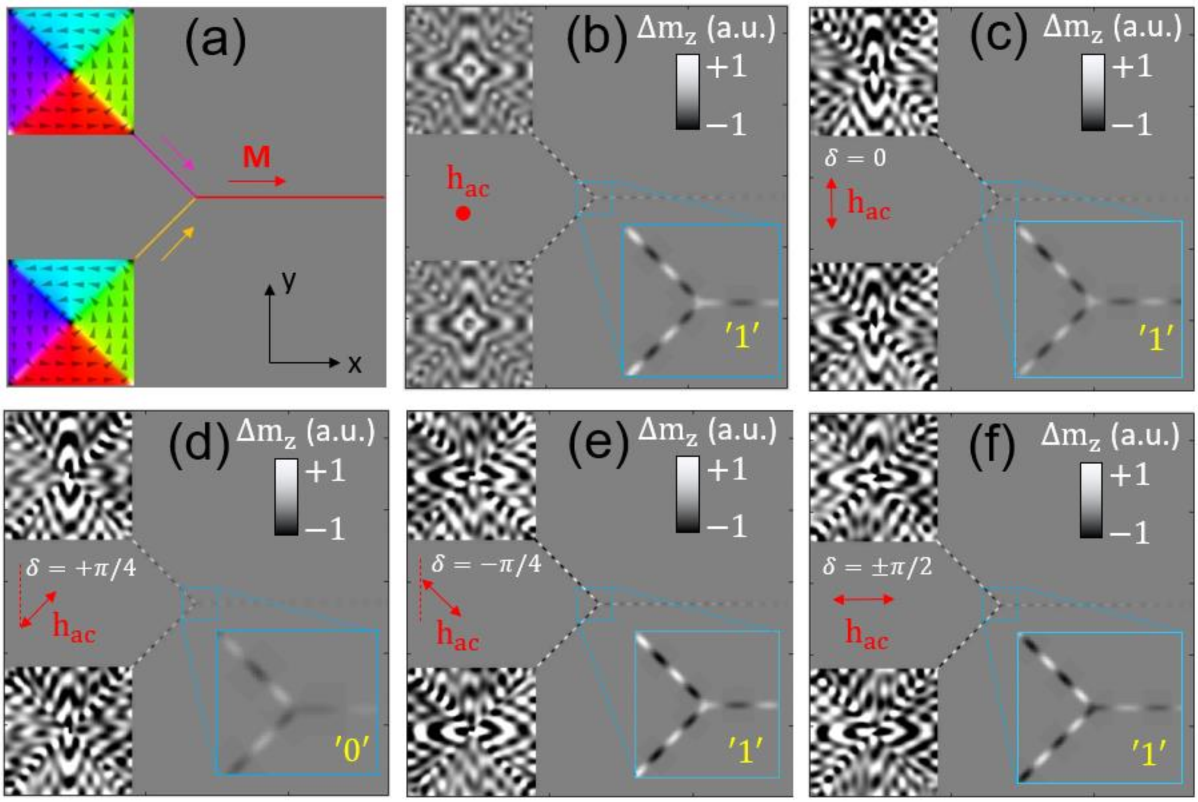

Figure 8.8 (a) Schematic of the proposed interferometer, based on two square patches and a Y shaped waveguide where magnetization orientation is indicated by the colour scale. Micromagnetic results of the normalized dynamic out-of-plane component of magnetization when a pumping field (h_{ac}) is applied (b) perpendicular to the sample plane and in-plane with an angle (c) $\delta = 0$, (d) $\delta = \pi/4$, (e) $\delta = -\pi/4$ and (f) $\delta = \pi/2$ with respect to the y-direction. The interpreted bits '1' or '0' could be coded in the output spin wave amplitude due to constructive or destructive interference, respectively.

Fig. 8.8 shows the basic operation of this interferometer: When an out-of-plane pumping is applied to the centre of the square elements, the spin waves from emitter are channelled along the 'input' branches of the Y-shape structure, constructively interfering in the 'output' branch (mode 'ON'). We also observe magnetic frustration happening at the joint between the 'stripe' and the square corner, see Fig.8.8(a). This frustration makes magnetisation to point out-of-plane, analogous to a partial Bloch Line in a Bloch domain wall (Wang & Wang, 2015). This inhomogeneity may introduce a phase shift to the spin waves, but since this will occur in both arms of the structure, the global effect is self-compensated. Depending on the angle of the in-plane pumping field, we observe that a variety of different interference scenarios can occur, from fully constructive for $\delta = 0$ radians (Fig.8.8(c)), fully destructive (Fig.8.8(d)) for $\delta = \pi/4$ and partially constructive (Fig.8.8(e and f)), for $\delta = -\pi/4$ and $\delta = \pi/2$. The 'bits' 1 or 0, can be coded in the type of interference obtained and therefore into the spin wave amplitude for a given logical level.

We believe this diversity of interferences has an origin in the complex total phase of the spin wave that reaches the square vertex and then the Y-shape structure, which is a combination of the domain wall and the triangular domains spin dynamics at such high frequencies. Despite of this complexity, micromagnetic simulations clearly show that the applied field can be orientated in such a way ($\delta = \pi/4$) that the channelled spin waves are almost completely out-of-phase and they destructively interfere in the 'output' branch (mode 'OFF'), see Fig.8.8(d). More importantly, micromagnetic simulations show that, depending on the field orientation, constructive or destructive interference may happen. We believe the right combination of spin waves from each of the squares allows more intermediate combinations and all are susceptible to be controlled by means of an external oscillating pumping field.

To further understand the outcomes from the simulated scenarios from Fig. 8.8, Fig.8.9 shows results for an excitation frequency of 3 GHz, and thus, only confined modes are excited. At such low frequency, they are not efficiently coupled to the Y structure due to the differences in the dispersion relations (see section 8.1) and so, they only propagate in the squares. One can see that, depending on the field orientation, the intensity of the spin wave along one diagonal is enhanced in contrast to the other. This agrees with the flexural nature of a domain wall mode, which is enhanced if the microwave field is applied perpendicular to the wall axis.

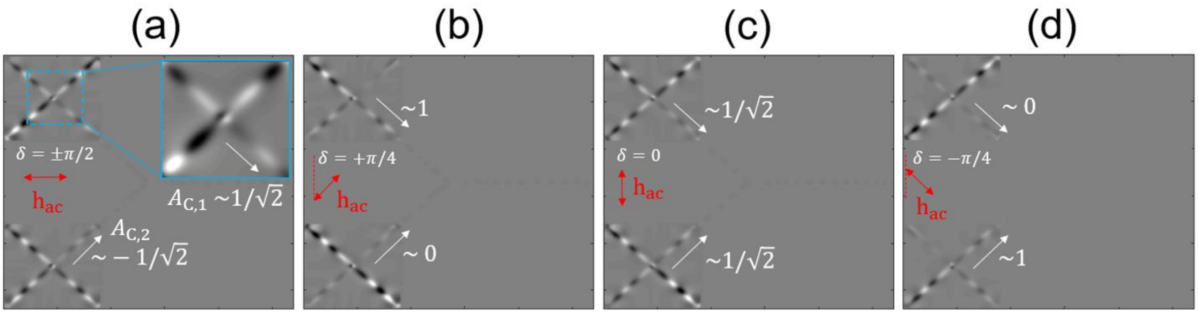

Figure 8.9 Micromagnetic results for an excitation frequency of 3 GHz applied in an angle (a) $\delta = \pi/2$, (b) $\delta = \pi/4$, (c) $\delta = 0$ and (d) $\delta = -\pi/4$ with respect ot he y-direction. Confined spin waves are excited more or less efficiently upon the field orientation, but there is also a balanced pairing in phase along the different diagonals (see inset in (a)). The normalised approximate amplitudes of the excited spin waves travelling along the diagonals of the squares (white arrows), connected to the Y-structure, are shown.

When the pumping field is applied along x- or y-directions ($\delta = \pi/2$ and $\delta = 0$, respectively), spin waves along both diagonals (domain walls) seem to be more equally excited although with less intensity due to the orientation of the applied field and the exerted torque. Also, in Fig. 8.9, for $\delta = \pi/2$, both waves seem to be in opposite phase. This implies that destructive interference should occur only when $\delta = \pi/2$, since maximum amplitudes of both spin waves would be alike and in opposite phase. From visual inspection and taking into account these conditions, the channelled spin waves' amplitudes can be naively modelled as,

$$A_1 = \cos\left(\delta - \pi/4\right)\ , \tag{8.3.10}$$

$$A_2 = \cos\left(\delta + \pi/4\right) . \tag{8.3.11}$$

However, when the dynamics of the spiral spin wave radiated into the domains is accounted for, an additional term must be added to each channelled spin wave amplitude. It is worth noting that the wavelength of the spiral into the domain is considerably larger than the one of the wall confined mode, but this difference is less pronounced close to the domain wall (as discussed in Chapter 4) and thus, the contribution of the spiral wave close to both sides of the domain wall can be generally assumed.

Fig. 8.10(a) shows a schematic for the contribution of a spiral wavefront to the spin wave phase front. For example, for an applied field in an angle of $\delta = 0$ radians, the spiral wavefront aligned with the domain walls is $\pi/4$ radians shifted to the reference phase that is in the orientation of the applied field. Therefore, the effect of the spiral wavefront will modify angle at which the destructive interference occurs.

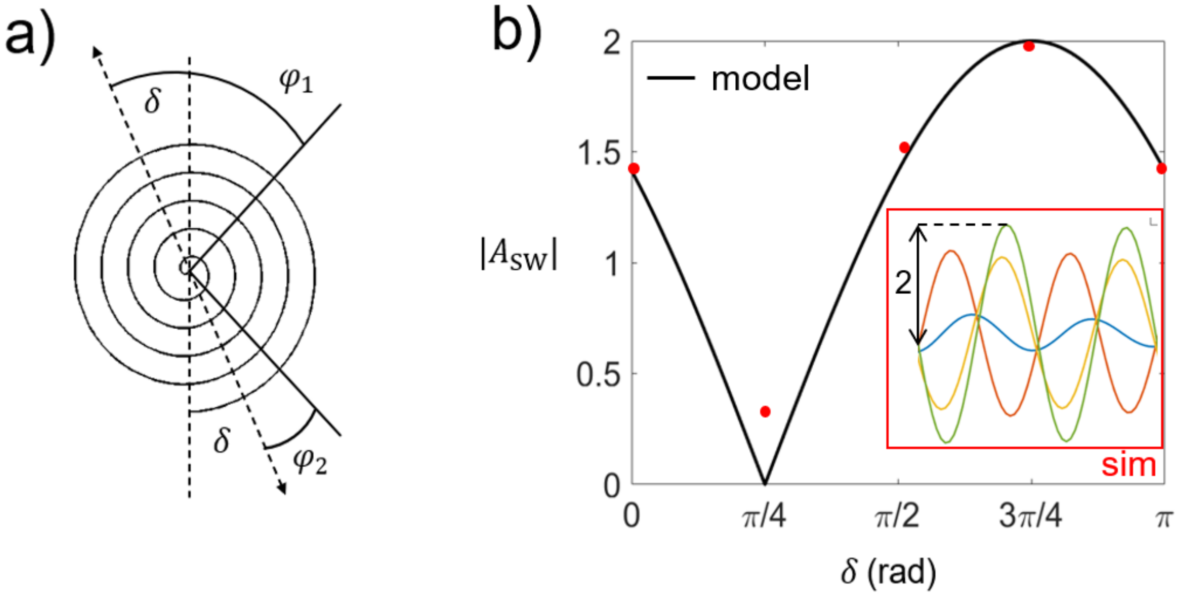

Figure 8.10 (a) Schematic showing the contribution in phase (φ_1 and φ_2) from the spiral spin wave dynamics to the channelled spin wave along the domain wall (solid black lines) as a result of a pumping field in an angle δ (dashed black arrows). (b) Modulus of the total amplitude expected in the 'output' branch as a function of the pumping field angle from the analytical model (black solid curve) and from simulations (red dots, obtained from inset), normalised to 2 for comparison with the model. Inset in (b) shows an horizontal cut of the simulated spin wave profiles in the 'output' branch of the structure for angles $\delta = 0$ (yellow), $\delta = \pi/4$ (blue), $\delta = \pi/2$ (orange) and $\delta = -\pi/4$ (green) (as in Fig. 8.8).

We proceed to calculate the contributions from the spiral wave as follows. The phasors for the respective wavefronts in the directions shown in Fig. 8.10(a) are $Ce^{i(\varphi_1)} = Ce^{i(\delta-\pi/4)}$ and $-Ce^{i(\varphi_2)} = -Ce^{i(-\pi/4-\delta)}$, where C is the chirality number of the vortex state ($C = +1$ is clockwise, $C = -1$ is counterclockwise). For a counterclockwise chirality as in Fig.8.8(a), the contributions from the spiral wavefront to the channelled spin waves amplitudes are (see Fig.8.10(a)),

$$A_{S,1} = \cos\left(-\frac{\pi}{4} - \delta\right) = \cos\,(\delta + \frac{\pi}{4})\ , \tag{8.3.12}$$

$$A_{S,2} = -\cos\left(\delta - \frac{\pi}{4}\right)\ . \tag{8.3.13}$$

Thus, the final amplitude for the output spin wave can be described as $A_{SW} = A_1 + A_2 + A_{S,1} + A_{S,2}$ (see Fig. 8.10(b)),

$$|A_{SW}| = 2\left|\cos\left(\delta + \frac{\pi}{4}\right)\right|\ . \tag{8.3.14}$$

For the CCW chirality of the vortex state in the disc, the final amplitude effectively shows a destructive interference only when the orientation of the applied field is $\delta = \pi/4$ radians with respect to the y-direction, as it is observed in micromagnetic simulations. Moreover, when substituting $\delta = -\pi/4 = 3\pi/4$, Eq. (8.3.14) yields a maximum constructive interference. If $\delta = \pi/2$ or $\delta = 0$ the constructive interference is partial, final amplitude is attenuated and the output spin wave is in opposite phase. All these scenarios can be observed as well in micromagnetic simulations (see Fig. 8.8 and red dots in Fig. 8.10(b)) and are in good agreement with the model from Eq. (8.3.14) (black curve in Fig. 8.10(b)).

This interpretation of various self-interfering spin wave dynamics explains the different wave interferences obtained at the 'output' branch of the proposed interferometer. More importantly, it shows that a variety of amplitudes for the 'output' signal can be obtained by just rotating the applied pumping field, which may be useful for implementing a spin wave analogic amplitude modulator. The proposed device is an externally switchable interferometer that does not require external biasing fields in any of its operational modes.

The device could also be used as a digital transmitter in an ASK (Amplitude Shift Keying) modulation since, for instance, the output signal of a maximum amplitude can be mapped to a '1' and an attenuated output to a '0'. More specifically, regarding the constructive/destructive interferences used for keying, an OOF (On/Off Keying) modulation could be employed. In a similar way to the phase-shifter from section 8.2, the bitrate would be predominantly determined by the speed of switching the orientation of the in-plane pumping field.

Now we explore the effects of additive noise or any ‘angular error’ that may affect the orientation of the pumping field and therefore, the robustness of the symbol transmission. Eq. (8.3.14) can be linearly approximated as,

$$|A_{\mathrm{SW}}|_0 = \left|\frac{6}{\pi}\delta - \frac{3}{2}\right|. \tag{8.3.15}$$

It can be trivially found that a variation (or error) of ε radians ($\delta \rightarrow \delta + \varepsilon$) in the angle of the applied pumping field will modify the detected amplitude as,

$$|A_{\mathrm{SW}}|_\varepsilon = |A_{\mathrm{SW}}|_0 + \varepsilon\frac{6}{\pi} \approx |A_{\mathrm{SW}}| + 1.91\varepsilon\ . \tag{8.3.16}$$

Fig. 8.11 shows some coding schemes for the total amplitude of the ‘output’ spin wave and the resulting quantization. For $M = 2$, intersymbol interference can be avoided if the angle error ε, related to the quantization error, is less than $\frac{\pi}{6}$ radians for the OFF (‘0’) state (dashed blue line).

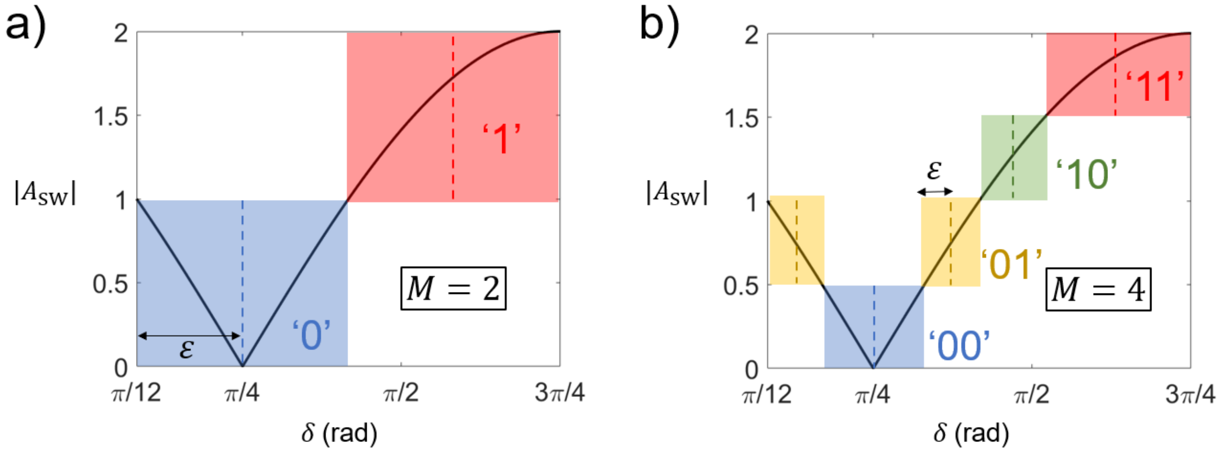

Figure 8.11 Logical levels (dashed lines) for (a) $M = 2$ and (b) $M = 4$ assigned to the total spin wave amplitude (shaded areas) in the ‘output’ branch of the interferometer. Some symbols set the maximum tolerable angular error ε as M increases.

In a binary alphabet, if M symbols are coded with a number b of bits, the range of all possible total amplitudes must be split accordingly in intervals of $2/M$, to accommodate all M symbols. A multilevel M-ASK ($M = 2^b$) implemented this way is only possible if the angle error is kept under a certain limit. Following the coding scheme shown in Fig. 8.11(b), some symbols (‘00’ or ‘11’) seem to be more robust to angular additive noise while other symbols (‘01’ or ‘10’) are less and impose a larger restriction in the angle of the pumping field. From Eq. (8.3.14), the maximum tolerable error ε to correctly detect a symbol in the M-signal space ($M > 2$) is calculated as,

$$\varepsilon = \frac{\pi}{4} - \frac{\delta}{2} = \frac{\pi}{4} - \frac{1}{2}\mathrm{acos}\left(\frac{1}{M}\right). \tag{8.3.17}$$

Fig. 8.12 shows results for $M = 2$ and from Eq. (8.3.15) for a selected number of symbols $M > 2$. Although the quantization error will decrease with a greater number of bits, the tolerable error for the angle of the applied pumping field quickly drops (~ 7.2 degrees with a 4-ASK modulation) to be practical. We observe that, despite of the coarse approach taken, this is already a considerable practical limitation for developing a digital magnonic transmitter based on these interferometry principles. In the same figure, a bit rate of 20 Gbps could be ideally achieved for a 4-ASK modulation, according to the analytical description proposed here. A 2-ASK (OOK) yields a more practical tolerable error of 30 degrees and, ideally, 10 Gbps for a spin wave carrier frequency of 10 GHz.

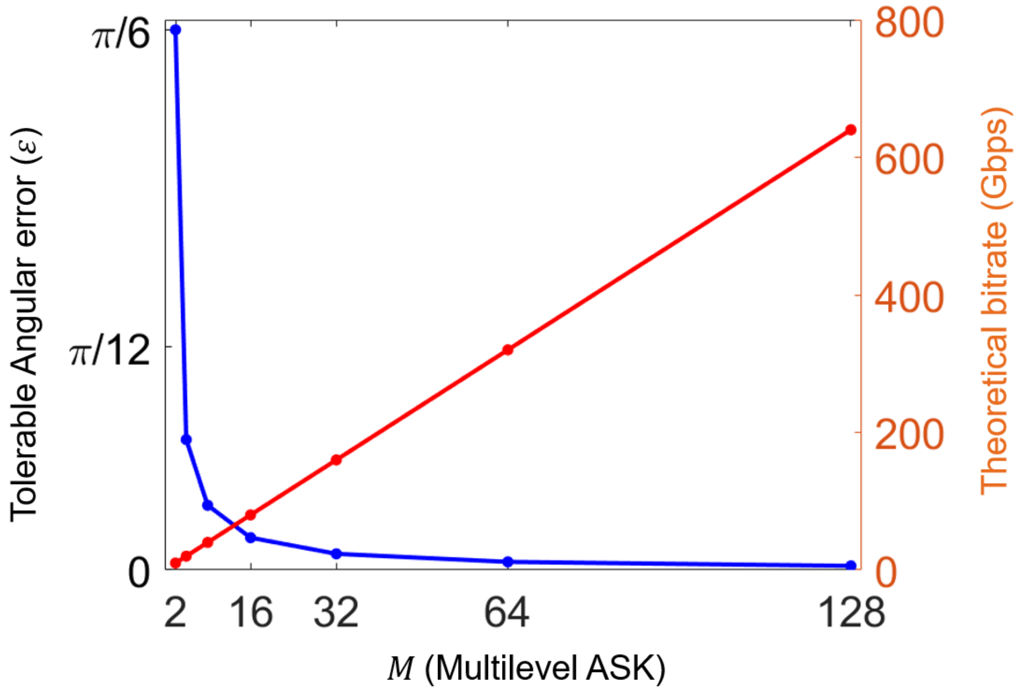

Figure 8.12 Tolerable angular error as a consequence of additive noise (blue curve, Eq. (8.3.17)) and the ideally expected bitrate (red curve) for a spin wave frequency of 10 GHz and for several numbers of symbols in a multilevel ASK modulation.

8.5 Discussion

We acknowledge that the current results showed here need experimental confirmation, but they proof the potential of non-saturated nanomagnets as emitters of spin waves and, to be potentially used as parts of a more complex spin wave device. We propose a full π-delay 'spin wave phase shifter' self-operational in a wide linear bandwidth in absence of high bias fields. Also, exploiting the spiral wavefront of the spin wave, a balanced phase-shifter that can perform as a high field magnetic nano-sensor is proposed. Finally, a highly tunable spin wave interferometer is discussed. Due to the outward propagation of the spiral spin waves emitted from the core region, these structures can be extended to a more complex network of interconnected patches. Such a display of the disks/square elements would allow a more complex network of spin wave waveguides, although all this is not dealt in this chapter and is left for future research.

One of the main drawbacks of these designs is the mode conversion between a surface spin wave or confined modes and a Backward Volume spin wave, which in theory, is only efficient for some selected frequencies. In terms of feasibility and manufacturing, the ‘output’ branch or the Y-shape structure could be difficult to implement due to its fragility (its dimensions are 10 nm wide by 80 nm high). To avoid these problems, a shared frequency range between the two different spin wave regimes (Balynsky, et al., 2017) may increase the operational bandwidth of the device. Also, the multiplexing structure in a Y-shape could be implemented differently, like in circular shapes (Kim, et al., 2018), or using domain walls as channels in a sufficiently long rectangular shape. All this would improve the problem of the single frequency coupling and make the fabrication process easier. As stated previously, these questions are left open for future work and further research, and they are not addressed in this chapter.

8.6 Summary

In this chapter, and as the finishing touch, we propose various conceptual spin wave devices based on the spin wave dynamics studied in this Thesis. These are a phase shifter, a magnetic sensor and a spin wave interferometer, which are based on the emission of short wavelength exchange dominated spin waves from a vortex core region and coupled to uniformly magnetised waveguides. The devices can perform well at high frequencies (> 8 GHz) in a non-saturated regime, e.g. in absence of high biasing fields. Even if biasing fields are required, for instance for tuning and reconfigurability, these are very low and always below saturation fields, so the overall magnetic state of the structures is not irreversibly altered. The implementation of these devices is left for future work and further research on the topic.

Chapter 9 Final conclusions

In this Thesis we have explored the spin wave dynamics in non-saturated nano-sized ferromagnets, with a special focus in vortex core and domain wall configurations in thick samples (80 nm) of various shapes. The aim has been to explain the sourcing, to explore and mathematically model and control high-amplitude spin waves emitted from the inhomogeneities of the internal field in such configurations. These dynamics are, mainly, the emission of short wavelength spiral spin waves from the vortex core and confined modes – Winter's magnons – in Bloch domain walls, numerically and experimentally investigated by means of VNA-FMR and mathematically modelled in Chapter 4. In Chapter 5, more interesting vortex dynamics have been explored, modelled, and experimentally resolved by TR-SKM. Their connection with the spiral spin waves, previously studied, is also explored. In Chapter 6, a study on confined modes was carried out, more focused on describing the confined wave propagation and to analytically model its spatial-dependent wavenumber along domain walls in a non-homogeneous magnetic environment, typically found in flux closure configurations. In Chapter 7, a teardrop-shaped ferromagnet is proposed as a spin wave emitter and its dynamics explored again by means of VNA-FMR, showing a rich collection of modes in various non-saturated states, which makes the proposed shaped element highly re-configurable using external low biasing fields. Its high sensitivity to these fields may be useful for active tuning of the emission of spin waves in the patch. Finally, in Chapter 8, potential applications of the studied dynamics are proposed and discussed, based on more complex shapes and interconnections of nano-sized ferromagnets.

In this chapter 9, the main conclusions from all the previous chapters are highlighted and some future work is proposed for further investigation. The main results from each chapter (♦) and the future work proposed (◊) can be listed as follows.

- Chapter 4
  - ♦ High amplitude exchange-dominated spiral spin waves can be emitted from the vortex core region in thick enough discs in a wide range of frequencies due to the competition

between dipolar and exchange fields. The generation of these waves can be explained in terms of local ferromagnetic resonances in the core region.

- ♦ By modifying the shape of the patch, a richer collection of modes can be excited, which allows to tailor the radial spin wave wavefront.
- ♦ The modes can be identified by means of standard VNA-FMR techniques.
- ♦ A mathematical model for describing the radial wavefront is proposed, based on the number of vertices of the patch and Hippopede curves. The model establishes a connection between the mathematical equation of the Hippopede curves and the dispersion relation of surface spin waves in a Damon-Eshbach configuration.
- ◊ A more accurate model can be further developed if radial dependence of the spin wave radial wavefront is accounted for. As first approach, this can be implemented as a limiting radius beyond which the proposed model applies. Below that limit, the spin wave presents a classical Damon-Eshbach configuration as in a circular disk.

- Chapter 5
  - ♦ The curling spin wave modes of a ferromagnetic vortex confined to a microscale disc have been directly observed in response to a microwave field excitation using time-resolved scanning Kerr microscopy
  - ♦ Splitting of azimuthal modes with counter propagating wavevector allow the direction of the core gyration to be determined through hybridization rules, while higher frequency radial modes that reveal evidence of excitation at the disc perimeter also show evidence of superposition with higher order gyrotropic modes.
  - ♦ Micromagnetic simulations demonstrate that the observed curling nature of confined spin waves in the region of circulating in-plane magnetization at higher frequencies is a result of the combination of different gyrotropic eigenmodes of the vortex core with the radial-azimuthal (6 - 9 GHz) and radial (~10 GHz) eigenmodes of the disc and is correlated with the emitted short spiral spin waves.
  - ♦ The measured spatio-temporal character of the curling modes is accurately reproduced by simulations which demonstrates that the mechanism that activates the emission of propagating short-wavelength spiral spin waves from the core is also taking place.

- ♦ Features from the spiral spin waves such as ‘chirality’ can therefore be determined through the observed curling modes.

- Chapter 6
  - ♦ We propose an analytical model, based on linearized Bloch equations of motion, describing the effects of a non-uniform demagnetising field transversal to the wall, on the propagation of confined spin waves in a straight domain wall of arbitrary angle (α) between the separated domains.
  - ♦ The consequence of such inhomogeneous field is the variation of the instantaneous k-vector of the confined wave, which leads to a ‘down/up spatial chirping’ effect on the spin wave. This model can be suitable for spin wave propagation in confined nanostructures, where domain walls of arbitrary angles are easily found in finite shapes.
  - ♦ When $\alpha = \pi/2$, the model mathematically implies that ‘zero index spin waves’ ($k = 0$) should take place. The physical interpretation is linked to the FMR main mode of an in-plane magnetised film and other ‘no wall-confined’ modes. This implies the possibility of reconfiguring the magnonic landscape of a particularly shaped patch to convert locally excited confined modes into domain modes.
  - ◊ Following on the latter, this scenario could be further explored to come up with a more complete model that describes the change in wavelength between the confined mode and the BVSW in the magnetised stripe with more accuracy.
  - ◊ The mathematics of the model also predict ‘evanescent spin waves’ ($k \in \mathcal{J}$). The physical interpretation of this result is suggested to be related to dipolar interactions only.

- Chapter 7
  - ♦ We show the potential applications of a teardrop-shaped magnetic patch as a reconfigurable spin wave emitter in a wide range of frequencies.
  - ♦ The proposed system is based on the excitation of a vortex core acting as source of spin waves and a single Bloch domain wall as a channel for the confinement and propagation

of the mode towards the only sharp corner of a sufficiently thick (80 nm) magnetic patch.

- ♦ The novelty consists in the simplicity and uni-directionality of the system, where only one Bloch domain wall and a single movable vortex core can be formed and naturally retained without providing external constant fields.
- ♦ Micromagnetic simulations confirm the high tunability of the system, enhancing or reducing the confined mode intensity by means of low bias fields.
- ♦ VNA-FMR results allow to identify spatially localised modes and suggest that the required configuration of a single core and domain wall can be easily obtained.
- ◊ Simulations show the presence of high amplitude Winter's magnons in the domain wall in a parallel pumping VNA-FMR scheme, although they were not experimentally resolved with sufficient accuracy. However, other measuring techniques such as X-ray scanning microscopy are proposed for direct visualisation of these spin waves.

- – Chapter 8
  - ♦ Some examples of potential applications based on the studied dynamics are proposed, such as a nano-sized magnetometer, a spin wave interferometer and spin wave phase shifter. Micromagnetic simulations demonstrate that these devices retain the required magnetic configuration in absence of constant biasing fields and require extremely low intensity biasing fields for their operation and tunability (some below 4 times less intense than saturation fields).
  - ◊ Further study of the practical applications and properties of these devices are left for further investigations, as well as their fabrication, implementation, and experimental verification.

Appendix A Software

A.1 MUMAX3 scripts

MuMax3 provides a dedicated scripting language that resembles a subset of the Go programming language. More information can be found in Ref. (Vansteenkiste, et al., 2014). In this appendix, a few examples of scripts are shown for running standard simulations as those used in this Thesis.

A.1.1 Continuous wave excitation

As an example, a standard script for obtaining a dynamical response to a continuous wave (CW) excitation and the simulation key parameters are shown here.

```
//Model parameters for a disc of 900 nm diameter and 80 nm thickness:
ModelSize := 900e-9
// The number of cells in x and y direction (N) and z direction (Nz) sets the cells size,
// (Nc), typically smaller than the exchange length of the material.
N := 256
Nz := 16
Nc := ModelSize/N
Nc_z := 5e-9
// The model is set in a hexahedral grid with the following dimensions:
pbc  := 1
setGridSize(N,N,Nz);
setCellSize(Nc,Nc,Nc_z);
EdgeSmooth = 8;
// The shape geometry can be created or imported as .png files:
disc := cylinder(900e-9, 900e-9, 80e-9)
setgeom(imageShape("DISC.png"))
saveas(geom, "imageShape")
```

```
// Material parameters for permalloy:
// Magnetisation saturation (A/m) for Permalloy© in Exeter at room temperature:
MSat := 8e5
// Exchange constant, Aex = 13e-12 for Permalloy©:
Aex = 13e-12
// Lowest reasonable damping for permalloy:
alpha = 0.008

// Dynamic parameters:
// Power of CW excitation in tesla, 0.3mT.
pulsePower := 0.3e-3
// Frequency of CW excitation in Hz:
pulseFreq := 8.8*1e9
// Sampling frequency in Hz, 25 ps sampling period:
sampleFreq  := 40e9
samplePeriod  := 1/sampleFreq
// Number of .ovf files to save, increases simulation time. For example, for a frequency
of 40 GHz, 300 files cover 7.5 ns:
sampleNum := 300

// We can save spatial average magnitudes, for example, full & normalised
// magnetisation, external field, dipolar field and energy and exchange field and
// energy in a table
tableAdd(m_full)
tableAdd(m)
tableAdd(B_ext)
tableAdd(B_demag)
tableAdd(E_demag)
tableAdd(B_exch)
tableAdd(E_exch)
// Save the table at the same sampling period:
```

```
tableautosave(25e-12)
// Initial magnetisation – Either set from Mumax3 (example, a vortex configuration)
and left to relax, or imported already as an equilibrium magnetisation state .ovf file.
m = Vortex(1, -1)
m.loadfile("groundstate_DISC.ovf")
// Defining regions:
defregion(1, cylinder(200e-9,80e-9))  // center of the disc
save(regions)
// Defining the excitation field (globally or in a particular region):
B_ext.SetRegion(1,vector(pulsePower*sin(2*pi*pulseFreq*t),0, 0))
// We save full magnetisation per unit cell (.ovf files) every sampling period:
for i:=0; i<sampleNum; i++{
        run(samplePeriod)
        save(m_full)
        }
```

A.1.2 Sinc wave excitation

The dynamic parameters in the code can be changed slightly to include other excitation signals such as sinc pulses:

```
// Dynamic parameters:
// Power of sinc pulse in tesla, 3mT.
pulsePower := 3e-3
// Frequency range of sinc pulse in Hz:
pulseFreq := 30*1e9
// Time at which the pulse starts in seconds, 5 ns.
pulseDelay := 5e-9
// Sampling frequency in Hz, 25 ps sampling period:
sampleFreq  := 40e9
samplePeriod  := 1/sampleFreq
```

```
// Number of .ovf files to save, increases simulation time, so increases Fourier
resolution, use a power of 2 for faster Fourier transforms in analysis:
sampleNum := 1024
// Power of sinc pulse in tesla, 3mT.
pulsePower := 0.3e-3
// Frequency range of sinc pulse in Hz:
pulseFreq := 30*1e9
// Time at which the pulse starts in seconds, 20ns.
pulseDelay := 5e-9
// Defining the excitation field (optionally, with an additional bias field in T):
B_bias := 0. 03
B_ext = vector(B_bias,pulsePower*sinc(2*pi*pulseFreq*(t-pulseDelay)), 0)
```

A.1.3 Hysteresis loop simulation

A further modification to the dynamic parameters can be made for recording the magnetostatic properties of the model and plot a hysteresis loop as those shown in chapter 7. A snippet of the script is shown here.

```
// Dynamic parameters:
m.loadfile("groundstate_TEARDROP.ovf")
// Full hysteresis loop (three sweeps from zero bias):
Bmax  := 70.0e-3
Bstep :=  1.0e-3
MinimizerStop = 1e-6
tableAdd(m_full)
tableAdd(B_ext)
for B:=0.0; B<=Bmax; B+=Bstep{
   B_ext = vector(B, 0, 0)
   minimize()   // small changes best minimized by minimize()
   tablesave()
```

```
}

for B:=Bmax; B>=-Bmax; B-=Bstep{
   B_ext = vector(B, 0, 0)
   minimize()   // small changes best minimized by minimize()
   tablesave()
}

for B:=-Bmax; B<=Bmax; B+=Bstep{
   B_ext = vector(B, 0, 0)
   minimize()   // small changes best minimized by minimize()
   tablesave()
}
```

Appendix B Calculations

B.1 Spatial dependent domain wall width

Fig.B.1.1 shows a schematic of the displayed magnetic moments **m** in a variable domain angle α with respect to the domain wall along x.

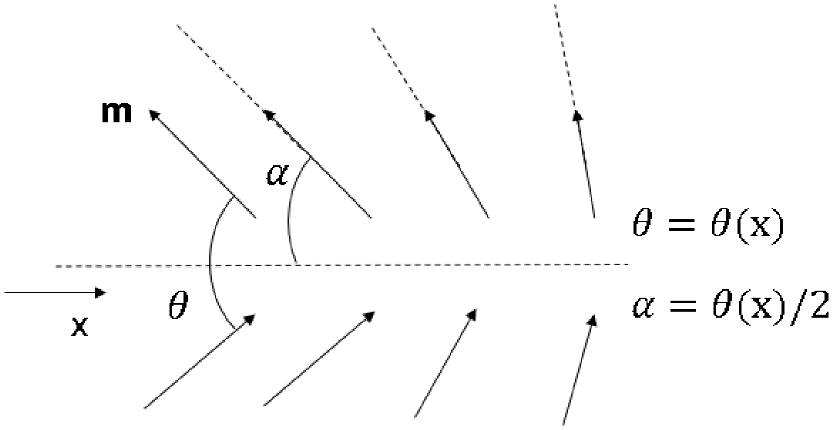

Figure B.1.1. Schematic showing a domain wall of reduced, variable angle θ between magnetic moments in two separated magnetic domains. The angle α is therefore defined to be between one magnetic moment and the domain wall and it is half the angle θ, assumed symmetry with respect to the domain wall axis (in the x-direction). Magnetic moments are exaggerated for clarity.

The domain wall is formed due to the competition of exchange and dipolar magnetic energies. Although the definition of *domain wall width* is rather arbitrary due to the continuous transition between domains, the calculation to find out the width of the domain wall is based on a minimisation of the total exchange and dipolar energy densities as in Ref. (Lecture 26 Magnetic Domains, 2013).

$$\frac{\partial \sigma_{\mathrm{ex}}^{\mathrm{Total}}}{\partial N} + \frac{\partial \sigma_{\mathrm{an}}^{\mathrm{Total}}}{\partial N} = 0 \tag{B.1.1}$$

$$\Rightarrow \frac{-J \cdot S^2 \cdot (\pi - 2\alpha)}{a^2 N^2} + \frac{K_u\left(\pi - 2\alpha + \sin(2\alpha)\, cos(2\alpha)\right)a}{\pi - 2\alpha} = 0 \ ,$$

where N is the discretised cell size across the domain wall and a is the lattice periodicity of the resulting hexahedral grid and K_u the magnetocrystalline anisotropy constant. We can replace this variable in terms of the exchange constant $A_{\mathrm{ex}} = \frac{2S^2J}{a}$. The domain wall width, $\Delta = N \cdot a$, can be found from the previous equation,

$$\Delta(x) = N \cdot a = \sqrt{\frac{A_{ex}(\pi - 2\alpha)^3}{K_u cos(\alpha)(\sin(2\alpha) + \pi - 2\alpha)}} \tag{B.1.2}$$

$$\Rightarrow \Delta(x) = \Delta_0 \frac{\pi - 2\alpha}{\pi} \sqrt{\frac{\pi - 2\alpha}{cos(\alpha)(\sin(2\alpha) + \pi - 2\alpha)}} ,$$

where $\Delta_0 = \pi \sqrt{\frac{A_{ex}}{K_u}}$ is the domain wall width for a 180 degrees Bloch domain wall ($\alpha = 0$). This equation for a variable domain wall width can be approximated as:

$$\Delta(x) = \Delta(\alpha) = \Delta_0 \left(1 - \frac{2}{\pi}\alpha\right) , 0 < \alpha < \frac{\pi}{2} . \tag{B.1.3}$$

This equation describes the domain wall width dependent on the angle of magnetic moments with respect to the wall.

B.2 Magnetization profiles in a domain wall of reduced angle α < 180

An approximate analytical solution of the static magnetisation profiles in such domain walls is obtained here, based on the introductory work developed in (Hubert & Schäfer, 1998), chapter 3.6. For a standard 180 degrees Bloch domain wall, the static solution for the LLG equation yields the domain wall configuration between domains,

$$\begin{cases} m_{\mathrm{x}} = \mathrm{M_s}\tanh\left(\frac{y}{\Delta_0}\right) \\ m_{\mathrm{y}} = 0 \\ m_{\mathrm{z}} = \mathrm{M_s}\,\mathrm{sech}\left(\frac{y}{\Delta_0}\right), \end{cases} \tag{B.2.1}$$

In Ref. (Hubert & Schäfer, 1998), chapter 3.6, different approximated methods for an analytical solution for domain walls of reduced angle ($0 < \alpha < \pi/2$) are proposed. Most of them are based on an additional generalised anisotropy function that leads to a generalized anisotropy component transversal to the Bloch wall. This generalised function can be physically interpreted as the result of an applied external magnetic field (orientated with an angle Ψ to the Bloch wall), shape and regular anisotropies or even external stress energy. Assuming a Bloch wall configuration to which this additional anisotropy term is added, the following relation between φ, the acute angle between the normal to the wall in the plane of the film and the magnetization in the centre of the wall, and α, the angle between the wall and the domain magnetization is obtained (Hubert & Schäfer, 1998),

$$\cos(\varphi) = \frac{1 + \sin(\alpha)\cosh\left(\cos(\alpha)\frac{y}{\Delta_0}\right)}{\sin(\alpha) + \cosh\left(\cos(\alpha)\frac{y}{\Delta_0}\right)} - \sin(\alpha)\,, \tag{B.2.2}$$

which particularised to $\alpha = 0$, effectively leads to the Walker profile for the static magnetic out-of-plane component of a pure (180 degrees) Bloch domain wall (Eq. (B.2.1)). As in (Bayer, et al., 2005), replacing the explicit relation $\varphi(y)$ from Eq. (B.2.2) into the expression of the out-of-plane magnetisation yields a solution for its y-position dependent profile,

$$m_{\mathrm{z}} \propto M_s \left(\frac{1 + \sin(\alpha)\cosh\left(\cos(\alpha)\frac{y}{\Delta_0}\right)}{\sin(\alpha) + \cosh\left(\cos(\alpha)\frac{y}{\Delta_0}\right)} - \sin(\alpha) \right) = M_s m_{\mathrm{z,B,0}}\,\xi(\alpha, y)\,. \tag{B.2.3}$$

In order to find the relations with the other components, one can use the condition $M_s = |\boldsymbol{m}|$, which must be satisfied for all values of y and the boundary conditions at the centre of the domain wall, and in the magnetic domains when $y = 0$ and $y \to \infty$, respectively. However, these calculations can very easily become unpractical, and instead, for sake of simplicity, a further approximation is taken and explained below.

In a mixed Bloch-Neel domain wall each magnetization component can generally be assumed as a sum of each one of the two wall types, Bloch (B) and Neel (N), as $\boldsymbol{m}_{(\mathrm{x,y,z})} = \boldsymbol{m}_{(\mathrm{x,y,z}),\mathrm{B}} + \boldsymbol{m}_{(\mathrm{x,y,z}),\mathrm{N}}$. Eq. (B.2.2) describes, in polar coordinates, the out-of-plane component of magnetization in the intermediate wall profile, which reflects the effect of anisotropy to magnetic moments in the domains which puts them in a new equilibrium position with an angle α with respect to the domain wall. Consequently, in-plane components of the magnetic moments are modified as well along this anisotropy axis. The in-plane component transversal to the wall (m_{y}) can be described entirely as the transversal in-plane Neel component of the intermediate wall ($m_{\mathrm{y,N}}$). Since the condition $M_s = |\boldsymbol{m}|$ must be satisfied for all values of y, the following ansatz for $\boldsymbol{m}_{(\mathrm{x,y,z}),\mathrm{B}}$ and $\boldsymbol{m}_{(\mathrm{x,y,z}),\mathrm{N}}$ is proposed as an approximate solution for the hybrid Bloch-Neel type domain wall profile,

$$\begin{cases} m_{\mathrm{x,B}} = \dfrac{M_s}{2}\sqrt{1-\sin^2(\alpha)\,\mathrm{sech}^2\left(\dfrac{y}{\Delta_0}\right) - \dfrac{1-\sin^2(\alpha)}{(1-\sin(\alpha))^2}\xi(\alpha,y)^2} \\ m_{\mathrm{y,B}} = 0 \\ m_{\mathrm{z,B}} = M_s\dfrac{\sqrt{1-\sin^2(\alpha)}}{1-\sin(\alpha)}\xi(\alpha,y)\,, \end{cases} \tag{B.2.4}$$

$$\begin{cases} m_{\mathrm{x,N}} = \dfrac{M_s}{2}\sqrt{1-\sin^2(\alpha)\,\mathrm{sech}^2\left(\dfrac{y}{\Delta_0}\right) - \dfrac{1-\sin^2(\alpha)}{(1-\sin(\alpha))^2}\xi(\alpha,y)^2} \\ m_{\mathrm{y,N}} = M_s\sin(\alpha)\,\mathrm{sech}\left(\dfrac{y}{\Delta_0}\right) \\ m_{\mathrm{z,N}} = 0, \end{cases} \tag{B.2.5}$$

where

$$\xi(\alpha, y) = \left(\frac{1 + \sin(\alpha)\cosh\left(\cos(\alpha)\frac{y}{\Delta_0}\right)}{\sin(\alpha) + \cosh\left(\cos(\alpha)\frac{y}{\Delta_0}\right)} - \sin(\alpha) \right), \tag{B.2.6}$$

and the condition $M_s = |\boldsymbol{m}|$ must be satisfied for all values of y. Note that, for $\alpha = 0$, $\xi(0, y) = \operatorname{sech}(y/\Delta_0)$ and the system of equations (B.2.4) collapse into the magnetization profile of a 180 Bloch wall (Eq. B.2.1). The coefficients $m_{\mathrm{x,B,0}}$, $m_{\mathrm{x,N,0}}$ and $m_{\mathrm{z,B,0}}$ from the Bloch and the Neel parts of the mixed profile were found from the condition $M_s = |\boldsymbol{m}|$ and the boundary conditions at the centre of the domain wall and in the magnetic domains where $y = 0$ and $y \to \infty$, respectively.

Fig. B.2.1 shows $m_{\mathrm{(x,y,z),B}}$ and $m_{\mathrm{(x,y,z),N}}$ as a function of the x-position, for several domain wall angles α and assuming a domain wall width of 100 nm. A 'sign' function is added to $m_{\mathrm{x,B}}$ so the negative values of the trigonometric functions are not hidden after squaring them,

$$\operatorname{sign}(x) = \begin{cases} 1 & \text{if } \ x > 0 \\ -1 & \text{if } \ x < 0. \end{cases} \tag{B.2.7}$$

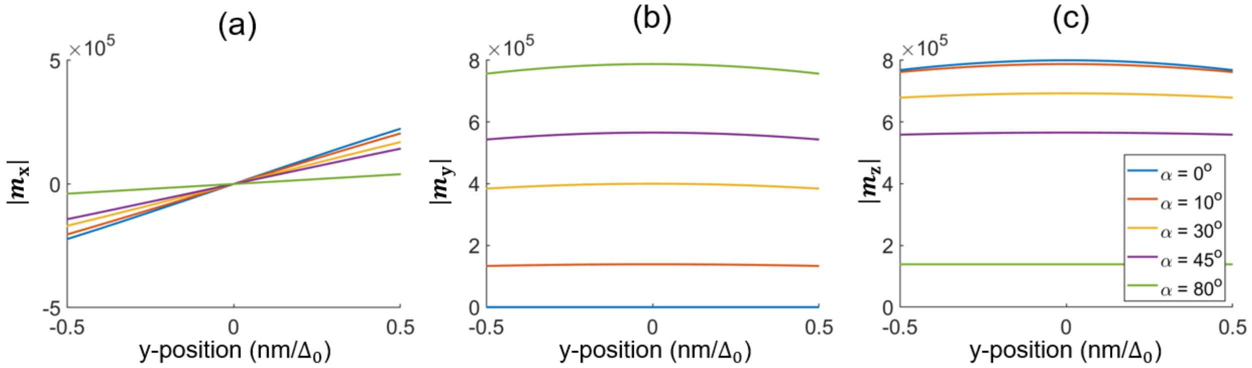

Figure B.2.1. Magnitude of magnetization components as a function of y-position, normalised to the domain wall width (Δ_0) across the wall, obtained from the system of equations (B.2.4) assuming $M_s = 800$ kAm^{-1}. Results for several angles of magnetization in the domains, between 0° and 80°, are shown.

In the wall region, centred at x = 0 nm, results from Fig. B.2.1 show an increase in the magnitude of m_{y} in detriment of m_{z} as the angle α increases. This 'trade-off' between the out-of-plane and the in-plane components is qualitatively consistent with a transition from a Bloch to a Neel type wall as α increases. The in-plane component parallel to the wall, m_{x}, is less affected which means that the model assumes a greater interplay between the component m_{y}, parallel to the direction of the added new anisotropy (in-plane and perpendicular to the wall), and the out-of-plane component m_{z}.

Far from the wall region (into the domains), $m_{\mathrm{x}}(\pm\infty, \alpha) = 0$ and $m_{\mathrm{y}}(\pm\infty, \alpha) = 0$, the model does not account for the influence of α, which implies that the model is also less accurate far from the wall centre. However, this reduced accuracy can be expected from the approach taken from the beginning, where (1) an original Bloch domain wall is assumed, (2) the equations are intended to model magnetization at the wall region only and (3) the model assumes an intermediate Bloch-Neel wall for all angles and therefore does not account for any threshold angle α_{c} beyond which the wall collapses into one type or another. In reality, there is a critical angle α_{c} beyond which, a Neel wall is energetically more favourable to be formed than an intermediate wall (Torok, et al., 1965). Therefore, the 'smoother' transition between the Bloch and the Neel type in the proposed equations, for the whole range of angle α, may become a loose approximation for large angles. Also, the model is intended to describe the dipolar field at the very centre of the wall ($y = 0$ nm), therefore the model is expected to lose accuracy far from that position. Fig. B.2.1 shows a consistent description of magnetization configuration at the centre of the wall.

Nevertheless, the proposed model is regarded as physically consistent for intermediate domain walls ($\alpha < \alpha_{\mathrm{c}}$). However, in order to find an analytical solution more physically meaningful to the scenario studied in Chapter 6, a critical angle (α_{c}) for the domain magnetization, above which the Neel component in the wall region is dominant (Torok, et al., 1965) must be considered. Under that situation, the model can be considerably simplified, since the out-of-plane component can be neglected from the systems of equations. Ref. (Torok, et al., 1965) shows that for a magnetic film as thick as the domain wall width ($t \approx \Delta_0$), this critical angle is very close to zero. As the domain wall effectively collapses into a Neel wall, only in-plane components are considered hereon in the model. Therefore, regardless of the acute angle α, magnetisation profile in the wall region can be simply regarded as,

$$\begin{cases} m_{\mathrm{x}} = m_{\mathrm{x,N}} = \dfrac{M_s}{2}\sqrt{1 - \sin^2(\alpha)\,\mathrm{sech}^2\left(\dfrac{y}{\Delta_0}\right) - \dfrac{\cos^2(\alpha)}{(1-\sin(\alpha))^2}\xi(\alpha, y)^2} \\ m_{\mathrm{y}} = m_{\mathrm{y,N}} = \mathrm{M_s}\sin(\alpha)\,\mathrm{sech}\left(\dfrac{y}{\Delta_0}\right) \\ m_{z,\mathrm{N}} = 0\,. \end{cases} \tag{B.2.7}$$

Note that, regardless of the critical angle, the in-plane component of magnetization perpendicular to the intermediate wall can be expressed as $m_{\mathrm{y}} = m_{\mathrm{y,N}}$. Fig. B.2.2 shows the magnitude of magnetization in the wall region for several angles α.

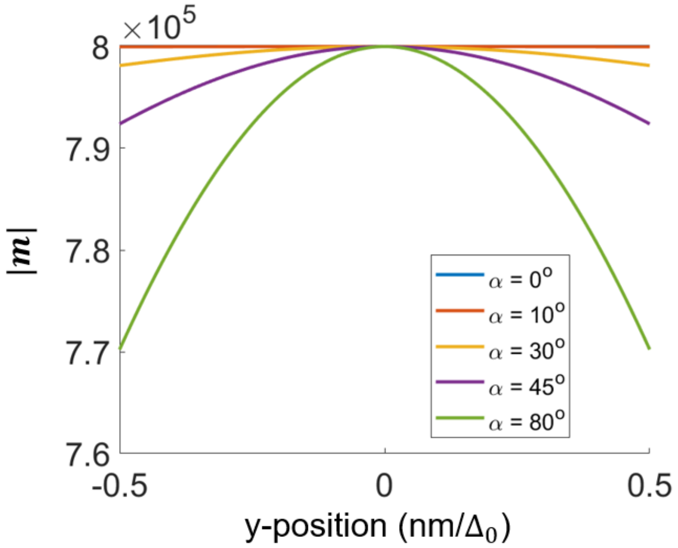

Figure B.2.2. Magnitude of magnetization as a function of y-position, across the wall, normalized to the domain wall width (Δ_0), obtained from the system of equations (B.2.7). Results for several angles of magnetization in the domains are shown.

As the angle α increases, results are less accurate, as it is reflected by the total magnitude of magnetization, different to M_s. However, one can see that the necessary condition of $M_s = |\boldsymbol{m}| = 8 \cdot 10^5\ \mathrm{Am}^{-1}$ for a Permalloy sample is reasonably satisfied for angles $\alpha < \pi/4$ radians with an approximate maximal error of 2.5% at $\alpha = \pi/4$ rad. This means that the model gives a good approximate description of the magnetisation profile in intermediate walls formed in a sample as thick as four times the domain wall width $t = 4\Delta_0$, for which the critical angle is $\alpha_{\mathrm{c}} = \pi/4$ rad (Torok, et al., 1965).

B.3 Spatial dependent demagnetising field transversal to the wall

The demagnetising field $\mathbf{H_d}$ in the sample is determined by the volume and surface magnetic charge distributions. The static magnetic configuration is also established based on these distributions, as well as on exchange interactions. From Eq. (B.2.7), we obtain the volume density of magnetic charges in the wall region,

$$\rho_m(r') = \nabla M(r') \approx \frac{\partial m_y}{\partial y} = \frac{-M_s \sin(\alpha) \tanh\left(\frac{y}{\Delta_0}\right) \operatorname{sech}\left(\frac{y}{\Delta_0}\right)}{\Delta_0} \tag{B.3.1}$$

Next, one can define a magnetic potential $\mathrm{U}(r)$ from which the associated dipolar field $\mathrm{H_d}(r)$ can be derived. The volume of integration, in cartesian coordinates, is defined as a prism of the same height (z-direction) as the thickness of the sample and as wide (y-direction) and long (x-direction) as the domain wall width (t nm × Δ_0 nm× Δ_0 nm). For sake of simplicity, we only account for the contributions of magnetic charges in a plane perpendicular to the wall, this is, magnetic charges along the y-direction for a given x position $(r = 0, r' = y')$ and uniform across thickness ($\frac{\partial m_z}{\partial z} = 0\,, \int_{-\infty}^{\infty} dz' = t$) and length ($\frac{\partial m_x}{\partial x} = 0\,, \int_{-\infty}^{\infty} dx' = \Delta_0$) of the volume of integration.

$$\begin{aligned} \mathrm{U}(r) &= \int \frac{\rho_m(r')}{4\pi|r - r'|} dV' \\ &= \iiint \frac{-M_s \sin(\alpha) \tanh\left(\frac{y'}{\Delta_0}\right) \operatorname{sech}\left(\frac{y'}{\Delta_0}\right)}{\Delta_0 4\pi\sqrt{r'^2}} dx' \cdot dy' \cdot dz' \\ &= \int \frac{-M_s \sin(\alpha) \tanh\left(\frac{y'}{\Delta_0}\right) \operatorname{sech}\left(\frac{y'}{\Delta_0}\right)}{\Delta_0 4\pi y'} \Delta_0 \cdot dy' \cdot t. \end{aligned} \tag{B.3.2}$$

Finally, realizing that $y' = y$, an expression for the transversal dipolar field in the wall region can be found from $\mathbf{H_d}(y) = -\nabla\mathrm{U}(r)$,

$$\mathrm{H_d}(y) = \frac{\partial \mathrm{U}}{\partial y} = \frac{-M_s \sin(\alpha) \tanh\left(\frac{y}{\Delta_0}\right) \operatorname{sech}\left(\frac{y}{\Delta_0}\right)}{\Delta_0 4\pi y} \Delta_0 \cdot t \tag{B.3.3}$$

$$= \frac{-t M_s \sin(\alpha) \tanh\left(\frac{y}{\Delta_0}\right) \operatorname{sech}\left(\frac{y}{\Delta_0}\right)}{4\pi y}.$$

At the centre of the wall ($y = 0$), Eq. (B.3.3) yields an indeterminate that can be solved by applying L'Hôpital rule $\left(\lim_{y\to c} \frac{f(y)}{g(y)} = \lim_{y\to c} \frac{f'(y)}{g'(y)} = L\right)$,

$$\mathrm{H_d}(0) = \lim_{y\to 0} \frac{-t M_s \sin(\alpha) \tanh\left(\frac{y}{\Delta_0}\right) \operatorname{sech}\left(\frac{y}{\Delta_0}\right)}{4\pi y} \tag{B.3.4}$$

$$= \lim_{y\to 0} \frac{-t M_s \sin(\alpha) \frac{\partial\left(\tanh\left(\frac{y}{\Delta_0}\right) \operatorname{sech}\left(\frac{y}{\Delta_0}\right)\right)}{\partial y}}{4\pi \frac{\partial y}{\partial y}}$$

$$= \lim_{y\to 0} \frac{-t M_s \sin(\alpha) \left(\operatorname{sech}^3\left(\frac{y}{\Delta_0}\right) - \tanh^2\left(\frac{y}{\Delta_0}\right) \operatorname{sech}\left(\frac{y}{\Delta_0}\right)\right)}{4\pi \Delta_0}$$

$$= \frac{-t M_s \sin(\alpha)(1 - 0 \cdot 1)}{4\pi \Delta_0} = \frac{-t M_s \sin(\alpha)}{4\pi \Delta_0}.$$

Finally, one can assume $t \approx \Delta_0$, which yields the approximated expression for the dipolar field transversal to the domain wall of variable angle α, considered in Chapter 6.

References

Adhikari, K. et al., 2018. Tunable Angle-Dependent Magnetization Dynamics in Ni80Fe20 Nanocross Structures of Varying Size. *Physical Review Applied,* 3 10, 10(4), p. 044010.

Aharoni, A., 1998. Demagnetizing factors for rectangular ferromagnetic prisms. *Journal of Applied Physics,* 15 3, 83(6), pp. 3432-3434.

Alberto, N. et al., 2018. Optical fiber magnetic field sensors based on magnetic fluid: A review. *Sensors,* 1 12.18(12).

Albisetti, E. et al., 2018. Nanoscale spin-wave circuits based on engineered reconfigurable spin-textures. *Communications Physics,* 1 12, 1(1), pp. 1-8.

Aliev, F. G. et al., 2011. Localized domain-wall excitations in patterned magnetic dots probed by broadband ferromagnetic resonance. *Physical Review B - Condensed Matter and Materials Physics,* 4 10, 84(14), p. 144406.

Aliev, F. G. et al., 2009. Spin waves in circular soft magnetic dots at the crossover between vortex and single domain state. *Physical Review B - Condensed Matter and Materials Physics,* 1 5, 79(17), p. 174433.

Anon., n.d. *Compact USB Vector Network Analyzer | Anritsu Europe.* [Online]
Available at: https://www.anritsu.com/en-GB/test-measurement/products/ms46122b

Asfour, A., 2017. *Magnetic Sensors - Development Trends and Applications.* s.l.:InTech.

Atalay, S. et al., 2015. One-Dimensional Magnonic Crystal for Magnetic Field Sensing. *Journal of Superconductivity and Novel Magnetism,* 24 7, 28(7), pp. 2071-2075.

Au, Y., Dvornik, M., Dmytriiev, O. & Kruglyak, V. V., 2012. Nanoscale spin wave valve and phase shifter. *Applied Physics Letters,* 23 4, 100(17), p. 172408.

Awad, A. A. et al., 2010. Spin excitation frequencies in magnetostatically coupled arrays of vortex state circular Permalloy dots. *Applied Physics Letters,* 27 9.97(13).

Bailleul, M., Höllinger, R. & Fermon, C., 2006. Microwave spectrum of square Permalloy dots: Quasisaturated state.

Bailleul, M., Höllinger, R., Perzlmaier, K. & Fermon, C., 2007. Microwave spectrum of square permalloy dots: Multidomain state. *Physical Review B - Condensed Matter and Materials Physics,* 3 12, 76(22), p. 224401.

Balynsky, M. et al., 2017. A Magnetometer Based on a Spin Wave Interferometer. *Scientific Reports,* 1 12, 7(1), pp. 1-11.

Bayer, C. et al., 2005. Spin-wave excitations in finite rectangular elements of Ni80Fe20. *Physical Review B - Condensed Matter and Materials Physics,* 1 8, 72(6), p. 064427.

Bayer, C., Schultheiss, H., Hillebrands, B. & Stamps, R. L., 2005. *Phase shift of spin waves traveling through a 180° Bloch-domain wall.* s.l., s.n., pp. 3094-3096.

Belanovsky, A. D. et al., 2012. Phase locking dynamics of dipolarly coupled vortex-based spin transfer oscillators. *Physical Review B - Condensed Matter and Materials Physics,* 30 3, 85(10), p. 100409.

Berger, A. J. et al., 2014. A versatile LabVIEW and field-programmable gate array-based scanning probe microscope for in operando electronic device characterization. *Review of Scientific Instruments,* 1 12, 85(12), p. 123702.

Berkov, D. & Gorn, N., 2005. Transition from the macrospin to chaotic behavior by a spin-torque driven magnetization precession of a square nanoelement. *Physical Review B - Condensed Matter and Materials Physics,* 15 2, 71(5), p. 052403.

Bhallamudi, V. P. et al., 2013. Experimental demonstration of scanned spin-precession microscopy. *Physical Review Letters,* 10 9, 111(11), p. 117201.

Bloembergen, N., Purcell, E. M. & Pound, R. V., 1948. Relaxation effects in nuclear magnetic resonance absorption. *Physical Review,* 1 4, 73(7), pp. 679-712.

Bloembergen, N., Purcell, E. M. & Pound, R. V., 1948. *Relaxation Effects in Nuclear Magnetic Resonance Absorption*,* s.l.: s.n.

Brächer, T., Pirro, P. & Hillebrands, B., 2017. *Parallel pumping for magnon spintronics: Amplification and manipulation of magnon spin currents on the micron-scale.* s.l.:Elsevier B.V..

Broers, A. N., 1988. Resolution limits for electron-beam lithography. *IBM Journal of Research and Development,* 32(4), pp. 502-513.

Buchner, M. et al., 2018. Tutorial: Basic principles, limits of detection, and pitfalls of highly sensitive SQUID magnetometry for nanomagnetism and spintronics. *Journal of Applied Physics,* 28 10, 124(16), p. 161101.

Bukin, N. et al., 2016. Time-resolved imaging of magnetic vortex dynamics using holography with extended reference autocorrelation by linear differential operator. *Scientific Reports,* 31 10, 6(1), pp. 1-10.

Buschow, K. H. J., ed., 2001. *Encyclopedia of Materials: Science and Technology.* s.l.:Elsevier.

Chang, L. J. et al., 2020. Spin Wave Injection and Propagation in a Magnetic Nanochannel from a Vortex Core. *Nano Letters,* 13 5, 20(5), pp. 3140-3146.

Chang, L. J. et al., 2018. Ferromagnetic domain walls as spin wave filters and the interplay between domain walls and spin waves. *Scientific Reports,* 1 12, 8(1), pp. 1-7.

Chiriac, H., Tibu, M., Moga, A. E. & Herea, D. D., 2005. *Magnetic GMI sensor for detection of biomolecules.* s.l., North-Holland, pp. 671-676.

Chumak, A. V., 2019. Fundamentals of magnon-based computing. *arXiv.org,* 24 1.

Chumak, A. V., Serga, A. A. & Hillebrands, B., 2014. Magnon transistor for all-magnon data processing. *Nature Communications,* 21 8.Volume 5.

Chumak, A. V., Serga, A. A. & Hillebrands, B., 2017. Magnonic crystals for data processing. *Journal of Physics D: Applied Physics,* 23 5, 50(24), p. 244001.

Chumak, A. V., Vasyuchka, V. I., Serga, A. A. & Hillebrands, B., 2015. *Magnon spintronics.* s.l.:Nature Publishing Group.

Ciprian, R. et al., 2016. New strategy for magnetic gas sensing. *RSC Advances,* 31 8, 6(86), pp. 83399-83405.

Cumming, D. R., Thoms, S., Beaumont, S. P. & Weaver, J. M., 1995. Fabrication of 3 nm wires using 100 keV electron beam lithography and poly(methyl methacrylate) resist. *Applied Physics Letters,* 15 1, 68(3), p. 322.

Dai, J. et al., 2011. Magnetic field sensor based on magnetic fluid clad etched fiber Bragg grating. *Optical Fiber Technology,* 1 5, 17(3), pp. 210-213.

Davies, C. S. et al., 2015. Towards graded-index magnonics: Steering spin waves in magnonic networks. *Physical Review B - Condensed Matter and Materials Physics,* 20 7, 92(2), p. 020408.

Davies, C. S. & Kruglyak, V. V., 2015. Graded-index magnonics. *Low Temperature Physics,* 1 10, 41(10), pp. 760-766.

Davies, C. S. & Kruglyak, V. V., 2016. Generation of Propagating Spin Waves from Edges of Magnetic Nanostructures Pumped by Uniform Microwave Magnetic Field. *IEEE Transactions on Magnetics,* 1 7.52(7).

Davies, C. S., Poimanov, V. D. & Kruglyak, V. V., 2017. Mapping the magnonic landscape in patterned magnetic structures. *Physical Review B,* 25 9, 96(9), p. 094430.

Davies, C. S. et al., 2015. Generation of propagating spin waves from regions of increased dynamic demagnetising field near magnetic antidots. *Applied Physics Letters,* 19 10, 107(16), p. 162401.

Dejong, M. D. & Livesey, K. L., 2015. Analytic theory for the switch from Bloch to Néel domain wall in nanowires with perpendicular anisotropy. *Physical Review B - Condensed Matter and Materials Physics,* 14 12, 92(21), p. 214420.

Demidov, V. E. et al., 2016. Direct observation of dynamic modes excited in a magnetic insulator by pure spin current. *Scientific Reports,* 9 9, 6(1), pp. 1-8.

Demidov, V. E. et al., 2011. Excitation of short-wavelength spin waves in magnonic waveguides. *Applied Physics Letters,* 22 8, 99(8), p. 082507.

Demidov, V. E., Urazhdin, S. & Demokritov, S. O., 2009. Control of spin-wave phase and wavelength by electric current on the microscopic scale. *Applied Physics Letters,* 28 12, 95(26), p. 262509.

Dieterle, G. et al., 2019. Coherent Excitation of Heterosymmetric Spin Waves with Ultrashort Wavelengths. *Physical Review Letters,* 21 3, 122(11), p. 117202.

Ding, J. et al., 2014. Higher order vortex gyrotropic modes in circular ferromagnetic nanodots. *Scientific Reports,* 25 4, 4(1), pp. 1-6.

Dogaru, T. & Smith, S. T., 2001. *Giant magnetoresistance-based eddy-current sensor.* s.l., s.n., pp. 3831-3838.

Donahue, M. J. & Porter, D. G., n.d. *OOMMF User's Guide, Version 1.0,* s.l.: s.n.

Dussaux, A. et al., 2011. Phase locking of vortex based spin transfer oscillators to a microwave current. *Applied Physics Letters,* 28 3, 98(13), p. 132506.

Enkrich, C. et al., 2005. Magnetic metamaterials at telecommunication and visible frequencies. *Physical Review Letters,* 11 11, 95(20), p. 203901.

Eshbach, J. R. & Damon, R. W., 1960. Surface magnetostatic modes and surface spin waves. *Physical Review,* 1 6, 118(5), pp. 1208-1210.

Fischbacher, T., Franchin, M., Bordignon, G. & Fangohr, H., 2007. *A systematic approach to multiphysics extensions of finite-element-based micromagnetic simulations: Nmag.* s.l., s.n., pp. 2896-2898.

Fruchart, O. & Thiaville, A., 2005. *Magnetism in reduced dimensions.* s.l.:No longer published by Elsevier.

Garcia-Sanchez, F. et al., 2015. Narrow Magnonic Waveguides Based on Domain Walls. *Physical Review Letters,* 18 6, 114(24), p. 247206.

Gladii, O. et al., 2016. Spin wave amplification using the spin Hall effect in permalloy/platinum bilayers. *Applied Physics Letters,* 16 5, 108(20), p. 202407.

Goldstone, J., Salam, A. & Weinberg, S., 1962. Broken symmetries. *Physical Review,* 1 8, 127(3), pp. 965-970.

Gurevich, A. G., Melkov, G. A. & Sci, D., 1996. *Magnetization Oscillations and Waves,* s.l.: s.n.

Guslienko, K. Y. et al., 2006. Magnetic vortex core dynamics in cylindrical ferromagnetic dots. *Physical Review Letters,* 16 2, 96(6), p. 067205.

Guslienko, K. Y. et al., 2002. Eigenfrequencies of vortex state excitations in magnetic submicron-size disks. *Journal of Applied Physics,* 15 5, 91(10 I), pp. 8037-8039.

Guslienko, K. Y. et al., 2015. Giant moving vortex mass in thick magnetic nanodots. *Scientific Reports,* 10 9.Volume 5.

Guslienko, K. Y. et al., 2002. Magnetization reversal due to vortex nucleation, displacement, and annihilation in submicron ferromagnetic dot arrays. *Physical Review B - Condensed Matter and Materials Physics,* 1 1, 65(2), pp. 244141-2441410.

Guslienko, K. Y., Slavin, A. N., Tiberkevich, V. & Kim, S. K., 2008. Dynamic origin of azimuthal modes splitting in vortex-state magnetic dots. *Physical Review Letters,* 8 12, 101(24), p. 247203.

Haidar, M. et al., 2019. A single layer spin-orbit torque nano-oscillator. *Nature Communications,* 1 12, 10(1), pp. 1-6.

Hämäläinen, S. J. et al., 2018. Control of spin-wave transmission by a programmable domain wall. *Nature Communications,* 1 12, 9(1), pp. 1-8.

Hansen, U. H., Demidov, V. E. & Demokritov, S. O., 2009. Dual-function phase shifter for spin-wave logic applications. *Applied Physics Letters,* 22 6, 94(25), p. 252502.

Heremans, J., 1993. Solid state magnetic field sensors and applications. *J. Phys. D: Appl. Phys.,* 26(1149), pp. 1149-1168.

Herring, C. & Kittel, C., 1951. On the theory of spin waves in ferromagnetic media. *Physical Review,* 1 3, 81(5), pp. 869-880.

Hertel, R., Wulfhekel, W. & Kirschner, J., 2004. Domain-wall induced phase shifts in spin waves. *Physical Review Letters,* 17 12, 93(25), p. 257202.

Hoffmann, A. & Bader, S. D., 2015. Opportunities at the frontiers of spintronics. *Physical Review Applied,* 5 10, 4(4), p. 047001.

Hubert, A. & Schäfer, R., 1998. *Magnetic domains : the analysis of magnetic microstructures.* s.l.:Berlin : Springer.

Im, M. Y. et al., 2019. Dynamics of the Bloch point in an asymmetric permalloy disk. *Nature Communications,* 1 12, 10(1), pp. 1-8.

Inoue, M. et al., 2011. Investigating the use of magnonic crystals as extremely sensitive magnetic field sensors at room temperature. *Applied Physics Letters,* 28 3, 98(13), p. 132511.

Ivanov, B. A. & Zaspel, C. E., 2002. Magnon modes for thin circular vortex-state magnetic dots. *Applied Physics Letters,* 12 8, 81(7), pp. 1261-1263.

J Heremans, 1993. Solid state magnetic field sensors and applications. *Journal of Physics D: Applied Physics,* 26(8), pp. 40-46.

Jamali, M. et al., 2013. Spin wave nonreciprocity for logic device applications. *Scientific Reports,* 7 11, 3(1), pp. 1-5.

Jones, G. A. C., 1987. Very high voltage (500 kV) electron beam lithography for thick resists and high resolution. *Journal of Vacuum Science & Technology B: Microelectronics and Nanometer Structures,* 4 1, 5(1), p. 120.

Jorzick, J. et al., 1999. Spin-wave quantization and dynamic coupling in micron-size circular magnetic dots. *Applied Physics Letters,* 13 12, 75(24), pp. 3859-3861.

K Y Guslienko, G. N. K. Y. V. K. G. A. M. V. N. a. A. N. S., 2014. Microwave absorption properties of permalloy nanodots in the vortex and quasi-uniform magnetization states. *New Journal of Physics,* 6.Volume 16.

Kakazei, G. N. et al., 2004. Spin-wave spectra of perpendicularly magnetized circular submicron dot arrays. *Applied Physics Letters,* 85(3).

Kalinikos, B., 1980. Excitation of propagating spin waves in ferromagnetic films. *IEE Proceedings H Microwaves, Optics and Antennas,* 127(1), p. 4.

Kalinikos, B. & Slavin, A., 1986. Theory of dipole-exchange spin wave spectrum for ferromagnetic films with mixed exchange boundary conditions. *Journal of Physics C: Solid State Physics,* 19(35), pp. 7013-7033.

Kalinkos, B. & Slavin, A., 2005. *Theory of dipole-exchange spin wave excitation for ferromagnetic films with mixed exchange boundary conditions.* s.l., Institute of Electrical and Electronics Engineers (IEEE), pp. BP13-BP13.

Kammerer, M. et al., 2011. Magnetic vortex core reversal by excitation of spin waves. *Nature Communications,* 12 4, 2(1), pp. 1-6.

Kanazawa, N. et al., 2016. Demonstration of a robust magnonic spin wave interferometer. *Scientific Reports,* 22 7, 6(1), pp. 1-8.

Kang, L., Zhao, Q., Zhao, H. & Zhou, J., 2008. Magnetically tunable negative permeability metamaterial composed by split ring resonators and ferrite rods. *Optics Express,* 9 6, 16(12), p. 8825.

Karnaushenko, D. et al., 2015. Self-Assembled On-Chip-Integrated Giant Magneto-Impedance Sensorics. *Advanced Materials,* 1 11, 27(42), pp. 6582-6589.

Keatley, P. S. et al., 2009. Time-and vector-resolved magneto-optical Kerr effect measurements of large angle precessional reorientation in a 2×2μm2 ferromagnet. *Citation: J. Appl. Phys,* Volume 105, p. 23501.

Keatley, P. S. et al., 2008. Time-resolved investigation of magnetization dynamics of arrays of nonellipsoidal nanomagnets with nonuniform ground states. *Physical Review B - Condensed Matter and Materials Physics,* 1 12, 78(21), p. 214412.

Keatley, P. S. et al., 2017. A platform for time-resolved scanning Kerr microscopy in the near-field. *Review of Scientific Instruments,* 1 12, 88(12), p. 123708.

Kerr, J., 1877. XLIII. On rotation of the plane of polarization by reflection from the pole of a magnet. *The London, Edinburgh, and Dublin Philosophical Magazine and Journal of Science,* 5, 3(19), pp. 321-343.

Khitun, A. & Wang, K. L., 2011. Non-volatile magnonic logic circuits engineering. *Journal of Applied Physics,* 4 8, 110(3), p. 034306.

Khivintsev, Y. V. et al., 2010. Spin wave resonance excitation in ferromagnetic films using planar waveguide structures. *Journal of Applied Physics,* 15 7.108(2).

Kimel, A. V. & Zvezdin, A. K., 2015. Magnetization dynamics induced by femtosecond light pulses. *Low Temperature Physics,* 30 9, 41(9), pp. 682-688.

Kim, S. K. et al., 2018. Spin-wave duplexer studied by finite-element micromagnetic simulation. *Scientific Reports,* 1 12, 8(1), pp. 1-8.

Kittel, C., 1948. On the theory of ferromagnetic resonance absorption. *Physical Review,* 15 1, 73(2), pp. 155-161.

Kittel, C., 1958. Excitation of spin waves in a ferromagnet by a uniform rf field. *Physical Review,* 15 6, 110(6), pp. 1295-1297.

Kostylev, M. P. et al., 2005. Spin-wave logical gates. *Applied Physics Letters,* 10 10, 87(15), pp. 1-3.

Krawczyk, M. & Grundler, D., 2014. Review and prospects of magnonic crystals and devices with reprogrammable band structure. *Journal of Physics: Condensed Matter J. Phys.: Condens. Matter,* Volume 26, p. 32.

Landau, L. & Lifshits, E., 1935. *ON THE THEORY OF THE DISPERSION OF MAGNETIC PERMEABILITY IN FERROMAGNETIC BODIES,* s.l.: s.n.

Langner, T. et al., 2018. Spin-wave propagation through a magnonic crystal in a thermal gradient. *Journal of Physics D: Applied Physics,* 30 7, 51(34), p. 344002.

Lan, J., Yu, W., Wu, R. & Xiao, J., 2015. Spin-Wave Diode. *Physical Review X,* 28 12, 5(4), p. 041049.

Lara, A., Metlushko, V. & Aliev, F. G., 2013. Observation of propagating edge spin waves modes. *Journal of Applied Physics,* 7 12, 114(21), p. 213905.

Lara, A., Robledo Moreno, J., Guslienko, K. Y. & Aliev, F. G., 2017. Information processing in patterned magnetic nanostructures with edge spin waves. *Scientific Reports,* 1 12, 7(1), pp. 1-12.

Lecture 26 Magnetic Domains (2013).

Lee, I. et al., 2012. Local magnetic characterization of (Ga,Mn)As continuous thin film using scanning probe force microscopy. *Physical Review B - Condensed Matter and Materials Physics,* 2 5, 85(18), p. 184402.

Lee, I. et al., 2010. Nanoscale scanning probe ferromagnetic resonance imaging using localized modes. *Nature,* 12 8, 466(7308), pp. 845-848.

Lee, K. S. & Kim, S. K., 2007. Gyrotropic linear and nonlinear motions of a magnetic vortex in soft magnetic nanodots. *Applied Physics Letters,* 24 9, 91(13), p. 132511.

Lee, K. S. & Kim, S. K., 2008. Conceptual design of spin wave logic gates based on a Mach-Zehnder-type spin wave interferometer for universal logic functions. *Journal of Applied Physics,* 12 9, 104(5), p. 053909.

Lei, M. et al., 2016. Magnetically tunable metamaterial perfect absorber. *Journal of Applied Physics,* 28 6, 119(24), p. 244504.

Lisenkov, I., Tyberkevych, V., Nikitov, S. & Slavin, A., 2015. Electrodynamic boundary conditions for planar arrays of thin magnetic elements. *Applied Physics Letters,* 24 8, 107(8), p. 082405.

Louis, S. et al., 2016. Bias-free spin-wave phase shifter for magnonic logic. *AIP Advances,* 1 6, 6(6), p. 065103.

Lupo, P., Kumar, D. & Adeyeye, A. O., 2015. Size dependence of spin-wave modes in Ni80Fe20 nanodisks. *AIP Advances,* 1 7, 5(7), p. 077179.

Machida, K. et al., 2005. Magnetic structure of cross-shaped permalloy arrays embedded in silicon wafers. *Journal of Magnetism and Magnetic Materials,* 1 4, Volume 290-291 PART 1, pp. 779-782.

Manfrinato, V. R. et al., 2013. Resolution limits of electron-beam lithography toward the atomic scale. *Nano Letters,* 10 4, 13(4), pp. 1555-1558.

Mansfeld, S. et al., 2012. Spin wave diffraction and perfect imaging of a grating. *Physical Review Letters,* 26 1, 108(4), p. 047204.

Martinez-Chapa, S. O., Salazar, A. & Madou, M. J., 2016. Two-Photon Polymerization as a Component of Desktop Integrated Manufacturing Platforms. In: *Three-Dimensional Microfabrication Using Two-Photon Polymerization: Fundamentals, Technology, and Applications.* s.l.:Elsevier Inc., pp. 374-416.

Matatagui, D. et al., 2015. A magnonic gas sensor based on magnetic nanoparticles. *Nanoscale,* 7 6, 7(21), pp. 9607-9613.

Mc Donald, L., 2019. *Magnonics, an alternative to conventional electronics | The American Ceramic Society.* [Online]
Available at: https://ceramics.org/ceramic-tech-today/basic-science/magnonics-an-alternative-to-conventional-electronics

McDonald, L., 2019. *Magnonics, an alternative to conventional electronics | The American Ceramic Society.* [Online]
Available at: https://ceramics.org/ceramic-tech-today/basic-science/magnonics-an-alternative-to-conventional-electronics

Metlov, K. L., 2001. Simple analytical description for the cross-tie domain wall structure. *Applied Physics Letters,* 15 10, 79(16), pp. 2609-2611.

Meydan, T., 1994. Application of amorphous materials to sensors. *Journal of Magnetism and Magnetic Materials,* 1 5, 133(1-3), pp. 525-532.

Mushenok, F. B. et al., 2017. Broadband conversion of microwaves into propagating spin waves in patterned magnetic structures. *Applied Physics Letters,* 24 7, 111(4), p. 042404.

Nahrwold, G. et al., 2010. Structural, magnetic, and transport properties of Permalloy for spintronic experiments. *Journal of Applied Physics,* 1 7, 108(1), p. 013907.

Neudecker, I. et al., 2006. Modal spectrum of permalloy disks excited by in-plane magnetic fields. *Physical Review B - Condensed Matter and Materials Physics,* 27 4, 73(13), p. 134426.

Nisar, S., Khan, O. & Tariq, M., 2016. An Efficient Adaptive Window Size Selection Method for Improving Spectrogram Visualization. *Computational Intelligence and Neuroscience,* Volume 2016, pp. 1-13.

Noske, M. et al., 2016. Three-dimensional Character of the Magnetization Dynamics in Magnetic Vortex Structures: Hybridization of Flexure Gyromodes with Spin Waves. *Physical Review Letters,* 14 7, 117(3), p. 037208.

Novosad, V. et al., 2002. Spin excitations of magnetic vortices in ferromagnetic nanodots. *Physical Review B,* 66(052407).

Nyquist, H., 1928. Certain Topics in Telegraph Transmission Theory. *Transactions of the American Institute of Electrical Engineers,* 47(2), pp. 617-644.

Obry, B. et al., 2013. A micro-structured ion-implanted magnonic crystal. *Applied Physics Letters,* 20 5, 102(20), p. 202403.

Obukhov, Y. et al., 2008. Local Ferromagnetic Resonance Imaging with Magnetic Resonance Force Microscopy. *Physical Review Letters,* 14 5, 100(19), p. 197601.

Olson, A. L., Oredson, H. N., Torok, E. J. & Spurrier, R. A., 1967. Calculations of the structure of Néel, Bloch, and intermediate walls and the influence of their stray fields on bitter powder patterns. *Journal of Applied Physics,* 29 3, 38(3), pp. 1349-1351.

Osborn, J. A., 1945. Demagnetizing factors of the general ellipsoid. *Physical Review,* 1 6, 67(11-12), pp. 351-357.

Osuna Ruiz, D. et al., 2019. Dynamics of spiral spin waves in magnetic nanopatches: Influence of thickness and shape. *Physical Review B,* 27 12, 100(21), p. 214437.

Papp, Á., Porod, W., Csurgay, Á. I. & Csaba, G., 2017. Nanoscale spectrum analyzer based on spin-wave interference. *Scientific Reports,* 1 12.7(1).

Parker, N. W., Brodie, A. D., McCoy, J. H. & Engineering, S.-I. S. f. O., 2000. *High-throughput NGL electron-beam direct-write lithography system [3997-115].* s.l.:SPIE.

Park, J. P. & Crowell, P. A., 2005. Interactions of spin waves with a magnetic vortex. *Physical Review Letters,* 14 10, 95(16), p. 167201.

Park, J. P. et al., 2003. Imaging of spin dynamics in closure domain and vortex structures. *Physical Review B - Condensed Matter and Materials Physics,* 17 1, 67(2), p. 020403.

Pendry, J. B., 2000. Negative refraction makes a perfect lens. *Physical Review Letters,* 30 10, 85(18), pp. 3966-3969.

Perzlmaier, K. et al., 2005. Spin-wave eigenmodes of permalloy squares with a closure domain structure. *Physical Review Letters,* 11 2, 94(5), p. 057202.

Pirro, P. et al., 2015. Experimental observation of the interaction of propagating spin waves with Néel domain walls in a Landau domain structure. *Applied Physics Letters,* 8 6, 106(23), p. 232405.

Polder, D., 1949. On the theory of ferromagnetic resonance. *Physica,* 1 4, 15(1-2), pp. 253-255.

Popović, R. S., 1989. Hall-effect devices. *Sensors and Actuators,* 3 5, 17(1-2), pp. 39-53.

Prabhakar, A. & Stancil, D. D., 2009. *Spin waves: Theory and applications.* s.l.:Springer US.

Pufall, M. R., Rippard, W. H., Schneider, M. L. & Russek, S. E., 2007. Low-field current-hysteretic oscillations in spin-transfer nanocontacts. *Physical Review B - Condensed Matter and Materials Physics,* 19 4, 75(14), p. 140404.

Qiu, Z. Q. & Bader, S. D., 2000. *Surface magneto-optic Kerr effect.* s.l.:American Institute of Physics Inc..

Ramsden, E., 2006. *Hall-Effect Sensors.* 2nd ed. s.l.:Elsevier.

Reig, C., Cubells-Beltrán, M. D. & Muñoz, D. R., 2009. *Magnetic field sensors based on Giant Magnetoresistance (GMR) technology: Applications in electrical current sensing.* s.l.:s.n.

Rinkevich, A. B. et al., 2015. Interaction of microwave electromagnetic waves with 3D magnetic metamaterials. *Photonics and Nanostructures - Fundamentals and Applications,* 1 6, Volume 15, pp. 59-72.

Rosenfield, M. G., 1987. Submicron electron-beam lithography using a beam size comparable to the linewidth control tolerance. *Journal of Vacuum Science & Technology B: Microelectronics and Nanometer Structures,* 1, 5(1), p. 114.

Ruotolo, A. et al., 2009. *Phase-locking of magnetic vortices mediated by antivortices.* s.l.:Nature Publishing Group.

Saker, K. et al., 2019. Magnetic field sensor based on a magnetic-fluid-infiltrated photonic crystal L4 nanocavity and broadband W1 waveguide. *Journal of Computational Electronics,* 15 6, 18(2), pp. 619-627.

Savitzky, A. & Golay, M. J., 1964. Smoothing and Differentiation of Data by Simplified Least Squares Procedures. *Analytical Chemistry,* 1 7, 36(8), pp. 1627-1639.

Schlömann, E., 1964. Generation of spin waves in nonuniform magnetic fields. I. Conversion of electromagnetic power into spin-wave power and vice versa. *Journal of Applied Physics,* 20 1, 35(1), pp. 159-166.

Scholz, W. et al., 2003. *Scalable parallel micromagnetic solvers for magnetic nanostructures.* s.l., Elsevier, pp. 366-383.

Shim, J. H. et al., 2011. Nonlinear motion of magnetic vortex under alternating-current magnetic field: Dynamic correction of a gyrovector and a damping tensor of the Thiele's equation. *Applied Physics Letters,* 3 10, 99(14), p. 142505.

Shinjo, T. et al., 2000. Magnetic vortex core observation in circular dots of permalloy. *Science,* 11 8, 289(5481), pp. 930-932.

Slavin, A. & Tiberkevich, V., 2008. *Excitation of spin waves by spin-polarized current in magnetic nano-structures.* s.l., s.n., pp. 1916-1927.

Slonczewski, J. C., 1996. Current-driven excitation of magnetic multilayers. *Journal of Magnetism and Magnetic Materials,* 1 6, 159(1-2), pp. L1-L7.

Sluka, V. et al., 2019. Emission and propagation of 1D and 2D spin waves with nanoscale wavelengths in anisotropic spin textures. *Nature Nanotechnology,* 1 4, 14(4), pp. 328-333.

Smith, K. R., Kabatek, M. J., Krivosik, P. & Wu, M., 2008. Spin wave propagation in spatially nonuniform magnetic fields. *Journal of Applied Physics,* 15 8, 104(4), p. 043911.

Stancil, D. D. & Morgenthaler, F. R., 1983. Guiding magnetostatic surface waves with nonuniform in-plane fields. *Journal of Applied Physics,* 4 3, 54(3), pp. 1613-1618.

Stancil, D. D. & Prabhakar, A., 2009. Introduction to Magnetism. In: *Spin Waves.* Boston, MA: Springer US, pp. 1-31.

Stoll, H. et al., 2015. Imaging spin dynamics on the nanoscale using X-Ray microscopy. *Frontiers in Physics,* 21 4, Volume 3, p. 26.

Sukhov, A. et al., 2014. Dipole-dipole interaction in arrays of Fe/FexOy Core/shell nanocubes probed by ferromagnetic resonance. *IEEE Transactions on Magnetics,* 1 12.50(12).

Taurel, B. et al., 2016. Complete mapping of the spin-wave spectrum in a vortex-state nanodisk. *Physical Review B,* 23 5, 93(18), p. 184427.

Thiele, A. A., 1973. Steady-state motion of magnetic domains. *Physical Review Letters,* 5 2, 30(6), pp. 230-233.

Toedt, J. N. et al., 2016. Design and construction of a spin-wave lens. *Scientific Reports,* 21 9, 6(1), pp. 1-6.

Tokunaga, M. et al., 1989. Magnetic properties of isotropic and anisotropic Nd-Fe-B bonded magnets. *Journal of Magnetism and Magnetic Materials,* 1 8, 80(1), pp. 80-87.

Torok, E. J., Olson, A. L. & Oredson, H. N., 1965. Transition between Bloch and Néel walls. *Journal of Applied Physics,* 14 4, 36(4), pp. 1394-1399.

Uchiyama, T. & Takiya, T., 2017. Development of precise off-diagonal magnetoimpedance gradiometer for magnetocardiography. *AIP Advances,* 1 5, 7(5), p. 056644.

Urban, R. et al., 2006. Perturbation of magnetostatic modes observed by ferromagnetic resonance force microscopy. *Physical Review B - Condensed Matter and Materials Physics,* 14 6, 73(21), p. 212410.

V V Kruglyak, S O Democritov & D Grundler, 2010. Magnonics. *Journal of Physics D: Applied Physics,* 43(1), pp. 260-301.

Van De Wiele, B. et al., 2016. Tunable short-wavelength spin wave excitation from pinned magnetic domain walls. *Scientific Reports,* 17 2, 6(1), pp. 1-11.

Vaňatka M., U. M. J. R. F. L. D. M. I. M. M. J. U. V. a. Š. T., 2017. Magnetic vortex nucleation modes in static magnetic fields. *AIP Advances,* 7(10).

Vansteenkiste, A. et al., 2014. The design and verification of MuMax3. *AIP Advances,* 1 10, 4(10), p. 107133.

Vasiliev, S. V., Kruglyak, V. V., Sokolovskii, M. L. & Kuchko, A. N., 2007. Spin wave interferometer employing a local nonuniformity of the effective magnetic field. *Journal of Applied Physics,* 14 6, 101(11), p. 113919.

Vavassori, P. et al., 2004. Magnetization reversal via single and double vortex states in submicron Permalloy ellipses. *Physical Review B - Condensed Matter and Materials Physics,* 6.69(21).

Vaz, C. A. et al., 2005. Multiplicity of magnetic domain states in circular elements probed by photoemission electron microscopy. *Physical Review B - Condensed Matter and Materials Physics,* 1 12, 72(22), p. 224426.

Verba, R. V. et al., 2016. Spin-wave excitation modes in thick vortex-state circular ferromagnetic nanodots. *Physical Review B - Condensed Matter and Materials Physics,* 28 6, 93(21), p. 214437.

Vogel, M. et al., 2018. Control of Spin-Wave Propagation using Magnetisation Gradients. *Scientific Reports,* 1 12, 8(1), pp. 1-10.

Vogt, K. et al., 2014. Realization of a spin-wave multiplexer. *Nature Communications,* 23 4, 5(1), pp. 1-5.

Vogt, K. et al., 2009. All-optical detection of phase fronts of propagating spin waves in a Ni81 Fe19 microstripe. *Applied Physics Letters,* 2 11, 95(18), p. 182508.

Vogt, K. et al., 2012. Spin waves turning a corner. *Applied Physics Letters,* 23 7, 101(4), p. 042410.

Vogt, K. et al., 2011. Optical detection of vortex spin-wave eigenmodes in microstructured ferromagnetic disks. *Physical Review B - Condensed Matter and Materials Physics,* 1 11, 84(17), p. 174401.

Wagner, K. et al., 2016. Magnetic domain walls as reconfigurable spin-wave nanochannels. *Nature Nanotechnology,* 1 5, 11(5), pp. 432-436.

Wang, J. et al., 2017. Magnetic domain wall engineering in a nanoscale permalloy junction. *Applied Physics Letters,* 14 8, 111(7), p. 072401.

Wang, K., Cai, C., Yamamoto, M. & Uchiyama, T., 2017. Real-time brain activity measurement and signal processing system using highly sensitive MI sensor. *AIP Advances,* 1 5, 7(5), p. 056635.

Wang, X. G. et al., 2013. An analytical approach to the interaction of a propagating spin wave and a Bloch wall. *Applied Physics Letters,* 1 4, 102(13), p. 132401.

Wang, X. S. & Wang, X. R., 2015. Domain Walls as Spin Wave Waveguides. *arXiv.org,* 18 12.

Wang, X. S., Zhang, H. W. & Wang, X. R., 2018. Topological Magnonics: A Paradigm for Spin-Wave Manipulation and Device Design. *Physical Review Applied,* 27 2, 9(2), p. 024029.

Wei, J., Zhu, Z. & Feng, H., 2016. Annealing influence on the exchange stiffness constant of Permalloy films with stripe domains. *J. Phys. D: Appl. Phys,* 49(), p. 265002.

Weiss, P., 1907. L'hypothèse du champ moléculaire et la propriété ferromagnétique. *J. Phys. Theor. Appl,* 6(1).

Whitehead, N. J., Horsley, S. A., Philbin, T. G. & Kruglyak, V. V., 2018. A Luneburg lens for spin waves. *Applied Physics Letters,* 19 11, 113(21), p. 212404.

Whitehead, N. J., Horsley, S. A., Philbin, T. G. & Kruglyak, V. V., 2019. Graded index lenses for spin wave steering. *Physical Review B,* 3 9, 100(9), p. 094404.

Whitehead, N. J. et al., 2017. Theory of linear spin wave emission from a Bloch domain wall. *Physical Review B,* 11 8.96(6).

Winter, J. M., 1961. Bloch wall excitation. Application to nuclear resonance in a bloch wall. *Physical Review,* 15 10, 124(2), pp. 452-459.

Wintz, S. et al., 2016. Magnetic vortex cores as tunable spin-wave emitters. *Nature Nanotechnology,* 1 11, 11(11), pp. 948-953.

Xing, X., Yu, Y., Li, S. & Huang, X., 2013. How do spin waves pass through a bend?. *Scientific Reports,* 16 10, 3(1), pp. 1-6.

Yakata, S. et al., 2013. Wide range tuning of resonant frequency for a vortex core in a regular triangle magnet. *Scientific Reports,* 20 12, 3(1), pp. 1-5.

Yamanoi, K., Yakata, S., Kimura, T. & Manago, T., 2013. Spin wave excitation and propagation properties in a permalloy film. *Japanese Journal of Applied Physics,* 1 8, 52(8), p. 083001.

Yan, M. et al., 2006. Spin-wave modes in a cobalt square vortex: Micromagnetic simulations. *Physical Review B,* Volume 73, p. 014425.

Yu, W. et al., 2015. Observation of vortex dynamics in arrays of nanomagnets. *Physical Review B - Condensed Matter and Materials Physics,* 22 5, 91(17), p. 174425.

Zhang, W., Pan, Z., Zhou, H. & Wang, E., 2017. *A novel micro-magnetic sensor based on GMI effect.* s.l., American Institute of Physics Inc., p. 020099.

Zhu, R., 2015. Grace: A cross-platform micromagnetic simulator on graphics processing units. *SoftwareX,* 1 12, Volume 3-4, pp. 27-31.

Zil, P. E., Terniryazev, A. G. & Tikhornirova, M. P., 1995. *Excitation and propagation of exchange spin waves in films of yttrium iron garnet,* s.l.: s.n.